

Search for high-mass bosons of an extended Higgs sector in b quark final states using the 2017 data set of the CMS experiment

Dissertation
zur Erlangung des Doktorgrades
an der Fakultät für Mathematik, Informatik und Naturwissenschaften
Fachbereich Physik
der Universität Hamburg

vorgelegt von
Jan Paul Asmuß

Hamburg
2021

Hiermit versichere ich an Eides statt, die vorliegende Dissertationsschrift selbst verfasst und keine anderen als die angegebenen Hilfsmittel und Quellen benutzt zu haben.

Die eingereichte schriftliche Fassung entspricht der auf dem elektronischen Speichermedium.

Die Dissertation wurde in der vorgelegten oder einer ähnlichen Form nicht schon einmal in einem früheren Promotionsverfahren angenommen oder als ungenügend beurteilt.

Hamburg, den 2. Juni 2021

Paul Asmuß

Gutacher/innen der Dissertation:	Dr. Rainer Mankel Prof. Dr. Elisabetta Gallo
Zusammensetzung der Prüfungskommission:	Dr. Rainer Mankel Prof. Dr. Elisabetta Gallo Prof. Dr. Florian Grüner Prof. Dr. Kerstin Tackmann Prof. Dr. Georg Weiglein
Vorsitzender der Prüfungskommission:	Prof. Dr. Florian Grüner
Datum der Disputation:	06. Juli 2021
Vorsitzender Fach-Promotionsausschuss PHYSIK:	Prof. Dr. Wolfgang Hansen
Leiter des Fachbereichs PHYSIK:	Prof. Dr. Günther H. W. Sigl
Dekan der Fakultät MIN:	Prof. Dr. Heinrich Graener

“There is a theory which states that if ever anyone discovers exactly what the Universe is for and why it is here, it will instantly disappear and be replaced by something even more bizarre and inexplicable. There is another theory which states that this has already happened.”

– Douglas Adams, *The Hitchhiker’s Guide To The Galaxy*

ABSTRACT:

A search for heavy, neutral Higgs bosons produced in association with b quarks and decaying into a pair of b quarks is presented. It is based on LHC Run 2 data, produced at a center-of-mass energy of 13 TeV in pp collisions and collected by the CMS experiment in 2017, corresponding to an integrated luminosity of 36.02 fb^{-1} .

Several theories beyond the Standard Model predict additional Higgs bosons and, depending on the specific model, the coupling to b quarks can be significantly enlarged. This is for example the case in the minimal supersymmetric extension of the Standard Model (MSSM) and in the type-II and flipped scenarios of the general Two-Higgs-Doublet Model (2HDM).

A dedicated trigger is utilized to select the events for this analysis. At least three highly energetic jets are required in the final state. Out of these, the two jets with the largest energy contributions are selected as candidates for the Higgs boson decay and the third one is originating from an associated b quark. The invariant mass of the leading two jets is therefore the main observable in this analysis and Higgs boson masses from 300 to 1600 GeV are investigated. To avoid overlap with the complementary semi-leptonic analysis, no muon is required to be present within any final-state jet, leading to an all-hadronic signature.

The dominant background contribution consists of heavy-flavor QCD-multi-jet events and is estimated based on a fully data-driven approach.

No significant deviation from the background-only prediction of the Standard Model is observed. Therefore, limits on the production cross-section times branching fraction of the signal process are calculated. These limits are translated into the parameter space of several specific models, namely the $(m_A, \tan \beta)$ plane for MSSM benchmark scenarios and the $(\cos(\beta - \alpha), m_A, \tan \beta)$ parameter space of 2HDM models.

ZUSAMMENFASSUNG:

Eine Suche nach schweren, neutralen Higgs-Bosonen, die in Assoziation mit b-Quarks produziert werden und in ein b-Quark-Paar zerfallen, wird präsentiert. Sie basiert auf LHC-Run-2 Daten, die bei einer Schwerpunktsenergie von 13 TeV in Proton-Proton-Kollisionen erzeugt und im Jahr 2017 vom CMS Experiment aufgezeichnet wurden und die einer integrierten Luminosität von 36.02 fb^{-1} entsprechen.

Mehrere Theorien, die über das Standardmodell hinaus gehen, sagen weitere Higgs-Bosonen voraus und abhängig vom spezifischen Modell kann die Kopplung an b-Quarks signifikant erhöht sein. Dies ist beispielsweise der Fall in der minimalen supersymmetrischen Erweiterung des Standardmodells (MSSM) und in den type-II und flipped Szenarien des allgemeinen Zwei-Higgs-Doublet Modells (2HDM).

Ein speziell entwickelter Trigger wird genutzt, um die Events für diese Analyse zu selektieren. Mindestens drei hochenergetische Jets werden im Endzustand gefordert. Von diesen werden die beiden Jets mit den höchsten Energiebeiträgen als Kandidaten für den Zerfall des Higgs-Bosons ausgewählt und der dritte stammt von einem assoziierten b-Quark. Die invariante Masse der führenden beiden Jets ist daher die Hauptobservable in dieser Analyse und Higgs-Boson-Massen von 300 bis 1600 GeV werden untersucht. Um Überschneidungen mit der komplementären semileptonischen Analyse zu vermeiden, wird gefordert, dass kein Myon in einem der Jets im Endzustand präsent ist, was zu einer vollständig hadronischen Signatur führt.

Der dominante Untergrundbeitrag besteht aus heavy-flavor QCD-Multi-Jet-Events und wird basierend auf einem vollständig datenbasierten Ansatz geschätzt.

Keine signifikante Abweichung von der Untergrundvorhersage des Standardmodells wird beobachtet. Deshalb werden Limits auf das Produkt des Produktionswirkungsquerschnitts und der Zerfallswahrscheinlichkeit des Signalprozesses berechnet. Diese Limits werden in den Parameterraum spezifischer Modelle übersetzt, genauer die $(m_A, \tan \beta)$ -Ebene für MSSM Szenarien und den $(\cos(\beta - \alpha), m_A, \tan \beta)$ -Parameterraum für 2HDM Modelle.

Contents

1. Introduction	1
2. Theoretical Background	5
2.1. Standard Model of Particle Physics	5
2.1.1. Quantum Field Theories	7
2.1.2. Electromagnetism	8
2.1.3. Strong Interaction	9
2.1.4. Weak Interaction	11
2.1.5. Electroweak Unification	13
2.1.6. Spontaneous Symmetry Breaking and Higgs Mechanism	14
2.1.7. The Higgs Boson	16
2.1.8. Open Questions of the Standard Model	20
2.2. Extensions of the Standard Model	20
2.2.1. Supersymmetry	21
2.2.2. Two-Higgs-Doublet Models	31
3. Experimental Setup	39
3.1. Large Hadron Collider	39
3.2. The Compact Muon Solenoid Detector	42
3.2.1. Silicon Tracking System	44
3.2.2. Electromagnetic Calorimeter	46
3.2.3. Hadronic Calorimeter	48
3.2.4. Muon System	49
3.3. Trigger and Data Acquisition	51
3.4. Event and Detector Simulation	53
4. Physics Objects	55
4.1. Objects Reconstruction	55
4.1.1. Particle Flow Algorithm	55

4.1.2.	Tracks and Vertices	56
4.1.3.	Jets	58
4.1.4.	Jet Energy Corrections	60
4.2.	B-Tagging	62
4.2.1.	Comparison of Different b-Tagging Algorithms	63
5.	Search for Heavy, Neutral Higgs Bosons Decaying into a Pair of b Quarks	69
5.1.	Previous Results	69
5.1.1.	LEP and TeVatron	69
5.1.2.	LHC Run 1	71
5.1.3.	LHC Run 2	72
5.2.	Signal and Background Processes	74
5.3.	Analysis Strategy	77
5.4.	Data and Monte-Carlo Samples	79
5.5.	Triggers	81
5.5.1.	Analysis Triggers	82
5.5.2.	Jet Kinematic Trigger Efficiency	84
5.5.3.	B-Tag Trigger Efficiency	86
5.6.	Event Selection	91
5.6.1.	Primary Vertex Selection	91
5.6.2.	Jet Selection	92
5.6.3.	Corrections to Monte Carlo Events	95
5.7.	Signal Modeling	97
5.7.1.	Signal Mass Distributions	99
5.7.2.	Impact of Jet Energy Corrections	99
5.7.3.	Systematic Uncertainties	101
5.7.4.	Signal Efficiency	107
5.8.	Background Modeling	107
5.8.1.	Control Region Parametrization	110
5.8.2.	Transfer Factor Studies and B-Tag Weighting	114
5.8.3.	Transfer Factor	118
5.8.4.	Bias Study	120
5.9.	Signal Extraction and Validation	122
5.9.1.	Simultaneous Fit	122
5.9.2.	Validation of Signal-Extraction Approach	125

5.10. Statistical Procedures	127
5.10.1. Likelihood Function and Fit	127
5.10.2. Nuisance Parameters	134
5.10.3. Limit Extraction	135
6. Results	137
6.1. Before Unblinding	137
6.2. After Unblinding	139
6.3. Model Interpretation	146
7. Summary and Outlook	159
Appendices	163
Appendix A. Tracker Alignment	165
A.1. Global Position of High-Level Structures	165
A.2. Track-Based Alignment	166
A.3. Weak Modes	168
A.4. Alignment Strategies	168
A.5. Validation Techniques	169
A.6. Conclusion	175
Appendix B. Cross-Sections and Branching Fractions in the 2HDM	177
Appendix C. Model Dependent Limits	191
Appendix D. Higgs Physics Within and Beyond the Standard Model at CMS	197
List of Figures	211
List of Tables	217
Bibliography	219

1. Introduction

Since ancient times, mankind aimed to understand its environment, on earth and beyond, in the universe. With time, moving stars were identified as planets (from the Greek word $\pi\lambda\alpha\nu\eta\tau\eta\varsigma$, “wanderer”) [1] and it was assumed that the smallest constituent of matter would be the atom (from the Greek word $\alpha\tau\omicron\mu\omicron\varsigma$, “undividable”) [2]. Much more recently, in the 19th century, sub-atomic particles were detected, starting with the electron, which was discovered in 1897 by J. J. Thomson [3]. Throughout the 19th and 20th centuries, further particles were established like the up and down quarks which constitute the nucleons proton and neutron.

The current understanding of elementary particles is summarized by the Standard Model of particle physics (SM) [4]. It describes all known fundamental particles as well as their non-gravitational interactions, i.e. the electroweak and strong forces, in terms of a renormalizable quantum field theory. The SM has been tested over several decades and it is found to describe the observed data very well while reliably predicting the outcome of experiments. Examples for the latter are the relatively recent discoveries of the W and Z bosons [5, 6] as well as the top quark [7, 8]. The latest triumph of the SM was the discovery of the Higgs boson in 2012 at the LHC by the ATLAS and CMS collaborations [9–11]. Moreover, respective properties of these particles such as production and decay modes are correctly predicted by the SM [12–15]. Extensive tests of the SM confirmed its validity up to an energy scale of $\mathcal{O}(1 \text{ TeV})$ with larger scales still to be investigated.

Despite the tremendous success of the SM so far, it is widely accepted that this theory is not the final explanation of all fundamental processes. Within the framework of the SM, there is, for example, no explanation of the observed non-zero neutrino masses [16–18]. Similarly, observation strongly implies the existence of Dark Matter (DM) [19–22]. However, no particle of the SM would be a suitable DM candidate [23]. Furthermore, gravity, one of the fundamental forces, could not yet be included in the SM as a quantum field theory. Hence, it is assumed that the SM is only valid up to a certain energy, or cut-off, scale at which quantum gravitational effects become non-negligible. This scale could be the Planck scale of 10^{19} GeV . Additional shortcomings arise from a naturalness argument. For instance, the SM provides no explanation for the large energy difference between the electroweak scale and any assumed cut-off scale.

Therefore, the Higgs boson mass would receive large radiative corrections [24], which have to be fine-tuned to provide the observed mass. This is known as the hierarchy problem. Also the mass hierarchy of fermions and the observed number of respective generations as well as the matter-antimatter asymmetry in the universe can not be explained by the Standard Model.

Many theories beyond the SM (BSM) have been developed, targeting an explanation of phenomena which the SM can not provide. Several of these theories predict additional Higgs bosons, for example the general Two-Higgs-Doublet Model (2HDM) [25]. By adding a second Higgs doublet, four additional degrees of freedom are introduced. After symmetry breaking, the five resulting Higgs bosons comprise three neutral particles $\phi = \{h, H, A\}$, where h and H are CP-even scalars and A is a CP-odd pseudoscalar, as well as two charged Higgs bosons H^\pm . The thereby established larger scalar sector allows for explanations of the observed matter-antimatter asymmetry by introducing additional sources of CP violation. By exploiting the coupling structure of the two doublets to the different fermions, also their mass structure could be explained. One particular model with two Higgs doublets is the inert model [26], which was designed to explain the observed massiveness of neutrinos and also provides a candidate for Dark Matter as well as an explanation for the number of fermionic generations. Another, well-established theoretical extension of the SM is the Minimal Supersymmetric Standard Model MSSM [27]. It introduces a symmetry between fermions and bosons, which solves the hierarchy problem by the price of doubling the SM particle content. Since it is assumed that supersymmetric particles do not decay into SM particles, the lightest SUSY particle (LSP) is a viable DM candidate. Around 10^{16} GeV, the MSSM predicts a unification of the electromagnetic, weak, and strong coupling strengths. Thus, it could serve as an effective theory of an even wider Grand Unified Theory (GUT) [28]. At tree-level, only two parameters are necessary to describe the properties of the MSSM Higgs sector. They are conventionally selected to be the mass of the A boson and $\tan \beta = v_1/v_2$, i.e. the ratio of the vacuum expectation values of the two Higgs doublets. All of this motivates to investigate the possible existence of an extended Higgs sector. The additional Higgs bosons are usually assumed to feature a phenomenological behavior relatively similar to the already observed 125 GeV boson. Therefore, experimental setups are required that can on the one hand provide the required large energies and integrated luminosities to produce the Higgs bosons in a sufficient number to identify them correctly. On the other hand, these experiments should have the precision to detect, identify, and reconstruct as many possible decay products of a Higgs boson as possible.

This is achieved by particle colliders like the Large Hadron Collider (LHC) [29, 30] at CERN and general-purpose detectors like ATLAS (A Toroidal LHC ApparatuS) [31] and CMS (Compact Muon Solenoid) [32]. The search presented in this analysis is based on data collected in

2017 by the CMS detector, corresponding to an integrated luminosity of 36.02 fb^{-1} . In both the SM and certain BSM theories, e.g. the MSSM and some 2HDM scenarios, the Higgs bosons may feature a large Yukawa coupling to bottom quarks. This leads to branching fractions up to above 99 %, depending on the specific parameters under investigation, making this decay channel a promising candidate in the search for additional Higgs bosons. Therefore, this decay mode is chosen for the analysis presented here. Specifically in the 2HDM type-II and flipped models, Higgs boson couplings to up-type quarks are suppressed and in case of the flipped scenario, this also affects the coupling to leptons, making the decay into a pair of τ leptons inaccessible. Moreover, the coupling to b quarks is further enhanced in certain models. Hence, instead of the gluon-fusion production mode which is dominant for the $h(125)$ [33], the b-associated production is selected for this study. Furthermore, in the limit $m_A \gg m_Z$, it is assumed that H and A are nearly mass degenerate and, thus, the Higgs boson production cross-section in the b-associated production mode is enlarged by a factor of about $2 \tan^2 \beta$. Exploiting this particular production mechanism also allows to reduce the overwhelming QCD multi-jet background significantly with respect to the gluon-fusion production mode. In the final state, at least three highly energetic, b-tagged jets are required of which the leading two are candidates for the Higgs boson decay and the third one is originating from an associated b quark. The main analysis observable is therefore the mass of the leading two jets, m_{12} . A dedicated trigger is developed and utilized and Higgs boson masses from 300 to 1600 GeV are investigated. The corresponding results are further interpreted in terms of specific models. To complement the existing semi-leptonic analysis [34] and avoid double-counting, the events used in this search are vetoed here.

This thesis is structured in the following way: In Chapter 2, the theoretical foundation of this analysis is reviewed, discussing the SM as well as theories beyond, particularly those featuring extensions of the Higgs sector. Chapter 3 is dedicated to the experimental setup, comprising the LHC and the CMS detector. Afterwards, the identification and reconstruction of physics objects used for this analysis are presented in Chapter 4. The analysis strategy is described in Chapter 5. This comprises the most important signal and background processes, the used data sets as well as the methods of selecting events. Furthermore, signal and background modeling, the signal extraction procedure and respective statistical treatments are described in this chapter. Corresponding results and interpretations in terms of specific models are then presented in Chapter 6, before a summary and an outlook are given in Chapter 7.

2. Theoretical Background

2.1. Standard Model of Particle Physics

Various attempts of formulating a conclusive theory which would describe all fundamental particles and their non-gravitational interactions have been made. By now, the Standard Model (SM) of particle physics is the theory which has come closest to a consistent model [35]. It has been extensively tested and so far, the experimental data support this theory particularly well.

All particles described by the Standard Model can be divided into two major groups which are distinguished by their spin. While fermions carry half-integer spin, bosons have integer spin. Thus, fermions follow the Fermi-Dirac statistic [36, 37] and bosons are described by Bose-Einstein statistics [38]. Depending on their interactions with other particles, fermions are further divided into quarks and leptons. While both of these groups of particles interact via the weak force and all charged particles interact electromagnetically, only quarks participate in the strong interaction.

Six leptons are known, of which three are charged, namely the electron (e), muon (μ), and tau lepton (τ). The other three leptons are electrically neutral neutrinos, which are named according to their weak interaction partner, i.e. ν_e , ν_μ , and ν_τ . Electron, muon, and tau lepton all carry an electrical charge of $-1e$, where e is the elementary charge. Also all of the six known quarks are electrically charged. While the up (u), charm (c), and top (t) quarks carry a charge of $+2/3e$, the down (d), strange (s), and bottom (b) quarks have an electrical charge of $-1/3e$. The former group is collectively referred to as up-type quarks and the latter is known as down-type quarks. All fundamental fermions in the SM are further described by a quantum number associated with the weak interaction, called the weak isospin. For left-handed fermions, which form weak isodoublets, this quantum number is $I = 1/2$. Right-handed fermions do not interact weakly and form weak isosinglets with a weak isospin of $I = 0$. The third component of this weak isospin, I_3 , is 0 for right-handed fermions. I_3 equals $+1/2$ for left-handed neutrinos and up-type quarks and it takes the value $-1/2$ for left-handed down-type quarks and charged leptons. Through the charged current of the weak interaction, I_3 is changed and thereby up- and down-type quarks as well as neutrinos and charged leptons interact with

2. Theoretical Background

Type	Generation			Charge [e]	I_3 (left-handed particle)
	I	II	III		
Charged leptons	e	μ	τ	-1	$-1/2$
Neutrinos	ν_e	ν_μ	ν_τ	0	$+1/2$
Up-type quarks	u	c	t	$2/3$	$+1/2$
Down-type quarks	d	s	b	$-1/3$	$-1/2$

Table 2.1.: Fermion content of the Standard Model

each other. However, entirely left- or right-handed particles are only possible if these particles are massless. Therefore, massive particles are usually described by their chirality which reflects the representation of the Poincaré group of this particle. The chirality is identical to the helicity for massless particles. Furthermore, all quarks carry color charge which is the charge of the strong interaction and can take on three states which are named red (r), blue (b), and green (g). Quarks are usually bound in color-neutral hadrons, so no color-charged particles are observed. Only inside a quark-gluon plasma, quarks are not confined [39]. The fermions are grouped into generations, where each generation consists of a charged lepton, a neutrino, an up-type quark and a down-type quark, as can be seen in Table 2.1. A full overview of all known particles is given at the end of this section. A particle can decay into a lighter particle of the same family via the weak interaction. While the mass of charged leptons and quarks is observed to increase from one generation to the next, this has not yet been experimentally proven for neutrinos since their masses could not be measured so far. The latest upper bounds for neutrino masses are $m_{\nu_e} < 1.1$ eV, $m_{\nu_\mu} < 0.19$ MeV, and $m_{\nu_\tau} < 18.2$ MeV [40].

All fermions in the Standard Model have an antiparticle which has reversed-sign quantum numbers but the same mass and spin. For charged leptons, this is denoted by a $+$ or $-$ sign, e.g. μ^- and μ^+ stand for the muon and its antiparticle. For all other fermions, a bar is placed over the letter to denote the antiparticle, e.g. bottom and anti-bottom quark are written as b and \bar{b} . Together, the family of fermions contains the constituents of matter, where particles of the first generation form ordinary matter (atoms).

In the SM, forces are mediated by bosons. These force-carriers are the photon (γ , mediating the electromagnetic force), the Z^0 and W^\pm bosons (carrying the weak force) and the gluons (g , carrier of the strong force). Out of these, photons and gluons were found to be massless [40, 41], while W and Z bosons are massive [5, 6], which is directly correlated to the short range – $\mathcal{O}(10^{-18}$ m) – of the weak interaction.

In the following, the basic concept of quantum field theories is discussed and a short explanation of each individual interaction is given. Furthermore, the basics of spontaneous symmetry

breaking and the Higgs theory are introduced and searches for the SM Higgs boson are presented. Finally, open questions in the Standard Model are discussed.

2.1.1. Quantum Field Theories

The SM is a quantum field theory (QFT), describing particles not by the use of single-particle wave functions as it is done in quantum mechanics but as excitations of quantum fields which can represent multiple particles. These fields satisfy the quantum mechanical field equations which are determined by the form of the Lagrangian density \mathcal{L} [42]. The Lagrangian density of the SM is a function of the present fields ϕ_i and the excitations of these fields, fermions and bosons, are physical observables. Following the Fermi-Dirac and Bose-Einstein statistics, the overall wave functions are antisymmetric for fermions and symmetric for bosons, leading to the observed differences in behavior. While any two fermions with identical quantum numbers can not occupy the same space, which leads e.g. to atomic orbitals, bosons can form Bose-Einstein condensates.

In general, Lagrangian densities are functions of the quantum fields $\phi_i(x, y, z, t)$ and their respective x, y, z , and t derivatives:

$$\mathcal{L} = \mathcal{L}(\phi_i, \partial_\mu \phi_i), \text{ where } \partial_\mu \phi_i \equiv \frac{\partial \phi_i}{\partial x^\mu}. \quad (2.1)$$

If \mathcal{L} is integrated over t , this yields the action S . An integral over all space coordinates gives the kinetic energy minus the potential energy, $L = T - U$. Often, the space-time coordinates x, y, z, t are shortened to just x , which will also be used in the remaining part of this section.

If a Lagrangian density is invariant under a certain transformation, i.e. its observable quantities do not change, it is called symmetric under this transformation. Noether's theorem [43] states that each such symmetry is related to a conservation law and each conserved variable is thus a reflection of an underlying symmetry. As an example, the symmetry of physical laws regarding translations in time reflects the conservation of energy, while a system which is invariant under translations in space conserves momentum. Most important for this chapter, a symmetry under gauge transformation is related to a conservation of charge.

Several types of symmetries can be distinguished. While space-time symmetries act on the coordinates x , internal symmetries affect ϕ itself. In special relativity [44], a system should be symmetrical under time and space transformation. This is reflected by Lorentz invariance, containing conservation rules for energy, momentum, and angular momentum.

While the above mentioned symmetries are global, in a gauge theory, local invariance is achieved by additional terms in the Lagrangian densities. Mathematically, it is the difference between a continuous and a discrete symmetry. This gauge theory can then be used to describe particles and their interactions. The added terms relate to additional fields, called gauge fields, which give rise to the gauge bosons. These bosons are mediating the interaction through the charge associated with the respective symmetry.

2.1.2. Electromagnetism

The Dirac Lagrangian, describing a free fermion with mass m , is given by

$$\mathcal{L} = i\bar{\psi}\gamma^\mu\partial_\mu\psi - m\bar{\psi}\psi, \quad (2.2)$$

where γ^μ are the Dirac matrices and $\psi = \psi(x)$ is the fermionic field spinor (spin-1/2) with the adjoint spinor $\bar{\psi}$. \mathcal{L} is invariant under the global phase transformation

$$\psi \rightarrow e^{iq\theta}\psi, \quad \bar{\psi} \rightarrow e^{-iq\theta}\bar{\psi} \quad (2.3)$$

for any real number θ and charge q . However, this is not true for the local, i.e. space-dependent, phase transformation

$$\psi \rightarrow e^{iq\theta(x)}\psi. \quad (2.4)$$

Here, $\theta(x)$ is the phase of the local transformation and due to its derivative, the Lagrangian would take the form

$$\mathcal{L} \rightarrow \mathcal{L} - q\partial_\mu\theta\bar{\psi}\gamma^\mu\psi. \quad (2.5)$$

Electromagnetic interactions in the SM are described by Quantum Electrodynamics (QED). Thus, the QED Lagrangian should be invariant under the transformation in Equation 2.4. This can be achieved by adding a new vector (spin-1) field A_μ with the transformation

$$A_\mu \rightarrow A_\mu + \partial_\mu\theta, \quad (2.6)$$

hence

$$\mathcal{L}_{\text{addition}} = -\frac{1}{4}F^{\mu\nu}F_{\mu\nu} + m_A^2 A^\nu A_\nu + \mathcal{L}_{\text{int}}, \quad (2.7)$$

where the field strength tensor $F^{\mu\nu} \equiv (\partial^\mu A^\nu - \partial^\nu A^\mu)$ is invariant under Equation 2.6, while $A^\nu A_\nu$ is not. Thus, invariance overall can only be achieved if $m_A = 0$. This massless field

represents the photon.

Accordingly, the overall QED Lagrangian consists of three parts, describing the free fermion (\mathcal{L}_f), the vector field ($\mathcal{L}_{\text{gauge}}$), and their interaction (\mathcal{L}_{int}):

$$\mathcal{L}_{\text{QED}} = \mathcal{L}_f + \mathcal{L}_{\text{gauge}} + \mathcal{L}_{\text{int}} = i\bar{\psi}\gamma^\mu\partial_\mu\psi - m\bar{\psi}\psi - \frac{1}{4}F_{\mu\nu}F^{\mu\nu} + q\bar{\psi}\gamma^\mu\psi A_\mu \quad (2.8)$$

with the electromagnetic current density $J^\mu \equiv q\bar{\psi}\gamma^\mu\psi$, which represents a three-particle vertex with a fermion-anti-fermion pair coupled to a photon. As can be seen in Equation 2.8, the *gauge* term has no dependency on q , implying that the photon is not only massless but also electrically neutral.

In a more general way, $e^{iq\theta}$ in Equation 2.4 can be thought of as a unitary matrix of order one, i.e. from the $U(1)$ group. If the Lagrangian density is invariant under the transformation $\psi \rightarrow U\psi$ for all matrices in the $U(1)$ group, it is called $U(1)$ gauge invariance. Thus, the $U(1)$ gauge symmetry reflects the conservation of electromagnetic charge.

The coupling strength of QED, $g_{\text{em}} = e$, is related to the fine-structure constant $\alpha_{\text{em}} = g_e^2/(4\pi)$. Although called constant, α_{em} actually has a logarithmic energy dependence, ensuring that the overall theory is renormalizable. For low energies approaching a squared momentum transfer Q^2 of zero, α_{em} equals $e^2/(4\pi) \approx 1/137$. For higher energies, the photon propagator receives virtual lepton and quark corrections, which change the effective coupling strength. This was directly observed in large- and small-angle Bhabha scattering processes [45, 46].

2.1.3. Strong Interaction

Originally, it was assumed that nucleons (protons and neutrons), as well as additional hadrons which were found later, are fundamental particles. In 1961, Gell-Mann described this theory which was called the eightfold way [47]. Later, it became clear that these particles are in fact bound states of even smaller constituents, called quarks [48]. Protons and neutrons can be described as a combination of up (u) and down (d) quarks, bound to each other by a particular force, named the strong force and mediated by massless gluons. Additional to these valence quarks, nucleons also consist of other quarks, called sea-quarks. They are produced and annihilated inside of protons and neutrons by gluon interactions. Furthermore, it was found that quarks can not be observed outside of hadrons. This property was later found to be associated to the charge of the strong interaction which is called color charge and comes in the variants red (r), green (g), and blue (b) [49]. All naturally observable particles are what is called color-neutral,

2. Theoretical Background

i.e. they either carry color and anti-color of the same flavor or they carry all (anti-)colors in the same amount.

Inside of the Standard Model, the structure of the strong interaction is described by the $SU(3)$ gauge symmetry group of Quantum Chromodynamics (QCD). Note that a $SU(n)$ matrix is not only unitary but also has a determinant of 1. Since quarks of all colors should have the same mass, the Dirac Lagrangian of a free quark (Equation 2.2) becomes the sum of the three color states, using

$$\psi \equiv \begin{pmatrix} \psi_r \\ \psi_b \\ \psi_g \end{pmatrix} \quad \text{and} \quad \bar{\psi} \equiv (\bar{\psi}_r \quad \bar{\psi}_b \quad \bar{\psi}_g). \quad (2.9)$$

Each spinor of Equation 2.2 then has to be interpreted as a vector with three components $\psi(x)$, where x describes the space-time components x, y, z, t as discussed in Section 2.1.1.

Analogous to QED, \mathcal{L}_{QCD} should be invariant under the local transformation

$$\psi \rightarrow e^{igs\theta} e^{igs\lambda_a} \psi, \quad (2.10)$$

where θ is the phase of the transformation, g_s is the strong coupling strength, and λ_a belongs to the $SU(3)$ group, representing the eight corresponding generators, the Gell-Mann matrices $\lambda_1 \dots \lambda_8$. For a $SU(n)$ group, the number of degrees of freedom is given by $n^2 - 1$. The deduction of one is caused by the absorption of a degree of freedom due to the requirement that the determinant must be 1. Also analogous to QED, this local gauge invariance requires an addition of gauge fields $G_a^\mu = G_1^\mu \dots G_8^\mu$. Each of them represents one possible configuration of the gluon and is associated with a color current $J_a^\mu \equiv g_s \bar{\psi} \gamma^\mu \lambda_a \psi$. Overall, including the strong coupling constant g_s (similar to the electric charge q in Equation 2.8), \mathcal{L}_{QCD} then reads

$$\mathcal{L}_{QCD} = i \bar{\psi} \gamma^\mu \partial_\mu \psi - m \bar{\psi} \psi - \frac{1}{4} G_{\mu\nu}^a G_a^{\mu\nu} + g_s \bar{\psi} \gamma^\mu \lambda_a \psi G_\mu^a \quad (2.11)$$

with the field-strength tensor

$$G_a^{\mu\nu} \equiv \partial^\mu G_a^\nu - \partial^\nu G_a^\mu - g_s f_{bc}^a G_b^\mu G_c^\nu, \quad (2.12)$$

where f_{bc}^a are the structure constants of $SU(3)$, allowing for gluon self-interaction vertices.

Finally, as α_{em} for QED, also $\alpha_S = g_s^2/(4\pi)$, the fine-structure constant of QCD, is dependent

on the momentum transfer Q :

$$\alpha_S(Q^2) = \frac{12\pi}{(11n - 2f) \ln(Q^2/\Lambda_{\text{QCD}}^2)}. \quad (2.13)$$

For the SM, $n = 3$ and $f = 6$ are the numbers of colors and quark flavors, respectively, while $\Lambda_{\text{QCD}} \sim 200 \text{ MeV}$ is the so-called QCD scale. It can only be determined experimentally and describes the Q^2 at which QCD processes become non-perturbative. As can be seen from Equation 2.13, unlike α_{em} , α_S decreases with energy. Implying that for very large Q^2 , quarks are not affected anymore by the strong force, this is called asymptotic freedom of quarks. Also, Equation 2.13 shows that for small Q^2 , the strong force increases, which explains the confinement of quarks within color-neutral states.

2.1.4. Weak Interaction

In 1934, Fermi [50] was the first one to formulate a theory of weak interactions, based on observations of the β decay. For low energies as in nuclear decays, this interaction can be well modeled as a four particle point-interaction with no Q^2 dependence. Later, in 1957, studying Co^{60} decays, Wu [51] found that parity is violated in weak interactions. This kind of behavior can not be described analogous to QED and QCD based on a vector current. It is instead incorporated using charged vector-minus-axial ($V - A$) currents

$$J^{(C)\mu} \equiv \frac{g_W}{\sqrt{2}} \bar{\psi} \frac{1}{2} \gamma^\mu (1 - \gamma^5) \psi \quad (2.14)$$

with the weak coupling strength g_W . Equation 2.14, together with the parity operators $P_{R,L} = (1 \pm \gamma^5)$, shows that, in the case of massless particles, only left-handed fermions and right-handed anti-fermions participate in the weak interaction. Also, the scalar product of two vector currents ($J^V \cdot J^V$) or two axial-vector currents ($J^A \cdot J^A$) is invariant under parity transformation, while this is not the case for $J^A \cdot J^V$ which flips its sign. Thus, the parity violation of weak interactions can be explained. Furthermore, the presence of β^+ decays implies that there should be two oppositely charged currents.

All fermions of the Standard Model participate in the weak interaction, while neutrinos are electrically neutral, thus not participating in electromagnetic interactions, and all leptons are colorless, i.e. they are not interacting via the strong force. It has to be noted, however, that right-handed neutrinos are not included here, since they could not be observed yet. As these particles carry no electromagnetic or color charge and their quantum numbers associated with

2. Theoretical Background

Force	Strength	Mediator	Spin	Mediator Mass
Strong	1	g	1	0
Electromagnetism	10^{-3}	γ	1	0
Weak	10^{-8}	W^\pm	1	80.379 GeV
		Z	1	91.188 GeV
Gravity	10^{-42}	G?	2	$< 6 \cdot 10^{-32}$ eV

Table 2.2.: Forces and mediators in the Standard Model. All strength values are estimates for two particles at a distance of about 1 fm. Gravity is assumed to be so weak that its role in particle interactions can not be measured with current methods. Table adapted from [42], particle properties from [40].

the weak force, i.e. weak isospin and hypercharge, are zero, they do not participate in an interaction which is covered by the SM. The weak force is mediated by Z^0 (neutral current) and W^\pm (charged current) bosons. As photons and gluons, they have spin 1. A relatively short range of the weak interaction (hence the naming) was observed, indicating that the mediator bosons should be rather heavy, which was found to be true. Table 2.2 summarizes the current knowledge on fundamental forces and their mediators.

Although this formulation of the weak theory worked very well for many processes, others could not be explained, like the $\Lambda \rightarrow p + \pi^-$ or $\Omega^- \rightarrow \Lambda + K^-$, or their predicted and measured rates did not match, like for $K^0 \rightarrow \mu^+ \mu^-$. This was resolved in several steps, starting with Cabibbo's theory (1963) [52], which was then refined and extended by Glashow, Iliopoulos, and Maiani (GIM, 1970) [53] as well as Kobayashi and Maskawa (KW, 1973) [54]. Their basic premise was that instead of the mass eigenstates

$$\begin{pmatrix} u \\ d \end{pmatrix}, \begin{pmatrix} c \\ s \end{pmatrix}, \begin{pmatrix} t \\ b \end{pmatrix}, \quad (2.15)$$

the weak interaction would couple to different eigenstates

$$\begin{pmatrix} u \\ d' \end{pmatrix}, \begin{pmatrix} c \\ s' \end{pmatrix}, \begin{pmatrix} t \\ b' \end{pmatrix}, \quad (2.16)$$

in the same way leptons interact via the weak force. The relation between mass eigenstates and

weak eigenstates is given by the CKM matrix:

$$\begin{pmatrix} d' \\ s' \\ b' \end{pmatrix} = \begin{pmatrix} V_{ud} & V_{us} & V_{ub} \\ V_{cd} & V_{cs} & V_{cb} \\ V_{td} & V_{ts} & V_{tb} \end{pmatrix} \begin{pmatrix} d \\ s \\ b \end{pmatrix}, \quad (2.17)$$

where V_{ij} describes the relative coupling strengths of quark i to quark j . Since these values are not predicted by the SM, they have to be determined experimentally [40].

2.1.5. Electroweak Unification

When the theory of weak interaction was first formulated, only charged currents were included, as described in Section 2.1.4. However, there were already thoughts that a neutral weak current might exist as well [55]. This idea also allowed for a combination of electromagnetic and weak forces, which was accomplished in the Glashow-Weinberg-Salam (GWS) scheme [56–60]. In 1973, evidence for the interaction $\bar{\nu}_\mu + e \rightarrow \bar{\nu}_\mu + e$, observed in a bubble-chamber experiment at CERN, suggested that the neutral current indeed existed [61].

The electroweak force is described as a gauge theory by the invariance of its Lagrangian under $SU(2)_L \times U(1)_Y$ transformation. Invariance under the $SU(2)_L$ group leads to the conservation of the weak isospin quantum number I . I is 0 for right-handed fermions (and left-handed anti-fermions) which do not participate in the weak interaction. Furthermore, the weak hypercharge Y is conserved because of the invariance under $U(1)_Y$ transformation. Y is related to electrical charge q and the third component of the weak isospin I_3 by

$$q = I_3 + \frac{1}{2}Y. \quad (2.18)$$

To achieve invariance under the transformation

$$\psi \rightarrow e^{ig_W\theta} e^{ig_W\tau_a\psi}, \quad (2.19)$$

where τ_1, τ_2 and τ_3 are the Pauli matrices, the covariant derivative

$$\mathcal{D}_\mu \equiv \partial_\mu + i\frac{g_W}{2}\tau_a W_{\mu a} + i\frac{g'_W}{2}Y B_\mu \quad (2.20)$$

2. Theoretical Background

is used instead of the ordinary derivative, leading to the Lagrangian

$$\mathcal{L} = \bar{\psi}_L \gamma^\mu \mathcal{D}_\mu \psi_L + \bar{\psi}_R \gamma^\mu \left(\partial_\mu + i \frac{g'_W}{2} Y B_\mu \right) \psi_R - \frac{1}{4} W_{\mu\nu}^a W_a^{\mu\nu} - \frac{1}{4} B_{\mu\nu} B^{\mu\nu}. \quad (2.21)$$

Here, g_W and g'_W are the couplings to the fields W_μ^a and B_μ , respectively. It has to be remembered that right-handed fermions have an isospin of 0, hence they do not interact with the charged currents of the weak interaction, which are represented by the fields W_μ^a . As can also be seen from Equation 2.21, additional to the three vector fields W_μ^a related to the $SU(2)_L$ group, there is one vector field B_μ related to the $U(1)_Y$ group.

These four fields describe the mediator bosons of the electroweak unification theory. First, the W^\pm bosons can be described as physical eigenstates of a superposition of the W_μ^1 and W_μ^2 fields:

$$W_\mu^\pm \equiv \frac{1}{\sqrt{2}} \left(W_\mu^1 \mp i W_\mu^2 \right). \quad (2.22)$$

Second, the two neutral fields W_μ^3 and B_μ mix to form two additional linear combinations, which are identified with the photon γ and the Z^0 boson:

$$\begin{pmatrix} \gamma \\ Z^0 \end{pmatrix} = \begin{pmatrix} \cos \theta_W & \sin \theta_W \\ -\sin \theta_W & \cos \theta_W \end{pmatrix} \begin{pmatrix} B_\mu \\ W_\mu^3 \end{pmatrix}, \quad (2.23)$$

where θ_W is the Weinberg angle, describing this mixture of vector fields.

To ensure gauge invariance under electroweak transformation, all vector fields in Equation 2.21 must be massless. Furthermore, the Dirac mass term $m\bar{\psi}\psi$ is not allowed because it is not invariant under $SU(2)_L$ transformation as left- and right-handed fermions represent different symmetries.

All of these findings are in contrast to the experimental observations that fermions as well as W and Z bosons are massive.

2.1.6. Spontaneous Symmetry Breaking and Higgs Mechanism

To incorporate the masses of the W^\pm and Z^0 bosons into the SM, the Brout-Englert-Higgs mechanism is used. It is based on the concept of spontaneous symmetry breaking and was developed independently by Higgs [62] as well as Brout and Englert [63]. Breaking the symmetry means that while the collection of all ground states still follows the symmetry, an individual minimum of the potential does not. Thus, the actual symmetry of the system is hidden by

choosing a particular minimum. The term spontaneous indicates that this is a property of the model and not initiated by external forces.

The Lagrangian density of the Higgs mechanism is given by

$$\mathcal{L}_{\text{Higgs}} = (\mathcal{D}_\mu \phi)^\dagger (\mathcal{D}^\mu \phi) - V(\phi), \quad (2.24)$$

with the two complex, positively charged and neutral, scalar fields

$$\phi = \begin{pmatrix} \phi^+ \\ \phi^0 \end{pmatrix} = \frac{1}{\sqrt{2}} \begin{pmatrix} \phi_1 + i\phi_2 \\ \phi_3 + i\phi_4 \end{pmatrix}, \quad (2.25)$$

the Higgs potential

$$V(\phi) = \mu^2 \phi^\dagger \phi + \lambda (\phi^\dagger \phi)^2, \quad (2.26)$$

and the covariant derivative of Equation 2.20. The parameters μ and λ of Equation 2.26 are newly introduced with this mechanism. For values $\mu^2 > 0$, the symmetry is not broken and there are no mass terms for W^\pm and Z^0 bosons. However, if $\mu^2 < 0$, $V(\phi)$ has an infinite set of degenerate minimum-energy states, satisfying

$$\phi^\dagger \phi = \frac{v^2}{2} = -\frac{\mu^2}{2\lambda} \quad (2.27)$$

with the vacuum expectation value (vev) v . The photon must still be massless to ensure invariance of QED, indicating a non-zero vev of ϕ^0 :

$$\langle 0 | \phi | 0 \rangle = \frac{1}{\sqrt{2}} \begin{pmatrix} 0 \\ v \end{pmatrix}. \quad (2.28)$$

This leads to a symmetry which is no longer invariant under $SU(2)_L \times U(1)_Y$ transformations, i.e. spontaneously broken.

By expanding the fields around the chosen minimum, they can be written as

$$\phi = \frac{1}{\sqrt{2}} \begin{pmatrix} 0 \\ v + h \end{pmatrix}, \quad (2.29)$$

where h represents a massive scalar boson, now known as the Higgs boson. Furthermore, the

2. Theoretical Background

masses of the W and Z bosons can immediately be read from the $(\mathcal{D}_\mu\phi)^\dagger(\mathcal{D}^\mu\phi)$ terms of $\mathcal{L}_{\text{Higgs}}$:

$$m_W = \frac{1}{2}g_W v \quad \text{and} \quad m_Z = \frac{1}{2}v\sqrt{g_W^2 + g_W'^2} = \frac{m_W}{\cos\theta_W}. \quad (2.30)$$

Using $m_W = 1/2g_W v$ and the measured values of m_W and g_W , the electroweak scale $v = 246$ GeV is obtained. Additionally, the coupling of the Higgs boson to the vector bosons can be extracted from the $\mathcal{O}(v)$ terms as

$$g_V = \frac{2m_V}{v}, \quad (2.31)$$

and because of the hVV and $hhVV$ terms, vertices with one or two Higgs bosons and two vector bosons are predicted. Since the gluons and photons are massless, the Higgs boson only couples to them via fermion loops. Finally, the mass of the Higgs boson is given by $m_H^2 = 2\lambda v^2$.

As mentioned in Section 2.1.5, also the Dirac term $m\bar{\psi}\psi$ is not allowed in the Lagrangian of the Standard Model as it would violate $SU(2)_L \times U(1)_Y$ gauge symmetry. However, the Higgs mechanism can also be used to include fermion masses to the SM by adding a gauge invariant interaction between the Higgs field and the fermions. This term is called Yukawa coupling and it is defined as

$$\mathcal{L}_Y = -g_Y\bar{\psi}\phi\psi, \quad (2.32)$$

where g_Y is the Yukawa coupling strength. Thus, after spontaneous symmetry breaking, a mass term for fermions remains present, which is given by

$$m_f = \frac{g_Y^f v}{\sqrt{2}}. \quad (2.33)$$

2.1.7. The Higgs Boson

Since the Higgs boson was postulated, it was searched extensively over several decades. It was finally discovered in 2012 at a mass of about 125 GeV by ATLAS and CMS at CERN [9–11]. After the discovery, characteristics like spin, decay and production rates, mass, CP properties, and the decay width of the boson have been investigated [12–14, 64, 65]. So far, all of these properties agree well with the Standard Model predictions.

At the LHC, the main production mechanisms of the Higgs boson are gluon-gluon fusion (ggF), vector-boson fusion (VBF), Higgsstrahlung or vector-boson associated production (VH), and production in association with heavy quarks ($t\bar{t}H$ or $b\bar{b}H$). For convenience, the latter are often referred to as $t\bar{t}H$ and $b\bar{b}H$. All respective Feynman diagrams are shown in Figure 2.1.

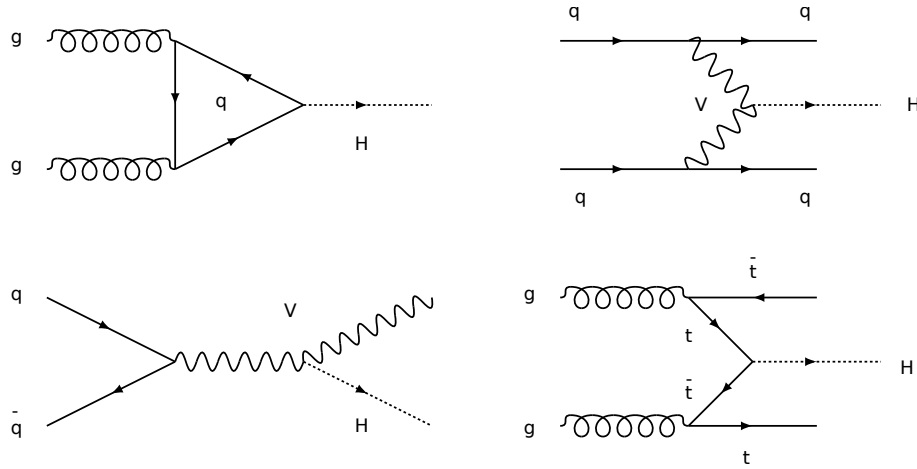


Figure 2.1.: Main Higgs boson production processes at the LHC: ggF (top left), VBF (top right), VH (bottom left), and $t\bar{t}H$ (bottom right). Diagrams drawn with [66].

Out of these production mechanisms, the ggF process $gg \rightarrow H$ has by far the largest cross-section at LHC conditions with about 49 pb at $\sqrt{s} = 13$ TeV and $M_H = 125$ GeV, as can be seen from Figure 2.2. Since the Higgs boson does not couple to gluons directly, this process is mediated by a quark loop.

Featuring the second largest production cross-section for Higgs bosons at the LHC, the VBF ($qq \rightarrow qqH$) production rate is about an order of magnitude less than for the ggF process. The Higgs boson is produced in the fusion of two vector bosons (W^\pm or Z^0) which are emitted by initial-state quarks. Therefore, quarks also remain present in the final state, forming two hard jets in forward and backward direction, making it relatively easy to distinguish a VBF event from QCD background.

The VH process $qq' \rightarrow VH$ describes interactions including both W^\pm and Z^0 bosons and features the third largest Higgs-production cross-section at the LHC. In this process, two quarks fuse into an off-shell vector boson which then radiates a Higgs boson and also yields the respective on-shell vector boson. This associated boson makes the process distinguishable from background events.

As the last mechanism discussed here, the quark associated production mode qqH ($gg \rightarrow qqH$) features the next largest cross-section. Here, $t\bar{t}H$ and $b\bar{b}H$ both have a cross-section of about 0.5–0.6 pb. In these processes, two initial gluons form a quark-antiquark pair by the exchange of a virtual quark which radiates a Higgs boson. This channel is particularly interesting since it allows a direct measurement of the top- and bottom-quark Yukawa couplings, respectively. Note that on-shell top quarks can not be produced in Higgs boson decays due to their large mass. While the $t\bar{t}H$ channel could be observed [67, 68] due to the top-quark decay

2. Theoretical Background

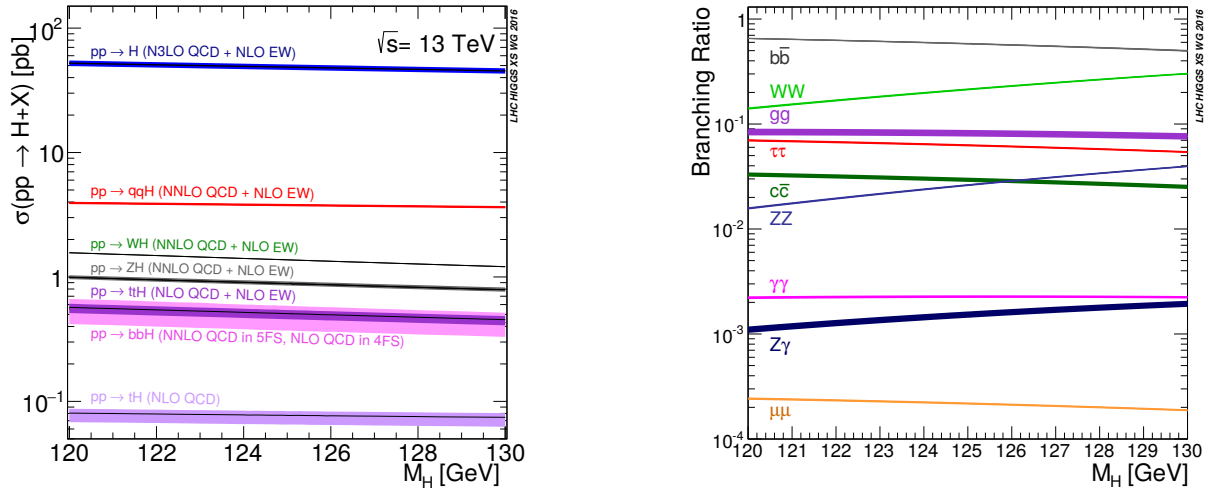


Figure 2.2.: Production cross-sections (left) and branching ratios (right) for the Higgs boson as a function of the Higgs mass M_H [15]

properties, the bbH channel suffers from an irreducible QCD background and could, thus, not be observed yet.

As predicted by the SM at this mass, the observed Higgs boson has a large variety of decay modes. It couples to all massive particles and, via intermediate quark or lepton loops, also to photons and gluons. The feasibility of detecting a specific decay channel does not only correspond to its branching ratio. For example, the first observation of the Higgs boson was performed based on – among others – the $H \rightarrow ZZ \rightarrow 4l$ and $H \rightarrow \gamma\gamma$ channels. These channels can be particularly well identified, making it easier to investigate them, despite their low branching ratios of about 1 % and 0.1 %, respectively. By now, Higgs boson decays into ZZ , W^+W^- , $\gamma\gamma$, $\tau^+\tau^-$, and $b\bar{b}$ have been observed as well as the above-mentioned production modes ggF, VBF, VH, and ttH [64, 69–74]. While featuring the largest branching ratio, the decay $H \rightarrow b\bar{b}$ is particularly difficult to identify as respective events are covered in a huge QCD multi-jet background. To observe this decay, the VH channel was used, providing a good Higgs boson identification due to the associated vector boson. It is even more difficult to identify $H \rightarrow c\bar{c}$ decays, which suffer from the same background as the $H \rightarrow b\bar{b}$ process. Furthermore, the branching ratio for this decay is about an order of magnitude lower than for $H \rightarrow b\bar{b}$. Also, an additional background arises from Higgs boson decays into b quarks. Searches for the $H \rightarrow c\bar{c}$ channel, as well as for $H \rightarrow \mu^+\mu^-$, which has an extremely low branching ratio, are currently in progress [75, 76]. With a reasonably large branching ratio of about 0.9 % and a rather clean signature, $H \rightarrow \tau^+\tau^-$ decays can be well identified and examined, which is

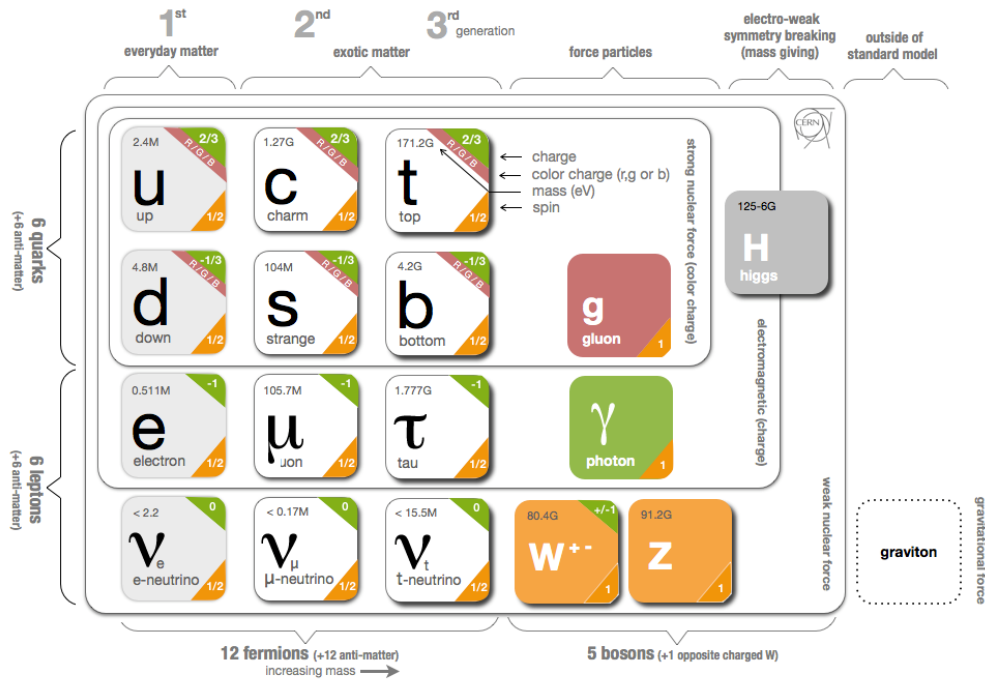


Figure 2.3.: Known Standard Model particle content: fermions on the left (quarks on the top, leptons below) and mediators (gluon, photon, and W^\pm and Z^0 bosons) on the right. The boxes represent the interactions the particles participate in and also include the respective mediator. Additionally shown are the Higgs boson in gray (the only spin-0 particle in the SM), which couples to massive particles only and arises from electroweak symmetry breaking (hence, it is shown in both corresponding boxes), and the not yet discovered graviton outside of the SM [78].

exploited in respective analyses [72, 73]. Decays into other fermions are currently outside the reach of experimental precision. Additionally, the SM predicts Higgs boson self coupling, i.e. vertices with three or four Higgs bosons. Searches for such $H \rightarrow HH$ or $HH \rightarrow HH$ events are also currently ongoing [77].

With the observation of the Higgs boson, all fundamental particles predicted by the SM have been found. They are summarized together with some of their main properties in Figure 2.3.

2.1.8. Open Questions of the Standard Model

Despite being tested to high accuracy, the SM is not considered complete. For example, neutrinos should be massless in the Standard Model, while the observation of neutrino oscillations [79] indicates that they must have a mass difference, which implies that not all neutrinos can be massless. Also gravitational interactions between particles are not integrated in the current theory. However, it is expected that they should play a significant role around the Planck scale, $M_{\text{Pl}} \sim 10^{19}$ GeV. Theoretically, the SM could be valid up to this scale, as it is renormalizable and UV-safe and could, thus, in principle be valid up to arbitrary energies. However, at a certain energy – or cutoff – scale, phenomena should be observable which are not yet included in the SM and the current theory is expected to become insufficient at this scale. Introducing any kind of cutoff scale at which gravitational effects become non-negligible, has implications on the scalar Higgs boson, called naturalness problem [24, 80]. Quadratic corrections to the mass term of the Higgs boson are given by

$$\delta m_{\text{H}}^2 = \frac{3G_{\text{F}}}{4\sqrt{2}\pi^2} \left(4m_{\text{t}}^2 - 2m_{\text{W}}^2 - m_{\text{Z}}^2 - m_{\text{H}}^2 \right) \Lambda^2, \quad (2.34)$$

where Λ is the cutoff scale, sensitive to the largest mass present in the model, G_{F} is Fermi's constant and m_{t} , m_{W} , m_{Z} , and m_{H} are the masses of the top quark and the W^{\pm} , Z^0 , and Higgs bosons, respectively. Λ is sensitive to the largest mass in the equation. If this is associated with the Planck mass, a fine tuning of at least 15 orders of magnitude is required to keep the Higgs boson mass roughly around the electroweak scale, which is of the order $\mathcal{O}(100 \text{ GeV})$. This amount of fine tuning is considered unnatural.

Moreover, no SM particle is considered to be a viable Dark Matter (DM) candidate. And since observation indicates that there is a significant amount of DM present in the universe, such a candidate should exist in a (more) complete theory.

In addition to the questions mentioned above, there are also several observations in the SM which are considered to require additional explanation. For example, the sizable number of parameters in the Standard Model as well as the number of fermionic generations and the particle quantum numbers are not explained.

2.2. Extensions of the Standard Model

In order to address open questions in the Standard Model, various theories have been proposed. Collectively, they are called Beyond-the-Standard-Model (BSM) theories. One feature that

is shared by several such theories is supersymmetry (SUSY) [27, 81]. It connects fermions and bosons by introducing super-partners for each particle. In the minimal supersymmetric extension of the Standard Model (MSSM), each fermion in the SM is assigned a bosonic super-partner and vice versa. Furthermore, a second Higgs doublet is introduced, featuring four extra degrees of freedom which manifest in four additional Higgs bosons. This structure of the Higgs sector is also featured in the more general group of Two-Higgs-Doublet (2HDM) models. Both SUSY, particularly the MSSM, and the 2HDM are discussed in this section.

2.2.1. Supersymmetry

In a supersymmetric theory, fundamental particles and their super-partners only differ in their spin quantum number by one half. Thus, in an unbroken symmetry, they would have identical masses. This would solve the hierarchy problem as radiative corrections to the Higgs boson mass cancel. Also, the strong and electroweak coupling constants could be unified by a supersymmetric theory. Note that, since no exact super-partners of fundamental particles have been found, unbroken (or “exact”) SUSY can not be realized [82].

Fundamental particles in a SUSY theory can be organized in super-multiplets containing a fermion and a boson. The particle spinors ψ are decomposed into the left- and right-handed Weyl spinors, with the indices α and β . The SUSY generators Q_α and Q_β are responsible for the transformation of each particle into its super-partner by a parity operation. In case the generators are hermitian operators, this parity operation equals a hermitian conjugation. The hermitian conjugate of the generator Q_α is written as $Q_{\dot{\alpha}}$. Symmetries in an interacting QFT are highly constrained by the Coleman-Mandula theorem [83], which implies that the SUSY generators should follow an anti-commutation rule connecting them to the momentum operator. Thus, the algebra defining SUSY is given by

$$\{Q_\alpha, Q_{\dot{\beta}}\} = 2\sigma_{\alpha\dot{\beta}}^\mu P_\mu, \quad (2.35)$$

where σ^μ represents the Pauli matrices and $P_\mu = -i\partial_\mu$ is the momentum operator.

In the Standard Model, lepton and baryon numbers L and B are conserved. They are defined as

$$L = n_l - n_{\bar{l}} \quad \text{and} \quad B = \frac{1}{3}(n_q - n_{\bar{q}}), \quad (2.36)$$

where n_l and n_q are the numbers of leptons and quarks, respectively, while $n_{\bar{l}}$ and $n_{\bar{q}}$ denote the numbers of the corresponding anti-particles. SUSY, however, can in general contain lepton-

2. Theoretical Background

and/or baryon-number violating terms but their simultaneous presence is strongly constrained by the observed lifetime of the proton, which is $\tau_p > 2 \times 10^{29}y$ [40]. A conserved, discrete quantum number is introduced in SUSY, discriminating SM and SUSY particles:

$$R = (-1)^{2s+L+3B}, \quad (2.37)$$

where L and B are lepton and baryon number, as defined above, and s is the spin of the particle. All SM particles have $R = +1$, while for all SUSY particles R equals -1 . Thus, SUSY particles can exclusively be produced in pairs from initial SM particles. Moreover, an exact conservation of R-parity forbids any mixing of SM and SUSY particles. This implies that at the end of a SUSY decay chain, there would be a lightest supersymmetric particle (LSP), which could not decay into any SM particle. Hence, it could be a candidate for Dark Matter [84, 85].

The Minimal Supersymmetric Extension Of The Standard Model (MSSM)

In the MSSM, the $SU(3) \times SU(2)_L \times U(1)_Y$ symmetry of the SM is conserved and embedded in a more general symmetry like $SU(5)$ or $SO(10)$. In this theory, each SM field is promoted to a superfield, which connects the SM particles with their respective super-partners. To describe SUSY particles, the bosonic super-partners of fermions are denoted by the prefix “s” (e.g. slepton, bottom-squark), while the fermionic partners of the gauge bosons are marked with the suffix “ino” (e.g. wino, higgsino). In a renormalizable theory, there are two classes of such supermultiplets, chiral and vector multiplets. The former connects the SM fermions to the SUSY sfermions, while the latter consists of the SM gauge bosons and the respective gauginos.

In Table 2.3, the particle content of the MSSM is summarized. Among the gauginos, zinos and photinos have the same quantum numbers as the higgsinos, indicating that all of these should mix and form four neutralinos $\tilde{\chi}_{1,2,3,4}^0$. Additionally, winos and charged higgsinos mix as well and create the mass eigenstates $\tilde{\chi}_{1,2}^\pm$, the charginos. A viable candidate for DM must be colorless and electrically neutral, i.e. only neutralinos or sneutrinos can be considered. From observations of the Z^0 decay to invisible particles, however, the second option can be excluded [85].

There are two Higgs doublets in the MSSM, ϕ_1 and ϕ_2 , which carry opposite hypercharge and are required in order to enable Yukawa interactions with up-type and down-type fermions. Two doublets are necessary since multiplets of different chirality, as is the case for a chiral multiplet and its complex conjugate, can not couple together in the Lagrangian. Analogous to Equation 2.26, the respective CP-conserving potential can be written without loop-corrections or SUSY

SM Particle	Spin (SM)	Super-Partner	Mass-Eigenstates	Spin (SUSY)
Quark q	1/2	Squark \tilde{q}_L, \tilde{q}_R		0
Lepton l^\pm	1/2	Slepton $\tilde{l}_L^\pm, \tilde{l}_R^\pm$		0
Neutrino ν	1/2	Sneutrino $\tilde{\nu}_L, \tilde{\nu}_R$ (?)		0
Gluon g	1	Gluino \tilde{g}		1/2
Photon γ	1	Photino $\tilde{\gamma}$	} Neutralino $\tilde{\chi}_{1,2,3,4}^0$	1/2
Z boson Z^0	1	Zino \tilde{Z}		1/2
Higgs boson H	0	Higgsino $\tilde{H}_1^0, \tilde{H}_2^0$		1/2
W boson W^\pm	1	Wino \tilde{W}^\pm	} Chargino $\tilde{\chi}_{1,2}^\pm$	1/2

Table 2.3.: Particle content of the MSSM with predicted mixing and spin values [42]. Note that since there are no right-handed neutrinos in the SM, there might not be a right-handed sneutrino as well.

breaking terms as

$$\begin{aligned}
 V_{MSSM}(\phi_1, \phi_2) = & |\mu|^2 |\phi_1|^2 + |\mu|^2 |\phi_2|^2 + \\
 & + \frac{1}{4} (g_W^2 + g_W'^2) (|\phi_1|^2 + |\phi_2|^2) + \frac{1}{4} (g_W^2 - g_W'^2) |\phi_1|^2 |\phi_2|^2 - \frac{1}{2} g_W^2 \phi_1^\dagger \phi_2 \phi_2^\dagger \phi_1, \quad (2.38)
 \end{aligned}$$

where μ is the higgsino mass parameter. Minimizing this potential while preserving electroweak symmetry breaking, only the electrically neutral parts of the Higgs doublets obtain a non-vanishing vacuum expectation value which can, in analogy to Equation 2.28, be expressed as

$$\langle 0 | \phi_1 | 0 \rangle = \frac{1}{\sqrt{2}} \begin{pmatrix} v_1 \\ 0 \end{pmatrix} \quad \text{and} \quad \langle 0 | \phi_2 | 0 \rangle = \frac{1}{\sqrt{2}} \begin{pmatrix} 0 \\ v_2 \end{pmatrix}. \quad (2.39)$$

To preserve the W and Z boson masses as introduced in Section 2.1.6, v_1 and v_2 must fulfill $v = \sqrt{v_1^2 + v_2^2} \simeq 246$ GeV. Furthermore, their ratio is conventionally written as $\tan \beta \equiv v_1/v_2$.

The two complex $SU(2)_L$ doublets creating the Higgs sector in the MSSM yield a total of eight degrees of freedom. After electroweak symmetry breaking, three of these are absorbed by the massive gauge bosons W^\pm and Z^0 . The five remaining mass eigenstates manifest in five Higgs bosons: two CP-even scalars h^0 and H^0 , a CP-odd pseudo-scalar A^0 and two charged scalars H^\pm . By convention, the lighter CP-even scalar is usually denoted by h and the three neutral Higgs bosons are often collectively denoted by $\phi = \{h, H, A\}$.

Overall, the mass eigenstates are related to the gauge-eigenstate fields via the angles α and

2. Theoretical Background

β . Here, α is the mixing angle of the CP-even states and β is defined as stated above:

$$A = \sqrt{2} \left(\sin \beta \Im(\phi_1^0 - v_1) - \cos \beta \Im(\phi_2^0 - v_2) \right) \quad (2.40)$$

$$\begin{pmatrix} h \\ H \end{pmatrix} = \sqrt{2} \begin{pmatrix} -\sin \alpha & \cos \alpha \\ \cos \alpha & \sin \alpha \end{pmatrix} \begin{pmatrix} \Re(\phi_1^0 - v_1) \\ \Re(\phi_2^0 - v_2) \end{pmatrix}. \quad (2.41)$$

The lighter CP-even boson has similar properties to the SM Higgs boson and is given as a mixture of h and H as well:

$$h^0 = h \sin(\alpha - \beta) - H \cos(\alpha - \beta). \quad (2.42)$$

At tree-level, α is obtained by

$$\frac{\sin 2\alpha}{\sin 2\beta} = - \left(\frac{m_H^2 + m_h^2}{m_H^2 - m_h^2} \right) \quad \text{and} \quad \frac{\tan 2\alpha}{\tan 2\beta} = \left(\frac{m_A^2 + m_Z^2}{m_A^2 - m_Z^2} \right), \quad (2.43)$$

such that it diagonalizes the matrix of quadratic masses [86]

$$\mathcal{M}_{tree}^2 = \begin{pmatrix} m_A^2 \sin^2 \beta + m_Z^2 \cos^2 \beta & -(m_A^2 + m_Z^2) \sin \beta \cos \beta \\ -(m_A^2 + m_Z^2) \sin \beta \cos \beta & m_A^2 \cos^2 \beta + m_Z^2 \sin^2 \beta \end{pmatrix}. \quad (2.44)$$

Subsequently, the mass eigenvalues of the five Higgs bosons are given by

$$m_A^2 = 2|\mu|^2 + m_{\phi_1}^2 + m_{\phi_2}^2, \quad (2.45)$$

$$m_{h,H}^2 = \frac{1}{2} \left(m_A^2 + m_Z^2 \mp \sqrt{(m_A^2 - m_Z^2)^2 + 4m_Z^2 m_A^2 \sin^2(2\beta)} \right), \quad \text{and} \quad (2.46)$$

$$m_{H^\pm}^2 = m_A^2 + m_W^2, \quad (2.47)$$

with μ being the supersymmetric equivalent to the Higgs boson mass in the SM. While there is a priori no limit on the masses of the heavy Higgs bosons, m_A , m_H , and m_{H^\pm} , an upper bound for m_h can be extracted from Equation 2.46 in the so-called decoupling limit $m_A \gg m_Z$:

$$m_h < m_Z |\cos(2\beta)|. \quad (2.48)$$

Moreover, in the decoupling limit, the four bosons A , H , and H^\pm form a heavy multiplet which can be seen from Equation 2.47 together with Equation 2.46, which simplifies to

$$m_H^2 \simeq m_A^2 + m_Z^2 \cos^2 2\beta. \quad (2.49)$$

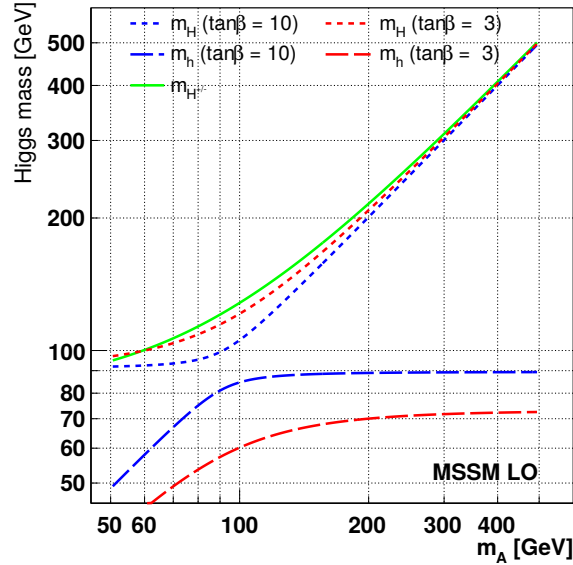


Figure 2.4.: Tree-level masses of the Higgs bosons in the MSSM against m_A for $\tan \beta$ values of 3 (blue lines) and 10 (red lines). m_H is shown as dotted lines, while m_h is marked by dashed lines. m_{H^\pm} is not affected by $\tan \beta$ and for large m_A , the masses m_H and m_{H^\pm} become degenerate, while m_h is bounded from above. Taken from [86].

This behavior is illustrated in Figure 2.4. In the decoupling limit, the expression for α in Equation 2.43 can also be simplified to

$$\alpha \approx \beta - \pi/2. \quad (2.50)$$

In this region, which is also described by $\cos(\beta - \alpha) \approx 0$, the couplings of the lighter CP-even boson h become SM-like. At $\cos(\beta - \alpha) = 0$, which is called alignment limit, the lighter CP-even boson of the MSSM has the same coupling structure as the SM Higgs boson.

At tree-level, it is possible to reduce the number of free parameters in the MSSM to two by expressing other parameters in terms of these free ones. Conventionally, the free parameters are chosen to be $\tan \beta$ and m_A . While m_A is not constrained, there are theoretical considerations for $\tan \beta$ which have to be taken into account. On the lower side, $\tan \beta$ should not be smaller than 1 to avoid the Yukawa coupling of the top quark, y_t , to become nonperturbatively large, i.e. exceed the electroweak scale. On the upper end, similar requirements on the τ and b Yukawa couplings require a limit $\tan \beta \lesssim 65$ for the computations to remain stable.

The discovery of a SM-like Higgs boson at about 125 GeV [14, 87–89] led to additional constraints on the MSSM parameter space. For example, the upper bound on m_h from Equation 2.48 is not considering radiative corrections. Thus, in order to match the observation, these

2. Theoretical Background

Boson	κ_V	κ_u	$\kappa_{d,l}$
h	$\sin(\beta - \alpha)$	$\cos \alpha / \sin \beta$	$-\sin \alpha / \cos \beta$
H	$\cos(\beta - \alpha)$	$\sin \alpha / \sin \beta$	$\cos \alpha / \cos \beta$
A	0	$\cot \beta$	$\tan \beta$

Table 2.4.: Coupling modifiers of neutral Higgs bosons in the MSSM with respect to the SM couplings. Decays $A \rightarrow VV$ are forbidden due to CP conservation and, in the alignment limit, decays $H \rightarrow VV$ are suppressed [86].

corrections have to be taken into account. The major contribution originates from the top quark t and its super-partner, the top squark \tilde{t} and m_h takes the form

$$m_h^2 < m_Z^2 \cos^2(2\beta) + \frac{3m_t^4}{2\pi^2 v^2} \ln \frac{m_{\tilde{t}}^2}{m_t^2}. \quad (2.51)$$

The main production and decay modes of the Higgs bosons in the MSSM are dictated by the respective coupling constants. These are usually given with respect to the pure SM-like couplings and they are differentiated between the coupling to vector bosons V , up-type quarks u , down-type quarks d , and leptons l . In the MSSM, the coupling modifiers to down-type quarks and leptons, κ_d and κ_l are identical. An overview of all coupling modifiers for the neutral Higgs bosons in the MSSM is given in Table 2.4. It can be seen that with larger $\tan \beta$, the coupling to down-type quarks increases. Thus, for smaller $\tan \beta$ up to a value of around 30, [90] the main production mode of heavy, neutral Higgs bosons in the MSSM is the ggF channel, while for larger $\tan \beta$, bbH/A becomes dominant.

In supersymmetric models, also the Yukawa couplings of fermions receive non-negligible radiative corrections. For example, for the bottom-quark Yukawa-coupling, one-loop corrections due to the coupling of ϕ_2 to down-type quarks are dominant. These corrections induce a coupling of the up-type Higgs-doublet to down-type quarks, which would not happen on tree-level. Additional terms of the form [91]

$$y_b \phi_1 b \bar{b} + \Delta y_b \phi_2 b \bar{b} \quad (2.52)$$

with the loop-suppressed coupling Δy_b have thus to be added to the Lagrangian. For neutral

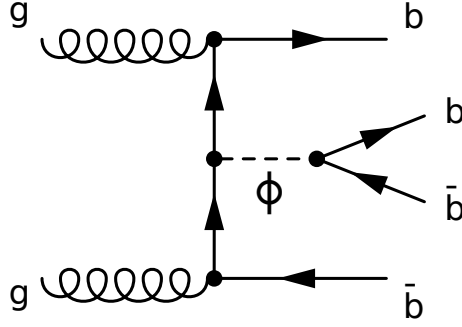


Figure 2.5.: Typical Feynman diagram of a neutral Higgs boson produced in the $bb\phi$ channel and decaying into a $b\bar{b}$ pair. Diagram drawn with [66].

Higgs bosons, it takes the form [92]

$$\mathcal{L} = \frac{g_W}{2m_W} \frac{\bar{m}_b}{1 + \Delta_b} \times \left[\tan \beta A_i \bar{b} \gamma_5 b + \left(\frac{\sin \alpha}{\cos \beta} - \Delta_b \frac{\cos \alpha}{\sin \beta} \right) h \bar{b}_L b_R - \left(\frac{\cos \alpha}{\cos \beta} + \Delta_b \frac{\sin \alpha}{\sin \beta} \right) H \bar{b}_L b_R \right], \quad (2.53)$$

with the coupling modifier Δ_b and the running b-quark mass \bar{m}_b [93] of the SM including QCD corrections. The factor $(1 + \Delta_b)^{-1}$ reflects the resummation of leading corrections to all orders, while the terms $\sim \Delta_b$ arise from the mixing of the CP-even h and H eigenstates. The coupling modifier itself consists of two major contributions, originating from sbottom-gluino ($\mathcal{O}(\alpha_S)$) and stop-higgsino ($\mathcal{O}(\alpha_t)$) loops:

$$\Delta_b \sim \mu \tan \beta \left(\frac{2\alpha_S}{3\pi} m_{\tilde{g}} \times \max(m_{\tilde{b}_1}, m_{\tilde{b}_2}, m_{\tilde{g}}) + \frac{\alpha_t}{4\pi} A_t \times \max(m_{\tilde{t}_1}, m_{\tilde{t}_2}, \mu) \right), \quad (2.54)$$

where α_S is the strong coupling constant and $m_{\tilde{g}}$ is the gluino mass. Furthermore, $m_{\tilde{b}, \tilde{t}_{1,2}}$ are the bottom- and top-squark masses obtained via coupling to $\phi_{1,2}$, respectively, $\alpha_t \equiv y_t^2/(4\pi)$ is the coupling based on the top-quark Yukawa-coupling, and A_t is the Higgs-stop coupling. It can be extracted from Equation 2.54 that with larger $\tan \beta$, the coupling of neutral Higgs bosons to bottom quarks is increasingly enhanced. Additionally, due to the Δ_b^{-1} dependence of \mathcal{L} , negative Δ_b also lead to enhanced bottom-quark Yukawa-coupling. This can happen if the higgsino mass-parameter μ becomes negative.

In this analysis, neutral Higgs bosons are analyzed in the decay into a $b\bar{b}$ pair and produced in association with b quarks. A corresponding Feynman diagram of this process is shown in Figure 2.5. While ϕ generally denotes $\{h, H, A\}$, the work presented here is focused on the higher mass ranges, thus targeting the H and A bosons.

2. Theoretical Background

The full process shown in Figure 2.5 is described by the sum of production cross-sections and decay branching ratios of the H and the A bosons. From Equation 2.53, it can be taken that the bbA production cross-section is enhanced with respect to the SM cross-section proportional to $\tan^2 \beta / (1 - \Delta_b)^2$. Assuming that the masses of SUSY particles are far larger than the Higgs boson mass, the branching fraction of the A boson into a pair of b quarks in the decoupling limit and for large $\tan \beta$ is given by [92]

$$\mathcal{B}(A \rightarrow b\bar{b}) \simeq \frac{9}{(1 + \Delta_b)^2 + 9}, \quad (2.55)$$

where the numerical factor of 9 equals the number of colors squared. Based on the mass degeneracy for large $\tan \beta$, the combined cross-section times branching ratio for A and H can be fully given based on the considerations for the CP-odd boson:

$$\begin{aligned} \sigma(b\bar{b}A/H)\mathcal{B}(A/H \rightarrow b\bar{b}) &\simeq 2 \times \sigma(b\bar{b}A)\mathcal{B}(A \rightarrow b\bar{b}) \simeq \\ &\simeq 2 \times \sigma(b\bar{b}A)_{SM} \times \frac{\tan^2 \beta}{(1 + \Delta_b)^2} \times \frac{9}{(1 + \Delta_b)^2 + 9}, \end{aligned} \quad (2.56)$$

where $\sigma(b\bar{b}A)_{SM}$ denotes the SM Higgs-production cross-section at the given mass of A .

Benchmark Scenarios

For large values of $\tan \beta$, the process investigated in this analysis is significantly enhanced for a wide array of SUSY parameters. However, in praxis it is not economic to perform a full scan of the parameter space. To obtain a representative insight, benchmark scenarios have been developed, investigating a particular combination of parameters. They are provided by the LHC Higgs Cross-Section Working Group (LHCHSWG) [94]. The scenarios discussed in this section restrict the set of free parameters to m_A and $\tan \beta$ as discussed in Section 2.2.1. Furthermore, all of the scenarios are designed such that they agree with the observation of a SM-like Higgs boson at 125 GeV [95]. While the mass of this boson is measured with high precision, all scenarios discussed here assign an uncertainty of ± 3 GeV to account for theoretical uncertainties in predicting the Higgs boson masses in the MSSM.

Many benchmark scenarios have been developed prior to the discovery of the 125 GeV boson and they have since been updated [96, 97] to include the additional constraints from the LHC Runs 1 and 2 [86, 98, 99]. One of the most important considerations in the context of scenario development was the question whether the observed boson is the lighter or the heavier CP-even state. By now, observation favors the former choice [100], i.e. $h(125) = h$. In this section, the

benchmark scenarios are discussed which are used for the presented analysis. They comprise two traditionally used scenarios, the hMSSM and the m_h^{mod+} scenarios, as well as a set of more recent scenarios based on the m_h^{125} scenario.

The hMSSM Scenario As a somewhat unique scenario, the hMSSM (“habemus MSSM”) model can be considered relatively model independent. To construct this scenario, several simplifying assumptions are made. First, the observed boson at 125 GeV is assumed to be the lighter scalar h . Second, only radiative corrections from top/stop-quark loops are taken into account. Third, since they have not been observed yet, all SUSY particles are expected to be very heavy, therefore not having significant effects on the Higgs sector. Using these assumptions, the mass of the heavy CP-even Higgs boson can be calculated from Equation 2.44 as

$$m_H^2 = \frac{(m_A^2 + m_Z^2 - m_h^2)(m_Z^2 \cos^2 \beta + m_A^2 \sin^2 \beta) - m_A^2 m_Z^2 \cos^2 2\beta}{m_Z^2 \cos^2 \beta + m_A^2 \sin^2 \beta - m_h^2}, \quad (2.57)$$

while the masses of the charged H^\pm bosons remain at their tree-level values (Equation 2.47). In this approach, only $\tan \beta$ and m_A , as well as the experimentally determined value of m_h are used as free parameters, while all others are expressed in terms of these three. Thus, there is no direct dependency on SUSY parameters. However, as radiative corrections to the bottom Yukawa-coupling are neglected, this scenario is only an approximate description of the MSSM for $\tan \beta \gtrsim 10$. Furthermore, analyses of the Higgs boson couplings by ATLAS and CMS [87, 88] were able to exclude a relatively large area of the hMSSM phase space, more precisely $m_A > 480$ GeV for $\tan \beta < 25$.

The m_h^{mod+} Scenario The second scenario used here is the m_h^{mod+} scenario [96], which is an update of the m_h^{max} scenario. The latter was originally designed to yield conservative exclusion limits in LEP searches [101]. The m_h^{mod+} scenario explicitly takes into account the discovery of the 125 GeV boson, while the m_h^{max} scenario would only allow this mass value for a narrow corridor in the $(m_A, \tan \beta)$ plane at rather low values of $\tan \beta$. This modification is achieved by reducing the mixing in the stop sector. Thus, the value of $|X_t/M_{SUSY}|$ is reduced to a value below 2.0, where M_{SUSY} denotes the mass of third-generation sfermions and X_t is the stop-quark mixing parameter $X_t = A_t \mu \cot \beta$. As X_t/M_{SUSY} is required to be positive, the scenario name is extended with a +.

Unlike the hMSSM scenario, the m_h^{mod+} scenario predicts relatively light SUSY particles, especially neutralinos and charginos. This reduces the fermionic Higgs boson decays into $b\bar{b}$ and $\tau^+\tau^-$ for low to moderate $\tan \beta \lesssim 20$, where the Higgs bosons dominantly decay into

2. Theoretical Background

neutralinos or charginos with branching fractions of up to about 80 %. Due to the relatively low value of μ , however, the decay into bottom quarks remains dominant for larger $\tan\beta$ because of the enhanced couplings.

The parameter settings for this scenario are:

$$\begin{aligned}
 m_t &= 173.2 \text{ GeV} & M_{SUSY} &= 1000 \text{ GeV} & \mu &= m_{gaugino} = 200 \text{ GeV} \\
 m_{\tilde{g}} = m_{\tilde{q}_{1,2}} &= 1500 \text{ GeV} & M_{\tilde{l}_3} &= 1000 \text{ GeV} & A_b &= A_t = A_\tau \\
 X_t^{OS} &= 1.5 m_{SUSY} & X_t^{MS} &= 1.6 m_{SUSY} & A_{f \neq b,t,\tau} &= 0.
 \end{aligned}$$

The m_h^{125} Scenarios In addition to the traditional hMSSM and m_h^{mod+} scenarios, the more recent family of m_h^{125} scenarios is investigated [97, 98]. In the basic m_h^{125} scenario, all SUSY particles are chosen to be so heavy that they do not impact Higgs boson decays significantly in the scrutinized range of $m_{A/H}$. Specifically, loop-induced SUSY corrections to the coupling of the lighter CP-even boson h are negligible and also the H and A only decay into SM particles for $m_{A/H} \lesssim 2 \text{ TeV}$. Thus, this model is similar to a 2HDM type II scenario (see Section 2.2.2) with MSSM-inspired couplings.

The mass parameters of third-generation squarks as well as the gluino mass are set so high that they are far outside current boundaries. Moreover, the higgsino-mass parameter μ is set to 1 TeV, which is also the value chosen for electroweak gaugino masses. Hence, the largest SUSY loop-corrections arise due to Higgs-bottom-quark coupling which is enhanced relative to $\tan\beta$ as mentioned before. At a value of $\tan\beta = 20$, Δ_b is about 0.2, while $\Delta_b \approx 0.6$ at $\tan\beta = 60$. As for the hMSSM and m_h^{mod+} scenarios, free parameters at tree-level are m_A and $\tan\beta$. Certain regions of this phase space are already excluded since there, the lighter CP-even Higgs boson is not compatible with the observed $h(125)$. Specifically, for low $\tan\beta$ values smaller than $\sim 6 - 8$, the MSSM prediction of m_h does not match $125.09 \pm 3 \text{ GeV}$. For $m_A \lesssim 500 - 600 \text{ GeV}$, the predicted modifications of the production and decay rates of the h boson, in particular of the dominant $h \rightarrow b\bar{b}$ decay mode, are inconsistent with observations at the LHC.

The parameter settings for this scenario are:

$$\begin{aligned}
 m_{Q_3} = m_{U_3} = m_{D_3} &= 1.5 \text{ TeV} & m_{L_3} = m_{E_3} &= 2 \text{ TeV} \\
 \mu &= 1 \text{ TeV} & m_1 = m_2 &= 1 \text{ TeV} & m_3 &= 2.5 \text{ TeV} \\
 X_t &= 2.8 \text{ TeV} & A_b = A_\tau = A_t & & A_{f \neq b,t,\tau} &= 0.
 \end{aligned}$$

Here, $m_{1,2,3}$ are the bino and wino masses, while m_{Q,U,D_3} represents the mass of third generation

squarks and m_{L,E_3} reflects third-generation slepton masses. As before, μ is the higgsino-mass parameter and A_X is the coupling term to a fermion X .

If the μ parameter of the m_h^{125} scenario is set to negative values, the Yukawa coupling of the bottom quark is enhanced. This mostly affects the heavier neutral bosons H and A , while the behavior of the lighter h is not significantly changed in the decoupling limit. While all other parameters remain the same as for the m_h^{125} scenario, μ is set to $-\{1, 2, 3\}$ TeV, respectively. Via Δ_b , this enhances the relative strength of decays into $b\bar{b}$. While this is true as well for the decay into $\tau^+\tau^-$, the sensitivity in this channel is not enhanced nearly as much as in the $b\bar{b}$ decay. This can be explained by the fact that while the decays in both channels are enhanced by the choice of μ , the $b\bar{b}$ channel also profits from the increased production cross-section of the $b\bar{b}H$ channel. However, effects based on Δ_b in production and decay for the $\tau^+\tau^-$ channel largely cancel.

As for the original m_h^{125} scenario, phase-space regions of low $\tan\beta$ and low m_A are excluded by the behavior of the 125 GeV boson as observed using up to 80 fb^{-1} of LHC Run 2 data from ATLAS [87] and CMS [88]. These regions, depending on the choice of μ , together with the impact of this choice on exclusion limits in the $b\bar{b}$ [102] and $\tau^+\tau^-$ [103] decay channels are shown in Figure 2.6.

2.2.2. Two-Higgs-Doublet Models

In Section 2.2.1, the two-Higgs-doublet (2HDM) structure of supersymmetric models is introduced. The general 2HDM model [25] is based on the addition of just one doublet to the SM. This means that the fermionic sector of the SM is not changed, while the Higgs-sector is structured in the same way as in the MSSM. The additional Higgs-doublet alone would open up several possibilities for explanations of open questions in the SM, e.g. the matter-antimatter asymmetry could be generated based on additional CP violation.

For the 2HDM potential, it is assumed that CP is not violated in the Higgs sector and quartic terms are not included. The potential then takes the form

$$\begin{aligned}
 V_{2HDM}(\phi_1, \phi_2) = & m_{11}^2 \phi_1^\dagger \phi_1 + m_{22}^2 \phi_2^\dagger \phi_2 - m_{12}^2 (\phi_1^\dagger \phi_2 + \phi_2^\dagger \phi_1) + \\
 & + \frac{\lambda_1}{2} (\phi_1^\dagger \phi_1)^2 + \frac{\lambda_2}{2} (\phi_2^\dagger \phi_2)^2 + \lambda_3 \phi_1^\dagger \phi_1 \phi_2^\dagger \phi_2 + \lambda_4 \phi_1^\dagger \phi_2 \phi_2^\dagger \phi_1 + \\
 & + \frac{\lambda_5}{2} \left[(\phi_1^\dagger \phi_2)^2 + (\phi_2^\dagger \phi_1)^2 \right], \tag{2.58}
 \end{aligned}$$

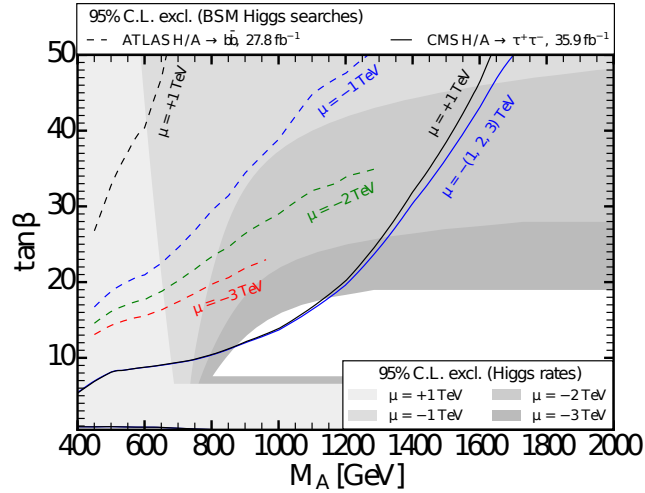


Figure 2.6.: Impact of μ on excluded areas of phase space in m_h^{125} scenarios. The areas shaded in gray are excluded by observed properties of the h boson, including up to 80 fb^{-1} of LHC Run 2 data from ATLAS [87] and CMS [88]. Dashed and solid lines represent the effect of μ on a search in the $b\bar{b}$ [102] and $\tau^+\tau^-$ [103] decay channel, respectively. While in the $b\bar{b}$ channel, a larger negative value of μ has additional impact, this is not observed for the $\tau^+\tau^-$ channel. Taken from [97].

where m_{11} , m_{22} , and m_{12} are the mass-matrix elements and $\lambda_{1,2,3,4,5}$ represent the Higgs self-couplings. Despite the significantly increased number of free parameters with respect to the MSSM, this potential also yields five physical Higgs bosons: two neutral CP-even states h and H , a CP-odd state A and two charged bosons H^\pm .

An additional constraint on the structure of the 2HDM Higgs sector is the assumption that no flavor-changing neutral currents (FCNC) exist at tree-level. In a general 2HDM, these currents would occur since the mass matrices are not generally diagonalizable simultaneously. However, if all fermions carrying the same electroweak quantum numbers couple to only one Higgs doublet, this problem does not occur. Therefore, based on the Paschos-Glashow-Weinberg theorem [104, 105], it is required that all fermions with the same charge and helicity transform according to the same irreducible representation of $SU(2)$. As in the Standard Model, there are left-handed doublets and right-handed singlets, this implies that all right-handed quarks carrying the same charge have to couple to the same Higgs doublet. This can be realized by imposing various discrete or continuous symmetries and in the case of the 2HDM, a discrete Z_2 symmetry is applied [25]. Thus, four distinct types of 2HDM can be identified which guarantee CP conservation and the absence of FCNCs at tree-level.

Focusing on the quark couplings, a $\phi_1 \rightarrow -\phi_1$ symmetry enforces interaction of all quarks

Model	Symmetry	u_R^i	d_R^i	l_R^i
Type I	$\phi_1 \rightarrow -\phi_1$	ϕ_2	ϕ_2	ϕ_2
Type II	$\phi_1 \rightarrow -\phi_1, d_R^i \rightarrow -d_R^i$	ϕ_2	ϕ_1	ϕ_1
Lepton-specific	$\phi_1 \rightarrow -\phi_1$	ϕ_2	ϕ_2	ϕ_1
Flipped	$\phi_1 \rightarrow -\phi_1, d_R^i \rightarrow -d_R^i$	ϕ_2	ϕ_1	ϕ_2

Table 2.5.: Coupling of right-handed fermions f_R^i (up-type quarks u , down-type quarks d and leptons l) to Higgs doublets ϕ_1 and ϕ_2 in the four 2HDM types [25]

with just the ϕ_2 doublet. If an additional symmetry of the form $d_R^i \rightarrow -d_R^i$ is applied, the right-handed up-type quarks are coupling to the ϕ_2 doublet, while the right-handed down-type quarks interact with the ϕ_1 doublet. These two models are called 2HDM “type I” and “type II”, respectively. For these two models, leptons are assumed to couple to the same doublet as down-type quarks, which is, however, not explicitly required by the Paschos-Glashow-Weinberg theorem. Therefore, in the “lepton-specific” model, sometimes referred to as “type IV” or “type X”, all right-handed quarks couple to ϕ_2 , while the right-handed leptons interact with ϕ_1 . In the “flipped” model, which is alternatively called “type III” or “type Y”, the up-type quarks couple to ϕ_2 and the down-type quarks as well as the leptons couple to ϕ_1 . An overview of this structure is given in Table 2.5.

Due to the interaction with additional Higgs bosons, also the Yukawa couplings of fermions are changed in 2HDMs. This change is described by factors κ , as reflected by the Yukawa Lagrangian

$$\mathcal{L}_{Yukawa}^{2HDM} = - \sum_{f=u,d,l} \frac{m_f}{v} \left(\kappa_h^f \bar{f} f h + \kappa_H^f \bar{f} f H - i \kappa_A^f \bar{f} \gamma_5 f A \right) - \mathcal{L}_{Yukawa,H^\pm}^{2HDM}, \quad (2.59)$$

where m_f/v is the SM Yukawa coupling g_Y^f and $\mathcal{L}_{Yukawa,H^\pm}^{2HDM}$ represents the Yukawa Lagrangian for charged Higgs bosons. All parameters κ are given as the ratio of g_Y^{2HDM} and g_Y^{SM} and they are shown in Table 2.6. The modified coupling strength for vector bosons with respect to the Standard Model is, independent of the 2HDM type, given by

$$\kappa_h^V = \sin(\beta - \alpha) \quad \text{and} \quad \kappa_H^V = \cos(\beta - \alpha). \quad (2.60)$$

Note that for a SM-like h boson with corresponding coupling properties, i.e. in the alignment limit $\cos(\beta - \alpha) = 0$, this transforms to $\kappa_h^V = 1$ and $\kappa_H^V = 0$. Due to CP conservation, the CP-odd A does not couple to vector bosons in this model.

While the Higgs sector in the 2HDM type II model resembles the structure in the MSSM,

2. Theoretical Background

	Type I	Type II	Lepton-specific	Flipped
κ_h^u	$\cos \alpha / \sin \beta$	$\cos \alpha / \sin \beta$	$\cos \alpha / \sin \beta$	$\cos \alpha / \sin \beta$
κ_h^d	$\cos \alpha / \sin \beta$	$-\sin \alpha / \cos \beta$	$\cos \alpha / \sin \beta$	$-\sin \alpha / \cos \beta$
κ_h^l	$\cos \alpha / \sin \beta$	$-\sin \alpha / \cos \beta$	$-\sin \alpha / \cos \beta$	$\cos \alpha / \sin \beta$
κ_H^u	$\sin \alpha / \sin \beta$	$\sin \alpha / \sin \beta$	$\sin \alpha / \sin \beta$	$\sin \alpha / \sin \beta$
κ_H^d	$\sin \alpha / \sin \beta$	$\cos \alpha / \cos \beta$	$\sin \alpha / \sin \beta$	$\cos \alpha / \cos \beta$
κ_H^l	$\sin \alpha / \sin \beta$	$\cos \alpha / \cos \beta$	$\cos \alpha / \cos \beta$	$\sin \alpha / \sin \beta$
κ_A^u	$\cot \beta$	$\cot \beta$	$\cot \beta$	$\cot \beta$
κ_A^d	$-\cot \beta$	$\tan \beta$	$-\cot \beta$	$\tan \beta$
κ_A^l	$-\cot \beta$	$\tan \beta$	$\tan \beta$	$-\cot \beta$

Table 2.6.: Yukawa coupling modifiers for up-type quarks u , down-type quarks d and leptons l to the neutral Higgs bosons h , H , and A in the four types of 2HDMs [25]

there are some important differences. For example, in the MSSM, a constraint for m_h is inherent, which is not true for any 2HDM. Also, the mass mixing parameter m_{12} and the CP-even mixing angle α as well as the scalar Higgs self-couplings are free parameters in the 2HDM. Moreover, requiring perturbativity of the top- and bottom-quark Yukawa couplings leads to different allowed $\tan \beta$ ranges in the two models based on slightly different constraints. While in the MSSM, a range of $1 \lesssim \tan \beta \lesssim 60$ is allowed, in the 2HDM values of $0.1 \lesssim \tan \beta \lesssim 100$ are possible without introducing instabilities into the calculations.

Benchmark Scenarios

Similar to the approach for the MSSM, benchmark scenarios are developed for 2HDMs as well [106]. Out of those, one scenario, called “scenario G”, closely resembles the MSSM in some respects. Its parameter settings are

$$\lambda_5 = 0, \quad m_{12}^2 = \frac{1}{2} m_A^2 \sin 2\beta, \quad m_h = 125 \text{ GeV}, \quad \text{and} \quad m_A = m_H = m_{H^\pm}. \quad (2.61)$$

With these choices, the number of free parameters from the physical basis proposed in [107] is reduced to three. These are m_A , $\tan \beta$, and $\cos(\beta - \alpha)$, which can be used instead of α without loss of generality.

For this analysis, the couplings to down-type quarks are particularly interesting. In the type II and flipped models, the coupling modifiers of the A and H bosons to down-type quarks are given by $\kappa_A^d = \tan \beta$ and $\kappa_H^d = \cos \alpha / \cos \beta = \cos(\beta - \alpha) + \tan \beta \sin(\beta - \alpha)$. The latter approaches $\tan \beta$ for small values of $\cos(\beta - \alpha)$. Therefore, in both scenarios, the coupling to down-type quarks is enhanced for larger values of $\tan \beta$, making it reasonable to investigate

these two models further.

To interpret the analysis result in terms of these scenarios, a fine scan of the parameter space in the three dimensions $\tan \beta$, m_A , and $\cos(\beta - \alpha)$ is performed. Production cross-sections for the processes $b\bar{b}H/A$ and decay branching fractions $H/A \rightarrow b\bar{b}$ are calculated for all types of the 2HDM at next-to-next-to-leading-order (NNLO) precision, using the SusHi (v. 1.6.1) [108], 2HDMC (v. 1.7.0) [107], and LHAPDF (v. 6.1.6) [109] program packages.

The calculated branching ratios of the A and H bosons in the type II and flipped scenarios are shown as functions of $\cos(\beta - \alpha)$ in Figures 2.7 and 2.8, respectively, for an intermediate value of $\tan \beta = 30$ and for a smaller mass $m_{A/H}$ of 400 GeV, an intermediate mass of 800 GeV as well as a larger mass of 1200 GeV. Due to the enhanced Yukawa coupling as shown in Table 2.6, the decay into $b\bar{b}$ is the dominant fermionic contribution for the full range of $\cos(\beta - \alpha)$ in all cases for $\tan \beta \gg 1$. Also, as expected, the $A/H \rightarrow b\bar{b}$ branching ratios for the type II and flipped scenarios are very similar due to the same Yukawa couplings in these models. In the flipped scenario around the alignment limit, the $A/H \rightarrow b\bar{b}$ decay mode is uniquely sensitive.

For the decays of the A boson, it can be seen that the $A \rightarrow Zh$ decay also contributes significantly for larger values of $|\cos(\beta - \alpha)|$. However, around the alignment limit, this decay is forbidden as it does not exist in the SM and, thus, the most important decay mode is by far the $b\bar{b}$ decay. Note that larger $|\cos(\beta - \alpha)|$ are also implicitly excluded based on the observed behavior of the h boson [110]. The $A \rightarrow \tau^+\tau^-$ decay has a branching fraction of about 10 % relative to the $b\bar{b}$ decay mode in the type II model. However, due to the suppressed coupling in the flipped scenario, the $\tau^+\tau^-$ channel does not play a major role there. The suppression factor can be extracted from the Yukawa coupling modifications in Table 2.6 to be $\tan^4 \beta$ with respect to the $b\bar{b}$ decay mode.

Similarly, for the H boson decays, the $b\bar{b}$ channel is the most important fermionic decay. The decay $H \rightarrow Zh$ is forbidden due to the CP conservation requirement and the $H \rightarrow hh$ decay becomes dominant instead. Altogether, bosonic decay modes dominate for larger $|\cos(\beta - \alpha)|$ values, while they are forbidden around the alignment limit. This is, however not directly true for the $\gamma\gamma$ decay mode, which is realized, as in the SM, via a fermionic loop. The slight asymmetry which can be observed for the $\tau^+\tau^-$ branching fractions in the flipped scenario originates from a “ τ -phobic” point at $\sin \alpha = 0$, as can be extracted from Table 2.6. It can be seen in the plots in Appendix B that this point approaches the alignment limit for larger $\tan \beta$.

The overall rate for the full process, $\sigma(b\bar{b}A)\mathcal{B}(A \rightarrow b\bar{b}) + \sigma(b\bar{b}H)\mathcal{B}(H \rightarrow b\bar{b})$, is shown in Figure 2.9 for all four types of the 2HDM at the alignment limit. It can be seen immediately that,

2. Theoretical Background

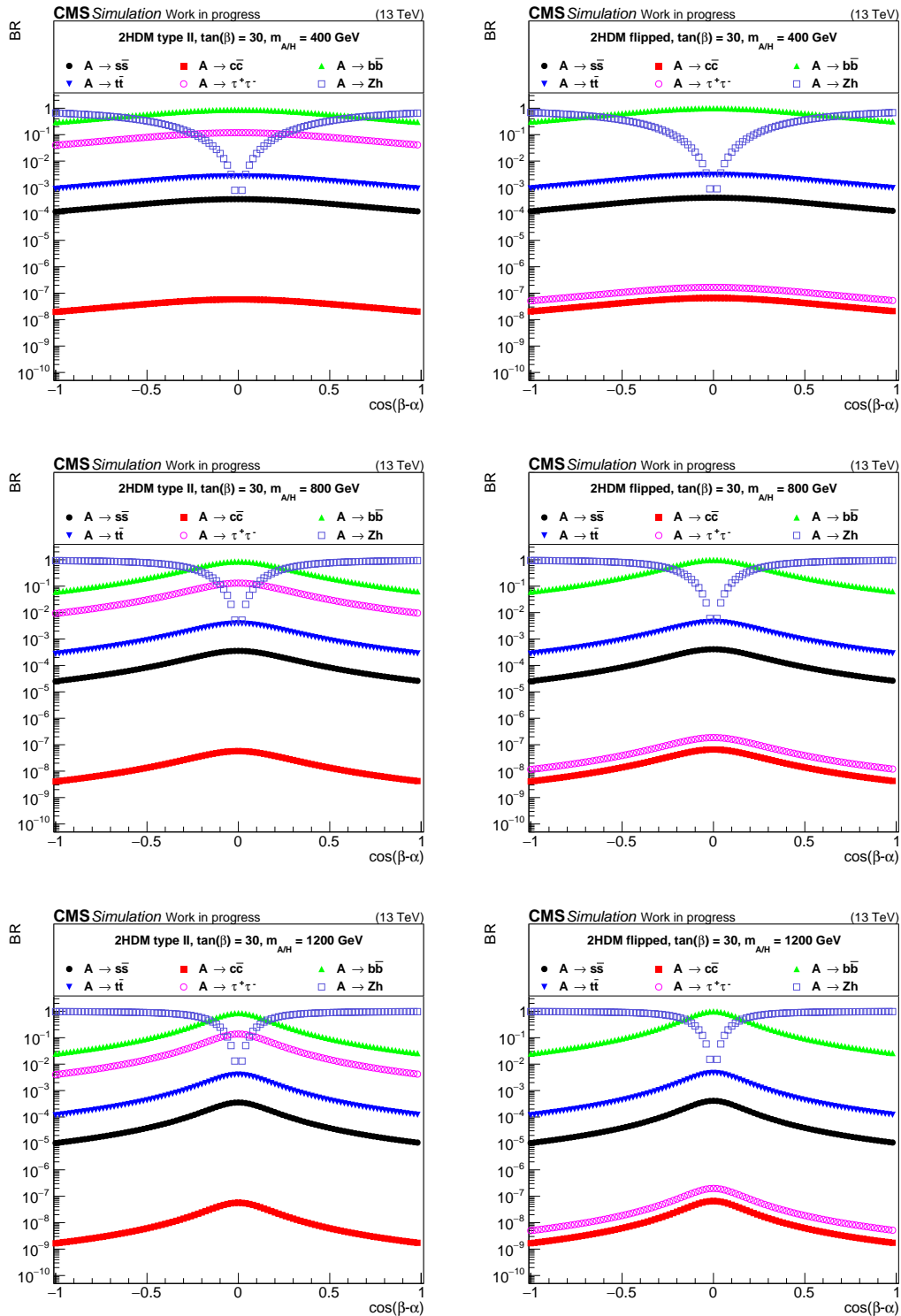


Figure 2.7.: Branching ratios of the A boson depending on $\cos(\beta - \alpha)$ in the 2HDM type II (left) and flipped (right) scenario for lower (400 GeV, top), intermediate (800 GeV, center) and higher (1200 GeV, bottom) masses for an intermediate $\tan \beta = 30$. In all cases, the $A \rightarrow b\bar{b}$ decay is marked by the green line, dominating around the alignment limit of $\cos(\beta - \alpha) \approx 0$.

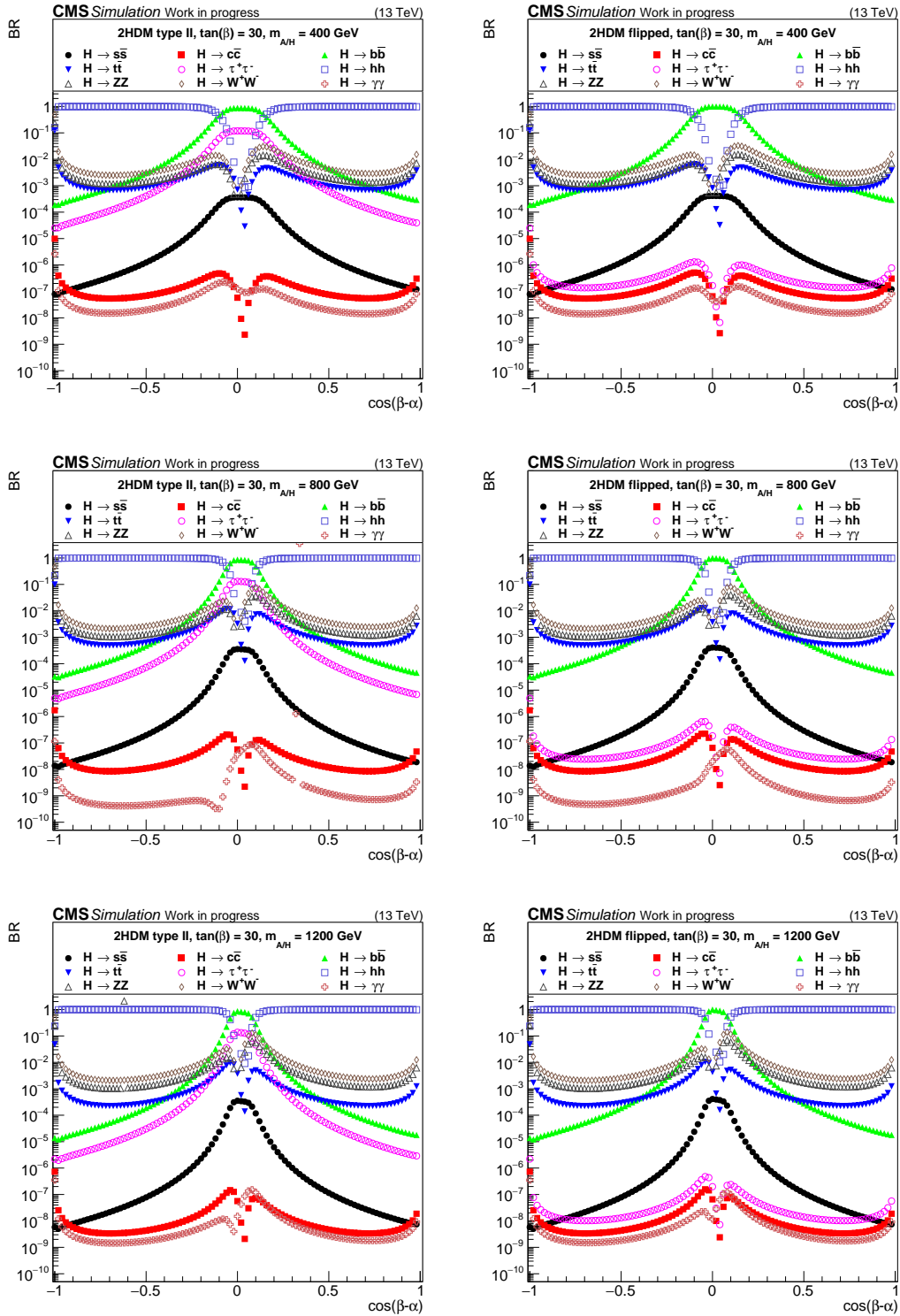


Figure 2.8.: Branching ratios of the H boson depending on $\cos(\beta - \alpha)$ in the 2HDM type II (left) and flipped (right) scenario for lower (400 GeV, top), intermediate (800 GeV, center) and higher (1200 GeV, bottom) masses for an intermediate $\tan \beta = 30$. In all cases, the $H \rightarrow b\bar{b}$ decay is marked by the green line, dominating around the alignment limit $\cos(\beta - \alpha) \approx 0$.

2. Theoretical Background

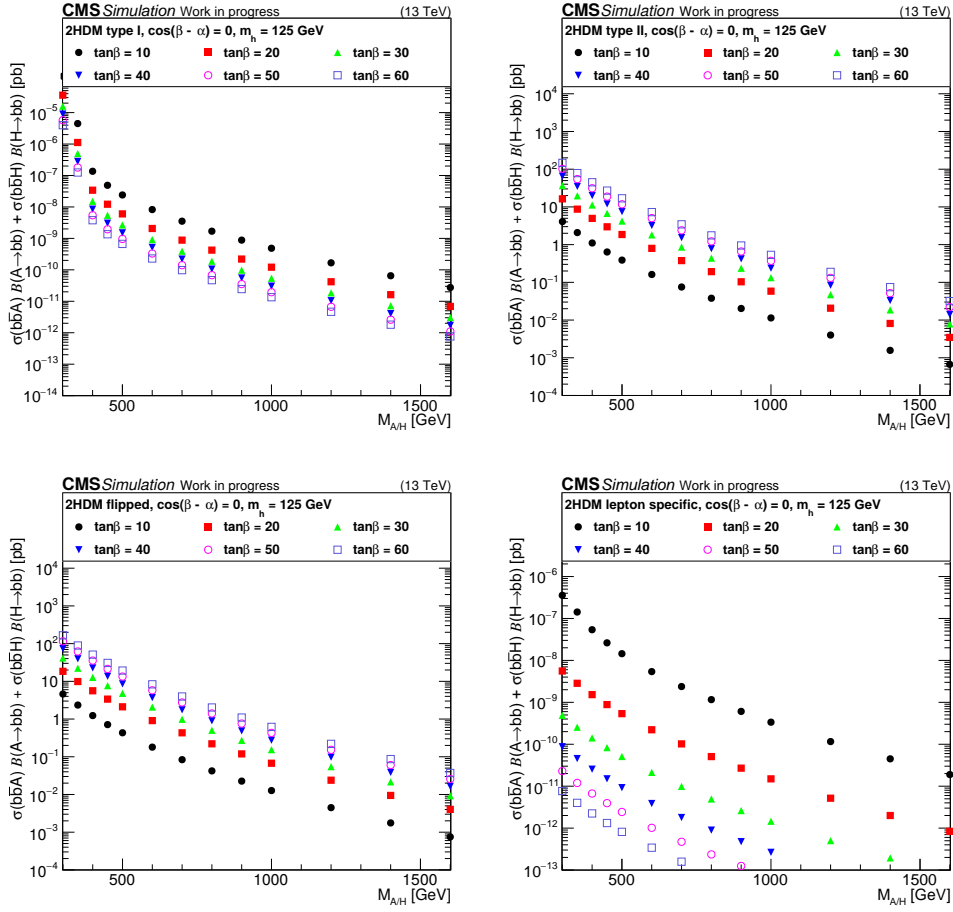


Figure 2.9.: Cross-section times branching ratio for the full process $\sigma(b\bar{b}A/H)\mathcal{B}(A/H \rightarrow b\bar{b})$ for the type I (top left), type II (top right), flipped (bottom left), and lepton-specific (bottom right) scenario. The different colors represent $\tan\beta$ values ranging from 10 to 60 and for all plots, $\cos(\beta - \alpha) = 0$, i.e. the alignment limit, is chosen.

in this combination of production and decay mode, the type II and flipped scenarios are more sensitive than the other two by several orders of magnitude. Since some other decay channels are suppressed around the alignment limit, the $A/H \rightarrow b\bar{b}$ mode achieves dominant sensitivity in this area. In the flipped scenario, the sensitivity around the alignment limit is unique.

3. Experimental Setup

3.1. Large Hadron Collider

Since first cathode ray experiments around the end of the 19th century [111], more and more powerful particle accelerators have been built. In modern high-energy physics, some examples at various research facilities around the world are PETRA (“Positron-Electron Tandem Ring Accelerator”) [112], TeVatron [113], and LEP (“Large Electron-Positron Collider”) [114]. At each of those machines, major scientific breakthroughs were achieved: the gluon was discovered in 1979 at PETRA [41, 115], the top quark was found at the TeVatron in 1995 [7, 8] and, besides measuring the masses of W and Z bosons to unprecedented precision, LEP showed that there are only three kinds of neutrinos [116].

Featuring a design center-of-mass energy of 14 TeV as well as an instantaneous luminosity about 50 times as large as the TeVatron’s [30, 117], the Large Hadron Collider (LHC) [29] is the most powerful particle accelerator ever built. It is located in the former LEP tunnel at CERN (European Organization for Nuclear Research, derived from “Conseil européen pour la recherche nucléaire”) and dedicated to the search for unknown, heavy particles.

With a circumference of about 27 km, the LHC crosses the Swiss-French border close to Geneva and stretches below both countries. It is the final part of the CERN accelerator chain which is shown in Figure 3.1. This chain starts with a linear accelerator (LINAC 2) which accelerates the protons to an energy of 50 MeV. Afterwards, the protons are directed through the Proton Synchrotron Booster (PSB, 157 m circumference, acceleration to 1.4 GeV) into the Proton Synchrotron (PS, 628 m, 25 GeV). The final step of acceleration happening before the protons enter the LHC is the Super Proton Synchrotron (SPS, 7 km, 450 GeV).

During this process of acceleration in various machines, many beam parameters of the LHC are already defined: the grouping of protons into bunches and the spacing of 25 ns between bunches take place in the PS. There, both properties are defined by the radio frequencies (RF) and their respective harmonics which are applied to the accelerating cavities.

In order to keep the protons inside the LHC as well as maintaining the beam focus, super-

3. Experimental Setup

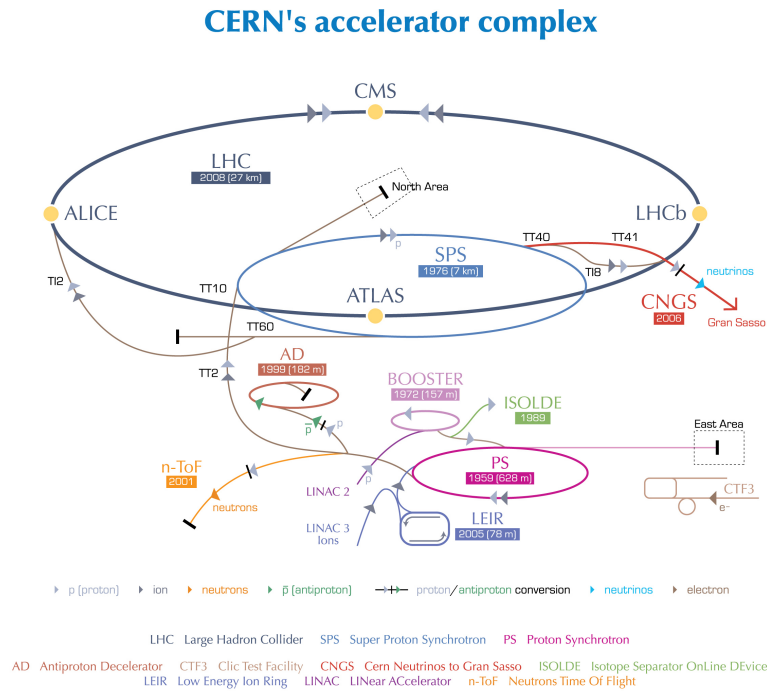


Figure 3.1.: CERN accelerator complex, starting with LINAC 2 [118]

conducting NbTi magnets are used, cooled to a temperature below 2 K using liquid helium, and providing a field up to 8 T. The LHC ring accommodates 1232 dipole magnets to bend the particle beam and almost 5000 multipole correctors which mainly focus it.

With increasing particle energy, the radio frequency applied to the accelerating cavities must be increased accordingly. For the LHC, accelerating protons from 450 GeV up to 7 TeV, this is realized with a 400 MHz superconducting niobium cavity system which – during a 20 minute energy ramp up – yields a proton energy gain of 485 keV per turn. The voltage applied to accelerate the protons is gradually increased from 8 MV at injection up to 16 MV at 7 TeV.

During proton operation, each beam consists of 2808 bunches, each containing about 10^{11} protons, with an interaction rate of about 40 MHz. There is also the possibility to use the LHC as a heavy-ion collider which is usually done for several weeks per year, mostly using lead ions with up to 2.76 TeV/nucleon.

There are eight currently active experiments located around the LHC, of which four are shown in Figure 3.1: ATLAS (“A Toroidal LHC ApparatuS”) [31] and CMS (“Compact Muon Solenoid”) [32] are general-purpose detectors, ALICE (“A Large Ion Collider Experiment”)

[119] is focused on heavy-ion physics and LHCb (“Large Hadron Collider beauty”) [120] is dedicated to b physics. Furthermore, there are two smaller experiments focusing on physics in the very forward regions around CMS and ATLAS, namely TOTEM (“Total, elastic and diffractive cross-section measurement”) [121] and LHCf (“Large Hadron Collider forward”) [122]. The two respective detectors of these two experiments are located on either side of both ATLAS and CMS for LHCf and TOTEM, respectively. As the two most recent experiments, MoEDAL (“Monopole and Exotics Detector at the LHC”) [123] is located close to LHCb, designed to search for magnetic monopoles, and FASER (“Forward Search Experiment”) [124] is situated 480 m from ATLAS, dedicated to investigate neutrinos and new, light particles.

One main quantity to describe the performance of a particle accelerator is the luminosity. It describes how many interactions take place per time and area of cross-section:

$$N_{\text{event}} = L\sigma_{\text{event}}, \quad (3.1)$$

with L being the luminosity and N_{event} the number of generated events per second in a process with the cross-section σ . The luminosity is defined as [32]

$$L = \frac{\gamma N_b^2 k_b f_{\text{rev}} F}{4\pi\epsilon_n \beta^*} \quad (3.2)$$

with the number of protons per bunch N_b , number of bunches per beam k_b , the revolution frequency f_{rev} , the Lorentz factor γ , the normalized transverse emittance ϵ_n , the betatron function at the interaction point β^* and a reduction factor accounting for the crossing angle of the interacting bunches, F . At the LHC design luminosity of $L = 10^{34} \text{cm}^{-2}\text{s}^{-1}$, around 25 proton-proton interactions take place in each bunch crossing, leading to an interaction rate of about 1 GHz. This effect is called pileup (PU).

Since the instantaneous luminosity is not constant over time due to effects like beam degradation and to measure the amount of data which is actually collected for analyses, the integrated luminosity is used:

$$\mathcal{L}_{\text{int}} = \int L dt. \quad (3.3)$$

In 2017, the CMS detector recorded 44.98 fb^{-1} out of the 49.79 fb^{-1} the LHC had delivered [125], which is shown in Figure 3.2. During the Run-II-period from 2015 to 2018, CMS recorded an integrated luminosity of about 150 fb^{-1} in addition to the roughly 30 fb^{-1} collected during Run I which lasted from 2010 to 2012.

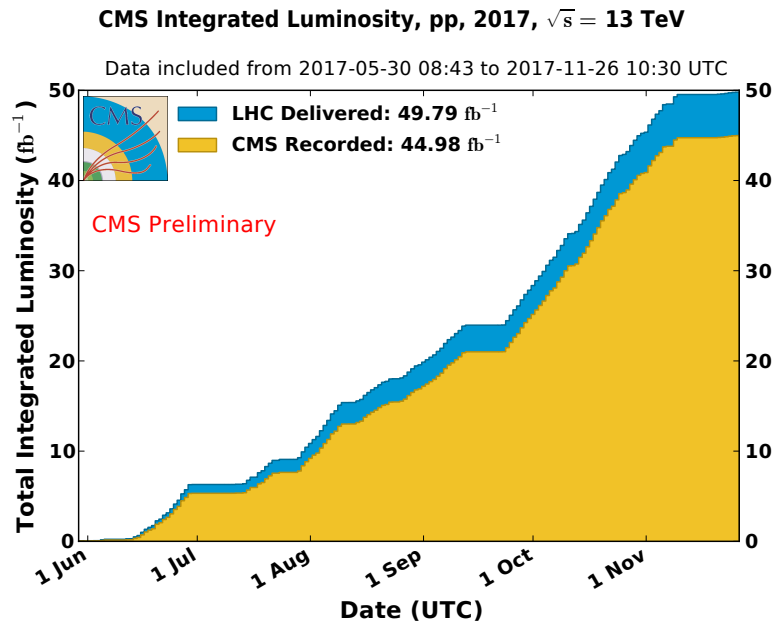


Figure 3.2.: Integrated luminosity as recorded by CMS (yellow) and delivered by the LHC (blue) [125]

3.2. The Compact Muon Solenoid Detector

As mentioned in Section 3.1, one of the two general purpose experiments at the LHC is CMS, the Compact Muon Solenoid detector [32]. It is located close to the French village of Cessy, roughly 100 m underground. The name contains three of the most important features of CMS. It is compact compared to ATLAS with a diameter of 15 m, a length of 21.6 m and a weight of about 12500 t. The large magnetic field of 3.8 T is created by a superconducting solenoid magnet. It is used to bend the trajectory of charged particles and, thus, measuring their charge and momentum accurately. Furthermore, the CMS detector has an excellent muon resolution due to its fine granularity and wide geometrical coverage. An onion-like shape of the detector ensures that particles are detected equally well in all directions. In this design, each sub-detector is layered around all previous structures and targeted on a specific kind of particle interaction. A schematic of the CMS structure in form of a slice through the detector is shown in Figure 3.3.

In order to describe the location inside the CMS detector, a right-handed cartesian coordinate system is used with the x -axis pointing towards the center of the LHC ring, a vertically upwards pointing y -axis and, thus, the z -axis being oriented along the beam pipe, following the counter-clockwise beam. This system can be used to define a set of widely used physical quantities.

Since the center-of-mass frame of the proton-proton system and the one of the parton-parton

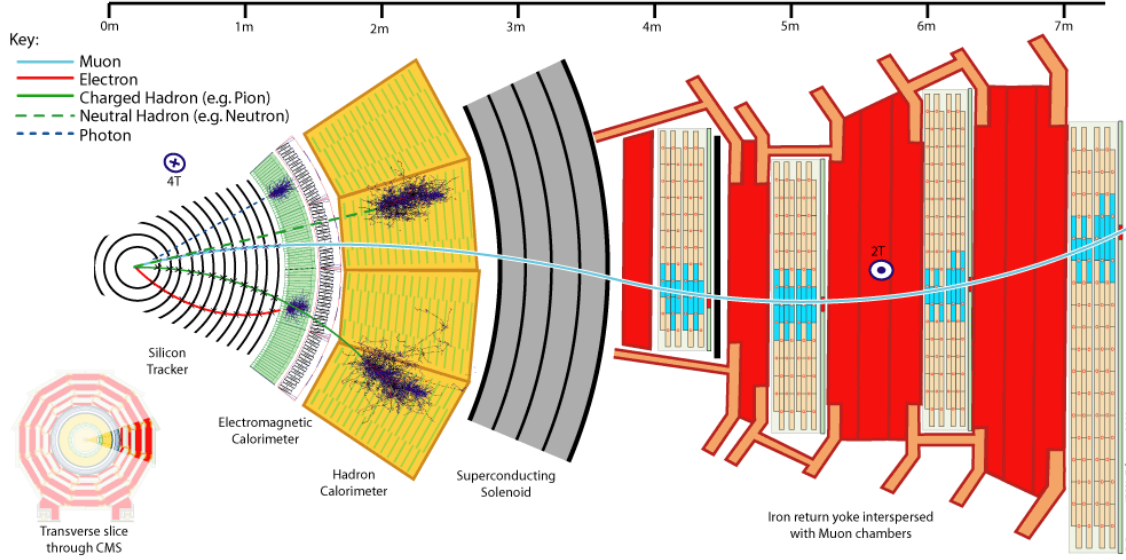


Figure 3.3.: Slice through the CMS detector. Properties of different particles are measured in specific parts of the detector and the respective trajectories are shown. Neutral particles, represented by dashed lines, do not leave a track and can only be measured in the calorimeters. [126]

system are not the same, the rapidity y is used. It is defined as [42]

$$y = \frac{1}{2} \ln \left(\frac{E + p_z}{E - p_z} \right). \quad (3.4)$$

Differences in rapidity are invariant under a Lorentz boost along the beam axis. For a particle traveling close to and along the beam axis, the rapidity approaches $\pm\infty$, while it is 0 for a particle on a trajectory perpendicular to the beam.

Two angles are usually used within the CMS coordinate system. θ , the polar angle, is measured from the z -axis, while ϕ , the azimuthal angle, is measured from the x -axis in the xy plane with $\phi = 0$ being the positive x direction and $\phi = \pi/2$ pointing along the positive y direction. For high energies of particles, their masses become negligible and $p_z \approx E \cos \theta$. Thus, the quantity mainly used in particle physics is the pseudorapidity

$$\eta = -\ln \left(\tan \frac{\theta}{2} \right) = -\frac{1}{2} \ln \frac{p + p_z}{p - p_z}. \quad (3.5)$$

Additionally, an angular distance between two particles i and j can be measured with

$$\Delta R_{ij} = \sqrt{\Delta \eta_{ij}^2 + \Delta \phi_{ij}^2}. \quad (3.6)$$

In general the angle of an object with respect to the beam axis can be measured well and particle interactions are assumed to be symmetric in ϕ . Thus, the x - and y -components of the momentum, i.e. the transverse momentum, are sufficient to describe an object:

$$\sqrt{p_x^2 + p_y^2} = p_T = p \sin \theta. \quad (3.7)$$

This quantity is also conserved in an interaction.

The CMS detector is intended for precision measurements of physics within the standard model as well as searches beyond it. To do so, its ability to reconstruct jets and leptons as well as missing energy equally precisely is used. In this context, due to the conservation of transverse momentum, the missing transverse energy is defined as the imbalance in transverse momentum or the negative sum of all p_T measurements, $\cancel{E}_T = -|\sum p_T|$. It represents the energy of particles escaping from the detector without being measured.

3.2.1. Silicon Tracking System

For the CMS tracking system, a design based on silicon modules was chosen. It covers an area of around 200 m^2 and a pseudorapidity range of $|\eta| < 2.5$. In the semiconductor silicon, trajectories of charged particles can be measured since they ionize the material and the respective charges of created electron-hole pairs can be collected by the application of an external electric field. Due to the high mobility of charge in silicon, the collection time is low with about 20 ns . In comparison, gas detectors with a similar size have a collection time in the order of one μs . Also, silicon has a high density and a minimally ionizing particle, i.e. most particles passing the tracking system, produces around 110 electron-hole pairs per μm . In combination with a low ionization energy of 3.6 eV , this leads to a large sensitivity throughout the whole volume of the tracking system. Since silicon detectors can be built out of individual modules, a high granularity yields excellent spatial resolution and a low noise level since the channels are less occupied. To take most advantage from these properties, the part of the tracking system closest to the beam, i.e. with highest occupancy, is realized in form of a high-granularity pixel detector. The coarser strip tracking system is built around it.

The tracking system provides an input to the p_T measurements. Due to the magnetic field from the solenoid which covers the full tracking system and the calorimeters, trajectories of charged particles are bent such that their transverse momentum can be measured. This happens following the relation

$$\frac{p_T}{[\text{GeV}]} = 0.3 \frac{B}{[\text{T}]} \frac{\rho}{[m]}, \quad (3.8)$$

where ρ is the curvature radius. For a particle with $p_T = 1$ TeV, a resolution of $\sigma_{p_T} \approx 100$ GeV is the design target. While tracks with larger p_T are still measured and analyzed, the resolution in these cases becomes worse since the tracks are less bent. Precise reconstruction of tracks is crucial not only in order to measure properties of individual particles correctly but also in order to reconstruct vertices which will be explained in more detail in Section 4.1.

Individual hits reflect the modules and positions a particle passed while traveling through the tracking system. Originally, these hits are an electric signal from the respective readout system which is then digitalized. If a certain signal-to-noise ratio is reached, the signal from this module and hits in adjacent channels are clustered. This cluster-charge profile together with positional information and pitch constitutes the final hit reconstruction. To account for different requirements depending on the distance to the beam, the CMS tracking system consists of two subparts, the pixel and strip tracking detectors. Both operate at low temperatures below 0° C in order to prevent radiation damage.

Pixel Detector

Closest to the beam pipe, at the core of CMS, is the pixel detector. In the year-end technical shutdown 2016/2017, it was upgraded to its phase-1 design [127] to cope with the increased instantaneous luminosity of around $2 \times 10^{34} \text{ cm}^{-2}\text{s}^{-1}$. This larger luminosity also increases the average pileup, the number of proton-proton interactions per bunch crossing, to around 50. The new design (phase-1) features four layers of barrel pixel (BPIX) modules instead of three and three end-caps on each side of the detector instead of two. Both the new and old design are shown in comparison in Figure 3.4. In the phase-1 design, barrel layers are arranged around the beam pipe at radii of 2.9, 6.8, 10.9, and 16.0 cm while the double-sided end-caps in the forward pixel (FPIX) are placed at 29.1, 39.6, and 51.6 cm from the nominal interaction point (IP). The innermost parts are closer to the IP than in the phase-0 design while the outermost layers cover a larger overall area. This improves the power of b tagging algorithms and accounts for possible degradation of individual modules. Furthermore, the area in which each track creates at least four hits somewhere inside the pixel detector is increased to $|\eta| < 2.5$.

In total, the pixel detector features 124 million sensors, 79 million of them for the barrel and 45 million in the end-caps. They are grouped into 1856 modules, each reading out the information from 66560 pixels. The individual pixels in both BPIX and FPIX have an active area of $16.2 \times 64.8 \text{ mm}^2$ with a thickness of $285 \mu\text{m}$.

The pixel detector has a spatial resolution of $10 \mu\text{m}$ in the $r\phi$ plane and of $20 \mu\text{m}$ in z direction.

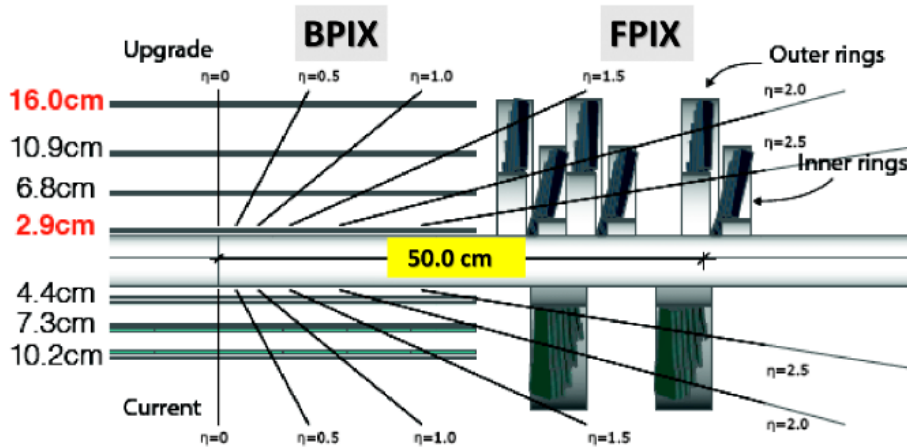


Figure 3.4.: Comparison of the pixel phase-1 design, used from the beginning of 2017 (top) and the previously installed phase-0 design (bottom) [127]. Tilting the end-cap disks enables additional charge sharing between adjacent modules due to the Lorentz drift of curved trajectories which improves the overall resolution.

Strip Detector

The silicon strip detector is the second part of the CMS tracking system. It consists of an inner (TIB) and outer barrel (TOB) in the central region as well as inner disks (TID) and end-caps (TEC) in the forward direction. Due to the reduced flux in outer parts of the tracking system, strips can be used instead of pixels.

In the four layers of the inner barrel ($r < 65$ cm), the strips have a maximum cell size of $10 \text{ cm} \times 80 \mu\text{m}$. For the six TOB layers ($65 \text{ cm} < r < 110$ cm) with even lower flux, larger strips of $25 \text{ cm} \times 180 \mu\text{m}$ are used. Also, the thickness is larger in the outer layers with $500 \mu\text{m}$ compared to $320 \mu\text{m}$ in the TIB.

Each TID – on either side of the detector – consists of three disks, filling the gap between TIB and TEC and being located up to 120 cm from the nominal interaction point, while the TEC comprises 9 disks, extending up to $|z| < 280$ cm. Again, sensors are $320 \mu\text{m}$ and $500 \mu\text{m}$ thick for inner and outer disks, respectively.

Overall, the strip detector achieves single-point resolutions ranging from $23 \mu\text{m}$ to $52 \mu\text{m}$ in both the $r\phi$ and z directions.

3.2.2. Electromagnetic Calorimeter

After transverse momentum and direction of motion of a charged particle have been determined by the tracking system, its energy is measured in calorimeters if it is stopped inside them. Prop-

erties of neutral particles are investigated only in the calorimeters. Since the calorimeters are segmented, additional directional information can be extracted. The calorimeters at CMS target a full absorption of all known particles but muons (and neutrinos), so a high density material is used. In order to avoid losing precision in the measurement due to premature absorption or energy loss of particles, both calorimeters are located inside the solenoid magnet. Therefore, particles do not have to cross the coil of the magnet before they can be analyzed in the calorimeters.

The electromagnetic calorimeter (ECAL) is specifically designed to examine electrons and photons. As they enter the calorimeter material, they induce a shower of particles which by themselves again start a new, smaller shower. Thus, the full energy of all the subsequent particles can be measured. In the ECAL, all of the material is active, meaning that it acts as absorber and measures the properties of particles at the same time. Overall, 75848 lead tungstate (PbWO_4) scintillating crystals are used in a barrel and two end-caps. This material provides the advantage of a fast signal: 80% of the light are emitted in 25 ns. To improve the relatively low gain of only 30 photons per MeV of incident electron energy, avalanche photodiodes (APDs, in the barrel) and vacuum phototriodes (VPTs, in the end-caps) are used.

To classify the stopping power of an electromagnetic calorimeter, the radiation length, X_0 , and the Molière radius, r_M , of an electron are used. The former is the average distance after which an electron reduces its energy to $1/e$ or a photon is converted to an electron-positron pair. The latter reflects the typical radius of the shower cone. For the ECAL, these quantities are $X_0 = 8.9$ mm and $r_M = 22$ mm.

Overall, the ECAL provides a depth of $25.8 X_0$ and covers a pseudorapidity range of $|\eta| < 3.0$, where the barrel reaches from $\eta = -1.479$ to $\eta = 1.479$ and the end-caps cover the remaining range. The barrel has an inner radius of 129 cm and stretches 3.14 m along the z axis around the IP. In z direction, it is immediately adjacent to the end-caps. Each crystal in the barrel is 23 cm long with an active front area of around 22×22 mm² or 0.0174^2 in $\Delta\eta \times \Delta\phi$. In ϕ , this equals one degree. The end-caps consist of slightly differently shaped crystals with an active cross-section of 28.6×28.6 mm² and a length of 22 cm ($24.7 X_0$ in total).

A preshower detector, consisting of two layers of lead absorber and active silicon strip detectors, totaling $5 X_0$, is placed in front of the end-caps to increase the identification efficiency of photons and neutral pions. Using tracker information, electrons and photons can be distinguished up to a pseudorapidity of $|\eta| < 2.5$ which is the tracker coverage.

An energy resolution σ_E of

$$\left(\frac{\sigma_E}{E}\right)^2 = \left(\frac{2.83\%}{\sqrt{E/\text{GeV}}}\right)^2 + \left(\frac{124\text{ MeV}}{E}\right)^2 + (0.26\%)^2 \quad (3.9)$$

is achieved for an electron energy E . Here, the first term is stochastic, the second represents the noise and the last term is a constant, accounting for calibration inaccuracies, energy leakage or non-uniform response of the detector. All values were determined in beam tests.

3.2.3. Hadronic Calorimeter

Leptons and hadrons behave differently inside calorimeters, making it necessary to distinguish the electromagnetic (ECAL) and hadronic (HCAL) calorimeters. Unlike the ECAL, the HCAL is a sampling calorimeter which consists of passive, absorbing parts and active, detecting parts. Since hadron showers are longer than electromagnetic ones, this does not cause a loss of sensitivity. For hadrons, the important quantity regarding stopping power is the interaction length λ_I . It measures how far a particle travels on average before initiating a shower. In order to improve the \cancel{E}_T measurement by containing as many particles as possible in the HCAL and measuring their energy, material is maximized in terms of λ_I inside the magnet coil. Furthermore, an additional layer of scintillators is placed outside of the magnet, using the coil as an absorber and increasing the number of interactions lengths to over 10.

As absorbing material, brass was chosen. It features a short interaction length, can be machined easily and is not magnetic. Plastic scintillators are used as active medium and their signal is read out with hybrid photodiodes (HPDs).

The HCAL covers a pseudorapidity range of $|\eta| < 5.0$, where the barrel accounts for $|\eta| < 1.4$, the end-caps cover $1.3 < |\eta| < 3.0$ and a forward calorimeter detects particles in the range of $3.0 < |\eta| < 5.0$. In the barrel, scintillator towers with a segmentation of $\Delta\eta \times \Delta\phi = 0.087^2$ are installed. The end-caps are segmented differently depending on their location. At smaller η , a 5° segmentation is used in ϕ , while otherwise each tower covers 10° . The η segmentation reaches from 0.087 to 0.35. Overall, the HCAL consists of 2304 towers.

Separated from the other parts of calorimetry, the forward part of HCAL is located 11.2 m from the IP with a thickness of 1.65 m. It consists of steel, which is used as passive material, and quartz fibers as active material. In the fibers, Cherenkov light is produced which is then enhanced by photomultipliers. Each tower covers $\Delta\eta \approx 0.175$, except for the lowest- and highest- η towers which cover $\Delta\eta \approx 0.1$ and $\Delta\eta \approx 0.3$, respectively. The towers are segmented

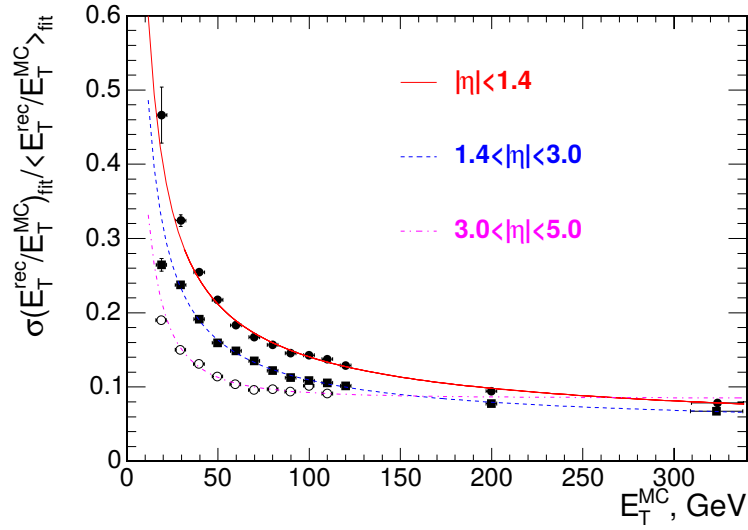


Figure 3.5.: E_T resolution as a function of E_T for the central (red), end-cap (blue) and forward (pink) calorimeter regions, based on simulation [32]

to 10° in ϕ , again except for the highest- η tower which features a larger $\Delta\phi$ coverage with 20° .

In combination with ECAL measurements, a resolution σ_E of

$$\left(\frac{\sigma_E}{E}\right)^2 = \left(\frac{100\%}{\sqrt{E/\text{GeV}}}\right)^2 + (4.5\%)^2 \quad (3.10)$$

can be achieved for particles with energies between 30 GeV and 1 TeV [128]. For HCAL alone, the resolution of transverse energy is shown in Figure 3.5.

3.2.4. Muon System

After being detected in the tracking system, muons are investigated thoroughly inside the muon system [129]. It surrounds the tracking system, the calorimeters, and the magnet. As the muon system is embedded in the return yoke of the solenoid, the muons' tracks are also bent. Furthermore, the return yoke acts as an additional hadron absorber which increases the purity of measurements in the muon system. This second muon measurement contributes substantially to the overall precision for transverse momenta of the muons above 200 GeV due to good spatial resolution of the muon system.

Muons are a key target of CMS, as they are present in many SM and BSM signatures. One major example is the $H \rightarrow ZZ \rightarrow 4\mu$ channel which contributed to the discovery of the Higgs boson in 2012 [130]. Due to their relatively large mass, muons do in general not lose a sig-

3. Experimental Setup

nificant amount of their energy in interactions with the detector material or to electromagnetic radiation. Thus, they pass the calorimeters and the magnet more or less unaffected. This means that they can be reconstructed well and with high purity in the muon system.

The muon system at CMS consists of three different types of gas-filled detectors which will be described in this section. Inside a gas detector, charged particles ionize the gas atoms. The resulting ions and electrons are separated from each other by an external electric field. While moving, these particles ionize further gas atoms, which amplifies the original, often relatively small signal by generating additional charge which can be detected. The drift of ions and electrons then induces a charge in the readout electrodes which is measured. Main requirements for all kinds of gaseous detectors are a low amount of multiple scattering, a high number of measurement points, and a good single-point resolution. All of these target the improvement of muon identification as well as energy measurements.

In total, the CMS muon system covers an area in the order of 25000 m^2 . With such a large volume, used materials were required to be inexpensive and the gas must not be flammable. This was taken into account for all three types of chambers.

For the barrel region, up to $|\eta| < 1.2$, drift tubes (DT) with coarse granularity are installed. In this region, the muon flux is assumed to be least intense, while also the neutron induced background should be smallest. The drift tubes consist of cells with an active area of $42 \times 13\text{ mm}^2$ which are filled by a mixture of 85 % argon (Ar) and 15 % carbon dioxide (CO_2). In the drift tubes, the position of a muon is calculated from the time it takes the created free electrons to drift to the anode of the cell. The maximum drift time is about 400 ns and a single-point spatial resolution of around $200\text{ }\mu\text{m}$ is achieved.

In the end-caps, cathode strip chambers (CSC) are used. Inside, a gas mixture of 50 % CO_2 , 40 % Ar and 10 % CF_4 is used. The CSC also cover a part of the barrel, more precisely the region $0.9 < |\eta| < 2.4$. They provide a faster response and a finer granularity than the DT in a region with a larger magnetic field, higher muon rate and larger neutron-induced background. The lower response time compared to the DT originates in how the signal emerges. While the drifting of particles takes some time to induce a charge, the electron avalanche in the CSC creates a charge directly at the anode and an image charge at the cathode. The layout is such that all anode layers are sandwiched in between cathode panels. This signal is directly available and, thus, allows for usage of CSC information in the L1 trigger, which is described in detail in Section 3.3. The fine segmentation in $r\phi$ allows for precision measurements and a resolution of about $40\text{--}150\text{ }\mu\text{m}$ in this plane. In the end-cap geometry, the $r\phi$ coordinate system is better suited than z to measure the muon momentum precisely.

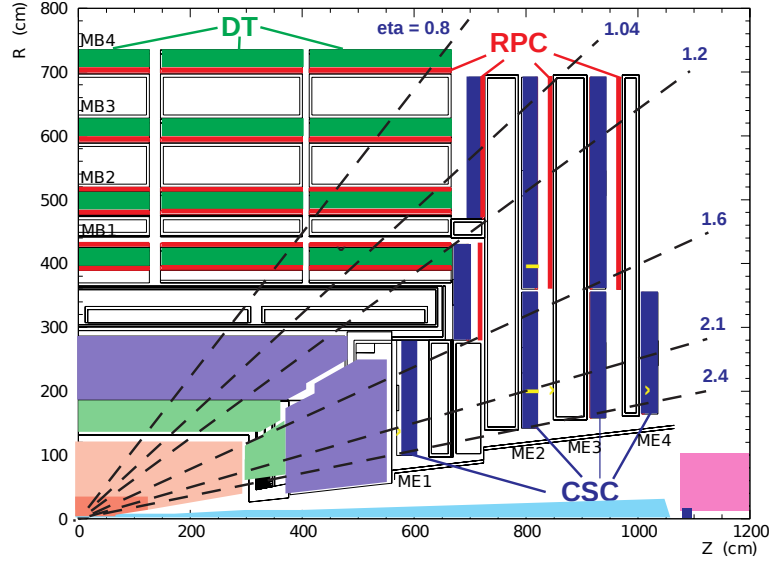


Figure 3.6.: Schematic setup of sub-detectors in CMS [32]. At the innermost part (orange), the tracking system is shown, surrounded by ECAL (green) and HCAL (purple), followed by the solenoid magnet (white). The outermost part is covered by the three types of muon detectors which are marked individually.

Finally, resistive plate chambers (RPC) are present in the overlap region up to a pseudorapidity of $|\eta| < 1.6$ as an additional layer. Due to their fast response, they provide an optimal timing resolution which is used to identify the correct bunch crossing for an event. The RPC provide a robust, independent, standalone muon identification which is essential for triggering.

Overall, the muon system covers a range up to $|\eta| < 2.4$ without gaps, has a time resolution of less than 3 ns and a muon identification rate above 90%. This rate has been tested together with misidentification rates in $Z \rightarrow \mu\mu$ events using a tag-and-probe approach. Misidentification rates due to pions and protons were found to be on the per mille level. The position of individual detector parts is shown in Figure 3.6, including the tracking system, the calorimeters, the solenoid, and the three types of muon detectors.

3.3. Trigger and Data Acquisition

With a bunch crossing rate of about 40 MHz and an average of more than 30 proton-proton interactions per bunch crossing, there are more than a billion interactions per second. As the computing system can only record with a rate of roughly 1 kHz, the trigger must provide a rejection factor of up to 10^6 [131]. This is achieved by pre-selecting events of potential interest, based on quantities like p_T or E_T . Thresholds are designed to keep as many potential signal

3. Experimental Setup

events as possible while at the same time rejecting as much background as possible.

The CMS trigger system consists of two parts, the Level-1 (L1) and the High-Level-Trigger (HLT). Based on hardware, the L1 reduces the event rate to about 100 kHz. Then, the software-based HLT, which runs on a processor farm consisting of several thousand CPUs, further shrinks the event rate to roughly 1 kHz.

In order to cope with changes in the instantaneous luminosity, the sets of thresholds which decide whether or not an event is recorded are adjusted to stay inside the computing limit. At the same time, they should still record as many events as possible. These sets of instructions are called trigger menus. They are associated with a varying number of pre-scale columns. This ensures that the rate of an existing menu can be adjusted easily without actually changing the trigger requirements defined in this menu. Then, with a pre-scale factor of n , only every n -th event is selected randomly. Depending on the available bandwidth, a different pre-scale column, i.e. a different factor, can be chosen.

As the first layer, the L1 filters events quickly within around $4 \mu\text{s}$. During this period, the full event data is kept in a buffer.

Several types of logic systems are used inside of the L1 trigger. Where possible and cost effective, Field Programmable Gate Arrays (FPGAs) are used. They are based on MicroTCA technology and enable a larger number of trigger paths as well as more detailed calculations like the invariant mass of an object. Additionally, Application Specific Integrated Circuits (ASICs) are installed. While being more resistant to high-PU conditions, they are more difficult to customize than FPGAs.

The decision process in the L1 is based on calorimeter and muon system information in relatively coarse granularity. It looks for the primitives, meaning photons, electrons, muons, and jets above certain p_T and E_T thresholds.

For the HLT [?], more pieces of information are collected from the sub-detectors than at the faster L1 trigger, allowing for a more thorough examination of the events. Furthermore, multiple simplified analysis algorithms run simultaneously, staged by the HLT path which is designed to evaluate the most exclusive selection steps first in order to discard an event as quickly as possible. Similar to the L1 trigger, the HLT thresholds reflect the computing limitations and pre-scaling can be used to reduce the trigger rate. All decisions are completed within less than 200 ms. After checking each event based on all given paths, an event is stored if it meets all requirements of at least one HLT path.

3.4. Event and Detector Simulation

Simulation is crucial to predict physical interactions between particles as well as those with the detector material. Simulated events are used for sensitivity studies and to develop analysis strategies. Since events with multiple-parton final states can not be assessed analytically, Monte-Carlo (MC) generators are used for these simulations. The Monte-Carlo method [132] is based on repeated, random sampling of data in order to achieve a numerical solution for a problem which is not solvable analytically.

To simulate how a physical process happens and how it is measured by a detector, several steps are required. First, the hard-scattering process itself is generated, including incoming and outgoing particles as well as respective decay products. In this step, the matrix element of the hard process is calculated using the Monte-Carlo method to obtain the properties of the incoming parton. Then, QCD effects of higher orders are taken into account before the hadronization is modeled. Afterwards, a simulated model of the detector is used in order to mimic the reconstruction of the generated particles. In all respective steps, the simulation is tuned to match the observations in data.

Various programs are used to simulate events at the LHC. Out of those, PYTHIA8 [133] is used for leading order (LO) event generation. It provides calculations for certain two-body hard-scattering events as well as the hadronization of final-state particles. Processes of higher orders can be estimated based on the parton shower content.

MadGraph 5 [134], on the other hand, is providing next-to-leading-order (NLO) events. This includes initial-state radiation (ISR) and final-state radiation (FSR). MadGraph calculates the matrix element on tree-level to arbitrary order. There, it has to be taken into account that interference terms in the NLO cross-section computations lead to negative weights being assigned to some generated events [135]. To simulate the parton shower and the hadronization, PYTHIA8 is interfaced by MadGraph.

After the particle interactions have been simulated, detector effects have to be taken into account. Thus, the complete CMS detector is modeled using GEANT4 [136, 137], including all support structures and detector material. In this step, the interaction of particles with the entirety of material in the detector is simulated, taking into account the magnetic field and creating tracks as well as vertex objects.

4. Physics Objects

4.1. Objects Reconstruction

4.1.1. Particle Flow Algorithm

Originally invented at the ALEPH experiment [138] at LEP, the particle flow (PF) algorithm [139] was adopted by CMS. It connects measurements from different parts of the detector in order to reconstruct an object correctly. Inputs from the tracking system, both calorimeters as well as the muon system are used. To provide the required identification efficiency to analyses, characteristic signatures of various types of objects in the respective part of the detector are used. This combination of measurements from the complete detector also provides an improved resolution compared to isolated measurements in an individual sub-detector.

At CMS, the PF algorithm profits from the large magnetic field which separates charged and neutral particles in the calorimeters. This is aided by the fine segmentation of the ECAL and the hermiticity, i.e. covering of 2π in ϕ and almost 2π in θ , of the HCAL. Furthermore, the finely grained and efficient tracking system provides accurate track reconstruction and the muon system guarantees excellent muon identification. Altogether, this allows clear distinction of different particles as well as the precise reconstruction of their energy and momentum.

Measurements from different sub-detectors are connected by a linking algorithm. The probability of correct connection for one particle is only limited by the detector granularity and the occupancy. First of all, the linking algorithm extrapolates tracks from the silicon tracking system to calorimeter energy deposits. If the extrapolated track matches a calorimeter cluster, the two objects are linked. In case of multiple candidate clusters, only the one with the smallest distance to the track is selected. To save computing time, the clearest identification steps are done first, i.e. muons followed by electrons and photons. Measurements which were already assigned to one particle are then excluded from the following reconstruction steps in order to avoid double counting.

4.1.2. Tracks and Vertices

Tracks are reconstructed based on individual hits in the silicon tracking system. This is done with a combinatorial track finder (CTF) which is based on a Kalman filter [140]. Out of the recorded hits, a vast amount of possible trajectories can be formed based on combinatoric possibilities. Hence, it is challenging to identify the actual path of an individual particle [141]. Nevertheless, when combining the hit information with clusters from other parts of the detector, the correct trajectory can be identified. In order to achieve a high reconstruction rate while keeping the purity of correctly identified tracks as high as possible, a method called iterative tracking is used. Hits already assigned to a track are masked in the next iteration of the CTF. For each iteration, quality criteria are relaxed in order to reconstruct more tracks, while the main steps remain unchanged. First, a seed is generated from multiple hits before the pattern recognition is run. To classify the quality of a track candidate, several quantities are evaluated such as the number of hits in certain tracking layers or the χ^2 value of the fit. Subsequently, the final fit determines the tracks which will be kept.

From the tracks, vertices can be reconstructed. Correctly identifying primary and secondary vertices (PV and SV) is a key ingredient to many analyses. In general, the primary vertex is the origin of the scattering event, while secondary vertices usually originate from decays of particles created in the original scattering. Therefore, several SV can be assigned to the same PV, e.g. in case of cascading decay structures. Thus, secondary vertices usually have a lower track multiplicity as well as a smaller sum of track p_T associated with them. At CMS, the deterministic annealing (DA) algorithm [142] together with an adaptive vertex fitter (AVF) is used [143]. Further iterations based on the AVF lead to improved reconstruction of both primary and secondary vertices [144]. Figures 4.1 and 4.2 show the resulting resolution of primary vertices for the 2016 and updated 2017 pixel-detector design and the pileup distribution for 2017, i.e. the mean number of proton-proton interactions per bunch crossing. In Figure 4.1, the benefit of the upgraded pixel detector is clearly visible as a higher PV resolution based on the same number of tracks assigned to the respective vertex.

In order to identify a vertex candidate, the DA algorithm is used. It clusters tracks to form vertices based on the z coordinates of the point where each track approaches the center of the beam pipe most closely. Then, within the AVF, first, a weight is assigned to each track, depending on its distance to the vertex candidate. Afterwards, the candidate is reevaluated based on all the tracks' weights. During this procedure, outlier tracks are not neglected but downweighted in order to prevent fake vertices. Vertex candidates with at least two assigned

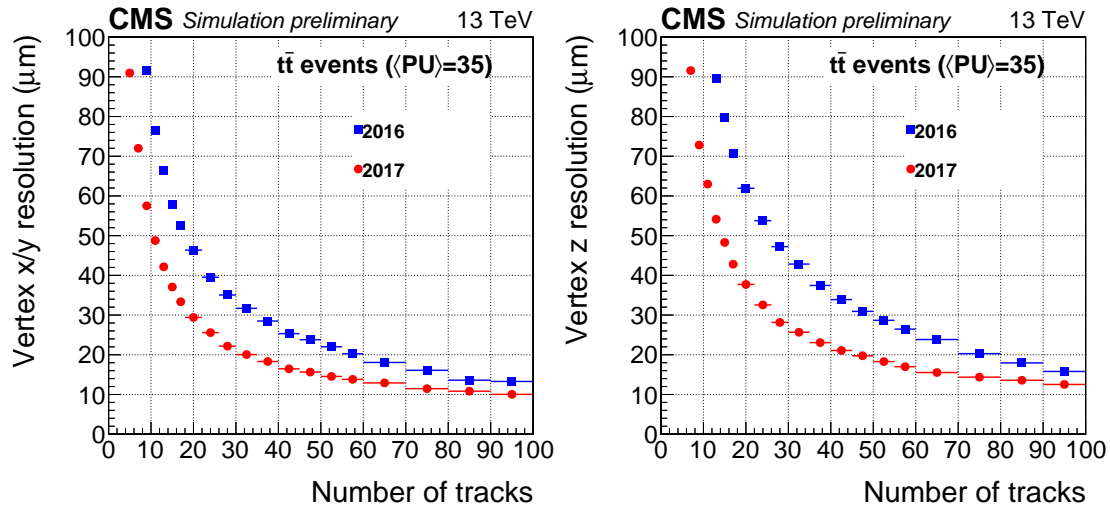


Figure 4.1.: Primary vertex resolution in x-y (left) and z (right) for the 2016 (blue) and 2017 (red) geometry of the tracking system, based on simulated $t\bar{t}$ events with an average pileup of 35 [145]

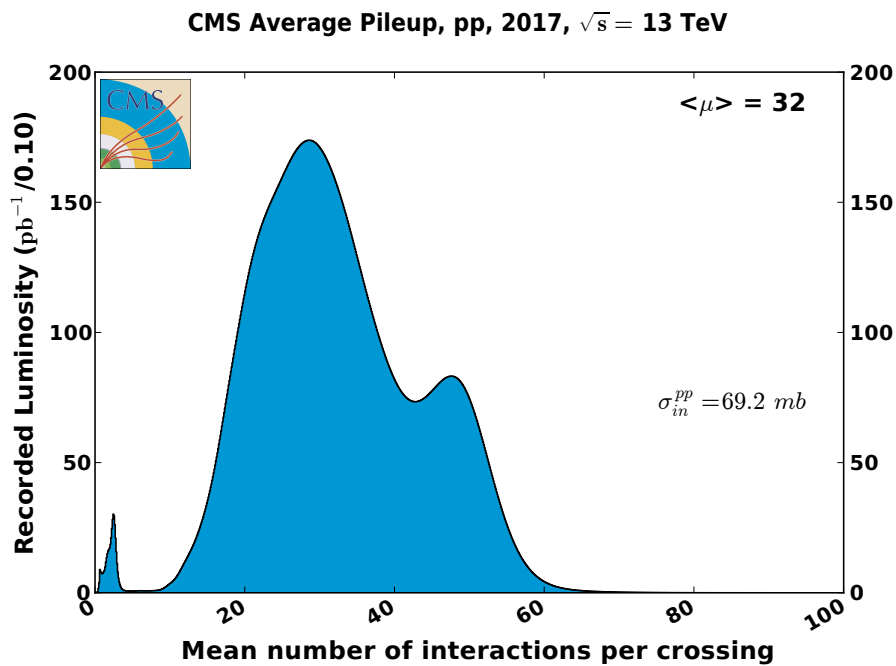


Figure 4.2.: Distribution of mean number of proton-proton interactions per bunch crossing for the 2017 data-taking period [125]

tracks enter the actual fitting procedure. Since vertex candidates with a large number of tracks with rather large respective weights are most likely to originate from a proton-proton interaction, the candidates are selected based on the number of degrees of freedom [146]

$$n_{\text{dof}} = -3 + 2 \sum_{i=1}^{\#tracks} w_i. \quad (4.1)$$

The weight of the track, w_i , reflects the compatibility between track and vertex candidate. The larger it is, the higher the probability that this track in fact originates from that vertex. These two steps are repeated until all tracks are assigned to a vertex candidate.

4.1.3. Jets

If a particle carrying color charge is produced in a collision, it will bind with other colored particles and form a color-neutral hadron. These other particles can be free previously or they are produced through radiation processes from the original parton. In general, each parton produced in the collision, i.e. quark or gluon, will not only yield one hadron but, through fragmentation and hadronization, a shower of color-neutral particles, the jet [147]. In order to use the jet as a link to the original parton, it is crucial to assign correctly as many hadrons as possible to this jet.

The algorithms which can be used for this procedure can be divided into two major classes, the cone and the recombination algorithms. A cone algorithm [148] starts from a particle track, which is linked to respective measurements in the calorimeters, and simply defines a cone around it, counting all particles detected inside of this cone towards the jet.

Alternatively, more complex recombination algorithms are used which combine detected particles iteratively, based on the distances between two objects i and j ,

$$d_{ij} = \min(k_{T_i}^{2p}, k_{T_j}^{2p}) \frac{\Delta_{ij}^2}{R^2}, \quad (4.2)$$

as well as between an object i and the beam B ,

$$d_{iB} = k_{T_i}^{2p}. \quad (4.3)$$

In these equations, k_T represents the transverse momentum, i.e. the momentum in the xy plane, R reflects the cone size, and p is the exponential parameter. The quantity Δ_{ij} is a distance parameter similar to R and based on the rapidity y as well as the azimuth ϕ . It is defined as

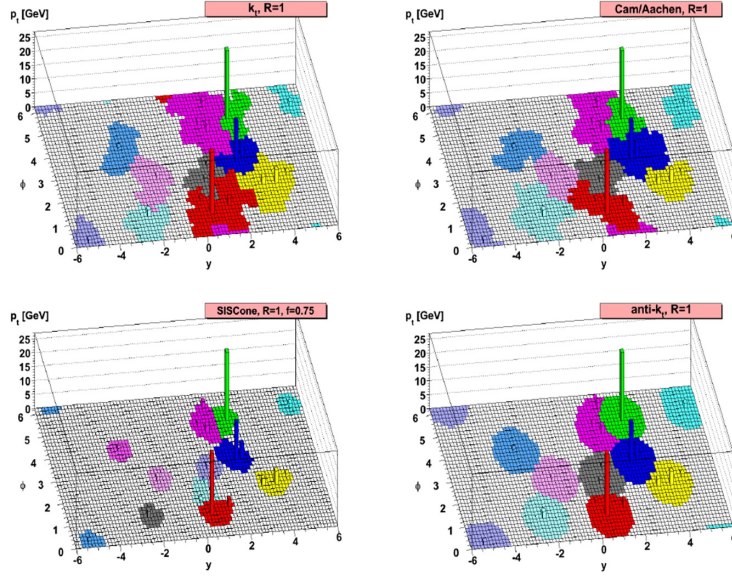


Figure 4.3.: Shape of jets based on various reconstruction algorithms [147], namely k_T (top left) and anti- k_T (bottom right), Cambridge-Aachen (top right) and a cone algorithm (bottom left). The cone radius R is set to 1 for all algorithms and the data on which they have been run is also the same in all four images. For the anti- k_T algorithm, it can be seen that the jet shape is usually conical if there are no overlapping jets.

$\Delta_{ij} = (y_i - y_j)^2 + (\phi_i - \phi_j)^2$. The distances are calculated between the object obtained in previous iterations of the algorithm and further present particles. If the nearest object to the jet is found to be the beam, the process is stopped and the object is kept as the final jet. Depending on the choice of p , different algorithms are distinguished. The k_T -algorithm [149] is based on $p = 1$, while the Cambridge-Aachen algorithm [150] features $p = 0$. With a value of $p = -1$, the algorithm is called anti- k_T [151]. Here, particles with large transverse momentum affect the shape and location of the jet most, since soft objects cluster to hard ones much faster than to other soft objects. This results in a conical shape. The anti- k_T algorithm with a cone size of $R = 0.4$ is used for the jets in this analysis. A comparison of these recombination algorithms and a cone algorithm is shown in Figure 4.3.

An extraordinarily important property of the anti- k_T jet clustering algorithm is the ability to avoid divergences. These could for example be caused by the presence of very soft final state particles or the splitting of an initial state particle into two collinear objects. The respective mechanisms to account for these two particular issues are called infrared and collinear safety [152].

Depending on which objects are used as input to the jet clustering algorithm, the resulting set

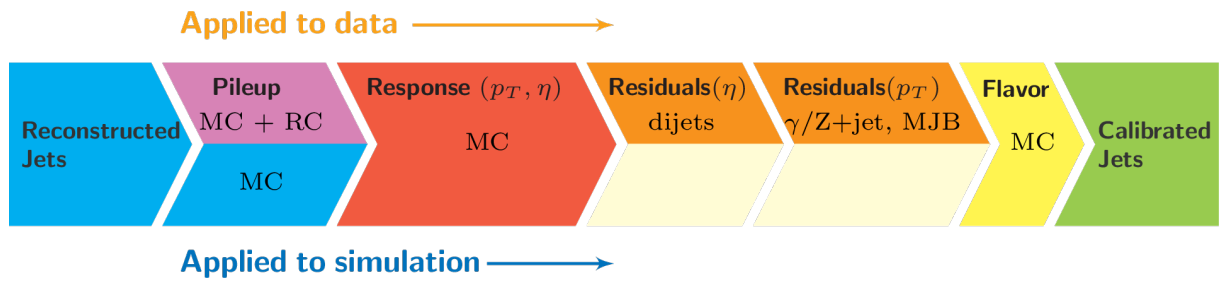


Figure 4.4.: Steps of Jet Energy Corrections in the order they are applied to data (top) and simulation (bottom) [155]

of jets is called “CaloJet” or “PFJet”. The former are based exclusively on calorimeter input, which allows a fast reconstruction and is thus used in trigger decisions. The latter uses particle flow input as well which requires more computing time but is also more accurate. Therefore, the energy resolution of PFJets is significantly improved with respect to CaloJets.

The reconstruction efficiency for jets at CMS is around 90 %. For central jets with a p_T above 30 GeV, it is higher than 95 % [153]. Depending on the quality of the jet identification by the PF algorithm, three working points are defined [154]. This definition also uses additional information from the calorimeters, for example hadronic activity or lepton multiplicity. The tight jet identification working point, for example, is defined such that it yields a selection efficiency above 99 % and a fake-jet rejection efficiency exceeding 98 % for all jets with $|\eta| \leq 2.7$. All jets must therefore feature less than 90 % neutral hadrons as well as electromagnetic components. Furthermore, they must consist of more than one particle and contain at least one charged hadron.

4.1.4. Jet Energy Corrections

In general, the reconstructed energy of a jet does not equal the original energy of the parton. Such a mismatch can originate, e.g., from non-uniform and non-linear calorimeter response as well as particles which belong to the jet but are not measured correctly or at all. Furthermore, pileup effects as well as noise in the detector and damaged modules affect the energy reconstruction of jets. To correct for these effects, both the detector measurement and MC simulation have to be adjusted. As analyses which are based on multi-jet final states depend on correctly reconstructed jets, two main sets of corrections are applied, namely the Jet Energy Scale (JES) and Jet Energy Resolution (JER) corrections [155]. Figure 4.4 illustrates the corrections which are applied to data and simulation. They also constitute main sources of systematic uncertainties as they directly impact the signal modeling.

Jet Energy Scale

Provided by the CMS JetMet group [156], the JES correction is a multiplicative term to the reconstructed energy of a jet in order to match the generated parton energy. It is the ratio of the reconstructed transverse momentum of the jet to the p_T of a jet clustered from the generator-level particles. By itself, the JES correction consists of four individual contributions.

First, the pileup offset correction subtracts energy contributions due to objects from other events being present in the detector at the same time. They may originate from the same bunch crossing as the analyzed event (in-time pileup) or from earlier as well as following bunch crossings (out-of-time pileup).

Second, the simulated-response correction targets non-linearities (in p_T) and non-uniformities (in η) of the detector response. Thus, this correction is calculated as a function of these kinematic quantities.

Third, the residual correction is designed to improve the agreement between data and simulation further. It is calculated based on Drell-Yan events to obtain the absolute scale as well as multi-jet events for large $p_T > 800$ GeV and residual η corrections.

Finally, an additional jet-flavor correction is applied, addressing differences in the reconstructed energy of light and heavy flavor jets. For b jets, this correction is extracted using Z+b events.

Jet Energy Resolution

As in general the p_T resolution is better in MC than in data, a JER correction is applied [157]. It introduces a smearing effect to the simulated p_T distribution of jets in order to match the actual detector resolution. This is important to avoid introducing a bias due to the jet resolution which can significantly impact steeply falling jet-energy spectra, i.e. the main observable for resonance searches.

The correction can be calculated using a similar approach as for the simulated-response part of the JES correction, based on $\gamma/Z + \text{jet}$ samples. It is designed to alter the width of the p_T spectrum without introducing an overall shift. While the relative p_T resolution σ_{p_T}/p_T can be considered Gaussian, the response is also impacted by e.g. detector effects, neutrinos passing the detector without interaction, or inactive areas. Thus, the p_T response distribution

$$\Delta = \frac{p_T^{reco} - p_T^{gen}}{p_T^{reco}}, \quad (4.4)$$

where p_T^{reco} and p_T^{gen} are the transverse momentum of a reconstructed and generated object, re-

spectively, is described by a double-sided Crystal-Ball function, featuring a Gaussian core and non-Gaussian tails.

Depending on whether or not the reconstructed jet can be matched to the generator-level jet, there are two methods to calculate the JER correction which is applied to the reconstructed jet.

If the reconstructed jet can not be matched, the stochastic smearing is applied. In this case, the four-momentum of the jet is multiplied with a factor

$$c_{\text{JER}} = 1 + N(0, \sigma_{\text{JER}}) \sqrt{\max(s_{\text{JER}}^2 - 1, 0)}, \quad (4.5)$$

where σ_{JER} is the relative p_{T} resolution as measured in simulation, $s_{\text{JER}} = \Delta_{\text{data}}/\Delta_{\text{MC}}$ is a data-to-MC scale factor and N is a random number sampled from a normal distribution which is centered at 0 and has a variance of the relative p_{T} resolution squared, σ_{JER}^2 .

If a generator-level jet can be matched to the reconstructed object, i.e. it fulfills the requirements

$$\Delta R < R_{\text{cone}}/2 \quad (4.6)$$

$$\text{and } |p_{\text{T}}^{\text{reco}} - p_{\text{T}}^{\text{gen}}| < 3 \sigma_{\text{JER}} p_{\text{T}}^{\text{reco}}, \quad (4.7)$$

with R_{cone} being the radius of the reconstructed jet, the scaling method can be used. There, the JER correction is calculated as

$$c_{\text{JER}} = 1 + (s_{\text{JER}} - 1) \frac{p_{\text{T}}^{\text{reco}} - p_{\text{T}}^{\text{gen}}}{p_{\text{T}}^{\text{reco}}} \quad (4.8)$$

using the same definitions as for the stochastic smearing method.

As for JES, also the JER calibrations are provided centrally by the CMS JetMet group.

4.2. B-Tagging

As bottom quarks are dominant decay products of e.g. Higgs bosons and top quarks, jets originating from b quarks – in the following called b jets – are of extraordinary importance for many analyses targeting physics within and beyond the Standard Model.

B hadrons have a relatively large mass of more than 5 GeV. Thus, their decay products usually also obtain a respectively high transverse momentum. Due to the rather long life time of the b hadrons, they also travel a distance from several hundred micrometers up to a few millimeters

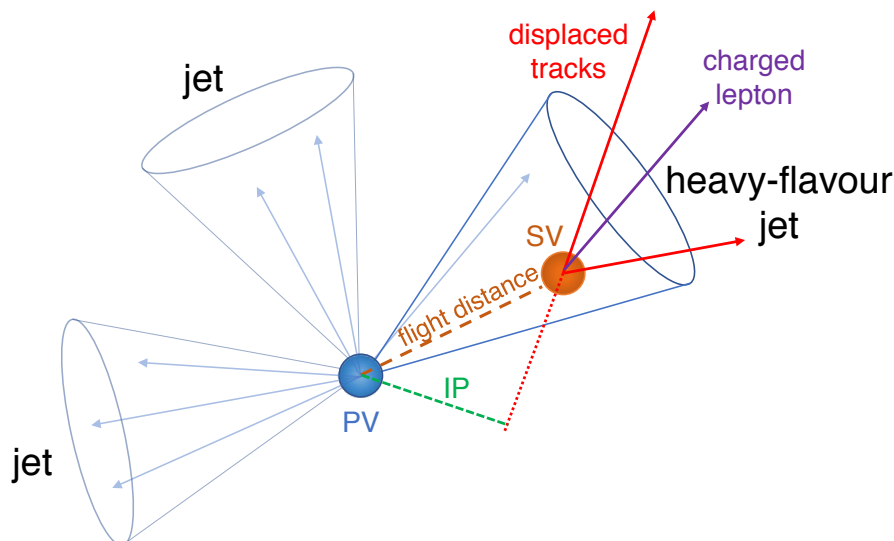


Figure 4.5.: Production of jets originating from a primary vertex (PV, blue) and a heavy-flavor jet as well as a charged lepton (purple) linked to a secondary vertex (SV, orange) with an impact parameter (IP, green) [159]

before decaying [40]. This leads to a secondary vertex being formed within the jet which results from the fragmentation and hadronization of the original b quark.

There are several decay processes which can lead to semi-leptonic modes. Muons, for example, can be produced directly from a b hadron decay or via a c hadron. The branching ratios for these processes are $\mathcal{B}(B \rightarrow \mu\nu X) \approx 11\%$ and $\mathcal{B}(B \rightarrow C \rightarrow \mu\nu X) \approx 10\%$ [158]. A schematic of how heavy-flavor jets are produced and how leptons and secondary vertices arise from them is shown in Figure 4.5.

Using these kinematic and topological properties to discriminate between jets which originate from b quarks on the one hand and light-quark and gluon jets on the other, various algorithms have been developed at CMS, the b (or flavor) taggers [159, 160].

4.2.1. Comparison of Different b -Tagging Algorithms

During the LHC Run 1, the combined secondary vertex (CSV) tagger was used [161]. While it was still partially used during Run 2, significant updates have been applied. The first b -tagging algorithm discussed in this thesis is the CSVv2 b -tagger, which is an update of the CSV algorithm and used for the main HLT path of this analysis. As the CSV algorithm, also the CSVv2 b -tagger is based on a multivariate analysis of the input observables. Second, the DeepCSV algorithm, which combines the CSV approach with machine learning is described.

Third, the DeepJet algorithm [162, 163] is the most recent of all mentioned b-taggers and it is based on a deep neural network. Unlike the previous b-taggers, which are based on a binary classification process, the DeepJet algorithm is a multi-class classifier, targeting different jet flavors simultaneously. This algorithm is used for the offline selection of events in the analysis presented here.

Commonly used among all algorithms used at CMS are the working points which are defined according to the mis-tag rate, i.e. how many light-flavor jets are wrongly classified as b jets. Three of these working points are set for jets with transverse momenta above 30 GeV and $|\eta| < 2.4$, namely loose, medium and tight with mis-tag rates of 10 %, 1 % and 0.1 %, respectively [164]. Each working point is given in terms of the b-tagging discriminant of the respective algorithm which is a dimensionless number describing the probability that the investigated jet originated from a b quark.

CSVv2 and DeepCSV

Both the CSVv2 and the DeepCSV b-tagging algorithms are based on the Inclusive Vertex Finder (IVF [165]). This algorithm identifies primary and secondary vertices based on the set of all reconstructed tracks in the event. These tracks are required to leave at least 8 hits in the silicon tracking system and to have a p_T larger than 0.8 GeV as well as an impact parameter (IP) smaller than 0.3 cm. Candidates for secondary vertices are considered if they have an IP above $50 \mu\text{m}$. Tracks are assigned to these vertex seeds and the adaptive vertex fitter is run. In this iterative procedure, the most likely secondary vertex is found by removing the seeds with lowest compatibility of tracks with the vertex candidates, which is described by a χ^2 fit. If good agreement of a track to a vertex seed is found, the track is removed from the remaining part of the vertex fitting to avoid assigning one track to multiple vertex candidates. To improve the exclusion of secondary vertices from other sources than b-hadron decays, candidates are rejected as well, if the invariant mass of tracks assigned to them matches the mass of the K_S^0 within a window of 30 MeV.

As b-tagging features a large exclusion power for events which are not of interest for analyses targeting b quark final states, a simplified version of the CSVv2 algorithm is also included in the HLT. In this context, also a simpler and faster vertex finding algorithm, the fast primary vertex finding (FPVF) algorithm, is used to project tracks which are compatible with a jet onto the z axis in order to obtain a PV candidate. Using simulated $t\bar{t}$ events, these candidates are found to have a resolution in the order of millimeters for an average PU of 35. With additional

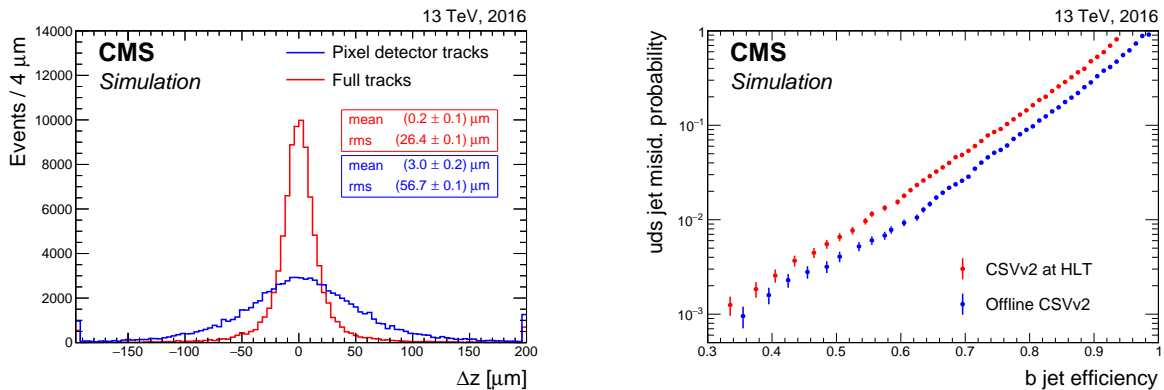


Figure 4.6.: Residuals on the position of primary vertices using either information from the pixel detector alone or the full tracking system (left, blue and red curve, respectively) and performance of the CSVv2 algorithm in the slimmed online version and the complete offline version (right, red and blue curve, respectively) [159]. Both comparisons are based on the phase-0 pixel detector which was used in 2016.

information from the strip tracking detector as well as the calorimeters, tracks and vertex candidates are refitted with the more accurate IVF. Including information from the strip tracking detector in addition to the measurements in the pixel detector already leads to a significantly better reconstruction of primary vertices. This can be seen in the distribution of residuals which is shown in Figure 4.6. Furthermore, Figure 4.6 illustrates the improved performance of the complete offline CSVv2 algorithm over the slimmed HLT version.

Including a machine learning technique, the CSVv2 algorithm was further improved. The DeepCSV algorithm is based on the same inputs as the CSVv2 but it uses more track-based variables from up to six tracks. These variables contain information on how much displaced tracks and one SV candidate are from the PV, the transverse momentum of the jets as well as the number of charged particles in each jet. For the DeepCSV training process, jets from the respective training data set are randomly selected, while ensuring that similar p_T and η distributions are obtained for all jet flavors. To speed up the training, all input variables are preprocessed in such a way that they are centered around zero and have a RMS value of one [159]. The improvement of this machine-learning based algorithm over the CSVv2 can be seen in Figure 4.7. Using the same working points of 0.1 %, 1 %, and 10 % mis-tag rate for jets with transverse momenta above 30 GeV and $|\eta| < 2.4$, the DeepCSV provides a larger b-jet efficiency, making it the advantageous choice for analyses.

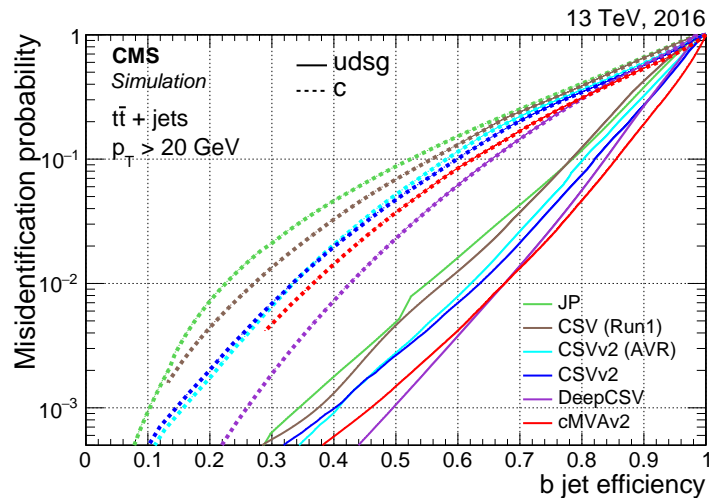


Figure 4.7.: Comparison of CSVv2 and DeepCSV b tagging algorithms (dark blue and purple lines) for jets with $p_T > 20$ GeV [159]. The Jet Probability (JP, light green lines) and CSV (olive lines) algorithms are not used anymore, the cMVA2 (red lines) algorithm is not discussed here.

DeepJet

As a further improvement over the DeepCSV algorithm, the DeepJet tagger is fully based on machine learning. While the formerly used algorithms were based on fewer, yet well identified high-level features of jet constituents, the DeepJet algorithm is based on including as many individual low-level objects as possible. This includes, among others, the track multiplicity of the jet, the number of secondary vertices as well as the mass of hadrons and the number of neutral particles in the jet. The DeepJet algorithm is also designed to find additional objects like, for example, highly energetic tracks which might not have been assigned to the jet originally. Hence, the overall reconstruction of the jet is improved, allowing for a more precise classification. Furthermore, the DeepJet tagger is not only dedicated to discriminating b jets from lighter flavors but it is designed to identify the flavor of the jet directly. Its training is based on simulated QCD and $t\bar{t}$ events and it is much more time consuming than for the previously used DeepCSV algorithm with about 24 hours instead of around 30 minutes [162]. This effort leads to a significantly better light-jet rejection rate while keeping the same b-jet efficiency. For jets with a larger p_T , this effect is even more pronounced. A comparison of the misidentification rate vs. the b-jet efficiency for DeepJet and DeepCSV is shown in Figure 4.7 for simulated events with two different ranges of jet p_T . Table 4.1 shows an overall comparison for the three flavor-identification algorithms discussed here, including the efficiencies for b, c, and light jet selection for a simulated data set of $t\bar{t}$ events with jets exceeding a transverse momentum of

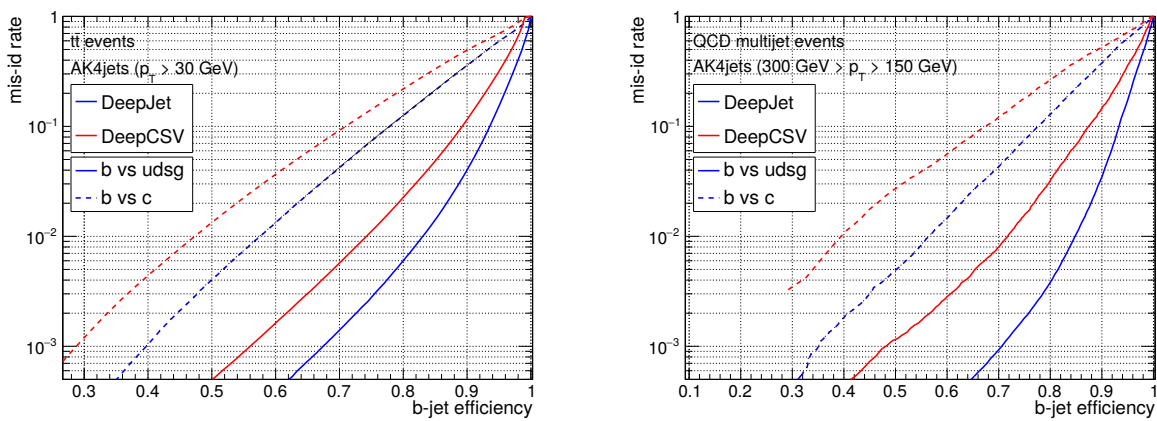


Figure 4.8.: Comparison of misidentification rates of the DeepCSV and DeepJet algorithms [163]. In general (left, jet p_T above 30 GeV) but even more significantly for larger jet p_T (right, jet p_T between 150 and 300 GeV), the DeepJet algorithm outperforms the DeepCSV tagger.

30 GeV.

Algorithm	$\epsilon_b(\%)$	$\epsilon_c(\%)$	$\epsilon_{light}(\%)$
CSVv2 (T)	49	2.2	0.1
CSVv2 (M)	69	12	0.9
CSVv2 (L)	83	37	8.9
DeepCSV (T)	51	2.1	0.1
DeepCSV (M)	68	11	0.9
DeepCSV (L)	86	32	10
DeepJet (T)	57	2.0	0.1
DeepJet (M)	76	12	1.1
DeepJet (L)	92	48	12

Table 4.1.: Efficiencies of the CSVv2, DeepCSV, and DeepJet algorithms for b, c, and light jets for the tight (T), medium (M), and loose (L) working points for jets with $p_T > 30$ GeV [166, 167]

5. Search for Heavy, Neutral Higgs Bosons Decaying into a Pair of b Quarks

5.1. Previous Results

5.1.1. LEP and TeVatron

First powerful attempts of searching for BSM Higgs bosons were made at the final configuration of the Large Electron-Positron Collider LEP, LEP-II, at CERN [168]. Overall, the LEP operated from 1989 until 2000 and LEP-II featured a center-of-mass energy of $\sqrt{s} = 209$ GeV in 1999 and 2000, making it the most powerful lepton accelerator built to that time. LEP collisions were investigated by the four experiments L3, ALEPH, OPAL, and DELPHI and their results concerning BSM Higgs bosons were combined in the end [169].

The most important production mechanisms for heavy, neutral Higgs bosons at LEP are Higgsstrahlung (VH production mode, $e^+e^- \rightarrow Z^0 \rightarrow ZH/h$) and pair production ($e^+e^- \rightarrow Z^0 \rightarrow AH/h$). Their respective Feynman diagrams are shown in Figure 5.1. The searches were focused on MSSM scenarios, among others the m_h^{max} scenario. As discussed in Section 2.2.1, these models can be described by two parameters at tree-level, the mass of the CP-odd neutral Higgs boson, m_A , and the ratio of the vacuum expectation values of the two Higgs doublets, $\tan\beta$. In these scenarios, at LEP energies, the Higgsstrahlung production mechanism dominates at low values of $\tan\beta$, while the pair production is most important at larger $\tan\beta$.

Several benchmark scenarios were tested, some of which were designed to conserve CP, while others included CP violation. In neither case, a significant deviation from the SM was observed. Therefore, limits were calculated in terms of the mass of a neutral Higgs boson as well as $\tan\beta$. Values of $m_h < 92.8$ GeV, $m_A < 93.4$ GeV, and $0.7 < \tan\beta < 2.0$ were excluded at 95 % confidence level.

5. Search for Heavy, Neutral Higgs Bosons Decaying into a Pair of b Quarks



Figure 5.1.: Main BSM Higgs boson production modes at LEP: Higgsstrahlung (left) and pair production (right). Diagrams drawn with [66].

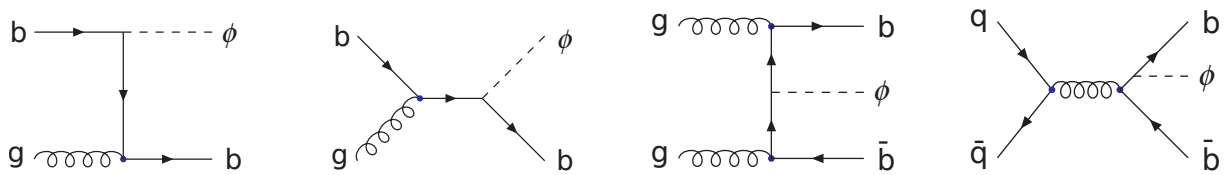


Figure 5.2.: Production processes for a heavy, neutral Higgs boson in association with b quarks at TeVatron and LHC with one (left) or two (right) additional bottom quarks in the final state [173]. While the two diagrams on the left are only possible in the 5-flavor-scheme, i.e. including b quarks as sea-quarks in the proton, the others are also accessible in the 4-flavor-scheme [174]. Due to the increased center-of-mass energy and because instead of protons and anti-protons only protons collide at the LHC, different production modes dominate at the two colliders. Diagrams drawn with [66].

Also at the TeVatron collider [170], located at Fermilab, heavy, neutral Higgs bosons were searched for in the $b\bar{b}$ decay channel. The TeVatron collided protons and anti-protons at a center-of-mass energy of $\sqrt{s} = 1.96$ TeV and the data was collected and the analyses were performed by the CDF and D0 collaborations [171–173]. A total integrated luminosity of 5.2 fb^{-1} and 2.6 fb^{-1} had been collected at D0 and CDF, respectively. Because of the significant background due to QCD multi-jet production, as it is expected to be present in hadron collisions, any search with a fully hadronic final state is extremely challenging. Thus, the b -associated production mode was chosen for the analyses. The respective Feynman diagrams are shown in Figure 5.2 for Higgs boson production in association with one or two associated b quarks. Not only does this production channel provide the possibility of additional background rejection based on the required number of b jets, but it also exploits enhanced production cross-sections in certain BSM models, as explained in Section 2.2.

Limits on the cross-section times branching ratio $\sigma(gb \rightarrow b\phi) \times \mathcal{B}(\phi \rightarrow b\bar{b})$ (cf. Figure 5.2 left) were calculated from the combined data of the CDF and D0 experiments. These were further interpreted in terms of a specific model, described by the m_h^{max} benchmark scenario.

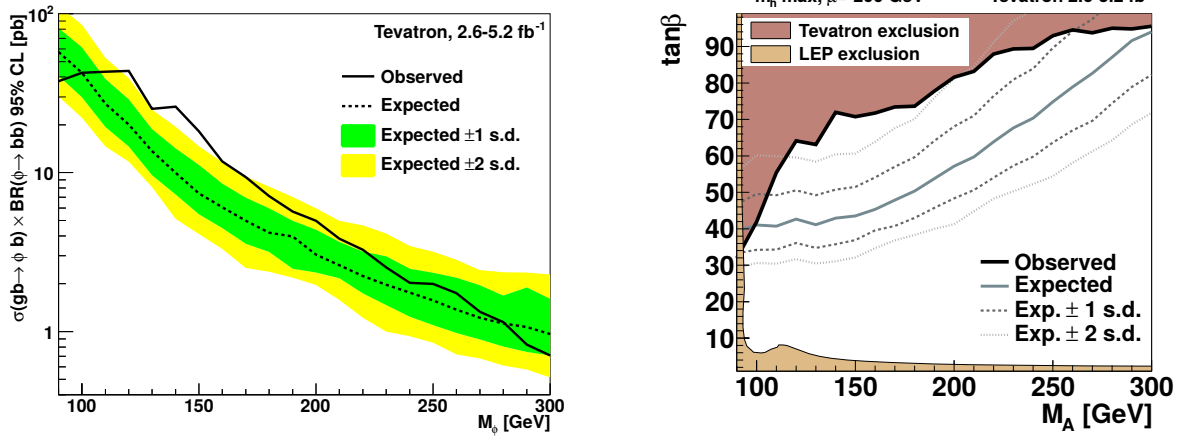


Figure 5.3.: Limits on cross-section times branching ratio (left) of the BSM Higgs boson search in the $b\bar{b}$ decay channel at TeVatron as well as interpretation in terms of the m_h^{max} scenario (right, with a comparison to LEP results in light brown). The excesses at 120 and 140 GeV, corresponding to deviations from the expectation of 2.5σ and 2.6σ , respectively, are not statistically significant. Taken from [173].

Both results are shown in Figure 5.3. Mild excesses were observed with deviations of 2.5σ and 2.6σ , respectively, from the background-only hypothesis in the cross-section times branching ratio limits at masses of $m_\phi = 120 \text{ GeV}$ and $m_\phi = 140 \text{ GeV}$. The model dependent limits were found to complement the LEP results well.

5.1.2. LHC Run 1

After the discovery of a Higgs boson at 125 GeV, the focus of searches for additional Higgs bosons changed slightly. Mainly, the benchmark scenarios had to be adapted in order to agree with the observation and analyses started investigating possible extensions of the Higgs sector instead of searching any kind of Higgs boson.

Searches for Higgs bosons of an extended Higgs sector were performed during LHC Run 1 similar to previous approaches at TeVatron, exploiting the properties of b-associated production. In contrast to the proton anti-proton collider TeVatron, however, the LHC beams only consist of protons which affects the cross-sections of different Higgs boson production modes. For example, the main production mechanism at the LHC for the 125 GeV Higgs boson is ggF. Using data from 2011 and 2012, with center-of-mass energies of $\sqrt{s} = 7 \text{ TeV}$ and $\sqrt{s} = 8 \text{ TeV}$, respectively, corresponding to a combined integrated luminosity of 24.6 fb^{-1} , a new analysis approach was included at CMS [175, 176] by introducing a semi-leptonic channel in the analysis

of the data collected in 2011. In this final state, a non-isolated muon is required to be identified in association with one of the b jets. The complementary final state is called all-hadronic, as there are no additional leptons required. Both approaches are designed to look for an excess in the invariant mass spectrum of the two b jets leading in transverse momentum. The results of both individual channels are combined at the end to obtain the overall limits.

The increased integrated luminosity and center-of-mass energy allowed for a significantly enlarged area of the $(m_A, \tan \beta)$ plane to be assessed with the LHC Run 1 results. Additionally, a dedicated trigger was used in the CMS analyses, identifying b jets already during the data-taking process, i.e. online. As in previous studies, limits were calculated on the production cross-section times branching ratio, depending on the Higgs boson mass. They are shown for the 8 TeV analysis in Figure 5.4 (top left). These limits were interpreted in terms of specific benchmark scenarios. As can be seen in Figure 5.4 (top right) for the 7 TeV analysis in the m_h^{max} scenario, the range in both m_A and $\tan \beta$ is significantly increased with respect to LEP and TeVatron analyses. The m_h^{max} scenario is explained in Section 2.2.1 and was used in the searches at LEP and TeVatron. It was almost completely excluded by the observation of the 125 GeV boson as it was designed to yield a maximized Higgs boson mass. Thus, it was replaced by the modified m_h^{mod} scenario. The difference in their respective behavior can be seen in Figure 5.4 (bottom). While only a narrow band, mainly at low $\tan \beta$, is still allowed in the m_h^{max} scenario, the m_h^{mod+} scenario allows for a much wider combination of m_A and $\tan \beta$. This is due to the removal of somewhat artificial constraints on internal parameters in the m_h^{mod+} scenario with respect to the m_h^{max} scenario which do not agree with the observation.

5.1.3. LHC Run 2

Based on data collected during the LHC Run 2, efforts in searching for heavy, neutral Higgs bosons decaying into b quarks [34, 177, 178] are continued at CMS, and ATLAS also introduced a similar analysis [174]. All of these studies are based on the main production processes shown in Figure 5.2, which are the same as for the TeVatron analyses. However, as discussed above, their respective cross-sections are different at the two colliders.

Similar to the CMS analyses during Run 1, b -associated production is exploited in all three of these searches. In the final state, at least three b quarks are required. In addition, a semi-leptonic channel is included again [34] in the CMS analysis of data collected in 2017, requiring a non-isolated muon to be found in association with one of the two b jets leading in p_T . This additional requirement is already imposed at trigger-level. Based on the thusly reduced rate, a lower cut on the jet p_T can be placed, leading to increased sensitivity at masses as low as 125 GeV. The

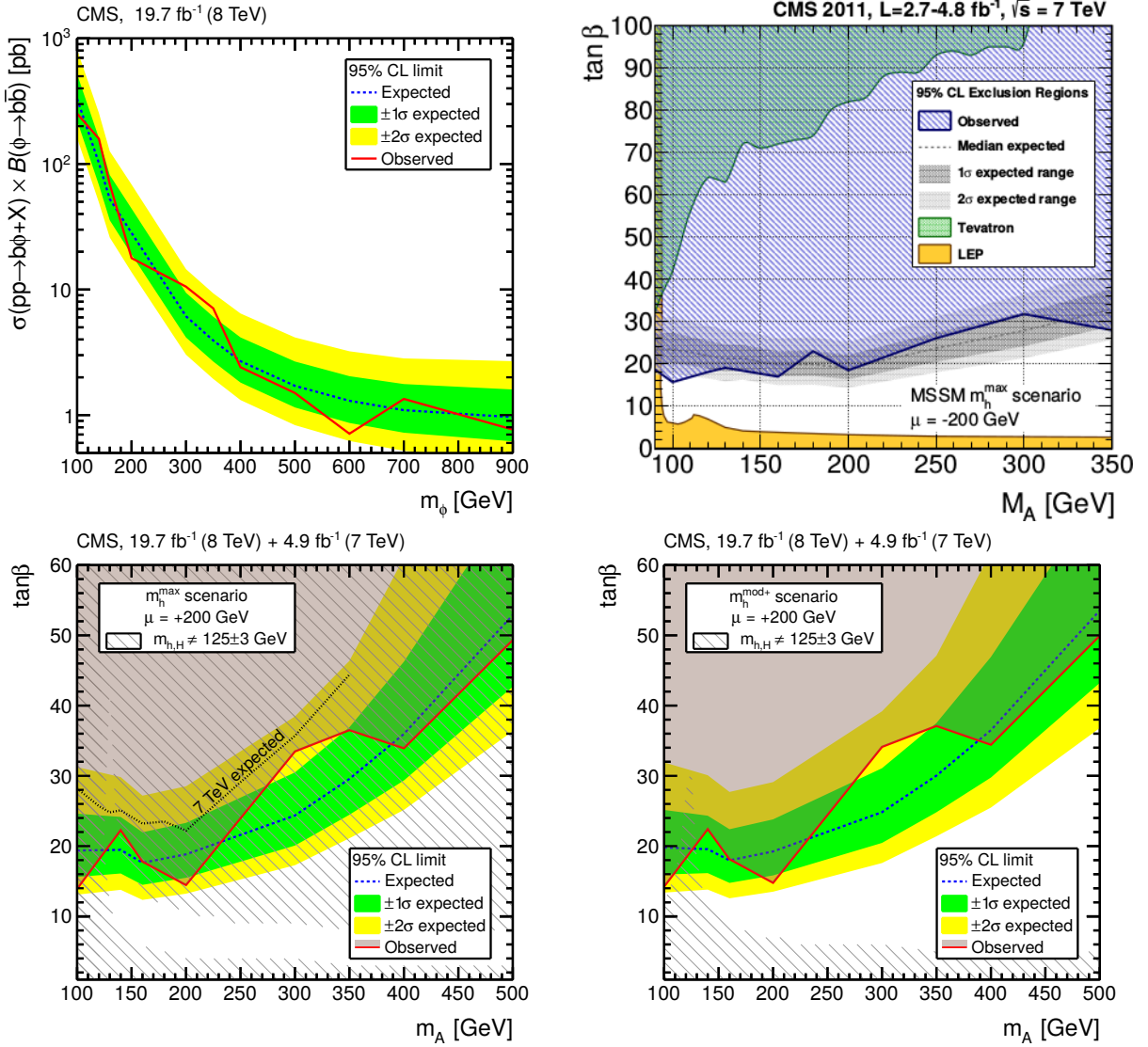


Figure 5.4.: Model independent limits of the LHC Run 1 analysis at 8 TeV (top left [176]) together with model interpretations in the m_h^{max} and m_h^{mod+} scenarios. In the top right plot, the LHC 7 TeV analysis [175] is compared to the LEP and Tevatron results. The used m_h^{max} scenario was later, i.e. after the Higgs boson discovery at 125 GeV, mostly excluded, as can be seen in the bottom left plot [176]. This scenario was then modified and results in terms of the newly developed m_h^{mod+} scenario are shown in the bottom right plot [176].

CMS analysis performed based on data collected in 2016 did not have this requirement but also did not reject these events. Therefore, relatively high p_T cuts were placed in order to keep the trigger rate under control.

Note that in general, also a four- b -jet final state could be identified. However, practical considerations lead to the choice of requiring only three well-identified b jets. First, it was observed that despite a more powerful background rejection, the signal efficiency was even more significantly reduced. Second, it can happen that not all jets are found within the experimental acceptance of the detector or a jet is misidentified as a light-flavor jet or any other object.

The two CMS analyses are based on a parametric description of a control region (CR) which is then applied as well to the signal region (SR). However, the ATLAS approach is slightly different. It is based on a simultaneous fit of control regions and signal regions with a certain jet multiplicity and it is required that the respective shapes only differ by a second-order polynomial. In all three analyses, limits on the production cross-section times branching ratio are extracted and then interpreted in terms of specific benchmark scenarios. In addition to the m_h^{mod+} scenario, all three analyses also interpret their respective results in terms of the hMSSM scenario. Moreover, some of the 2HDM benchmark scenarios discussed in Section 2.2.2, specifically the type-II and flipped scenarios, are also included. A summary of results is shown in Figure 5.5.

5.2. Signal and Background Processes

This analysis is focused on the search for neutral Higgs bosons, A and H , produced in association with additional b quarks and decaying into a pair of b quarks. As discussed in Section 2.2, these particular production and decay modes are favored by several models.

Depending on considerations regarding the bottom-quark mass, various processes can contribute to the signal cross-section as well as to the background. Two main methods are used in this context [179, 180]. The four-flavor scheme (4FS) is based on the assumption that the mass of the b quark largely exceeds the proton mass. Therefore, the b -quark contributions to the proton structure are neglected. This implies that mainly gluons and light-flavor quarks form the initial state, as shown in the two diagrams on the right of Figure 5.2. However, if the energy scale of the collision, Q , is much larger than the b -quark mass, the b quark can be treated as if it was massless in the leading-order calculations. Thus, it contributes to the proton structure and initial states with bottom quarks are possible. Hence, this method is called five-flavor scheme (5FS). Two examples of Higgs boson production based on the 5FS are shown in the two

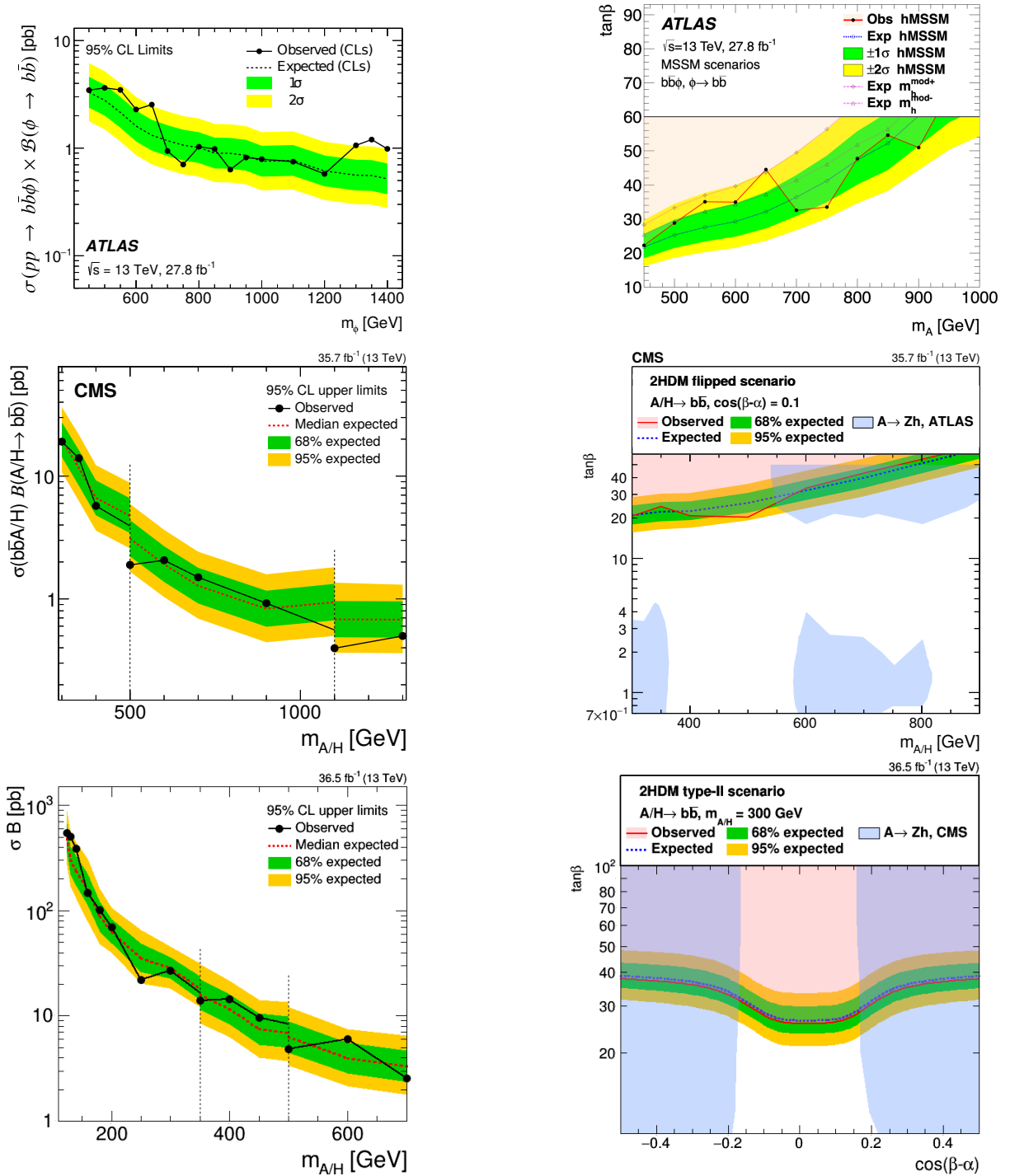


Figure 5.5.: Limits on the production cross-section times branching fraction (left) and interpretations in terms of specific benchmark scenarios (right) for LHC Run 2 searches. The ATLAS results (top [174]) are based on the 2015 data set and a part of the 2016 data set, while the 2016 CMS analysis (center [178]) is based on the 2016 data set. The semi-leptonic selection was re-introduced at CMS with the analysis of the 2017 data set (bottom [34]). The MSSM scenarios m_h^{mod} and hMSSM (top) are used as well as 2HDM benchmark scenarios (center and bottom; in the $(m_A, \tan\beta)$ and $(\cos(\beta-\alpha), \tan\beta)$ planes and for flipped and type-II models, respectively). Corresponding plots for this analysis are presented in Chapter 6. 75

diagrams on the left of Figure 5.2.

To obtain a result which is not biased by either the 4FS or the 5FS assumptions, inclusive production cross-sections are calculated using empirical approaches, combining the predictions of both schemes. For the m_h^{mod+} and hMSSM benchmark scenarios, production cross-sections are calculated based on the Santander matching scheme [179], while the cross-sections for the m_h^{125} benchmark scenarios are obtained by use of the FONLL matching scheme [181, 182]. This method was tested against the NLO+NNLLpart+ybyt scheme [183, 184] and found to yield precisely the same results. Both methods can be used for calculation at LO and NLO alike.

In the Santander matching scheme, the overall cross-section is defined based on a weighted mean, in which the weight is taking into account the mass of the 125 GeV Higgs boson:

$$\sigma_{\text{Santander}} = \frac{\sigma_{4\text{FS}} + w\sigma_{5\text{FS}}}{1 + w}, \quad \text{with} \quad w = \ln \frac{m_h}{m_b} - 2, \quad (5.1)$$

where $\sigma_{4\text{FS}}$ and $\sigma_{5\text{FS}}$ are the results based on 4FS and 5FS alone.

The FONLL scheme matches the 4FS and 5FS predictions to each other. In this method, the inclusive cross-section is defined as

$$\sigma_{\text{FONLL}} = \sigma_{4\text{FS}} + \sigma_{5\text{FS}} - \sigma_{\text{overlap}}, \quad (5.2)$$

where σ_{overlap} accounts for the overlap region, avoiding double-counting. Extending the 5FS calculations, logarithms of the form $\log(Q^2/m_b^2)$, which were summed in orders of α_S , are replaced by their counterparts from the calculations based on massive b quarks. This is done up to the order of α_S to which the results are known assuming massive b quarks. The overlap region is assessed from both sides: either the 5FS calculations are extended up to a certain order of α_S or the massless limit of the massive calculations is considered.

Independent of the initial state, the characteristic final state of the $b\bar{b}\phi(\phi \rightarrow b\bar{b})$ process consists of two b jets with large p_T , originating from the Higgs boson decay, as well as one or two additional jets from the b quarks which are produced in association with the Higgs boson. Due to the reasons discussed in Section 5.1.3 for previous analyses, at least three b -tagged jets are required for an event to be selected as a signal candidate.

Dominant background contributions originate from SM processes which feature the same signature of three b -tagged jets and QCD multi-jet events in which at least one of the light-flavor jets is misidentified as a b jet. Respective example diagrams are shown in Figure 5.6 on the left side.

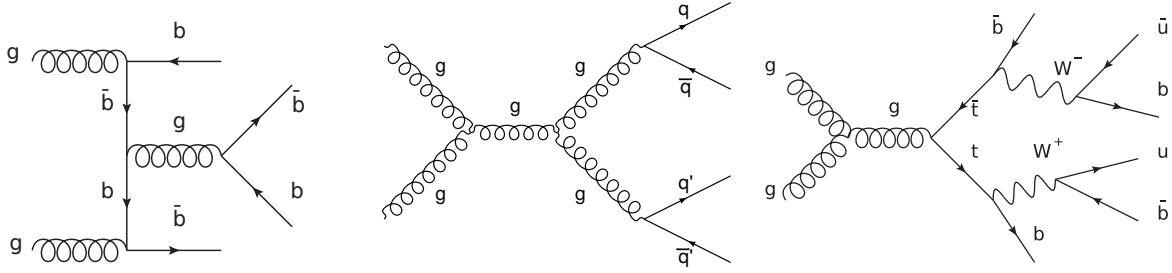


Figure 5.6.: Feynman diagrams of main background processes: SM production of four b jets (left), QCD multi-jet events (center), and $t\bar{t}$ (right). Diagrams drawn with [66].

Another source of background are $t\bar{t} + jets$ events. Based on the almost exclusive decay of top quarks into a bottom quark and a W^\pm boson, such a process usually features at least two b quarks. If one of the jets originating from a hadronic W^\pm boson decay either is a b jet or is misidentified as one, the event also contributes to the set of signal candidates. A corresponding example diagram is shown in Figure 5.6 on the right.

In the work presented here, a data-driven background estimation is used, considering all background contributions combined. Thus, individual background contributions will not be further distinguished or treated separately.

5.3. Analysis Strategy

The analysis presented here is starting from the inclusive analysis based on CMS data taken in 2016 [178], where no distinction between fully hadronic and semi-leptonic channels was made, and the semi-leptonic 2017 analysis [34]. It is based on data taken in 2017 by the CMS experiment with a center-of-mass energy of 13 TeV, equaling an integrated luminosity of 36.02 fb^{-1} . Events which are already included in the semi-leptonic analysis are explicitly excluded. Thus, the two analyses complement each other with the fully hadronic channel having better reach in the high-mass range, while the semi-leptonic channel can reach lower masses.

As discussed in Section 5.2, signal events in this analysis feature a final state consisting entirely of jets. The two jets originating from the Higgs boson decay are expected to be leading in p_T . Therefore, the signal is expected to manifest in the form of an excess in the invariant-mass distribution of these two jets, m_{12} , which is selected as the main analysis observable. The signal region (SR) consists of events in which the leading three jets are b-tagged (bbb) using the medium b-tagging working point (cf. Section 4.2.1), while in the control region (CR), the third leading jet is explicitly required not to be b-tagged ($bbnb$), i.e. the b-tagging discriminant must be below the loose working point. All other steps of the selection are identical for CR and SR.

Since one of the jets from the associated b quarks is explicitly required not to be b -tagged in the CR, this region is signal-depleted. However, based on the identical kinematic selection and results from previous analyses, it is assumed that the shape of the m_{12} distribution is extremely similar in both CR and SR, which is also investigated in this analysis by the use of simulated data sets. Thus, the control region is particularly important for the background estimation as it provides an unbiased insight to the main observable. By deploying an entirely data-driven background estimation, all processes contributing to the background are treated in a combined way. Furthermore, a blinding policy is enforced. This means that the analysis methods are fully developed and the approach is validated based on signal-depleted data regions and Monte-Carlo (MC) data sets, without considering the m_{12} distribution in the SR. In addition to the CR, a second signal-depleted region is defined, the validation region (VR). This region features events in which the b -tagging discriminant of the third leading jet lies in between the CR and SR requirements. Therefore, it is also called bsb , where sb refers to “semi- b -tagged”.

Although the approach is similar to the complementary, semi-leptonic analysis of the 2017 data and the previous, inclusive analysis of the 2016 data in certain aspects, several substantial changes are implemented. A key ingredient to the analysis strategy is the background estimation in the signal region based on the control region mentioned above. The respective b -jet selection relies on a deep-neural-network-based b -tagging algorithm (“DeepJet”), significantly improving the signal-to-background selection ratio with respect to previous analyses. In this analysis, the CR is parametrized and the SR background estimation is based directly on this CR description, multiplied with a relatively simple transfer factor (TF). The transfer-factor function is slowly varying depending on the observable m_{12} and its functional form is motivated by Monte Carlo studies. This technique is validated using the VR which is well-suited as it is signal-depleted and independent of both CR and SR. Finally, CR and SR are fitted simultaneously and in this final signal-plus-background likelihood fit, the production cross-section is evaluated. Since the CR features significantly larger statistics, the respective parameters of the background description in the SR are expected to be well constrained in the simultaneous fit. The TF parameters are exclusively determined based on the SR data, effectively decreasing the number of required background description parameters in the SR significantly with respect to previous analyses. Furthermore, the simultaneous fit ensures that the uncertainties of all CR parameters are rigorously taken into account. Note that the ATLAS analysis [174] exploited a similar approach with a strictly linear TF. Both signal and background MC data sets (see Section 5.4) are based on next-to-leading-order calculations. The m_{12} distributions which are extracted from the simulated signal data sets are included as histograms, also referred to as templates, in order to avoid systematic uncertainties due to a parametrization.

Era	Run range	\mathcal{L}_{int} (main trigger) [pb^{-1}]	\mathcal{L}_{int} (control trigger) [pb^{-1}]
2017C	299368 – 302029	9581	0.233
2017D	302031 – 302663	4224	0.357
2017E	303824 – 304797	8753	0.278
2017F	305040 – 306460	13462	0.260
Sum	299368 – 306460	36020	1.128

Table 5.1.: Recorded integrated luminosity for the analysis main and control triggers in the 2017 data-taking period, which is divided into four blocks of runs (eras) with relatively stable data-taking conditions

5.4. Data and Monte-Carlo Samples

For the work presented here, data from the CMS experiment is used, collected during the 2017 data-taking period at a center-of-mass energy of $\sqrt{s} = 13$ TeV. This period is divided into several blocks of runs, called eras, in which the conditions of data-taking are relatively constant. The eras used for this analysis are listed in Table 5.1 together with the runs they contain and the respective integrated luminosity. For the calculation of the latter, only runs which are officially certified by CMS to be used in analyses are taken into account. Moreover, the integrated luminosity is calculated with respect to a specific trigger path. Due to, e.g., modifications, pre-scaling because of excessive rates, or periods in which a trigger path was inactive, this reference is crucial. Thus, in Table 5.1, the integrated luminosity is given based not only on the certification but also with respect to the trigger which was developed specifically for this analysis and which is described in detail in Section 5.5.

In the process of calculating the kinematic trigger turn-on (see Section 5.5.2), different data sets are used than for the rest of the analysis. While for the main part of the analysis, b-tags are already required at the online-level, the kinematic trigger turn-on can be assessed with a much wider set of jets. Thus, events are included in this calculation, if they feature at least one jet above a certain p_T threshold. The respective integrated luminosity recorded by this reference trigger is also shown in Table 5.1. Because of the loose selection criterion of the reference trigger, this path is largely pre-scaled (cf. Section 3.3) in order to keep its rate within the bandwidth limits. Therefore, the recorded integrated luminosity is much lower than for the analysis main trigger.

The signal samples used in this analysis are based on next-to-leading-order calculations and are summarized in Table 5.2. The computations are performed by the MadGraph5 generator [134] which is able to calculate hard-scattering events at matrix-element level with up to four additional partons produced in initial- and final-state radiation processes. To simulate the parton

5. Search for Heavy, Neutral Higgs Bosons Decaying into a Pair of b Quarks

Event type	Generator	Fraction of neg. weights	Mass point	N_{events}
NLO: $\bar{b}A/H \rightarrow b\bar{b}$	MadGraph5	36 %	300 GeV	5147086
			350 GeV	9177000
			400 GeV	9936000
			450 GeV	9857000
			500 GeV	8385000
			600 GeV	10000000
			700 GeV	9144903
			800 GeV	9481420
			900 GeV	9800693
			1000 GeV	9686272
			1200 GeV	9370000
			1400 GeV	9640027
			1600 GeV	9853720

Table 5.2.: Signal samples for indicated hypothetical Higgs boson mass and number of events. Since the negative weights have to be considered in all steps of the analysis process, selection efficiencies and integrated luminosities are given with respect to the effective number of events which includes the fraction of negative events as listed here.

showers, MadGraph5 is interfaced with PYTHIA8 [133]. Using the central MC production grid provided by the CMS collaboration, samples for 13 mass points have been generated, each containing about 10 million events. It has to be noted, however, that about 40 % of these events come with a negative event weight, accounting for interference terms of the NLO computations. In the context of this analysis, the sign of the event weight is therefore considered.

To investigate the expected shape of the transfer factor and for the trigger scale factor calculations, QCD MC data sets are used, which are listed in Table 5.3. They describe the dominant overall background contributions and, thus, they are a well-suited tool to assess the shape of mass spectra in both CR and SR. However, due to the relatively exclusive requirement of two or three b-tags for CR and SR, respectively, the inclusive QCD samples provide too little statistics. Therefore, data sets with enhanced b-quark content are used, which are based on NLO QCD calculations. They are binned in H_T , i.e. the transverse hadronic activity of an event. In the context of these data sets, it reflects the sum of the transverse momenta of all jets in the event exceeding 20 GeV. For each H_T bin, two samples have to be generated. One is designed to enrich the content of b quarks at matrix-element level, while the other creates this enrichment at parton-shower level. This distinction is necessary since at matrix-element level, a lower ΔR

Generator	Type	H_T [GeV]	$N_{\text{events}}^{\text{eff}}$	σ [pb]	\mathcal{L}_{int} [1/pb]
MadGraph5	QCD	200 – 300	58689666	1547000	38
		300 – 500	60316577	322600	187
		500 – 700	56207744	29980	1875
		700 – 1000	47724800	6334	7535
		1000 – 1500	16595628	1088	15523
		1500 – 2000	11634434	99.11	117389
		2000 – Inf	5941306	20.23	293688
MadGraph5	QCD, b-enriched at matrix-element level	200 – 300	80430	9952918	123.75
		300 – 500	16620	3547725	213.46
		500 – 700	1487	2010208	1351.9
		700 – 1000	296.5	891925	3008.2
		1000 – 1500	46.61	267989	5749.6
		1500 – 2000	3.72	61250	16465
		2000 – Inf	0.6462	302499	468120
MadGraph5	QCD, b-enriched at parton-shower level	200 – 300	111800	8611681	77.03
		300 – 500	28070	5529691	197.00
		500 – 700	3082	7621842	2473.0
		700 – 1000	724.2	1816716	2508.6
		1000 – 1500	138.2	1261997	9131.7
		1500 – 2000	13.61	224332	16482
		2000 – Inf	2.909	214088	73595

Table 5.3.: Background samples with respective effective number of events, which includes negative weights, cross-section, and integrated luminosity. For the b-enriched data sets, the type on enrichment given, i.e. whether it is done at matrix-element or parton-shower level.

between the b quarks is implicitly applied to avoid divergence of the process. The three sets of QCD MC samples listed in Table 5.3 are mutually exclusive since for the general, i.e. not enriched, QCD data sets, a filter for b hadrons is applied at parton-shower level. An effective luminosity is calculated based on Equation 3.1 and the effective number of events for each sample as explained above.

5.5. Triggers

As described in Section 3.3, the trigger system at CMS consists of two steps, the L1 and the HLT. The L1 trigger is designed to decide quickly and reduce the event rate as much as possible without rejecting events of interest. Then, at the HLT, more complex algorithms are deployed,

5. Search for Heavy, Neutral Higgs Bosons Decaying into a Pair of b Quarks

Trigger name	N_{jets}	$p_{T,\text{jet}}$ [GeV]	$ \eta _{\text{jet}}$	$\Delta\eta_{ij}$	N_{btags}	d_{CSVv2}
Main analysis trigger						
HLT_DoublePFJets100 MaxDelta1p6_ DoubleCaloBTagCSV_p33	2	100	2.3	1.6	2	0.92
Control triggers						
HLT_DoublePFJets100_ CaloBTagCSV_p33	2	100	2.3	–	1	0.92
HLT_DoublePFJets200_ CaloBTagCSV_p33	2	200	2.3	–	1	0.92
HLT_DoublePFJets350_ CaloBTagCSV_p33	2	450	2.3	–	1	0.92
HLT_PFJet60	1	60	5	–	0	–

Table 5.4.: Triggers used in the analysis. Based on the main trigger, events are selected for the search for a BSM Higgs boson. The control triggers are used to assess efficiencies of the main trigger.

i.e. simplified versions of the offline selection.

Dedicated triggers are essential to collect as many signal-like events as possible, while simultaneously rejecting the majority of background-like events as well as keeping the required amount of bandwidth under control. Therefore, significant effort is put into their development. For the BSM Higgs boson searches at CMS, various such trigger paths have been implemented and their efficiency was studied.

5.5.1. Analysis Triggers

For this analysis, a main trigger was developed, together with several control triggers to test its efficiency in various regards. All of these paths are listed in Table 5.4 together with the properties an event must provide in order to be selected.

All triggers listed in Table 5.4 represent the HLT paths, which are based on looser L1 requirements, called seeds. The respective L1 seed L1_DoubleJet100er2p3_dEta_Max1p6 for the main analysis trigger quickly reduces the overall event rate based on the requirement of two jets with a p_T of at least 100 GeV. Furthermore, these jets must lie within a pseudorapidity range of $|\eta| < 2.3$ and they must not be separated by more than $\Delta\eta_{12} = 1.6$. The cut on $|\eta|$ can be implemented without constraining signal-like events significantly as they are expected to contain rather central jets due to the large mass of the targeted Higgs bosons. Placing the $\Delta\eta$ requirement reduces the overall rate at L1 by about 15 %. It is found (see Section 5.6.2) that

signal events show a much more centralized distribution in this observable than QCD events. Thus, the rate reduction affects background events significantly more than signal candidates, improving the purity of the remaining events.

The main HLT path for this analysis requires some additional cuts, mainly based on a b-tagging requirement. In order to optimize computing efficiency, the most time-consuming steps are run last. Hence, the first part of the selection sequence requires two jets with a cone-radius parameter of 0.4, which are detected in the calorimeter and identified with the anti- k_T algorithm. These jets are corrected for pileup effects by subtracting respective energy contributions and they are all required to have a transverse momentum above 100 GeV as well as $|\eta| < 2.3$. There must be at least one pair of jets with $\Delta\eta_{12} < 1.6$. A minimum of two and a maximum of six jets passing the previous requirements is passed on to the b-tagging sequence. This sequence is based on a slimmed version of the CSVv2 b-tagging algorithm, which is applying several quality criteria on primary and secondary vertices. A b-tagging discriminant value of 0.92 or larger is required for an event to be selected, corresponding to a rate of 0.33 % with which light-flavor jets are misidentified as b jets. Thus, this requirement is between the medium and tight working points. As the final step in the trigger sequence, since it is the most computationally expensive, the trigger version of the particle flow algorithm is run, based on input from all CMS sub-detectors. Afterwards, the event must fulfill all requirements described above to be selected.

The main analysis trigger is designed such that it ensures an event rate of not more than 10 Hz. Thus, all events passing the trigger requirements can be stored. For the control triggers, a maximum of one b-tag is required. Also, there is no cut on $\Delta\eta_{ij}$. The control triggers are mainly used to provide a data-driven opportunity to evaluate the online efficiency of the main trigger. To ensure a better statistical coverage of all p_T ranges, there are three control triggers with increasing p_T thresholds and respectively decreasing pre-scale factors.

Based on the simpler algorithms used at trigger-level compared to the offline selection, it is expected that additional efficiency factors are introduced relative to the selection based on offline quantities. These effects as well as the detector response are time-dependent and are taken into account by using scale factors. They have to be evaluated in data and MC, respectively, in order to correct the simulated trigger efficiency ϵ_t accordingly. This is done in a factorized approach based on the control triggers listed in Table 5.4 for two main parts which are most affected by the usage of simpler algorithms.

First, a kinematic part of the trigger efficiency, ϵ_{kin} , is defined. The L1 decision is based on the p_T of calorimeter jets instead of the fully reconstructed PF jets. Thus, the jet energy

might not be determined entirely accurately and jets with a p_T close to the trigger threshold are mistakenly rejected or accepted due to this uncertainty. The study is performed based on a general jet trigger which does not require any b-tag.

Second, the behavior of the b-tag selection, which is reflected by the corresponding efficiency ϵ_{btag} , is investigated. This part of the trigger efficiency is evaluated based on the single-b-tag control triggers.

5.5.2. Jet Kinematic Trigger Efficiency

The main analysis trigger is configured such that it selects two jets based on some of their kinematic properties. Therefore, the kinematic trigger efficiency ϵ_{kin} is evaluated in terms of the p_T and η values of the leading two jets,

$$\epsilon_{\text{kin}} = \epsilon(p_T^1, p_T^2, \eta^1, \eta^2), \quad (5.3)$$

where the indexes 1 and 2 reflect the two jets under investigation. In order to obtain a reliable, unbiased result, this must be done based on an independent data set, recorded by a much simpler, more inclusive trigger. This trigger has to be fully efficient at $p_T^{\text{jet}} = 100$ GeV and $|\eta|^{\text{jet}} < 2.3$, which are the requirements of the main trigger. Therefore, the jet trigger HLT_PFJet60 is chosen. It has been found to reach full efficiency around $p_T^{\text{jet}} = 85$ GeV and it accepts jets with a pseudorapidity well above the analysis selection. Furthermore, it only requires one single jet to be present in the event. Since this trigger is very inclusive, its rate would be very high without pre-scaling. Therefore, the trigger is significantly pre-scaled in order to keep its rate at a level suitable for the available bandwidth and storage capacity. Thus, this trigger is not an appropriate choice for the main analysis despite containing a similar, more inclusive set of events. In addition to the independent trigger, also the primary data set (PD), defined at the CMS experiment as an inclusive subset of events with a certain main property, is chosen differently than in the main analysis. While the PD used for the Higgs boson search already requires a b-tag, the sample used for this particular study contains any events which feature at least one jet. Similarly, not the b-enhanced QCD MC samples are used but the general QCD configuration is exploited.

In general, Equation 5.3 depends on four quantities simultaneously. Note that no $\Delta\eta$ dependence is expected since this requirement is only implemented at the HLT, where it can be determined almost as precisely as in the offline selection. Since in previous studies [178], cor-

relations were found to be negligible, a factorized approach is used:

$$\epsilon_{\text{kin}} \simeq \epsilon^1(p_{\text{T}}^1, \eta^1) \epsilon^2(p_{\text{T}}^2, \eta^2), \quad (5.4)$$

where ϵ^1 and ϵ^2 reflect the individual efficiencies of the leading two jets.

To determine the individual jet kinematic efficiencies, a simplified version of the analysis cuts is deployed, requiring that the event is triggered by the reference trigger `PFJet60`, $p_{\text{T}}^{(1,2)} > 100$ GeV, $|\eta|^{(1,2)} < 2.3$, and $\Delta R^{(1,2)} > 1.0$. Also, the sub-leading jet must match the trigger objects of the `PFJet60` trigger, i.e. agree with these objects within an angular distance of $\Delta R < 0.5$. This two-jet selection ensures that the resulting data set is unbiased and the reference trigger is 100 % efficient at $p_{\text{T}} = 100$ GeV. Additionally demanding the trigger objects, not only the reconstructed jets, to have a transverse momentum exceeding 100 GeV effectively emulates the kinematic trigger requirements of the main analysis trigger (`DoublePFJets100`, cf. Table 5.4). The final efficiency for the event is then calculated as the ratio of all events passing the offline selection based on the emulated analysis trigger and the reference trigger:

$$\epsilon(p_{\text{T}}, \eta) = \frac{N_{S_{60} \cap S_{100}}}{N_{S_{60}}}. \quad (5.5)$$

This procedure is done for data and MC in the same way and the resulting scale factor is

$$sf_{\text{kin}} = sf_{\text{kin}}^1 \times sf_{\text{kin}}^2 = \frac{\epsilon_{\text{kin,data}}^1(p_{\text{T}}^1, \eta^1)}{\epsilon_{\text{kin,MC}}^1(p_{\text{T}}^1, \eta^1)} \times \frac{\epsilon_{\text{kin,data}}^2(p_{\text{T}}^2, \eta^2)}{\epsilon_{\text{kin,MC}}^2(p_{\text{T}}^2, \eta^2)}. \quad (5.6)$$

In order to avoid significant impact due to statistical fluctuations, the efficiency is then fitted with an analytical function. It is found that the Gaussian error function,

$$\text{erf}(x) = \frac{2}{\sqrt{\pi}} \int_0^x \exp(-t^2) dt, \quad (5.7)$$

describes the data very well, if it is slightly extended to

$$\epsilon(x) = A \text{erf}(C[p_{\text{T}} - B]). \quad (5.8)$$

This function is continuous in p_{T} and it is evaluated in three distinct regions of η . The data is divided depending on whether the jet is detected in the central ($|\eta| < 1.0$), overlap ($1.0 \leq |\eta| \leq 1.4$), or end-cap region ($1.4 < |\eta| < 2.2$). In Figure 5.7, the respective data is shown together with the fit result based on Equation 5.8 for the 2017 data-taking period and the QCD MC.

5. Search for Heavy, Neutral Higgs Bosons Decaying into a Pair of b Quarks

Era	$ \eta $	A	B	C
C	0.0 – 1.0	1.000 ± 0.71	97.71 ± 0.76	0.039 ± 0.71
	1.0 – 1.4	1.000 ± 0.71	97.84 ± 0.89	0.037 ± 0.71
	1.4 – 2.2	$1.000 \pm 1 \times 10^{-8}$	99.03 ± 0.84	0.038 ± 0.71
D	0.0 – 1.0	$1.000 \pm 2 \times 10^{-7}$	96.82 ± 0.35	$0.037 \pm 6 \times 10^{-4}$
	1.0 – 1.4	1.000 ± 0.71	97.48 ± 0.90	0.035 ± 0.71
	1.4 – 2.2	$0.998 \pm 5 \times 10^{-4}$	100.59 ± 0.25	$0.040 \pm 6 \times 10^{-4}$
E	0.0 – 1.0	1.000 ± 0.71	92.56 ± 2.11	0.031 ± 0.71
	1.0 – 1.4	1.000 ± 0.71	99.09 ± 0.81	0.036 ± 0.71
	1.4 – 2.2	$0.999 \pm 4 \times 10^{-4}$	101.33 ± 0.16	$0.038 \pm 4 \times 10^{-4}$
F	0.0 – 1.0	1.000 ± 0.71	97.78 ± 0.75	0.033 ± 0.71
	1.0 – 1.4	$0.998 \pm 6 \times 10^{-4}$	100.28 ± 0.33	$0.032 \pm 5 \times 10^{-4}$
	1.4 – 2.2	$0.999 \pm 4 \times 10^{-4}$	101.89 ± 0.11	$0.031 \pm 3 \times 10^{-4}$
2017	0.0 – 1.0	$0.999 \pm 2 \times 10^{-4}$	98.60 ± 0.13	$0.039 \pm 3 \times 10^{-4}$
	1.0 – 1.4	$0.998 \pm 3 \times 10^{-4}$	99.03 ± 0.22	$0.036 \pm 4 \times 10^{-4}$
	1.4 – 2.2	$0.999 \pm 2 \times 10^{-4}$	101.00 ± 0.10	$0.037 \pm 2 \times 10^{-4}$
MC	0.0 – 1.0	$0.998 \pm 2 \times 10^{-4}$	93.59 ± 0.25	$0.040 \pm 4 \times 10^{-4}$
	1.0 – 1.4	$0.998 \pm 3 \times 10^{-4}$	93.35 ± 0.44	$0.037 \pm 7 \times 10^{-4}$
	1.4 – 2.2	$0.998 \pm 2 \times 10^{-4}$	96.22 ± 0.27	$0.041 \pm 5 \times 10^{-4}$
sf = 2017/MC	0.0 – 1.0	0.999 ± 0.005	89.84 ± 1.11	0.036 ± 0.002
	1.0 – 1.4	0.998 ± 0.008	90.96 ± 1.66	0.035 ± 0.003
	1.4 – 2.2	1.002 ± 0.006	93.74 ± 0.91	0.038 ± 0.002

Table 5.5.: Fit results of the jet kinematic trigger efficiency for data and MC. Since the results for eras C, D, E, and F are very similar in the respective η region, a combined result for the full 2017 data-taking period is also given. The ratio of data over MC reflects the resulting scale factor.

Figure 5.8 shows a direct comparison of the fit results for data and MC as well as the extracted scale factor. The fitting results for the parameters A , B , and C for the individual data-taking periods in 2017 as well as the QCD MC are shown in Table 5.5. It can be seen that, while there is a dependency on the η region, eras C, D, E, and F resemble each other rather closely. Therefore, a combined fit for the full 2017 data-taking period is performed and used for the scale factor calculation. The resulting scale-factor parameters are also listed in Table 5.5.

5.5.3. B-Tag Trigger Efficiency

Depending on the flavor of a jet, the probability that it is correctly identified as originating from a b quark or a lighter flavor parton varies. There are also differences in this identification

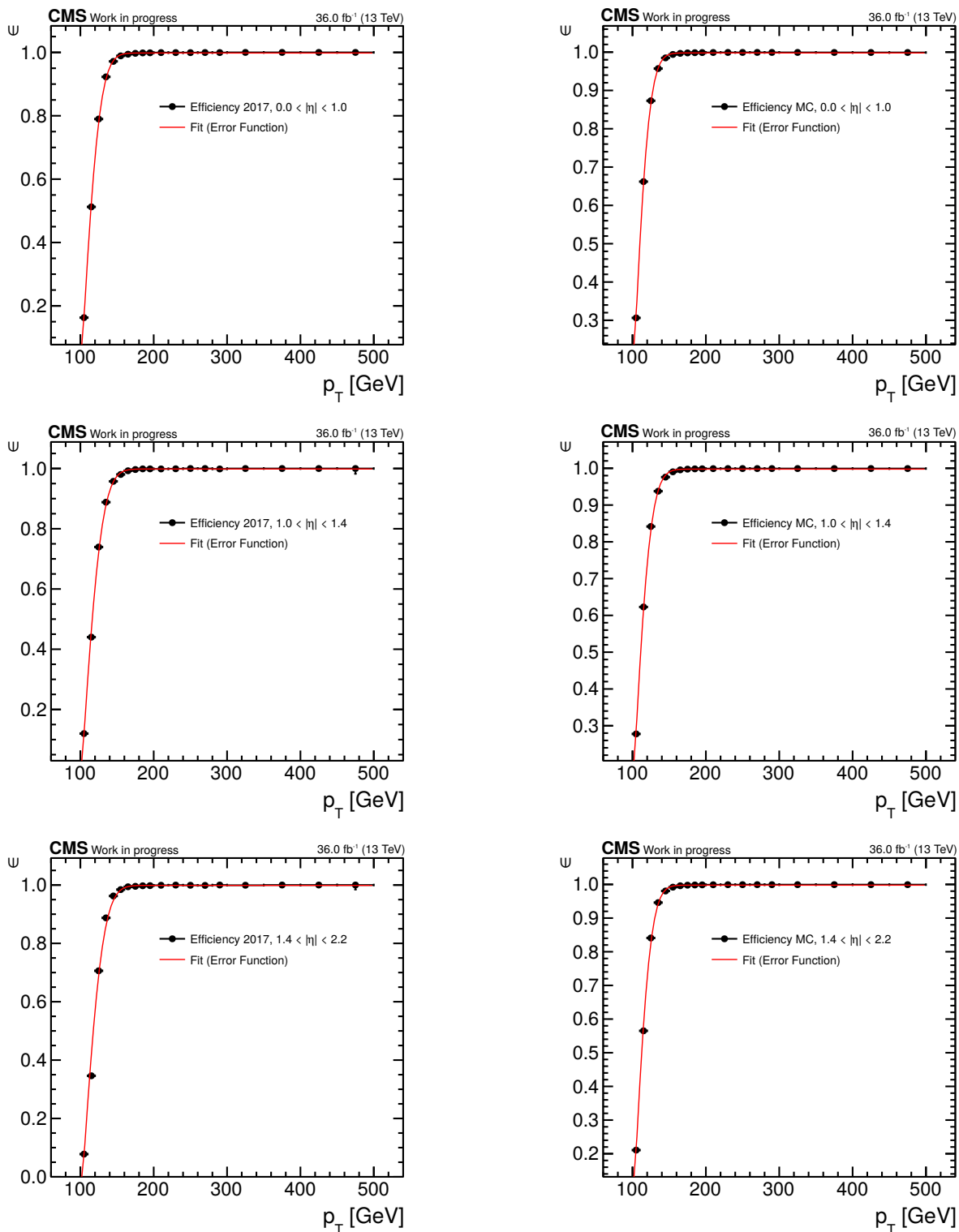


Figure 5.7.: Kinematic trigger efficiency ϵ for 2017 data (left) and MC (right). The study is performed in the central (top), overlap (center), and end-cap (bottom) regions. The turn-on behavior is parametrized using a Gaussian error function (red curves).

5. Search for Heavy, Neutral Higgs Bosons Decaying into a Pair of b Quarks

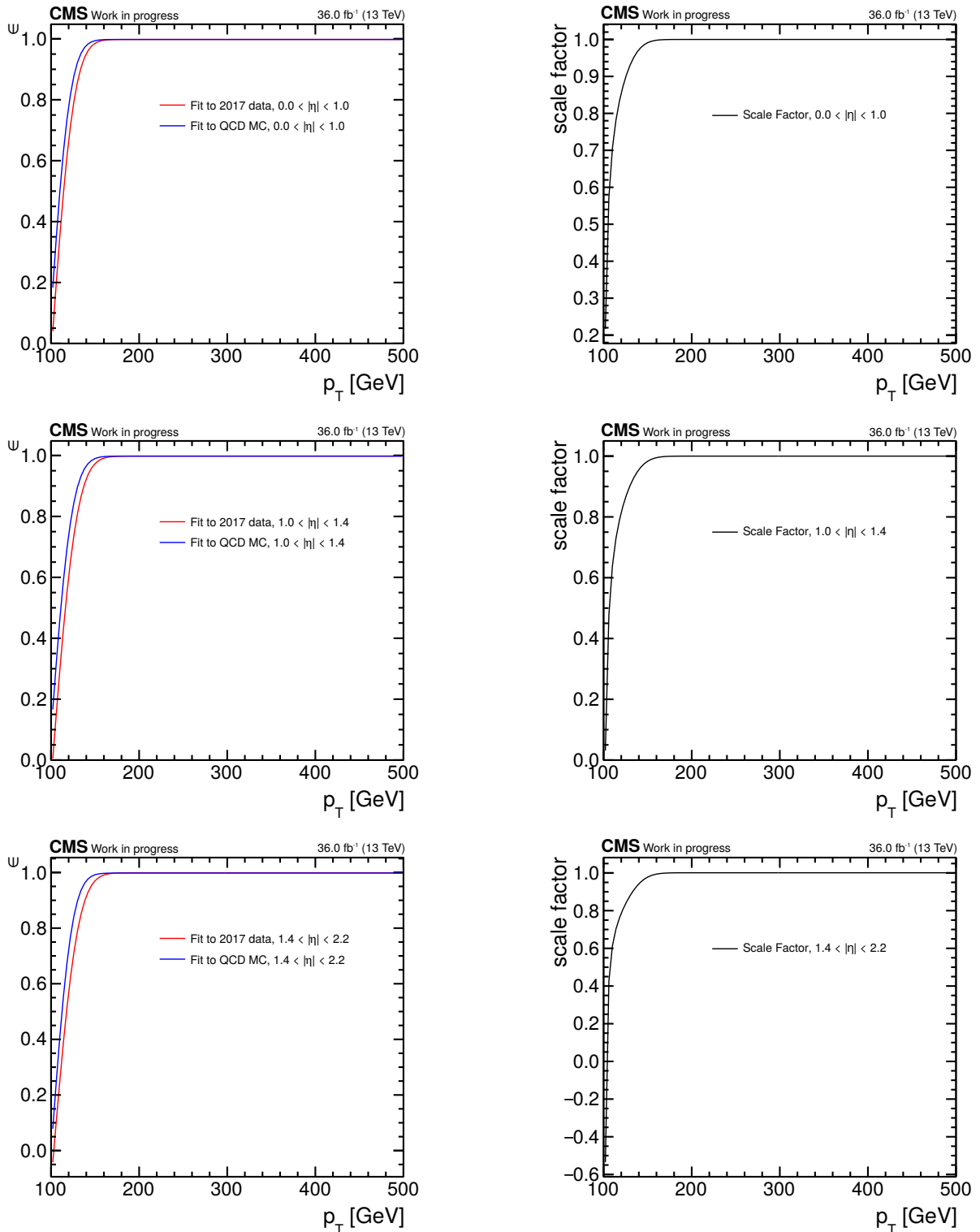


Figure 5.8.: Comparison of fit results for kinematic trigger efficiency in data and MC (left) as well as the resulting scale factor (right). The study is performed in the central (top), overlap (center), and end-cap (bottom) regions.

process between data and simulation. Depending on, e.g., detector effects, the identification procedure during data-taking can also vary slightly with time. Therefore, the simulated data does not describe the measurement exactly. In the context of this analysis, it is important to correct for the b-jet identification differences. Therefore, scale factors are calculated for the b-tagging processes at trigger level (online) as well as during the offline selection. Thus, the overall scale factor which is assigned to each simulated event consists of two main parts and can be calculated as

$$\text{sf}_{\text{evt}} = \prod_{i=1}^{n_{\text{onl}}} \text{sf}(p_{\text{T}}, \eta)_i^{\text{onl}} \times \prod_{j=1}^{n_{\text{off}}} \text{sf}(p_{\text{T}}, \eta)_j^{\text{offl}}, \quad (5.9)$$

where the indices i and j run over all jets tagged at trigger level (i) and in the offline selection (j). These jets are ordered in p_{T} and the scale factors for each individual jet depend on its p_{T} and η .

The offline b-tag scale factors are provided centrally by the CMS BTV group [166]. For the medium working point of the DeepJet algorithm, this is shown in Figure 5.9. As can be seen, two different methods have been used to calculate the correction factors before they were averaged for the final result. The LTSV (lifetime tagging secondary vertex) method adapts the jet probability (JP) tagger to evaluate the probability that a secondary vertex is found [161]. The JP algorithm can be calibrated directly with data using tracks with negative impact parameters to calculate their compatibility with the primary vertex. The discriminant of the JP algorithm is shaped differently depending on the flavor of the investigated jets. Therefore, it can be used to extract the true number of b jets in a data set. On the other hand, the Kin (kinematic selection) method is exclusively based on kinematic properties of the jet which are analyzed by a BDT. These properties are used to express the probability that an investigated jet originates from a b quark in order to provide a reference for the analyzed b-tag efficiency. The kinematic properties included in this method contain the distance and direction between PV and SV as well as track multiplicity and the energy of particles within the jet.

Online scale factors are calculated using a tag-and-probe approach. On trigger level, events with at least two jets and one b-tag are required. The sub-leading jet in p_{T} must pass the offline selection of the DeepJet b-tagging algorithm using the tight working point. It serves as the tag object and must, thus, also match the object which triggered the online b-tag requirement. The leading jet is the probe object and must fulfill the requirements of the medium b-tagging working point, which matches the offline selection. Together, these two b-tagging requirements are designed to increase the sample purity as much as possible. Furthermore, leading and sub-leading jet are required to be back-to-back in ϕ , exploiting the topological properties of QCD pair-production. This ensures that the probe jet has an enhanced probability of also being a b

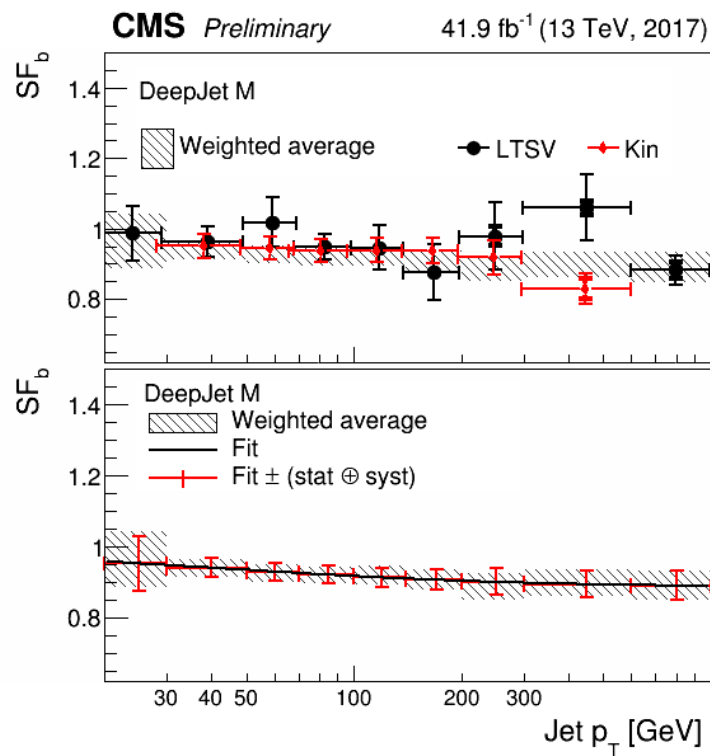


Figure 5.9.: Offline b -tag scale factor depending on the p_T of a jet for the DeepJet b -tagging algorithm based on different methods (top) and combined (bottom). Taken from [167].

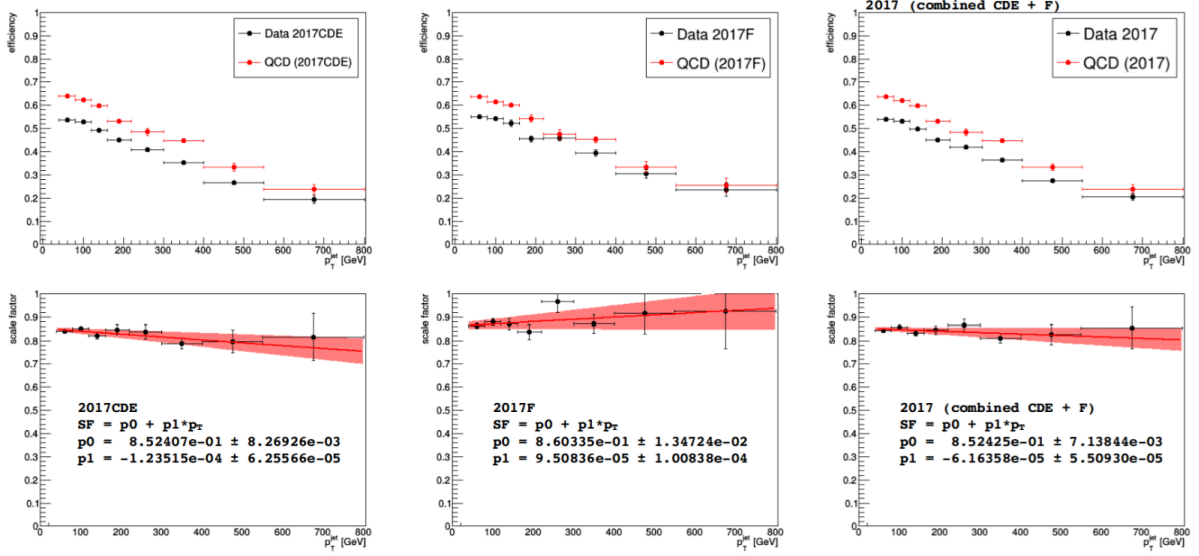


Figure 5.10.: Online b-tag efficiencies for data and Monte Carlo (top) as well as resulting scale factors (bottom) for data-taking periods 2017 C - E and F separately (left and center) and combined (right). Taken from [185].

jet while not being affected by a bias due to the trigger. By calculating the selection efficiency of the probe jet for data and simulation, the scale factor can be extracted as the ratio of these distributions as shown in Figure 5.10. As can be seen, the results differ slightly for the data taking periods C to E and F. This originates from issues with the new pixel detector which experienced unforeseen degrading of efficiency throughout the year. These effects could be fixed in the offline processing of the data and the eras are recombined, weighted by their luminosities.

5.6. Event Selection

For the search presented here, events are considered for further analysis, if they pass the trigger requirements described in Section 5.5. This means all events must have at least two highly energetic jet candidates which are also found likely to originate from b quarks. To enhance the signal-to-background ratio, further selection criteria are applied, which will be discussed in this section.

5.6.1. Primary Vertex Selection

All selected events are required to contain a well-reconstructed primary vertex (PV) from the hard-scattering process. Respective quality criteria are discussed in Section 4.1.2 and are ap-

plied centrally by the data-quality management system. For each event, the PV candidate with the largest p_T^2 sum is assumed to be the origin of the hard interaction.

5.6.2. Jet Selection

Since the signal processes in this analysis feature final states consisting entirely of jets, the selection of jets is particularly important. First, the jets must be reconstructed well. Second, jets with kinematic properties are selected such that the relative amount of signal candidate events is improved. Third, the jets are required to be originating from b quarks with high probability.

Identification and Kinematic Selection

The tight jet-identification working point, described in Section 4.1.3, is selected, which follows the recommendation for all analyses. Thereby, a jet selection efficiency of above 99 % and a fake-jet rejection above 98 % are ensured.

Additionally, contributions from pileup interactions have to be excluded from the reconstruction. This is done based on the loose pileup identification working point, which also follows central recommendations, suppressing pileup contributions while not significantly reducing the statistical power of the selection. Constituents from superimposed interactions are identified based on several parameters like the cone shape and the β function of the beam.

At least three jets are required in the final reconstruction of the event. Out of these, the leading two jets, which are assumed to originate from the Higgs boson in a signal event, must have transverse momenta above 110 and 100 GeV, respectively. In addition, the third leading jet must feature $p_T > 40$ GeV. A cut of $|\eta| \leq 2.2$, slightly tighter than the trigger requirement to guarantee full trigger efficiency, is enforced on all selected jets. To reduce the background contribution from gluon-splitting events (see Figure 5.6) and prevent impacts on the b -tagging by other jets, an additional requirement of a phase-space separation $\Delta R_{ij} > 1.0$ is placed on the leading three jets, where ij represents any combination of these three jets. Finally, it is found that a cut of $|\Delta\eta_{12}| \leq 1.5$ significantly improves the signal-to-background ratio, which is shown in Figure 5.11. This is also already implemented as a slightly looser requirement on trigger-level as it rejects background-like events much more efficiently than signal candidates.

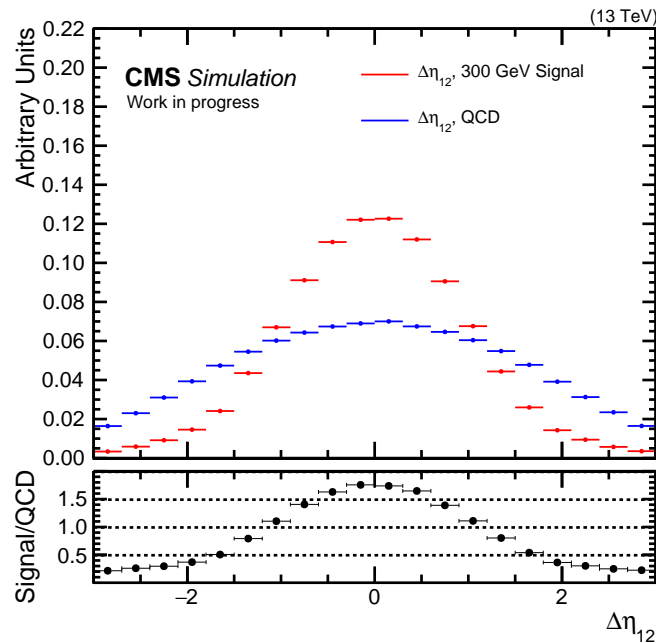


Figure 5.11.: Comparison of $\Delta\eta_{12}$ distributions in QCD MC (blue) and the 300 GeV signal sample (red). Even though also signal events are cut in the region $\Delta\eta_{12} > 1.5$, significantly more background events are rejected.

B-Tagging

Since all jets in the final states of the signal processes considered in this analysis (see Figure 5.2) originate from b quarks, this part of the selection is crucial. While a large fraction of signal candidates in the set of selected events is desirable, it is also critical to keep a sufficient amount of data after the selection. Furthermore, it has to be taken into account that the trigger already places some requirements on selected jets.

In order to select the most promising events, the most recent CMS b-tagging algorithm, the DeepJet tagger (cf. Section 4.2.1), is used. The choice of the b-tag working point is based on a sensitivity test which is performed on MC data sets. A simplified sensitivity estimate of S/\sqrt{B} is assumed, where S and B are the number of signal and background events, respectively. This is studied for the three recommended working points and results in the selection of the medium working point. Note that, as discussed in Section 5.5.1, at trigger level, the CSVv2 algorithm is used to select two highly energetic b jets using the respective tight working point. As discussed in Section 5.3, three b-tagged jets are only required in the signal region. To pass the medium working point, they must have a b-tag discriminant value $d > 0.3033$. In the control and validation regions, the b-tagging discriminant is required to be below the loose working point

($d < 0.0521$) or in between the two working points ($0.0521 \leq d \leq 0.3033$), respectively.

B-Jet Energy Regression

To account for missing energy, mostly because of neutrinos emitted in semi-leptonic decays of B hadrons, the deep-neural-network (DNN) based technique of b-jet energy regression [186] is included in the selection process. To calculate the amount of missing energy successfully, various observables are included, such as primary and secondary vertices, jet kinematics, tracking information and reconstructed soft leptons close to the investigated jet.

The training of the DNN is performed based on a simulated $t\bar{t}$ data set with jets featuring transverse momenta above 20 GeV and the resulting corrections are provided centrally by CMS [187]. They are given in form of a factor which has to be multiplied to the p_T value of the jet. Because of the DNN training process, mainly p_T values below 400 GeV are expected to be significantly corrected.

Recovery of Final-State-Radiation

It can happen that one of the final-state b quarks in the event radiates a gluon before hadronizing. This additional particle carries a finite amount of energy which is missing in the reconstruction of the original b jet if the resulting shower of particles is not located within the cone of the original jet. To account for the corresponding underestimation of energy of the b jet, a technique to recover final-state radiation (FSR) is deployed. For the two leading b-tagged jets, the four-momenta of all soft jets in close proximity ($\Delta R_{(\text{soft}, \text{bjet})} < 0.8$) with $p_T > 20$ GeV are added to the reconstructed b jet. The soft jets must also fulfill the same basic quality criteria as all selected jets, i.e. tight jet ID and loose pileup ID.

Muon Veto

In order to avoid overlap with the semi-leptonic analysis [34], events selected there are vetoed in the analysis presented here. This applies to all events with muons reconstructed in the immediate vicinity ($\Delta R_{(\mu, \text{jet}_{1,2})} < 0.4$) to either of the leading two jets. If such a muon is found with $p_T^\mu > 13$ GeV and $|\eta|^\mu \leq 2.2$ which also fulfills the requirements of a tight muon-selection ID, the event is rejected. Note that this explicitly does not veto semi-leptonic decays with electrons in the final state instead of muons. The effect of this veto on the signal shape is relatively small with a slight upwards shift and narrowing of the signal shapes being observed.

Step	CR	VR	SR
Trigger	11 320 136	11 320 136	11 320 136
Jet ID	11 229 045	11 229 045	11 229 045
Jet kinematics	5 415 879	5 415 879	5 415 879
ΔR_{ij}	3 776 645	3 776 645	3 776 645
$\Delta\eta_{12}$	3 178 004	3 178 004	3 178 004
b-tag (bbnb/bbsb/bbb)	1 118 794	209 057	228 644
Matching	1 090 782	199 998	160 161
μ veto	982 204	180 210	143 981

Table 5.6.: Cutflow in data for CR, VR, and SR. The only difference between these regions is the b-tag of the third leading jet. Before this cut is applied, all regions contain the same set of events.

Cutflow

Applying all the cuts mentioned above significantly reduces the initial amount of triggered events. The impact of each individual step in this cutflow is shown in Table 5.6 for the three analysis regions CR, VR, and SR. As these regions only differ in the b-tag of the third leading jet, it is expected that before this point in the cutflow no differences are observed. It can be seen that the CR contains about seven times as many events as the SR. This corresponds to the expectation due to the b-tagging requirements. The VR provides roughly the same amount of statistical power as the SR, which is mainly based on how the b-tagging discriminant is distributed and the respective selection window. It is also visible that the application of the muon veto excludes about 10 % of the remaining events.

5.6.3. Corrections to Monte Carlo Events

Various corrections need to be applied to simulated data sets. This can be related to theoretical or computational uncertainties as well as imperfections of the detector simulation. In order to overcome the latter kind of issue, corrections are applied to MC data sets so that they agree with the data as well as possible. In the context of this analysis, three major corrections are applied. First, a pileup reweighting procedure is included to model the distribution of proton-proton interactions per bunch crossing observed in data. Second, the trigger efficiencies are adjusted and, third, the b-tagging performance in the offline selection is scrutinized.

All of the corrections discussed here also introduce a systematic uncertainty which affects the signal efficiency and is considered in the signal-extraction procedure. These effects are described in Section 5.7.3.

Pileup Reweighting

The recorded pileup structure of the 2017 data-taking period is shown in Figure 4.2. Since this distribution depends on the interaction rate, beam parameters and other variables, it is usually not assumed to be precisely modeled in MC. Therefore, an event-by-event correction is applied, reweighting the simulated events such that the pileup distribution agrees with the measurement.

Trigger Efficiency

As discussed in Section 5.5, this correction consists of two parts, accounting for the trigger efficiency based on jet kinematics as well as the online b -tagging procedure. Corresponding scale factors are included accordingly. While the kinematic turn-on mainly affects jets with p_T values close to the trigger threshold, effects due to the b -tagging corrections are observed in the full energy range.

Offline b -Tagging

Similar to the pileup reweighting, jet identification efficiencies are not always modeled precisely in MC simulation. Therefore, a scale factor is applied to match the b -tagging performance in simulated data sets to the observed data. This particular correction is found to be affecting the event rate rather significantly with an $\mathcal{O}(10\%)$ effect over the full mass spectrum, as shown in Figure 5.9.

Comparison of Data and MC in the Control Region

Although the QCD MC data sets are not used for actual background predictions, their agreement with the data is studied in the control region. This is shown in Figure 5.12 for the main analysis observable m_{12} with and without the corrections discussed in this section. Since mainly the low-mass region disagrees without further corrections, it is assumed that predominant effects there are related to the jet kinematic trigger turn-on behavior. This is confirmed in a dedicated study, in which no other corrections are applied. It can be seen in Figure 5.12 that including all corrections (right plot), a reasonable agreement is achieved when an overall offset, or k -factor, of about 1.8 is considered. This is remarkable since the involved parton processes are clearly beyond leading order and, due to limitations in the physical modeling of these processes, a perfect agreement is not expected.

The process dominantly contributing to the overall background is QCD multi-jet production and the chosen MC data sets combined with the applied corrections provide an insight into this

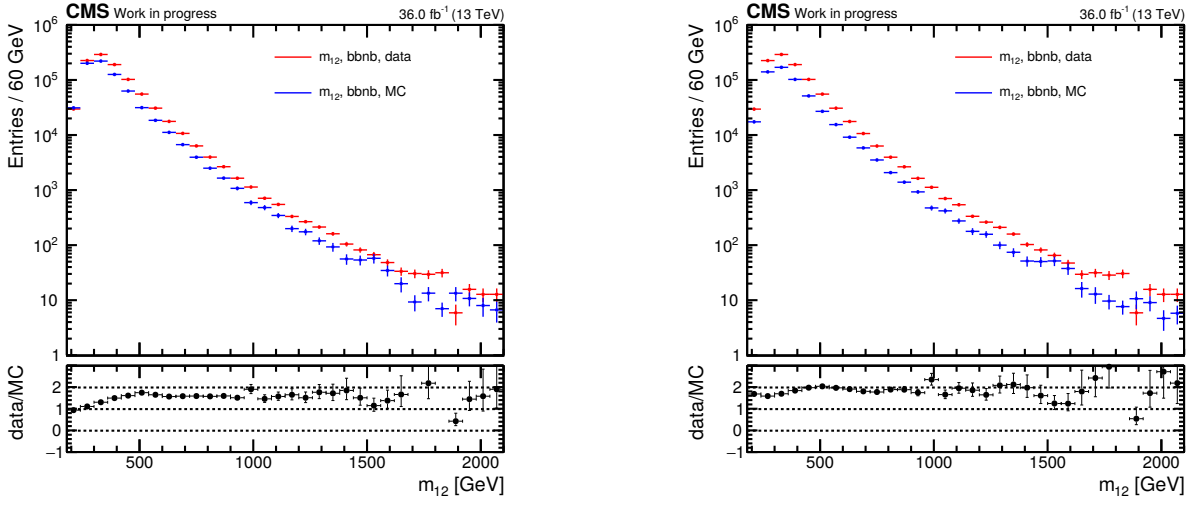


Figure 5.12.: Data (red) vs. MC (blue) in the bbnb control region with (right) and without (left) MC scale factors. While the applied corrections are able to improve the description in the low-mass region, the overall agreement is not perfect. A k -factor of about 1.8 is observed.

process. Due to the expected residual disagreement, no precise background prediction can be made based on simulation and a data-driven background estimation is indispensable in order to obtain an accurate prediction.

5.7. Signal Modeling

The signal model for this analysis is based on a simulation of the b -associated production of a heavy, neutral Higgs boson and its subsequent decay into a pair of b quarks. These calculations are performed to NLO precision with the MadGraph5 generator and the invariant mass spectrum is simulated for 13 different Higgs boson masses, ranging from 300 GeV to 1600 GeV. A trigger simulation is used to model the respective selection in data and the same offline selection is applied to the signal samples as is done for QCD MC as well as the actual data. Jet energy corrections, as described in Section 5.6.3, are included as well as trigger scale factors, as described in Sections 5.5.2 and 5.5.3 for the jet kinematic trigger efficiency and online b -tag efficiency, respectively.

For the final signal extraction, the invariant mass spectra after application of all cuts and calibrations are used as templates, i.e. the resulting histograms are utilized directly in binned form. The effect of each cut, depending on the investigated signal sample, is shown in Table 5.7.

5. Search for Heavy, Neutral Higgs Bosons Decaying into a Pair of b Quarks

Step	300 GeV	350 GeV	400 GeV	450 GeV	500 GeV
Initial	5 147 086	2 495 689	2 710 279	2 717 837	2 323 664
Jet ID	5 096 153	2 474 614	2 690 738	2 700 567	2 310 274
Jet kinematics	688 363	517 861	753 225	913 962	895 860
ΔR_{ij}	561 581	399 850	559 477	662 479	638 406
$\Delta\eta_{12}$	490 364	345 693	474 712	548 508	516 763
b tagging (SR, bbb)	205 936	133 961	173 169	189 588	172 787
Trigger & Matching	64 427	49 730	68 314	77 012	71 636
Muon veto	57 471	43 130	57 454	63 874	58 015
Step	600 GeV	700 GeV	800 GeV	900 GeV	
Initial	2 804 081	2 536 631	2 601 060	2 725 232	
Jet ID	2 790 193	2 526 430	2 592 365	2 717 397	
Jet kinematics	1 283 950	1 294 704	1 428 429	1 571 172	
ΔR_{ij}	898 701	897 725	980 777	1 071 693	
$\Delta\eta_{12}$	702 978	684 926	734 985	792 946	
b tagging (SR, bbb)	223 828	210 939	220 918	231 392	
Trigger & Matching	91 055	84 152	82 904	81 117	
Muon veto	72 162	65 595	64 483	61 530	
Step	1000 GeV	1200 GeV	1400 GeV	1600 GeV	
Initial	2 675 084	2 584 330	2 646 571	2 726 662	
Jet ID	2 668 978	2 579 575	2 642 781	2 723 250	
Jet kinematics	1 617 326	1 669 544	1 784 926	1 902 565	
ΔR_{ij}	1 098 106	1 126 771	1 197 865	1 271 776	
$\Delta\eta_{12}$	803 808	812 114	853 463	899 353	
b tagging (SR, bbb)	227 840	217 038	211 666	205 353	
Trigger & Matching	74 651	63 232	55 603	49 351	
Muon veto	56 338	47 451	42 122	37 112	

Table 5.7.: Cutflow for MC signal samples depending on the generated Higgs boson mass. Each number represents the amount of events left after application of the respective cut. Events generated with a negative event weight are already accounted for in the first line.

In this section, the general shape of the mass distributions in the signal samples is described as well as the effect of applied corrections and systematic uncertainties.

5.7.1. Signal Mass Distributions

Three representative mass distributions are shown in Figure 5.13 with one histogram for a mass point from the low (350 GeV), medium (600 GeV), and high mass (1200 GeV) range. It can be seen that the appearance of the templates significantly depends on the nominal mass. Furthermore, the peak position is generally found to be slightly below the nominal mass and this effect is more pronounced for higher nominal masses. Several effects have to be taken into account here since they affect the signal shapes.

First, the tails towards lower reconstructed masses mainly originate from incomplete reconstruction of the final-state products. This can happen because of undetectable particles like neutrinos or because not all constituents of a jet are reconstructed and assigned correctly. Furthermore, not recovered final-state radiation (FSR) also leads to an overall shift of the distribution towards lower masses. Together, these effects also account for the peak of the distribution being shifted to masses below the nominal mass.

Second, for the lower mass points, there are kinematic thresholds imposed by the trigger. Thus, tails in the mass distribution towards lower values are suppressed. This effect can be seen in Figure 5.13 for the 350 GeV mass distribution, while it does not play much of a role for the higher mass points.

Third, a combinatorical background is present, reflecting an incorrect assignment of reconstructed b jets to Higgs-daughter particles. This happens if at least one of the leading b jets is not originating from the Higgs boson decay. This effect accounts for tails on both sides of the peak.

Overall, these effects shape the di-jet mass distributions. The intrinsic width of any investigated Higgs boson is dependent on the respective model. For all models used here, this width is much smaller than the di-jet mass resolution for the accessible parameter space. Therefore, its impact on the templates is negligible.

5.7.2. Impact of Jet Energy Corrections

In addition to optimizing the event selection, which includes b-jet energy regression (cf. Section 5.6.2), and therefore increasing the signal efficiency, improvements on the signal resolution also enhance the overall sensitivity significantly. Hence, it is not only crucial to obtain a correct

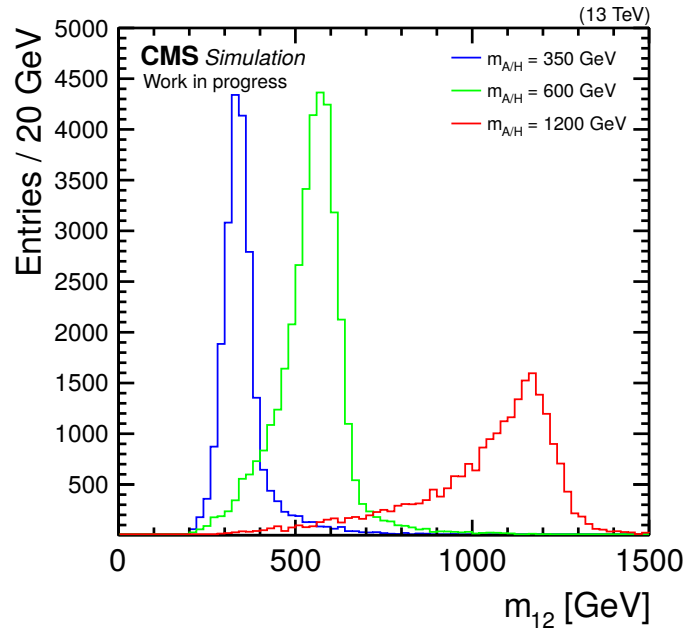


Figure 5.13.: Invariant mass spectrum of three representative signal mass points from the low (350 GeV, blue), intermediate (600 GeV, green), and high mass (1200 GeV, red) range of the available samples

estimate for this resolution but also to improve it where possible.

As a first step, the jet energy corrections discussed in Section 4.1.4, JES and JER are implemented for the MC data sets. While the JES information is already included in the data sets, JER corrections are applied during the event selection process.

All of the aforementioned corrections to the b -jet reconstruction have a direct impact on the invariant mass distribution. This is shown in Figure 5.14 for the same three mass points which are shown in Figure 5.13. In order to provide a more complete insight to all parts of the mass range, an additional histogram, representing the 900 GeV mass point, is included in all subsequent plots. The JER correction slightly widens the invariant-mass distributions, accounting for differences between MC and the actual reconstruction of jets. Applying b -jet energy regression mainly affects the lower mass points, shifting the distribution slightly towards higher masses and narrowing it at the same time. A similar effect is observed due to the muon veto which is applied to avoid overlap with the semi-leptonic channel. This resemblance is, however, expected since the b -jet energy regression accounts for lost energy due to neutrinos which are present in semi-leptonic decays.

Furthermore, it is described in Section 5.7.1 that there are significant effects due to FSR and neutrino emission. Thus, respective FSR-recovery efforts as well as b -jet energy regression are

included (see Section 5.6.2). Applying b-jet energy regression before the actual event selection allows jets with erroneously low reconstructed energy to pass the selection where they usually would have been discarded. Depending on the mass point, this can recover up to 10 % of the jets and at the same time improve the mass resolution accordingly. Similarly, the process of FSR recovery allows a more realistic assessment of the actual signal shape by re-adding objects to a jet which likely originate from radiation processes. Therefore, a slight shift of the whole distribution towards larger masses is expected. It can be seen in Figure 5.14 that the FSR recovery indeed shifts all distributions towards higher masses, while the shape is not significantly affected.

5.7.3. Systematic Uncertainties

Several systematic uncertainties, affecting the shape of the signal mass distribution on the one hand and the yield on the other hand, are considered in this analysis. It is also studied what kind of effect is expected due to any individual uncertainty, based on up- and down-variations of one standard deviation for each of the investigated uncertainties. This is incorporated in the final signal extraction fit as a nuisance parameter, in order to treat each uncertainty correctly. While shape uncertainties are modeled by means of additional templates, reflecting the upward and downward 1σ variations, for rate uncertainties, their effect on the signal efficiency is taken into account. The investigated uncertainties affecting this analysis are related to the

- Jet energy scale (JES),
- Jet energy resolution (JER),
- Online b-tag efficiency scale factors,
- Offline b-tag efficiency scale factors,
- Jet kinematic turn-on scale factor, and
- Pileup reweighting.

Figures 5.15 to 5.17 show the results of these studies for the 350, 600, and 1200 GeV mass points. It is visible that only the JES and JER uncertainties significantly impact the shape of the distributions, while all other uncertainties result in a mere change of the event yield. Also the luminosity measurement is correlated with a systematic uncertainty, leading to rate variations of 2.3 % [125].

5. Search for Heavy, Neutral Higgs Bosons Decaying into a Pair of b Quarks

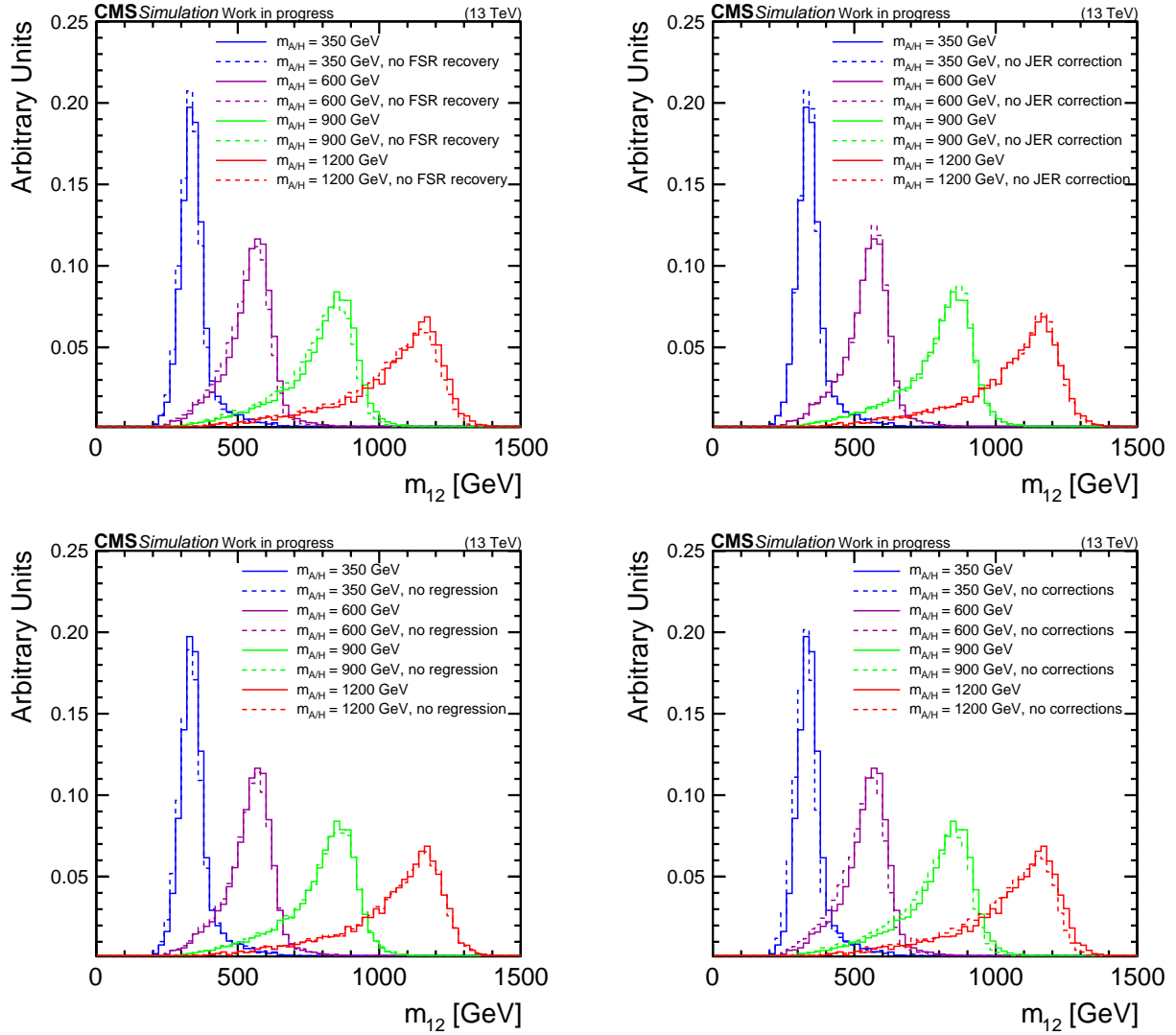


Figure 5.14.: Invariant-mass distributions of representative signal mass points with and without including FSR recovery (top left), JER correction (top right), b-jet energy regression (bottom left), and all of the three combined (bottom right). In each plot, all corrections but the investigated one are included. For the bottom right plot, this equals a comparison of the signal shape with and without all of the corrections. The selected mass points are the same in all four plots, representing the low mass range (350 GeV, blue), upper and lower edge of the intermediate mass range (600 and 900 GeV, purple and green), as well as the high mass range (1200 GeV, red).

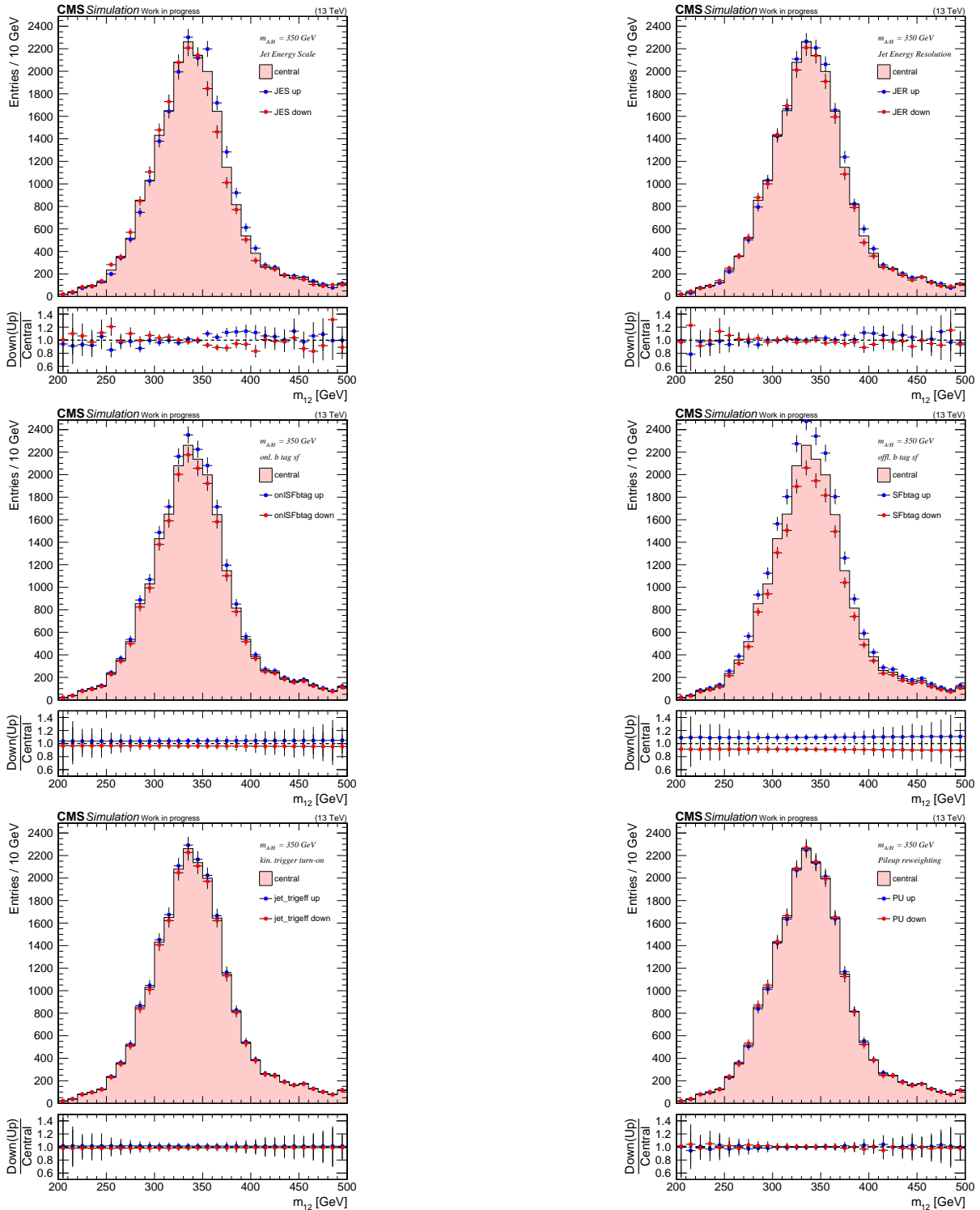


Figure 5.15.: Effect of systematic uncertainties on the shape (top) or the normalization (center and bottom) of the signal template of the 350 GeV mass point. In all plots, the light-red shaded histogram represents the nominal signal template. Red and blue points reflect the corresponding downward and upward 1σ variations of the investigated uncertainty and a ratio with respect to the central result is shown in the bottom panel.

5. Search for Heavy, Neutral Higgs Bosons Decaying into a Pair of b Quarks

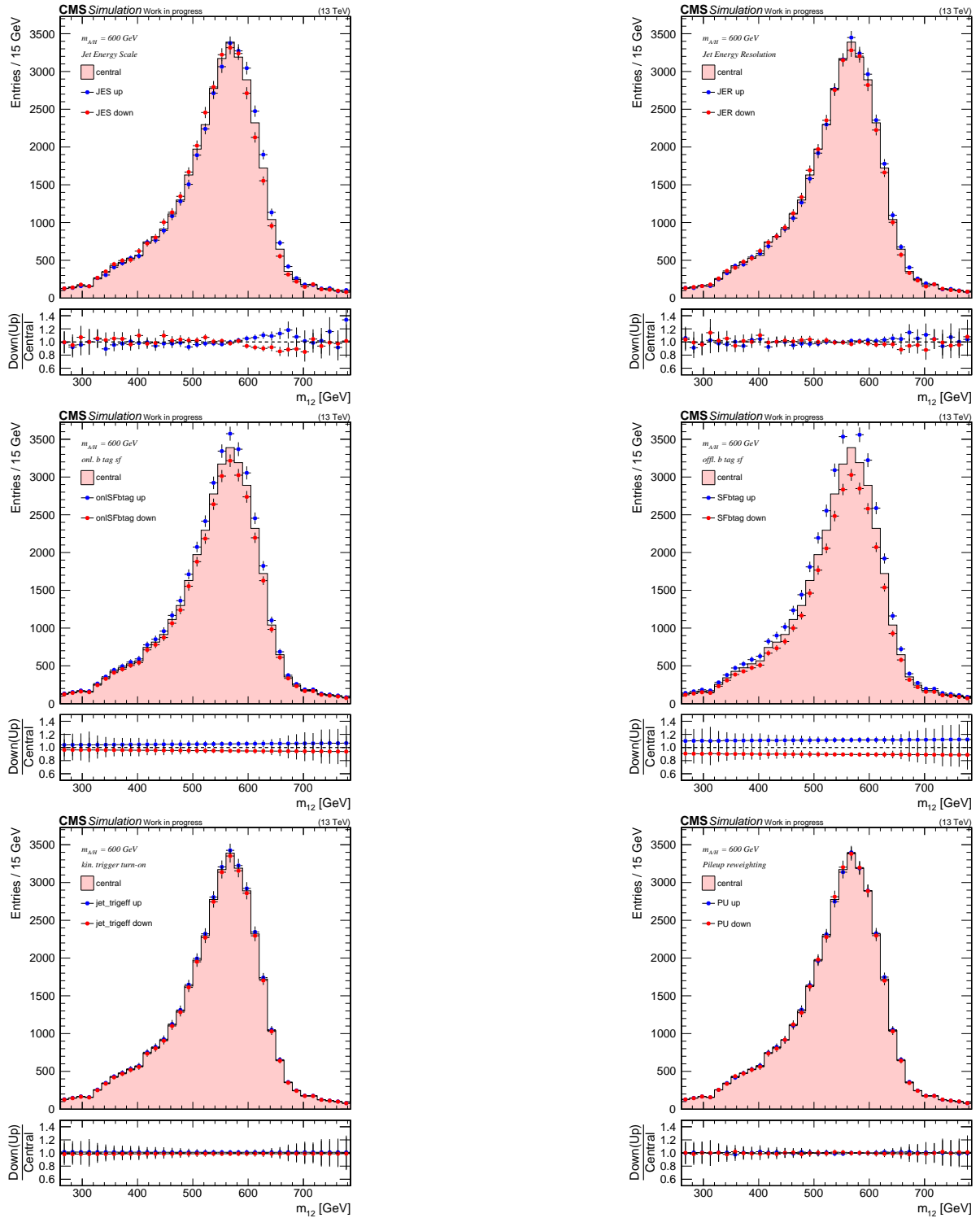


Figure 5.16.: Effect of systematic uncertainties on the shape (top) or the normalization (center and bottom) of the signal template of the 600 GeV mass point. In all plots, the light-red shaded histogram represents the nominal signal template. Red and blue points reflect the corresponding downward and upward 1σ variations of the investigated uncertainty and a ratio with respect to the central result is shown in the bottom panel.

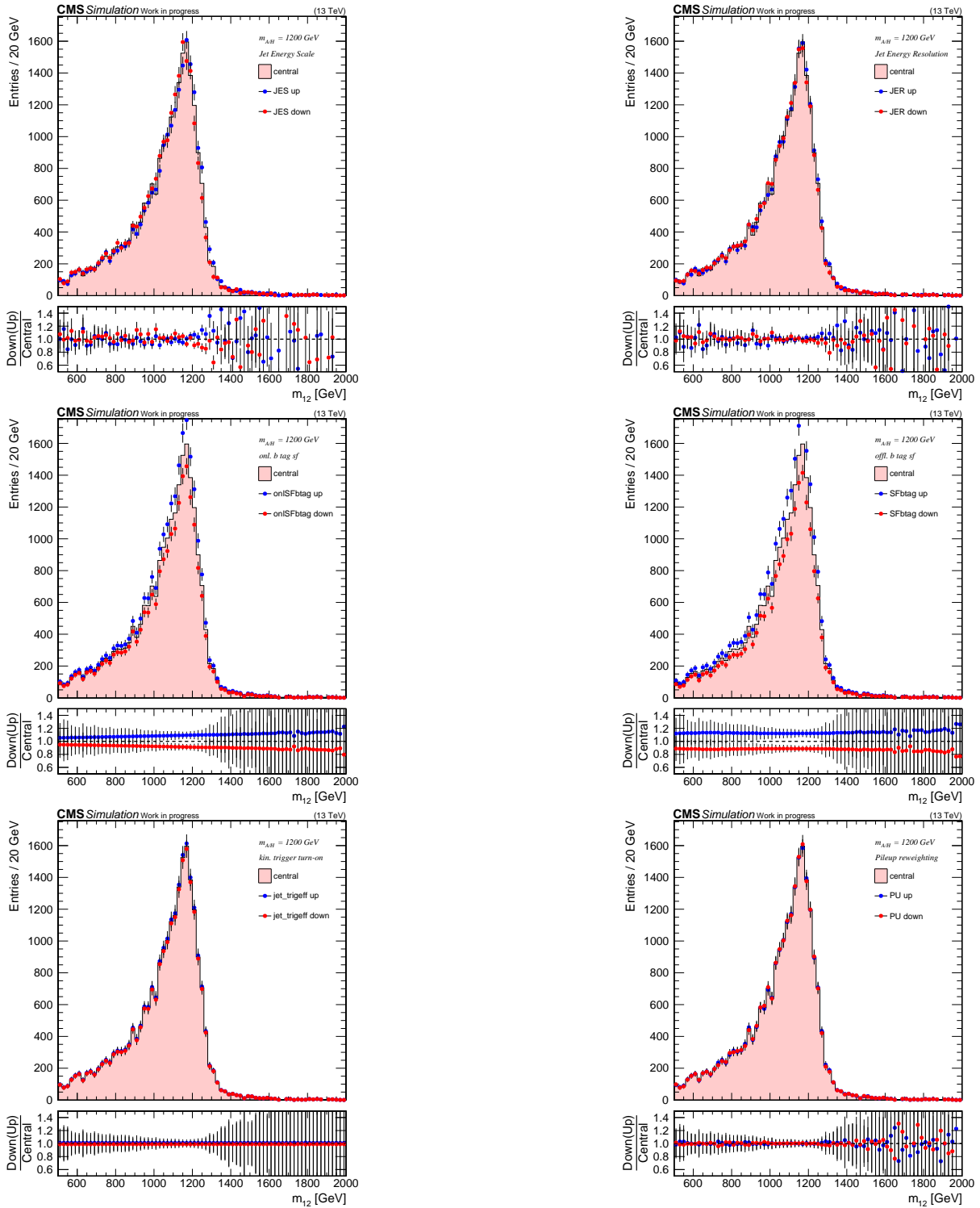


Figure 5.17.: Effect of systematic uncertainties on the shape (top) or the normalization (center and bottom) of the signal template of the 1200 GeV mass point. In all plots, the light-red shaded histogram represents the nominal signal template. Red and blue points reflect the corresponding downward and upward 1σ variations of the investigated uncertainty and a ratio with respect to the central result is shown in the bottom panel.

5. Search for Heavy, Neutral Higgs Bosons Decaying into a Pair of b Quarks

Mass	Offl. b-tag	Onl. b-tag	kin. trig. t.-o.	PU	Ren. scale	pdf & α_S	Theory
300 GeV	9.6	3.7	1.6	0.1	10.3	3.0	6.6
350 GeV	9.3	3.9	1.4	0.2	10.4	3.3	6.7
400 GeV	9.1	4.1	1.3	0.3	9.7	3.6	6.6
400 GeV	11.2	4.2	1.3	0.2	9.7	3.6	6.6
450 GeV	10.9	4.4	1.2	0.1	9.6	3.9	6.8
500 GeV	10.4	4.6	1.2	0.1	9.7	4.2	7.0
600 GeV	10.1	5.1	1.1	0.2	9.9	4.9	7.5
700 GeV	9.7	5.6	1.1	0.2	9.1	5.5	8.1
700 GeV	11.5	5.7	1.1	0.2	9.1	5.5	8.1
800 GeV	11.5	6.2	1.1	0.2	9.2	6.1	8.8
900 GeV	11.3	6.7	1.1	0.1	9.2	6.7	9.9
1000 GeV	11.2	7.2	1.1	0.1	9.2	7.4	10.6
1000 GeV	12.9	7.3	1.1	0.1	9.2	7.4	10.6
1200 GeV	12.4	8.3	1.1	0.0	9.0	8.6	12.6
1400 GeV	11.9	9.4	1.1	0.1	9.1	9.8	14.8
1600 GeV	11.6	10.5	1.1	0.0	9.2	11.1	17.6

Table 5.8.: Effect in percent on the normalization of the signal template due to systematic uncertainties, namely offline and online b-tag, jet kinematic trigger turn-on and pileup reweighting. Theory-related production cross-section uncertainties because of the renormalization scale as well as the choice of α_S and uncertainties related to the parton-density functions (pdfs) of the proton are included for the two “traditional” hMSSM and m_h^{mod+} scenarios. For the more recent m_h^{125} scenarios, a combined systematic uncertainty for the theory predictions is provided. Since the signal efficiency is also dependent on the fit range (see Section 5.8), effects on mass points at the respective edges are evaluated for both fit ranges.

An additional uncertainty has to be included as soon as the results are to be interpreted in terms of specific theoretical models. This accounts for uncertainties in the theoretical prediction of production cross-sections, based on the choice of the PDFs and α_S as well as the uncertainty of the QCD scale.

The effect on the signal normalization for all uncertainties discussed here is shown in percent in Table 5.8. The most important normalization uncertainties are found to be related to the on-line and offline b-tagging scale factors as well as the theoretical predictions. It is also observed that these effects become larger for the higher signal masses. Rather independent of the mass point, the kinematic trigger turn-on as well as the pileup reweighting do not add significant normalization uncertainties. They are included to the final fit nevertheless.

5.7.4. Signal Efficiency

Including all steps of selection and all corrections as described in the previous sections, the signal efficiency for each mass point is calculated. It is defined as the ratio of finally selected events over the effective number of events in the beginning. This results in the efficiencies which are shown in Figure 5.18 for the three analysis regions CR, VR, and SR.

For the SR, an efficiency in the order of 1 – 2% is observed for the entire mass range under consideration. The VR is found to have a signal selection rate around an order of magnitude lower than in the SR, while containing a similar number of events. Therefore, this region is well depleted of signal. Containing an even lower fraction of signal events, the signal-selection rate in the CR is found to be about a factor of two below the SR signal efficiency, while in the actual data, the CR features around seven times as many events as the SR.

The highest selection efficiency is observed with slightly more than 2% for the 500 GeV mass point. The decrease for higher masses is expected based on the additional challenges in b-tagging at larger jet energies. Therefore, maintaining the same light-flavor rejection efficiency directly implies a lower b-jet selection rate. However, including the DeepJet b-tagging algorithm instead of the previously used DeepCSV or CSVv2 algorithms significantly decreases this effect as the DeepJet algorithm provides a particularly strong light-jet rejection efficiency at large transverse momenta. The b-tagging performance is also improved based on the new pixel detector which was installed in between the 2016 and 2017 data-taking periods, as discussed in Section 3.2.1. This is, to some smaller extend, also the case for the general jet reconstruction. Overall, a signal efficiency roughly twice as large as in the 2016 analysis is observed.

5.8. Background Modeling

In previous analyses [34, 177, 178], CR and SR were fitted independently with the functional form of the parametrization being determined in the CR and then fitted again in the SR together with a signal hypothesis (see Section 5.3). The results of this process for the 2016 inclusive analysis, i.e. with no semi-leptonic channel defined, are shown in Figure 5.19. It is apparent that the di-jet mass-spectra in the CR and SR look extremely similar. This is partially expected based on the selection which only differs by the b-tag of the third leading jet. However, this difference in the b-tag selection leads to the inclusion of different QCD processes in the two regions. Based on the similarity of the m_{12} shape in the two regions, a new approach is developed in the analysis presented here.

Since QCD MC simulation is limited in precision, as shown in Section 5.6.3, it can not be

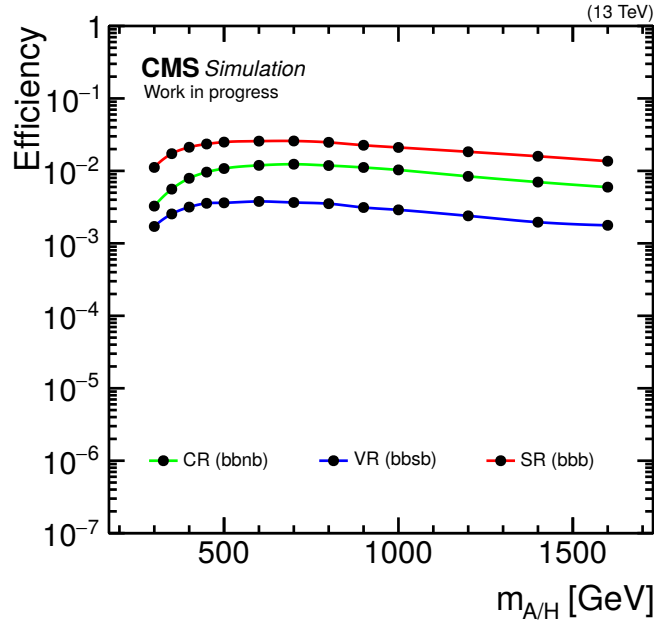


Figure 5.18.: Signal selection efficiency in the CR (green), VR (blue), and SR (red) depending on the analyzed signal sample. The highest signal efficiency is observed around 500 GeV for all regions. Both the CR and VR are found to be signal-depleted.

utilized to estimate the background in the signal region. On the other hand, as discussed in Section 5.2, the QCD multi-jet production is by far the dominant background contribution. Hence, a data-driven approach is chosen. Determining the major part of the parametrization in the CR and enabling this shape to adapt to the SR by adding a slowly varying transfer factor (TF) significantly reduces the number of shape parameters which are determined in the SR. Subsequently, the respective background estimation for the SR is not impacted by the choice of the background function as much. The respective systematic uncertainty, the bias, was dominant in previous analyses. The actual signal extraction is performed in a simultaneous fit of CR and SR. In this fit, the SR background is calculated based on the CR parametrization which is multiplied by the transfer factor. A signal is added based on the respective template and a signal-strength modification parameter μ .

In this section, an overview on the background estimation is provided, consisting of the CR parametrization and the MC-based determination of the TF shape. For the latter, a new method is implemented in order to reduce the impact of statistical fluctuations due to the limited MC statistics. Finally, an estimate of the resulting bias due to the function choices is calculated.

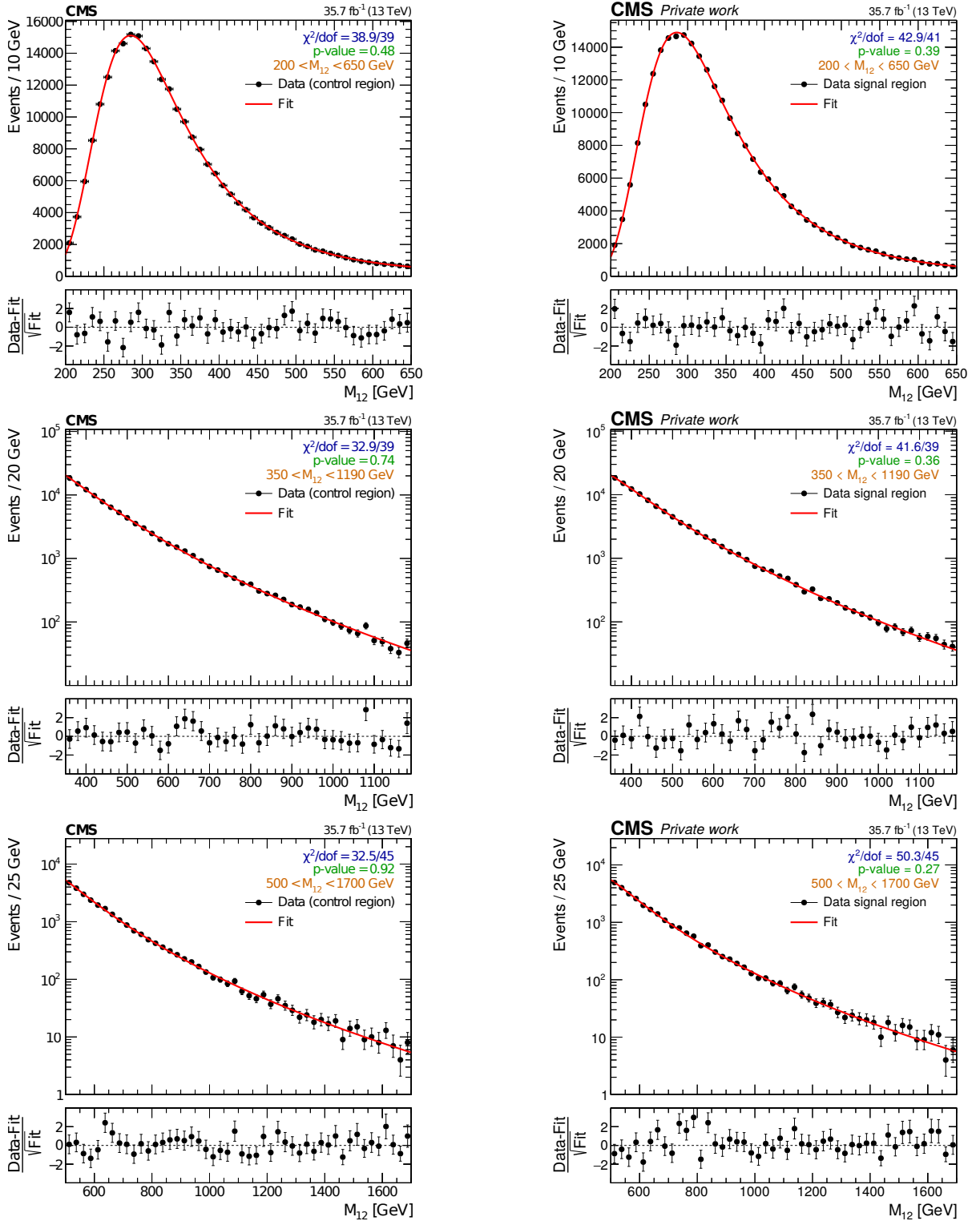


Figure 5.19.: Background parametrization in CR (left, [178]) and SR (right, [177]) for the 2016 inclusive analysis. The fits were performed in three mass-ranges in order to achieve a better description of the data based on analytical functions. In the bottom panel of each plot, the pulls are shown, reflecting the quality of the description of the data based on the analytical model.

5.8.1. Control Region Parametrization

As the first step in the background-modeling process, a parametrization of the control region distribution is determined to minimize the impact of statistical fluctuations in the background model. Since the chosen approach heavily relies on the statistical power of this region, the entire data set is utilized. However, this approach leads to some challenges in the parametrization process. Based on the large statistical precision, any selected analytical function must provide an excellent description of the full mass range under investigation. At the same time, it is not desirable to have too many free parameters since such a function might simply adapt to any structure in the data, including a potential signal. Furthermore, adding more parameters increases the correlations between fit variables which might affect the stability of the fitting procedure.

In order to keep the required number of parameters as low as possible while obtaining a good description of the CR data, four fit ranges (FR) have been defined. A parametrization of the invariant mass distribution is determined in each of these ranges. The lower edge of the first fit range, 200 GeV, is roughly defined by the trigger thresholds, excluding only a few events featuring a lower di-jet mass. Similarly, the upper end of the fourth fit range, 2000 GeV, is chosen such that there is still a significant amount of entries in each data bin. While the CR fit might work fine with a lower number of events in this region, it should be ensured that also in the SR, there are still sufficient events for a stable fitting procedure.

Each fit range overlaps with its adjacent fit ranges. This is done to make sure that the mass spectrum of each signal sample is well contained within at least one fit range. To avoid biasing final results at the edges of a FR, mass points at these borders are analyzed in either range. The nominal result is taken in the FR with the better, i.e. lower, expected limit which indicates a larger sensitivity to be provided by the respective FR. An overview of all mass points assigned to the respective fit ranges is given in Figure 5.20. For display purposes, in order to make them more comparable to each other, all of the distributions are normalized such that they have the same integral value.

After investigating various families of functions in terms of their power to describe the CR data, a good description could be found for each FR. First of all, it is observed that the low-mass region is dominated by a turn-on effect resulting from kinematic thresholds as well as the b -tagging efficiency. This rise smoothly changes into a power-law-like descent behavior with a peak slightly above 300 GeV. In order to model the turn-on behavior, a modified Gaussian error

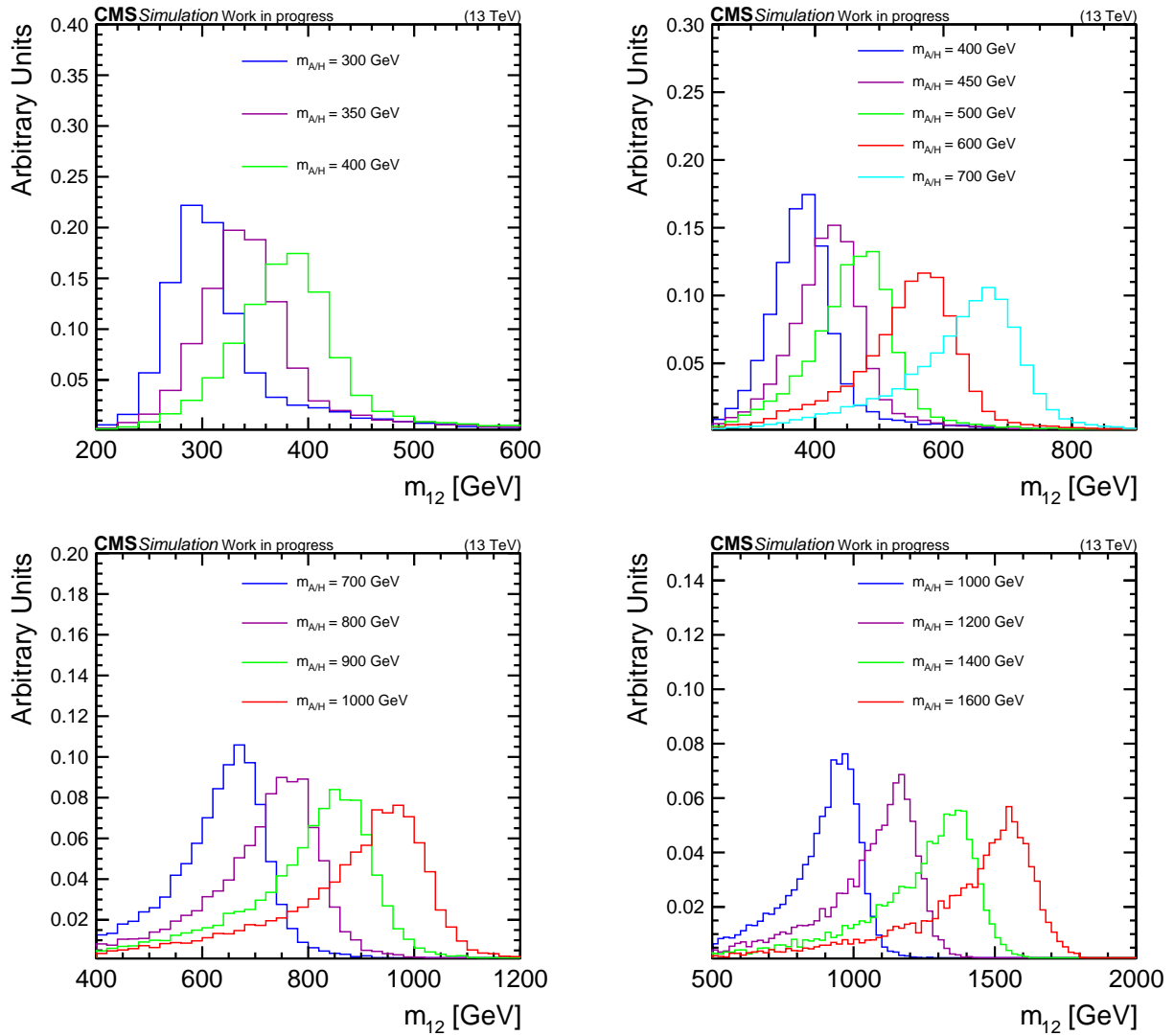


Figure 5.20.: Overview of mass shapes from signal samples in each fit range. Templates at the edge of fit ranges are evaluated in both adjacent ranges. Since all distributions are normalized in the same fashion, the decreasing maximum height of the templates reflects their widening.

5. Search for Heavy, Neutral Higgs Bosons Decaying into a Pair of b Quarks

function is chosen,

$$\text{TO}(x) = \frac{1}{2} \cdot \text{erf} [\lambda \cdot (x - x_0) + 1], \quad (5.10)$$

where the error function is defined in Equation 5.7, λ modifies the steepness of the function, and x_0 reflects an offset in x direction. The additional terms ensure that the function is positive for all x . This turn-on function is multiplied with a Bernstein polynomial [188] such that the product describes both parts of the data distribution well. The Bernstein polynomials are defined as

$$B_{i,n}(x) = \sum_{i=0}^n c_i \cdot \binom{n}{i} \cdot x^i \cdot (1-x)^{n-i} \quad (5.11)$$

with constants c_i . It is found that the sixth polynomial ($n = 6$) of this family of functions is well-suited to describe the data in the first fit range FR 1.

In the other three fit ranges, FR 2 to FR 4, the CR distribution can be described based on the Novosibirsk function, which is a convolution of a theoretical Compton spectrum with a logarithmic Gaussian function [189]. For FR 2, an extended version of this function is used,

$$\text{EN}(x) = N \exp \left(-\frac{1}{2w_0^2} \cdot \ln^2 \left(1 - \frac{(x - \rho) \cdot \eta}{\nu} - \left(p_1 \cdot (x - \rho)^2 \cdot \frac{\eta}{\nu} \right) \right) - \frac{w_0^2}{2} \right), \quad (5.12)$$

where $w_0 = \frac{2}{\xi} \cdot \sinh^{-1} \left(\eta \cdot \frac{\xi}{2} \right)$ and $\xi = 2\sqrt{\ln 4} = 2.3548$. In this definition, N is a normalization parameter, η , ρ , and ν modify the tail, peak, and width of the distribution, respectively, and p_1 defines the extension with respect to the nominal Novosibirsk function in which $p_1 \equiv 0$ and which is used to describe fit ranges 3 and 4. For η approaching 0, a Gaussian function is obtained, while for positive values, a tail towards larger x arises. For FR 2, the turn-on function as defined in Equation 5.10 is still required as the background peak is partially contained in this range as well. For FR 3 and FR 4, this is not necessary anymore.

All of the resulting fits are shown in Figure 5.21 for the four fit ranges. As can be seen, a very good description is obtained for each fit range. A summary of the function choices with the corresponding number of fit parameters, the mass range of each FR as well as the respectively assigned mass points are shown in Table 5.9. As described above, the mass points at the edges of fit ranges are evaluated in terms of both adjacent ranges covering the corresponding mass distribution.

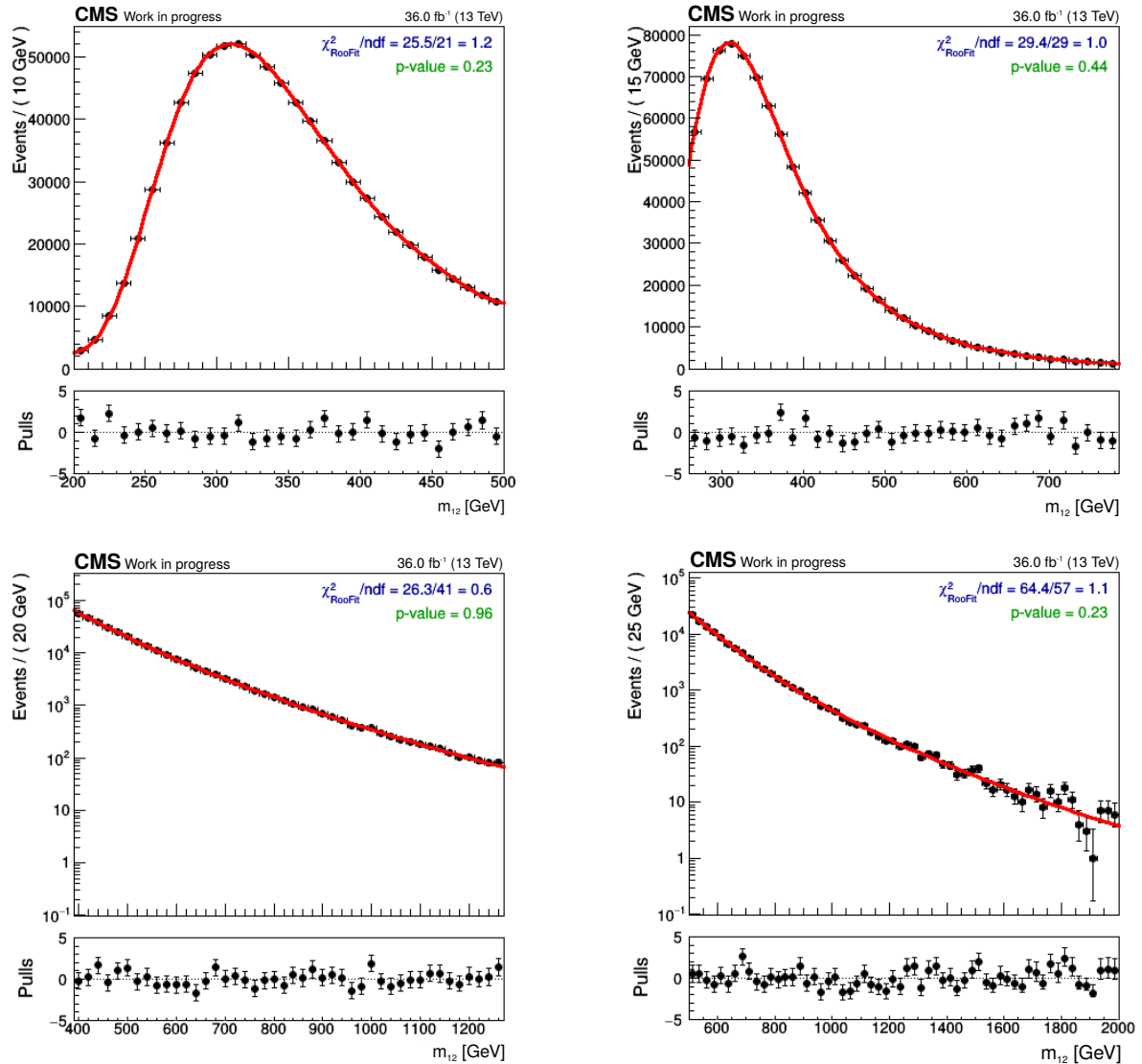


Figure 5.21.: Background parametrization results in CR fit ranges. FR 1 (top left) is modeled based on a Bernstein polynomial multiplied with a turn-on function, while the same functional form of the turn-on multiplied to an extended Novosibirsk function is well-suited to describe the mass distribution in FR 2 (top right). FR 3 and 4 (bottom left and right, respectively) are described based on a Novosibirsk function.

5. Search for Heavy, Neutral Higgs Bosons Decaying into a Pair of b Quarks

Fit range	Function (CR)	n_{par} (CR)	Range [GeV]	Fit prob.	χ^2/ndf	Mass Points
1	Bernstein \times erf	9	200–500	23 %	26/21 = 1.2	300, 350, 400
2	ext. Novo. \times erf	6	260–785	44 %	29/29 = 1.0	400, 450, 500 600, 700
3	Novosibirsk	3	390–1270	96 %	26/41 = 0.6	700, 800 900, 1000
4	Novosibirsk	3	500–2000	23 %	64/57 = 1.1	1000, 1200 1400, 1600

Table 5.9.: Fit ranges with parametrization function, mass range and assigned mass points as well as fit probability and corresponding χ^2/ndf value. The signal samples which are covered within two fit ranges, are evaluated in both of them. At each FR border, there is one overlapping mass point: 400 GeV (FR 1/2), 700 GeV (FR 2/3), and 1000 GeV (FR 3/4).

5.8.2. Transfer Factor Studies and B-Tag Weighting

Together with the CR parametrization, the transfer factor (TF) is the second integral part of the background estimation in the SR. Therefore, its shape determination is crucial for the analysis. The SR can not be used to determine the TF shape as it is blinded and also could contain a signal contribution which should not be modeled by the TF. Also the existing, unblinded 2016 signal region is not suitable since the selection as well as the detector were slightly different and due to the lack of a semi-leptonic channel, different processes are still present in the data set. Furthermore, any use of a signal region might introduce some kind of bias in the shape determination. Hence, a fully MC-based approach is chosen. After extracting a shape for the TF, the actual parameters will be determined based on the SR data in the simultaneous fit.

To obtain a general insight on how the TF might be shaped, b-enhanced QCD MC samples are utilized. As a first approach, the full mass range from 200 to 2000 GeV is investigated and the ratio of the mass distributions in the SR and CR is calculated. This ratio is shown in Figure 5.22. It is characterized by a relatively steep increase at the very beginning, a plateau from about 250 to 1000 GeV and, subsequently, a mild decrease. An initial fit is shown in Figure 5.22 as well, based on a Gaussian error function multiplied by a linear factor to model the decrease at higher masses,

$$f(m_{12}) = A \operatorname{erf}(C[m_{12} - B]) \cdot (1 - s \cdot m_{12}), \quad (5.13)$$

where s is the slope parameter of the linear term and the error function as well as the respective modification parameters are defined in Equations 5.7 and 5.8. It can be seen that, while the overall description seems reasonable, both the lowest and highest parts of the mass spectrum

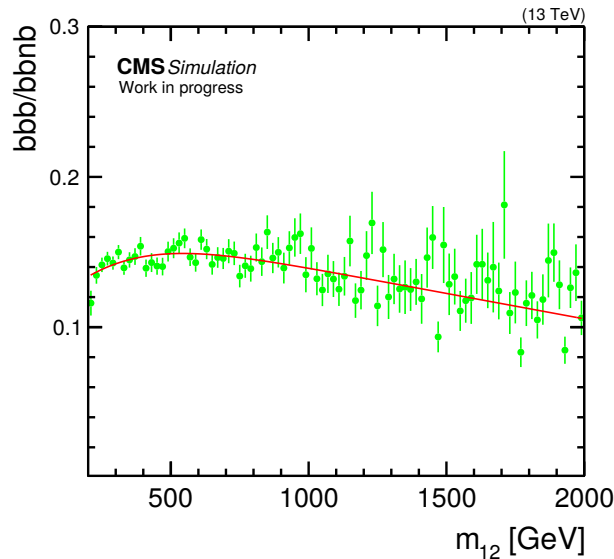


Figure 5.22.: First attempt of determining a TF shape for the full mass spectrum, based on the m_{12} distributions in SR and CR, which are extracted from b-enhanced QCD MC samples, and a fit with a Gaussian error function multiplied by a linear term. While the bulk of the data is described well, this is not true for the rather sharp increase at the beginning and the highest mass range, where also significant statistical errors prevail.

are not fitted well. This issue can be solved partially by fitting the TF in the same FR as the CR. Otherwise, despite the slowly varying nature of the function, introducing a large number of additional parameters to the fitting function would become necessary in order to describe the full range. In addition, however, especially for the higher mass range, significant statistical errors are observed. Although the shape determination might still be possible, it is not expected to be reliable based on such large errors. Thus, an increased statistical precision is required as well as the parametrization in fit ranges.

As a solution to decrease the dominant statistical errors in the high-mass range, it is more economic not to cut a majority of the events based on the b-tagging discriminant. Therefore, these events are kept and a weight is assigned to each of them, based on the b-tag efficiency with respect to the actual jet flavor which is known in MC data sets by construction. This method is hence called b-tag weighting and it allows to use significantly more events to determine the TF shape, correspondingly reducing the statistical error. The calculated efficiencies are shown in Figure 5.23, depending on five specifically defined jet flavors as well as the η and p_T of the investigated jet.

5. Search for Heavy, Neutral Higgs Bosons Decaying into a Pair of b Quarks

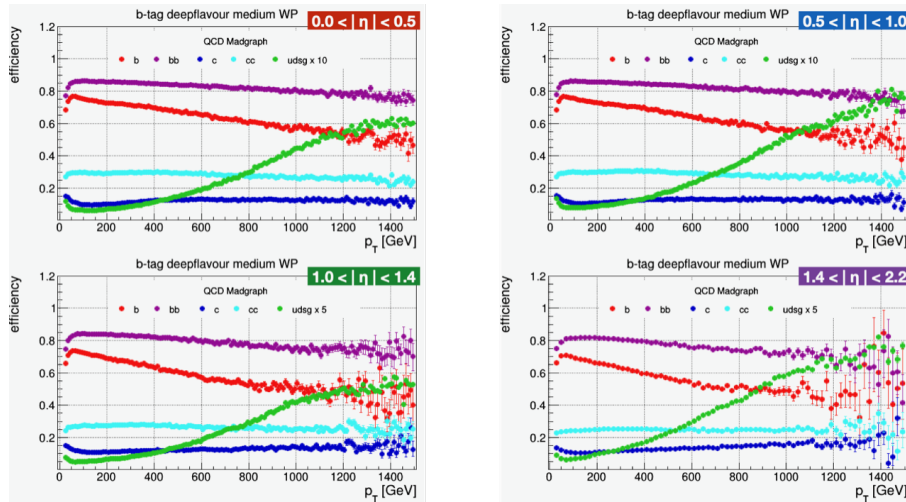


Figure 5.23.: B-tagging efficiencies for the medium working point of the DeepJet algorithm, here denoted by its old name “deepflavour”, depending on the corresponding jet p_T and η as well as the jet flavor. Note that for this method, five flavors have been defined specifically, differentiating between single (b) and double (bb) b-tags, single (c) and double (cc) c-tags and light flavors ($udsg$). The efficiency for the latter is multiplied by a factor of 10 in this depiction for visibility reasons only. The efficiencies are calculated based on MadGraph QCD samples. Taken from [190].

Before applying the b-tag weights to the events and proceeding with the TF shape determination, it has to be ensured that this new method does not alter the shape of the analyzed distributions. Therefore, a wide variety of closure tests is performed, comparing the distributions of various kinematic quantities as extracted from the utilized b-enhanced QCD samples based on the cut- and weight-based approaches, respectively. Some examples for such tests are shown in Figure 5.24. As can be seen, neither the normalization nor the shape of the distributions are significantly distorted, while the statistical errors for the weight-based distributions, predominantly in the SR, are drastically decreased. Thus, the method is considered to be save to use and promises significant improvements.

Utilizing the weight-based selection, the TF is calculated. The result is shown in Figure 5.25 together with a rescaled version of the cut-based TF which is shown in Figure 5.22. Again, while the shape is not altered, the statistical errors are significantly decreased in the weight-based selection. This effect is most pronounced in the high-mass range where significant errors are present in the cut-based distribution. Additionally, the slight downward trend towards higher masses is visible more clearly.

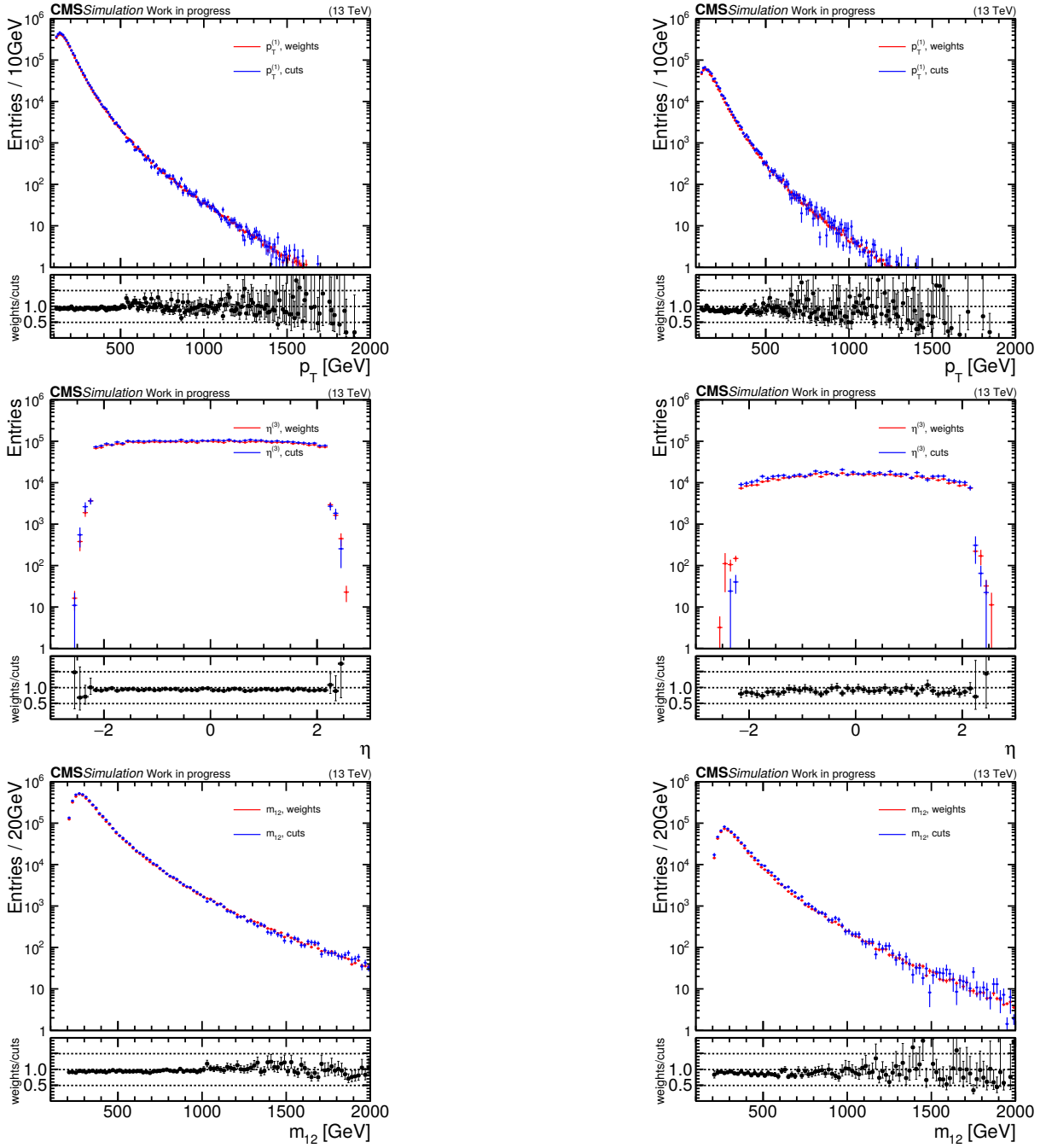


Figure 5.24.: Selected closure tests for the b-tag weighting method, showing comparisons of cut- and weight-based distributions in the CR (left) and SR (right) for the p_T of the leading jet (top), η of the third leading jet (center), and m_{12} (bottom). For each pair of distributions, their ratio is shown in the respective bottom panel. No significant changes in shape or normalization are present.

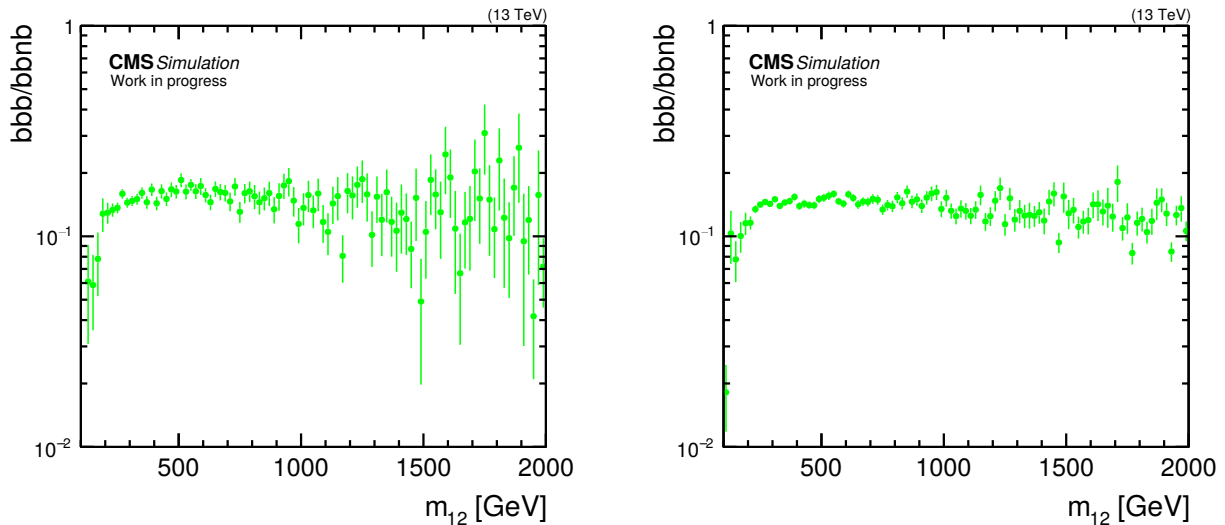


Figure 5.25.: B-tag-cut- (left) and b-tag-weight-based (right) ratios of m_{12} in SR and CR, as extracted from b-enhanced QCD MC samples. A drastic reduction of statistical errors, mainly for larger masses, is visible for the weight-based approach. The downward trend towards higher masses becomes clearer.

5.8.3. Transfer Factor

By incorporating the b-tag weighting method and dividing the assessment of the TF into four fit ranges in the same way as the CR, a good qualitative description of the TF shape can be obtained. The corresponding four m_{12} ratios of SR and CR are shown in Figure 5.26. While the same features are observed as for the full mass range, the breakdown into fit ranges enables a more precise assessment of these structures. In FR 1, the main characteristic is the turn-on like behavior in the low-mass range, originating from the presence of gluon-radiation events in the CR, i.e. a $b\bar{b}g$ parton-level final state, due to the b-tag veto on the third leading jet. FR 2 features an almost flat ratio of SR and CR distributions, slightly impacted by both the rise at low masses and the decrease towards higher m_{12} values. The third and fourth fit range are dominated by the decrease at high masses, although in FR 3, also a slight downward trend at the low-mass end is observed.

For all FR, a simple TF shape is desired, as described at the beginning of this section. However, restricting the function too much at this point might lead to issues later on if the SR behavior in the data differs from the MC expectation. In the analysis using the 2016 data set, a brief comparison of CR and SR was done, showing sigmoid-like behavior similar to the MC-based observations discussed here. Therefore, such functions are considered as most promising candidates to describe the TF shape.

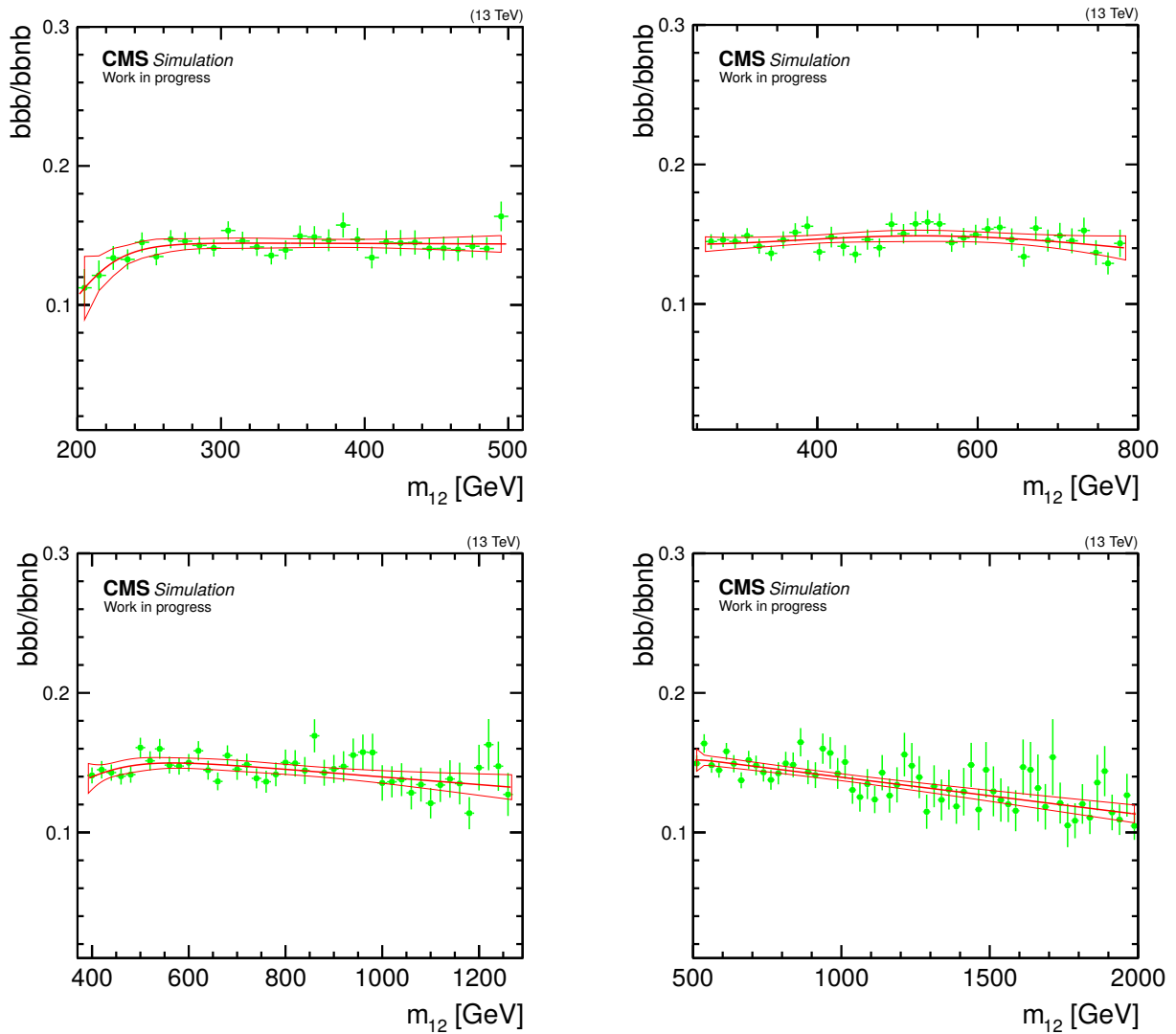


Figure 5.26.: Ratios of m_{12} in SR and CR, based on the b-tag weighting method, evaluated in the same fit ranges as the CR. Fits with respective error bands reflecting one standard deviation are also shown. They are based on an extended modified logistic function for FR 1, FR 2, and FR 3, while FR 4 is modeled using an extended error function. All fits describe the data very well, including all dominant features in the respective fit range.

5. Search for Heavy, Neutral Higgs Bosons Decaying into a Pair of b Quarks

Fit range	Function (TF)	n_{par} (TF)	Range [GeV]	Fit prob.	χ^2/ndf
1	ext. mod. logistic	4	200–500	89 %	17/25 = 0.7
2	ext. mod. logistic	4	260–785	78 %	24/30 = 0.8
3	ext. mod. logistic	4	390–1270	33 %	45/42 = 1.1
4	ext. erf	3	500–2000	73 %	49/56 = 0.9

Table 5.10.: TF fit results in the four fit ranges, together with the number of free shape parameters as well as the resulting χ^2/ndf and probability values, showing a very good description of the data in all fit ranges

After fitting the ratio of the SR and CR m_{12} distributions in each fit range with various adaptations of Gaussian error functions as well as logistic functions, for the fit ranges 1, 2, and 3, an extended modified logistic function is chosen,

$$f(m_{12}) = \frac{1 + \alpha \exp[-k(m_{12} - x_0)]}{1 + \exp[-k(m_{12} - x_0)]} \cdot (1 - s \cdot m_{12}), \quad (5.14)$$

where α is the modification parameter and the linear term is defined in the same way as in Equation 5.13. For a value of $\alpha = 0$ (and without the linear term), the original logistic function is obtained, while $\alpha = 1$ leads to a flat function and $\alpha > 1$ models a downward step instead of a rise in the low-mass region. The extended modified logistic function is found to provide a very good description of the data while not featuring an excessive amount of parameters which may become redundant. This function is very flexible on both sides of the fit range due to the modification parameter, which allows for variations in the steepness and direction of the initial rise, as well as the linear term modeling any decrease, or even increase, towards higher masses. This allows for the use of the extended modified logistic function not only for the modeling of the SR/CR TF, but also for the VR/CR TF, which is important for the validation of the overall strategy as detailed in Section 5.9.

For FR 4, where an almost entirely linear behavior is observed, the extended modified logistic function is found to be too complex, leading to parameters being redundant. Therefore, an extended version of the Gaussian error function, as defined in Equation 5.13, is selected. An overview of all function choices, the respective number of parameters, and the fit quality is given in Table 5.10.

5.8.4. Bias Study

By selecting a particular analytical description of the background, a potential systematic uncertainty may be introduced. The target of a bias study is to evaluate this uncertainty by comparing

Fit range	Nominal function (TF)	n_{par} (TF)	Range [GeV]	Alternative Functions
1	ext. mod. logistic	4	200–500	ext. erf; ext./mod. logistic
2	ext. mod. logistic	4	260–785	ext. erf; linear
3	ext. mod. logistic	4	390–1270	ext. erf
4	ext. erf	3	500–2000	ext. mod. logistic

Table 5.11.: Nominal and alternative TF descriptions in each fit range with the corresponding number of free shape parameters

the amount of signal which is identified in the analyzed data set based on different models for the TF description. The signal strength parameter $\hat{\mu}$ is chosen as a measure. It is defined as the ratio of the number of observed and expected signal events. Here, the expectation value is the sum of the background-only prediction and the signal template. For example, in any BSM search based on a specific signal assumption, like presented here, $\hat{\mu} = 0$ equals the background-only, i.e. SM, hypothesis, while $\hat{\mu} = 1$ indicates that a signal exactly identical to the respective signal hypothesis is observed. In the context of this analysis, all signal templates are normalized such that the production cross-section of the Higgs boson equals 1 pb.

Previous studies were based on rather complex background functions. Contrasting, the SR background in this analysis is described as the product of a description of the CR, which is well-defined due to the large statistical power of this region, and a relatively simple TF describing the differences of CR and SR shapes. As the CR absorbs most of the complexity, no significant bias is expected due to the choice of the transfer-factor function. Furthermore, the slowly varying nature of this function also limits the choice of different functional families. Nevertheless, a quantitative assessment of the systematic error due to the functional form of the TF is performed for each individual FR. As mentioned in Section 5.8.3, adaptations of both the logistic function and the Gaussian error function are found to describe the TF distributions well. In FR 2, as the TF appears almost flat, also a linear description seems reasonable. Table 5.11 summarizes the considered functions in each FR.

In order to calculate the bias, Asimov data sets are used, which are generated based on the CR parametrization and the nominal TF parameters as extracted from the MC study described in Section 5.8.3. Together with various amounts of injected signal events, these data sets serve as the test statistic [191]. A large number ($\mathcal{O}(5000)$) of Asimov data sets is generated in this way for each of the injected signal strengths $\hat{\mu}_{\text{inj}} = \{0, 1, 2, 3\}$, based on the most complex TF parametrization considered for the respective FR. These data sets are then fitted based on all of the alternative TF options, using a signal-plus-background fit, which minimizes the negative log-likelihood function (see Section 5.10.1).

By performing the signal-plus-background fit in the CR and Asimov-SR simultaneously, the signal strength is extracted in the same way as it is done for the main analysis. For each generated Asimov data set, a corresponding fitted signal strength $\hat{\mu}_{\text{fit}}$ is obtained as well as a respective fit uncertainty on this signal strength, $\hat{\sigma}_{\text{fit}}$. As a consistency check, the same TF shape can be used to generate the Asimov data sets and to perform the signal-extraction fit. In this case, the expectation value $\langle(\hat{\mu}_{\text{inj}} - \hat{\mu}_{\text{fit}})/\hat{\sigma}_{\text{fit}}\rangle$ should be consistent with zero. For different shape descriptions, the bias is quantified as,

$$B = \frac{\hat{\mu}_{\text{inj}} - \hat{\mu}_{\text{fit}}}{0.5(\hat{\sigma}_{\text{fit}}^+ + \hat{\sigma}_{\text{fit}}^-)}, \quad (5.15)$$

where $\hat{\sigma}^{\pm}$ correspond to the fit error in positive and negative direction, respectively. This distinction allows to take into account that the error might be asymmetric. Each bias value calculated in this way is then filled into a histogram, which is subsequently fitted by a Gaussian function. The mean of this Gaussian is the expectation value defining the actual bias for this particular combination of injected signal strength, generator TF function and fit function. The width of the Gaussian is expected to be unity which confirms the correct estimation of the signal strength uncertainty. An example for the 400 GeV mass point in FR 1 is shown in Figure 5.27. The resulting distribution of bias values is well described by a Gaussian with a width of $\sigma_G = 1.00$ and a mean of $\mu_G = -0.07$. Hence, the resulting bias equals -7% . Calculating bias values for each $\hat{\mu}_{\text{inj}}$ and each alternative TF function leads to the bias values shown in Figure 5.28. These results are observed to be almost independent of $\hat{\mu}_{\text{inj}}$, implying a good reliability of the fitting procedure. A conservative estimate of the bias for the entire fit range is targeted, represented by the dotted red lines in each plot. These assigned bias values equal 30% for FR 1 and 2 and 10% for FR 3 and 4. This is, as expected and discussed above, significantly smaller than in previous analyses which were based on the more complex analytical models in the SR.

5.9. Signal Extraction and Validation

5.9.1. Simultaneous Fit

As mentioned earlier, the signal extraction is performed based on a simultaneous binned maximum-likelihood signal-plus-background fit of the CR and SR. Generally, this involves a function

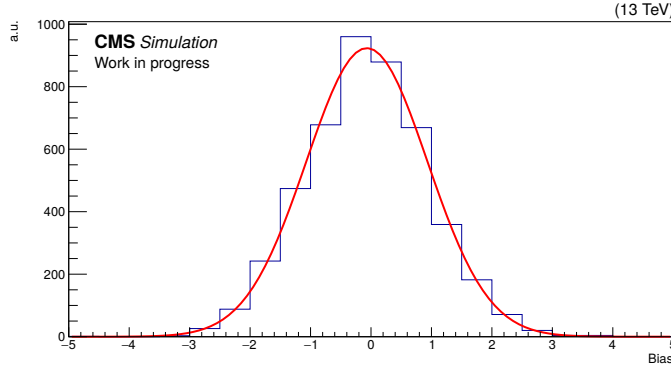


Figure 5.27.: Distribution of individual bias values of about 5000 Asimov data sets for the 400 GeV mass point in FR 1 with an injected signal strength of $\hat{\mu}_{\text{inj}} = 1$. An extended modified logistic function is used to model the TF in the data set generation and a modified logistic function serves as the respective fit function. The obtained mean and width of the Gaussian fit are $\mu_G = -0.07$ and $\sigma_G = 1.00$, indicating a bias of -7% .

describing the expected number of events in the CR and SR, respectively:

$$f_{\text{CR}}(m_{12}) = c \cdot f_c(m_{12}, \vec{\theta}_c) \quad (5.16)$$

$$f_{\text{SR}}(m_{12}) = s \cdot f_t(m_{12}, \vec{\theta}_t) \cdot f_c(m_{12}, \vec{\theta}_c) + \hat{\mu} \cdot f_{\text{sig}}(m_{12}, \vec{\theta}_{\text{sig}}), \quad (5.17)$$

where f_c and f_t represent the models of CR and TF, respectively, and c as well as s represent normalization parameters, while $\hat{\mu}$ reflects the signal strength. $\vec{\theta}$ describes the corresponding set of systematic uncertainties for each function, i.e. the shape parameters of the CR parametrization and the TF shape or the nuisance parameters for the signal template, respectively. All shape and nuisance parameters are determined in the combined signal-plus-background fit of CR and SR. The result of such a fit is shown in Figure 5.29 for an Asimov data set of both the CR and the SR. It can be seen that the combined fit describes both regions very well, as is expected for an Asimov data set without injected signal. Note that this plot is rebinned for presentation purposes only. The actual binning is chosen as fine as possible in order to allow the fitting procedure to rely on as many observables as possible. Hence, a 1 GeV binning is chosen for the fits in FR 1 and 2, while a 5 and 10 GeV binning are found to work well in FR 3 and 4, respectively.

In addition to the fit curve, it is also instructive to analyze the pulls and impacts of the corresponding fit parameters. This is done using Figure 5.30, showing these values for one representative mass point per FR. Note that a signal corresponding to $\hat{\mu}_{\text{inj}} = 1$ is injected in order to perform a test where $f_{\text{sig}} \neq 0$ and, thus, obtain actual information on the respective behavior of

5. Search for Heavy, Neutral Higgs Bosons Decaying into a Pair of b Quarks

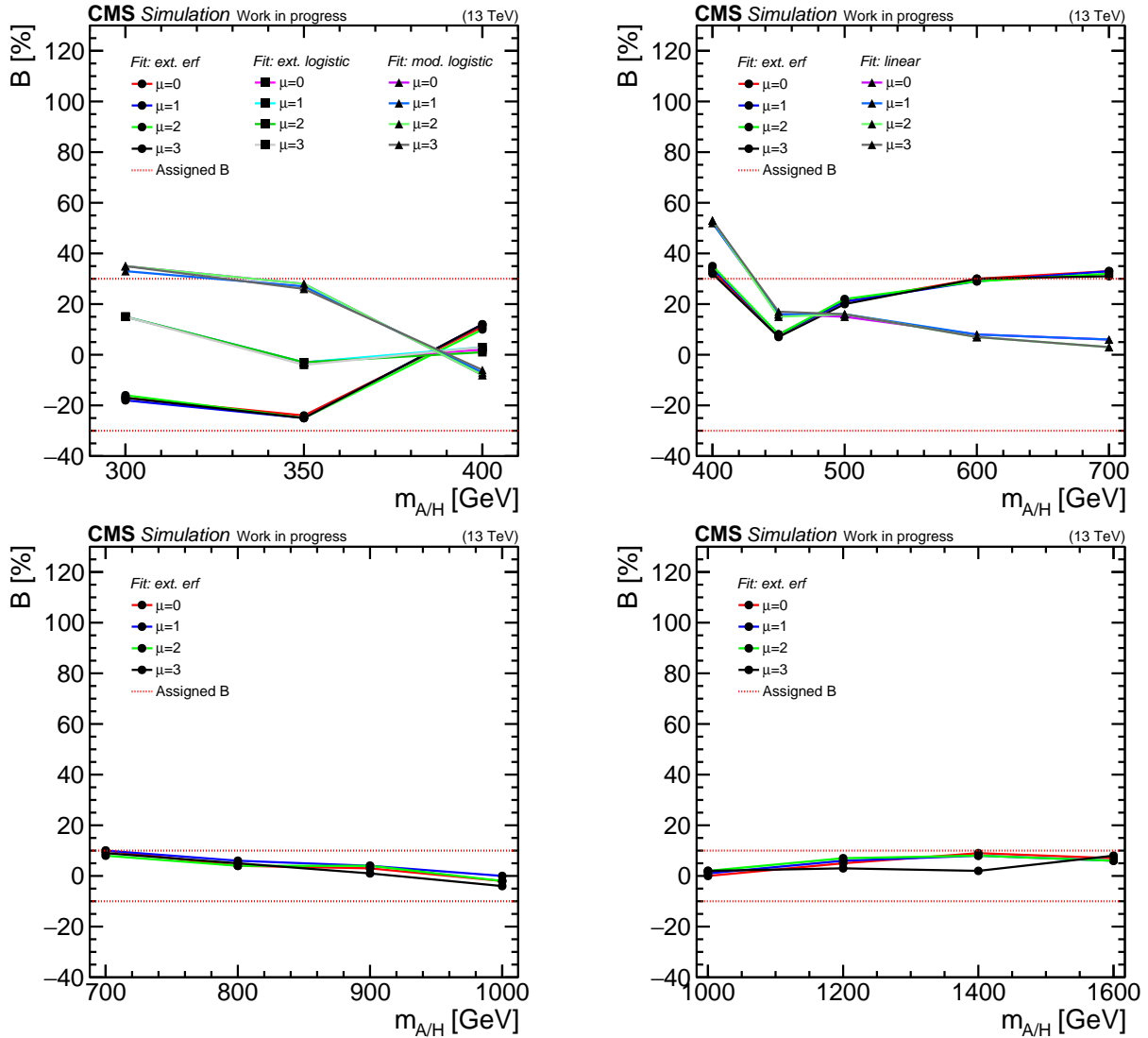


Figure 5.28.: Bias results in percent for the four fit ranges. While in FR 1 three alternative functions are considered, there are only two in FR 2 and one in FR 3 and 4. The dotted red lines represent the assigned bias for the respective FR, which is defined by a conservative estimate based on the individual results.

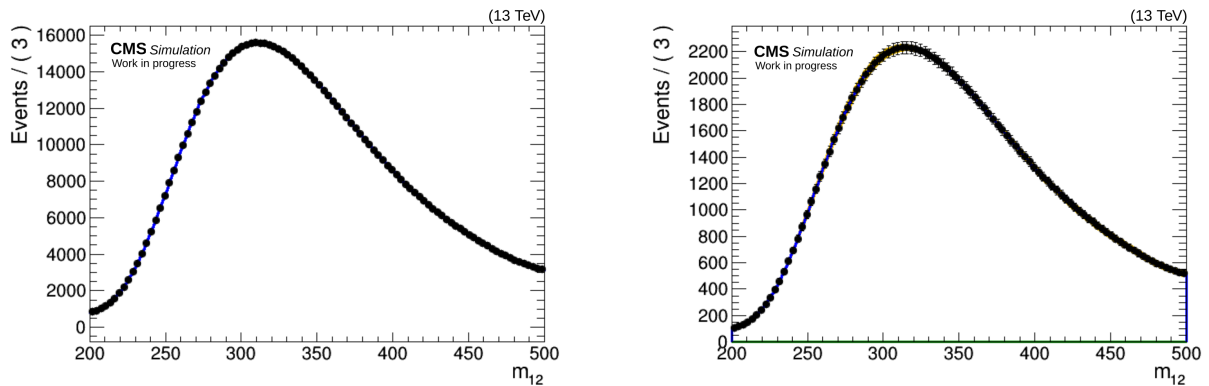


Figure 5.29.: Combined fit of Asimov data sets for the CR (left) and SR (right) for the 400 GeV mass point, evaluated in FR 1. The background fit is represented by the blue curve, which describes the data well and is mostly covered by the data points. The fitted signal is shown in green and found to be compatible with zero.

the nuisance parameters. The background shape parameters from the CR are heavily constrained by construction due to their large priors and their overall impact to the total fit uncertainty is relatively small. It can also be seen that no nuisance parameter associated with a systematic uncertainty is significantly constrained or pulled in this fit, which reflects the expected behavior. Major impacts are observed due to the TF parameters and the SR normalization, the latter representing the relatively small number of events in this region.

5.9.2. Validation of Signal-Extraction Approach

After establishing the approach based on Asimov data sets, an additional test with real data is performed exploiting the validation region. Due to a relatively similar number of events compared to the signal region, the VR is very well-suited for such a verification. However, the signal templates are not adjusted, i.e. they reflect the selection in the SR and not the VR. Thus, while the fitting and signal-extraction procedure can be validated, the calculated cross-sections and limits are not meaningful. Similar validations are performed as for the Asimov data sets, only that actual data is used in both the CR and VR. Results of the simultaneous fits as well as pulls and impacts of the nuisance parameters are shown for the data CR and VR in Figures 5.31 to 5.33. As with the Asimov data, all plots are rebinned for better visibility of the fit result. Both CR and VR are very well described by the fit results and all fitted signal strengths are compatible with zero. It can be seen in Figure 5.33 that no systematics-related nuisance parameter is significantly constrained. Some parameters are, however, found to be skewed in one direction. This can mostly be related to constraints, e.g. that the α parameter

5. Search for Heavy, Neutral Higgs Bosons Decaying into a Pair of b Quarks

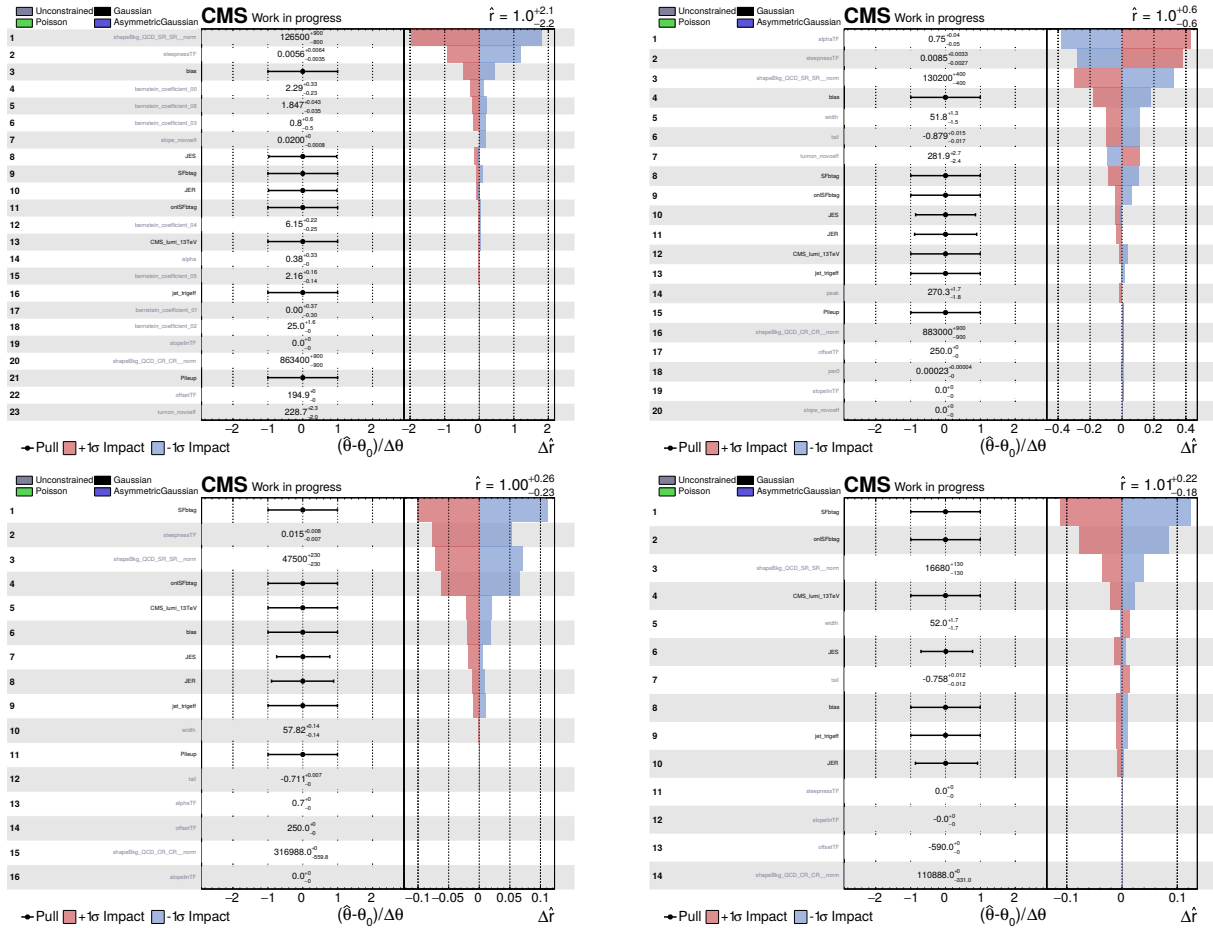


Figure 5.30.: Pulls and impacts for the 400 (FR 1, top left), 600 (FR 2, top right), 900 (FR 3, bottom left), and 1200 (FR 4, bottom right) GeV mass points, based on Asimov data sets for both CR and SR with an injected signal strength of 1, which is also returned by each fit result, as can be seen on the top right of each plot. No nuisance parameter related to a systematic uncertainty is found to be significantly constrained and major impacts are observed due to the TF parameters and the SR normalization.

of the extended modified logistic function is forbidden to become negative in order to avoid the possibility of negative expected bin contents. Also some of the parameters are significantly correlated and their impacts may therefore cancel partially.

Based on the validated fitting procedure, the signal extraction is performed as it is done for the SR and expected as well as observed limits are calculated accordingly. The results are shown in Figure 5.34. As can be seen, all observed limits agree with the expectation within two standard deviations, indicating no signal-like structure or any kind of significant excess or deficit in the VR.

The tests performed using the VR demonstrate the reliability of the background description and the signal-extraction procedure.

5.10. Statistical Procedures

Searches like presented in this analysis target a certain signal hypothesis which would for example be visible in a distribution of data as an excess in a specific region. In case no such excess is observed, exclusion limits are set on the investigated region of the phase space of the model. In the context of this analysis, the signal hypothesis corresponds to the simulated signal data sets. The background-only hypothesis, on the other hand, is represented by the control-region parametrization and the transfer factor. Exclusion limits are calculated for the production cross-section times branching ratio for a heavy, neutral Higgs boson which is produced in association with two b quarks and decaying into a pair of b quarks.

The statistical calculations presented here are based on a modified frequentist approach, the “Asymptotic CLs method” [191, 192]. They are performed using the COMBINE TOOL software package [193]. It allows to treat systematic uncertainties as nuisance parameters and extract their individual impact on the final result as well as calculating the upper limit on the signal cross-section.

5.10.1. Likelihood Function and Fit

The likelihood function which is used for the analysis describes the agreement of observed data and the tested model, where the background-only hypothesis is based on known physics. For the CLs method, the probability density functions (pdfs) for the background, $f_b(\vec{x}, \vec{\theta})$, and the signal, $f_s(\vec{x}, \vec{\theta})$, are investigated. They are dependent on physical observables \vec{x} and nuisance parameters $\vec{\theta}$. The latter are used to describe systematic uncertainties affecting the measurement, e.g. the detector performance or theoretical uncertainties. For n observables, m nuisance

5. Search for Heavy, Neutral Higgs Bosons Decaying into a Pair of b Quarks

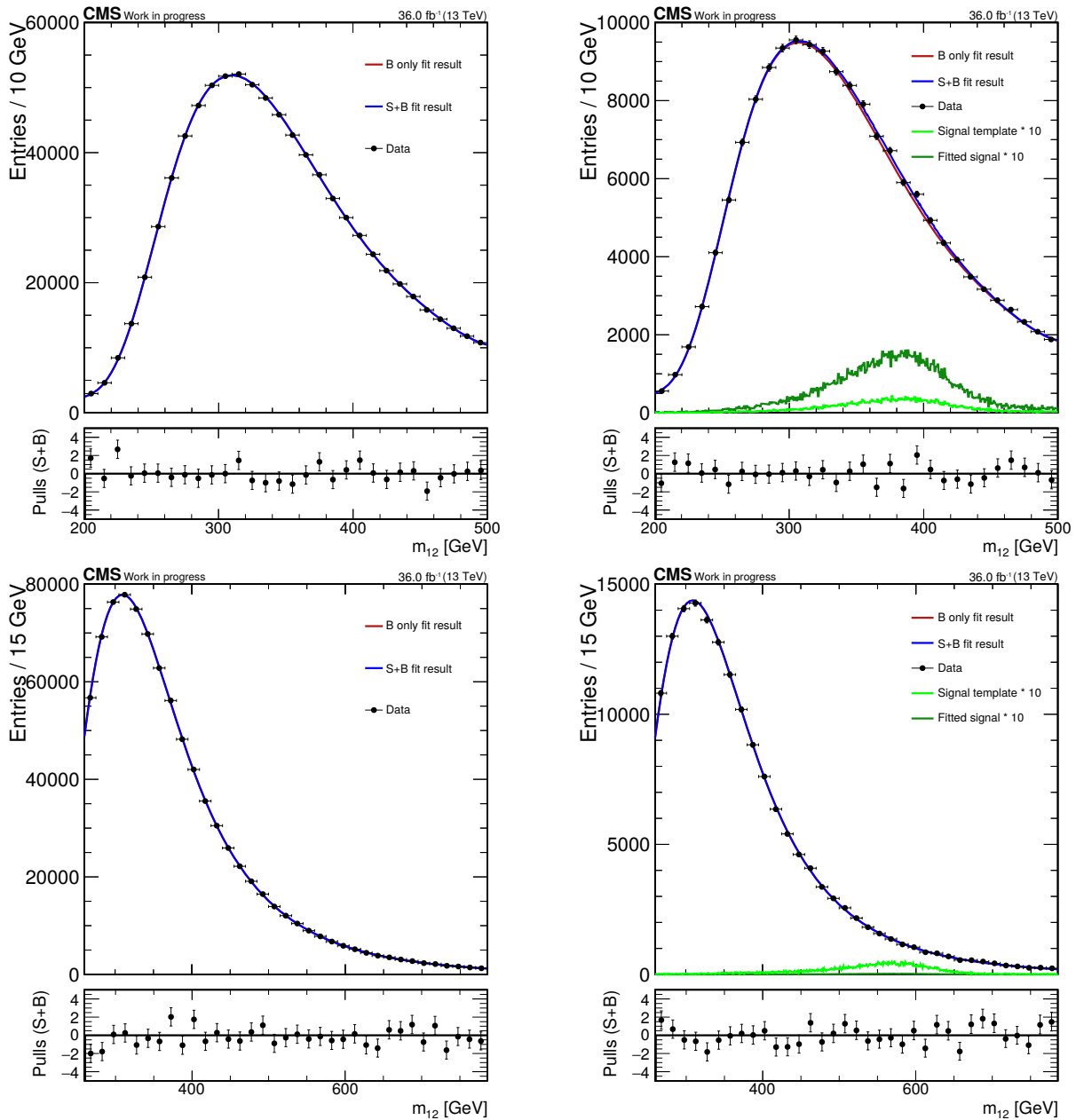


Figure 5.31.: Combined fit result of CR (left) and VR (right) for the 400 (FR 1, top) and 600 (FR 2, bottom) GeV mass points. The distributions of CR and VR are rebinned for the sake of visibility, while the fine binning in the signal template reflects the original settings. Blue and red curve are the signal-plus-background and background-only fit results, respectively, while the dark and light green curve represent the signal template and fit result. These two curves are multiplied by a factor of 10 for presentational purposes. At the bottom of each plot, the agreement of the signal-plus-background fit result and the data in the respective region is shown, defined as the difference between these two divided by the statistical uncertainty. No significant signal is observed. While the observed upward fluctuation in FR 1 exceeds the signal template, which is normalized to a Higgs boson production cross-section of 1 pb, the background fit describes the data closely in FR 2.

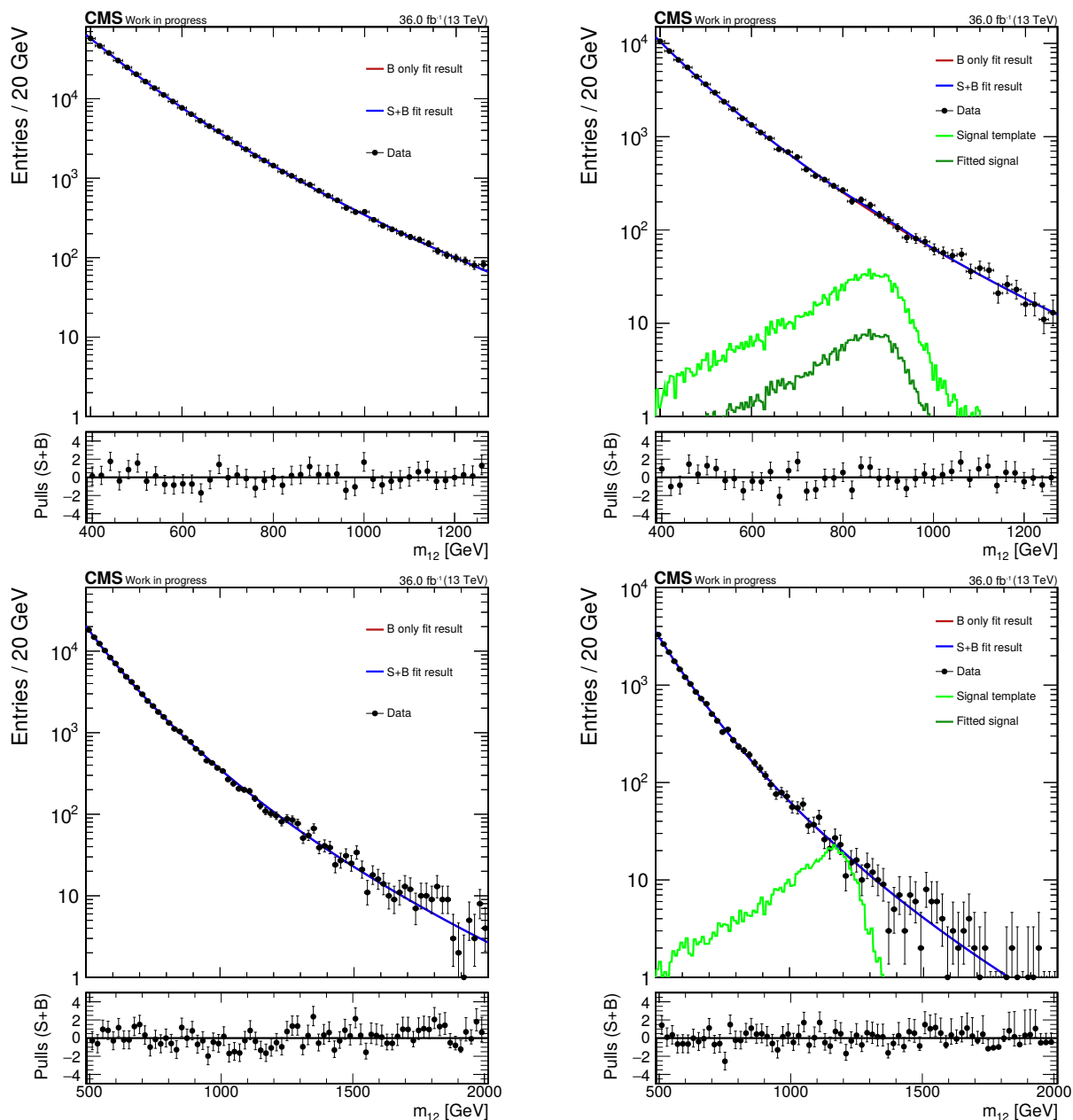


Figure 5.32.: Combined fit result of CR (left) and VR (right) for the 900 (FR 3, top) and 1200 (FR 4, bottom) GeV mass points. The distributions of CR and VR are rebinned for the sake of visibility, while the fine binning in the signal template reflects the original settings. Blue and red curve are the signal-plus-background and background-only fit results, respectively, while the dark and light green curve represent the signal template and fit result. At the bottom of each plot, the agreement of the signal-plus-background fit result and the data in the respective region is shown, defined as the difference between these two divided by the statistical uncertainty. No significant signal is observed. While the observed upward fluctuation in FR 3 is smaller than the signal template, which is normalized to a Higgs boson production cross-section of 1 pb, a negative signal strength parameter is fitted in FR 4 as reflected by the absence of a dark green curve.

5. Search for Heavy, Neutral Higgs Bosons Decaying into a Pair of b Quarks

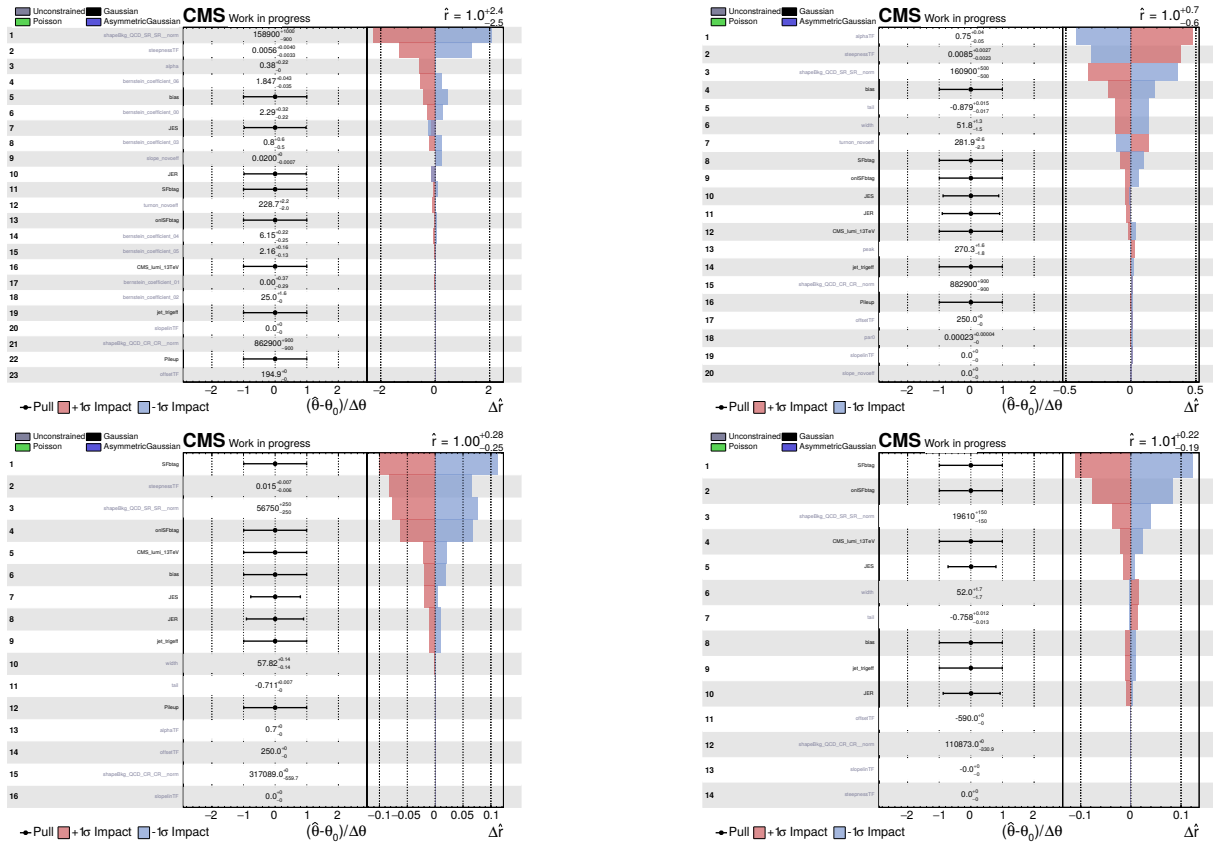


Figure 5.33.: Pulls and impacts for the 400 (FR 1, top left), 600 (FR 2, top right), 900 (FR 3, bottom left), and 1200 (FR 4, bottom right) GeV mass points, based on the simultaneous fit of CR and VR. No nuisance parameter related to a systematic uncertainty is found to be significantly constrained and major impacts are observed due to the TF parameters and the SR normalization.

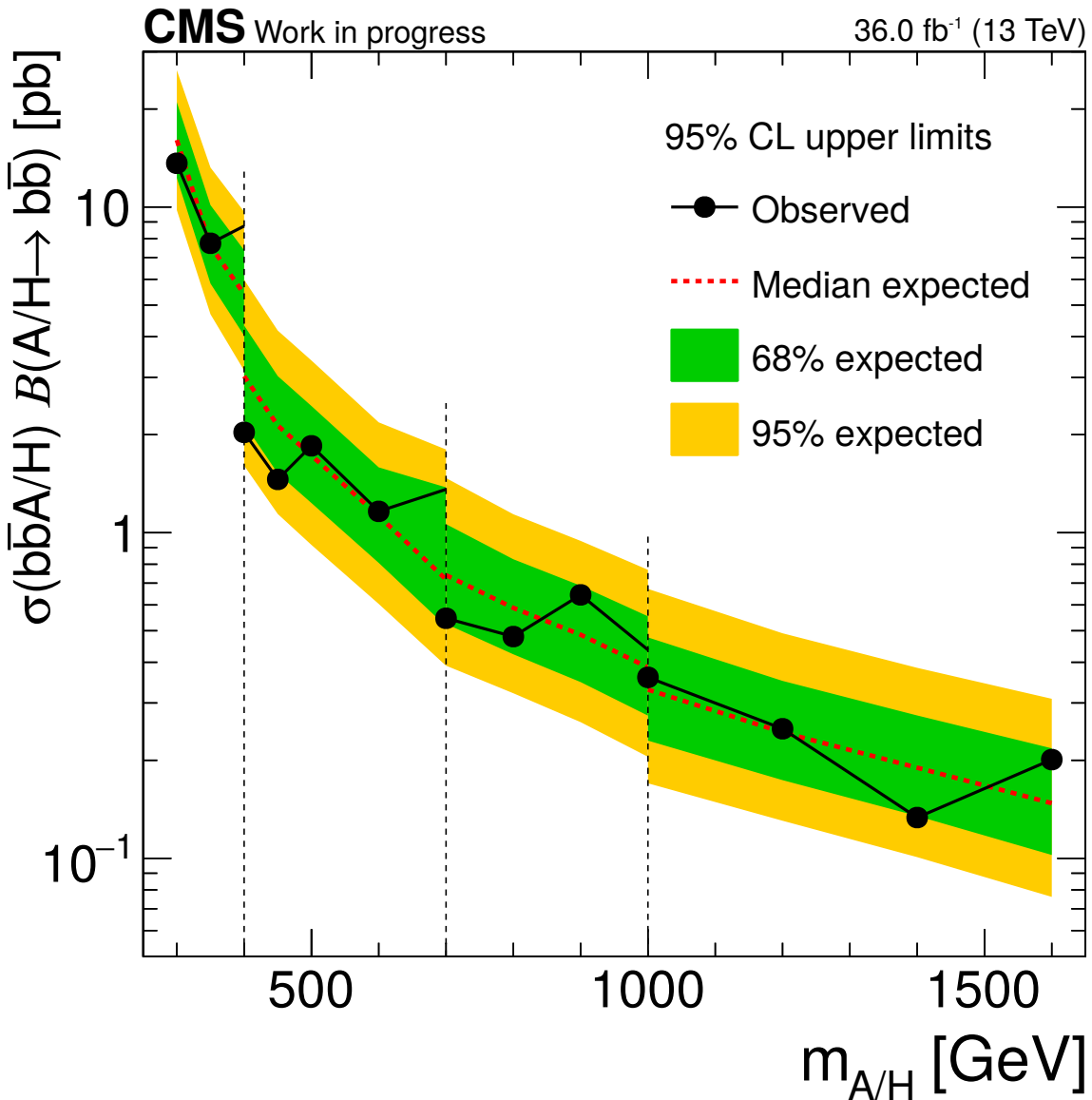


Figure 5.34.: Expected and observed model-independent limits based on the data in the validation region and signal templates covering the range from 300 to 1600 GeV. One and two standard-deviation bands are shown in green and yellow, respectively and the fit-range edges are indicated by the vertical dashed lines. Since the signal templates are not optimized for utilization in the VR, the calculated numbers for the cross-section limits do not have a meaningful physical implication.

5. Search for Heavy, Neutral Higgs Bosons Decaying into a Pair of b Quarks

parameters and N measurements, the overall likelihood can then be expressed as

$$L(\vec{x}, \vec{\theta}) = \prod_{i=1}^N L(x_1^i, x_2^i, \dots, x_n^i, \theta_1^i, \theta_2^i, \dots, \theta_m^i). \quad (5.18)$$

For one measurement, it can be written in the form

$$L(data|\mu, \theta) = P(data|\mu \cdot s(\theta) + b(\theta)) \cdot p(\tilde{\theta}|\theta). \quad (5.19)$$

Here, the likelihood is dependent on the signal strength parameter μ and the nuisance parameter θ for an actual measurement ($data$). A value of $\mu = 0$ corresponds to the background-only hypothesis, while $\mu = 1$ is the nominal signal hypothesis. In case of this analysis, the latter corresponds to a Higgs boson production cross-section of 1 pb. The total event yield is represented by the term

$$y = \mu \cdot s(\theta) + b(\theta), \quad (5.20)$$

with the expected signal and background yields, $s(\theta)$ and $b(\theta)$. $P(data|\mu \cdot s(\theta) + b(\theta))$ in Equation 5.19 reflects the probability to observe a specific number of events n_i in a bin i . Evaluating P for all bins in the data set, it is given by

$$P(data|\mu \cdot s(\theta) + b(\theta)) = \prod_i \frac{(\mu s_i + b_i)^{n_i}}{n_i!} e^{-(\mu s_i + b_i)}, \quad (5.21)$$

with the expected signal and background yields per bin, s_i and b_i . Finally, the measurement pdf p reflects the difference between a default value $\tilde{\theta}$ of a nuisance parameter and the actual measurement θ . It follows from the overall systematic-error pdf $\rho(\theta|\tilde{\theta})$ which is a prior and reflects the difference between measurement and the true value θ . Using Bayes' theorem, $\rho(\theta|\tilde{\theta})$ can be re-interpreted as a posterior:

$$\rho(\theta|\tilde{\theta}) \sim p(\tilde{\theta}|\theta) \cdot \pi_\theta(\theta), \quad (5.22)$$

where $\pi_\theta(\theta)$ are priors to the measurement. In general, it is convenient to formulate the pdf ρ of each nuisance parameter in a way that keeps $\pi_\theta(\theta)$ flat. This means that $\pi_\theta(\theta)$ does not bias the likelihood function and the measurement pdf $p(\tilde{\theta}|\theta)$ can be used instead of the prior $\rho(\theta|\tilde{\theta})$ without loss of information.

Subsequently, the likelihood function is given by

$$L(data, s, b, \theta) = L_x(data, s, b, \theta) \cdot \prod_j p_j(\tilde{\theta}|\theta), \quad (5.23)$$

where j covers all systematic uncertainties affecting the expected signal and background distribution. The two terms of Equation 5.23 are independent from each other with the first term describing the likelihood of measuring the data with the observed yield, while the second term represents the probability to find the nuisance parameters at the observed values.

During the fitting procedure, it is computationally more efficient to use a logarithmic formulation of Equation 5.23. Instead of maximizing the likelihood itself, $-2 \ln L$ (negative log-likelihood or NLL) is minimized, making the overall equation a sum instead of a product. This minimization process is performed by MINUIT [194], which is designed to find the minimum of the log-likelihood function and examine its shape around this minimum. The impact of nuisance parameters is then studied by profiling the likelihood function. This means that the respective best-fit values and uncertainties of nuisances are calculated based on the way the nuisance parameters shape the likelihood function.

In the next step, the compatibility of observed data with the background-only and signal-plus-background hypotheses is studied. This is done using the test statistic

$$q_\mu = -2 \ln \frac{L(data|\mu, \hat{\theta}_\mu)}{L(data|\hat{\mu}, \hat{\theta})}, \quad \text{with } 0 \leq \hat{\mu} \leq \mu. \quad (5.24)$$

It is based on the profile likelihood ratio with $\hat{\theta}_\mu$ representing an estimation of θ for a given $data$ and a specific value of μ . $\hat{\mu}$ and $\hat{\theta}$ refer to the overall maximum likelihood. The constraints on $\hat{\mu}$ ensure that, on the one hand, no unphysical negative signal is possible and, on the other hand, an upwards fluctuation which would lead to $\hat{\mu} > \mu$ will not be interpreted as evidence against the signal hypothesis. Mathematically, this means that a one-sided confidence interval is ensured by $\hat{\mu} \leq \mu$.

The test statistic q_μ is evaluated for the tested value of μ for the background-only and signal-plus-background hypotheses. From this q_μ^{obs} , nuisance parameter values can be calculated for both hypotheses ($\hat{\theta}_0^{obs}$ and $\hat{\theta}_\mu^{obs}$), referring to the respective signal strength and targeting the best possible description of the observed data. For the signal-plus-background hypothesis, a signal strength of μ is assumed, while for the background-only hypothesis μ is set to 0.

5. Search for Heavy, Neutral Higgs Bosons Decaying into a Pair of b Quarks

According to the Frequentist method, the pdfs $f(q_\mu|\mu, \hat{\theta}_\mu^{obs})$ and $f(q_\mu|0, \hat{\theta}_0^{obs})$ can be obtained from generated Monte-Carlo data sets. To fulfill the requirements of the asymptotic approximation and following Wilk's theorem [195], a significantly large number of test data sets has to be created.

With these pdfs, two p-values can be computed, reflecting the probability of the signal-plus-background (s+b, p_μ) and the background-only hypothesis (b, p_0), respectively. They are defined as

$$p_\mu = P(q_\mu \geq q_\mu^{obs} | \text{signal} + \text{background}) = \int_{q_\mu^{obs}}^{\infty} f(q_\mu|\mu, \hat{\theta}_\mu^{obs}) dq_\mu \quad (5.25)$$

$$\text{and } p_0 = 1 - p_b = P(q_\mu \geq q_\mu^{obs} | \text{background} - \text{only}) = \int_{q_\mu^{obs}}^{\infty} f(q_\mu|0, \hat{\theta}_0^{obs}) dq_\mu, \quad (5.26)$$

where p_μ and p_0 quantify the level of disagreement between the observed data and the signal-plus-background or background-only hypotheses, respectively.

5.10.2. Nuisance Parameters

Two major categories of systematic uncertainties affect this analysis. Both of them are expressed as nuisance parameters [196]. The first category affects the normalization of the event yield while not altering the shape of the signal.

In the most general way, normalization uncertainties could be expressed by a Gaussian distribution. This approach is well-suited for uncertainties which can be both positive and negative. For nuisances which can only be positive, however, the log-normal distribution is chosen. It avoids the necessity of truncating the Gaussian at or slightly above zero. The log-normal pdf is defined as

$$\rho(\theta) = \frac{1}{\sqrt{2\pi \ln \kappa}} \exp\left(-\frac{(\ln(\theta/\tilde{\theta}))^2}{2(\ln \kappa)^2}\right) \frac{1}{\theta}, \quad (5.27)$$

where $\tilde{\theta}$ is the best estimate of the nuisance parameter θ and κ describes the width of $\rho(\theta)$. This width parameter directly reflects the uncertainty of an observable. For example, a value of $\kappa = 1.1$ means that the parameter can be larger or smaller by a factor of 1.1, i.e. a 10% uncertainty, both with an equal probability of 16%, since uncertainties are given at one standard deviation from the central value. For small uncertainties, the log-normal and Gaussian pdfs are asymptotically identical.

The second major category of systematic uncertainties affects the shape of the data. As mentioned in Section 5.7.3, for the analysis presented here, this effect is exclusively observed

for the uncertainties associated with jet energy scale (JES) and jet energy resolution (JER).

To assess the impact of shape uncertainties on the final result, the investigated data set is evaluated not only at the central value of each uncertainty but also for its plus and minus 1σ values. From the central result, the parameter values are interpolated to the variation results. The efficiency for bin i associated with shape uncertainty j is then given by

$$\epsilon_{ij} = \epsilon_{ij}^0 + f \frac{\epsilon_{ij}^+ - \epsilon_{ij}^-}{2}, \quad (5.28)$$

where ϵ_{ij}^0 and ϵ_{ij}^\pm represent the efficiency for the central value and the up/down variations of the uncertainty, respectively, and f is the so-called morphing parameter which is centered at 0 and has a Gaussian width of $\sigma_f = 1$. Outside of the $\pm 1\sigma$ variations, the result can be linearly interpolated.

To evaluate the final result of the fitting procedure, a goodness-of-fit test is performed. In the analysis presented here, the saturated model is utilized [197, 198]. The goodness-of-fit parameter in this model resembles a χ^2 test but it is generalized such that it can be calculated for an arbitrarily binned distribution. Also arbitrary constraints can be included, e.g. truncations of Gaussian errors due to physical constraints like the requirement of a parameter to be non-negative.

5.10.3. Limit Extraction

Using the p-values discussed in Section 5.10.1 and the nuisance parameters as described in Section 5.10.2, exclusion limits can be calculated in case there is no significant signal. These limits refer to the analyzed hypothesis or physical model and are used to exclude a region of its phase space to a certain probability. This is done based on the modified confidence level

$$CL_s(\mu) = \frac{p_\mu}{p_0} = \frac{p_{s+b}}{1 - p_b}. \quad (5.29)$$

A given hypothesis is excluded with a confidence level of $1 - CL_s(\mu)$. This means that to obtain an exclusion limit of 95 %, as targeted in this analysis, CL_s has to be set to $1 - 0.95 = 0.05$.

In the same way as described above for the observation, expected exclusion limits can be calculated. Mostly, the median expected limit is given together with $\pm 1\sigma$ and $\pm 2\sigma$ uncertainty bands. This is usually done based on Asimov data sets which are generated from the background pdf with the central values for the nuisance parameters. The point at which the cumulative

5. Search for Heavy, Neutral Higgs Bosons Decaying into a Pair of b Quarks

probability distribution crosses the 50 % quantile, the median expected limit is located. In the same way, the $\pm 1\sigma$ band (68 %) corresponds to the crossings with 16 % and 84 %, while the $\pm 2\sigma$ band (95 %) is defined by the crossings at 2.5 % and 97.5 %.

6. Results

6.1. Before Unblinding

Before the data in the signal region can be unblinded, the overall analysis approach has to be developed and validated. This is done using Asimov data sets and the signal-depleted validation region, as described in Section 5.9 and shown in Figures 5.29 to 5.34, after optimizing the event selection and calculating MC corrections based on simulation and the CR. The systematic uncertainties, including a bias study, which are included in this analysis are presented in Section 5.7.3 and the statistical procedures used to extract the final results are shown in Section 5.10.

Following all the preceding steps, expected upper limits can be calculated based on Asimov data sets. These are generated utilizing the CR parametrization result and the nominal values for the TF parameters as found in the MC studies. Signal samples are evaluated in their respective fit range and those mass points which are situated at a fit-range border, are analyzed in both of the ranges.

Figure 6.1 shows the resulting expected upper limits on the Higgs boson production cross-section times the branching fraction into a pair of b quarks. They reach from slightly below 10 pb at 300 GeV down to just above 0.1 pb at 1600 GeV. Results of previous analyses [34, 174, 178] are shown for comparison and it can be seen that the search presented here provides a significantly improved sensitivity for the entire investigated mass range. It has to be noted that the semi-leptonic analysis of the 2017 CMS data is most sensitive in lower mass ranges down to 125 GeV for which it was optimized. In comparison to the 2016 CMS analysis, an improvement in sensitivity of roughly a factor of two can be observed. The steps visible in the expected upper limits reflect the borders of fit ranges and the correspondingly different signal efficiency. Overall, the limits mirror the monotonously falling di-jet mass spectrum in data. In the right plot of Figure 6.1, each mass hypothesis is only evaluated in the fit range yielding the lower expected limit, i.e. the higher sensitivity, which eliminates the discontinuities.

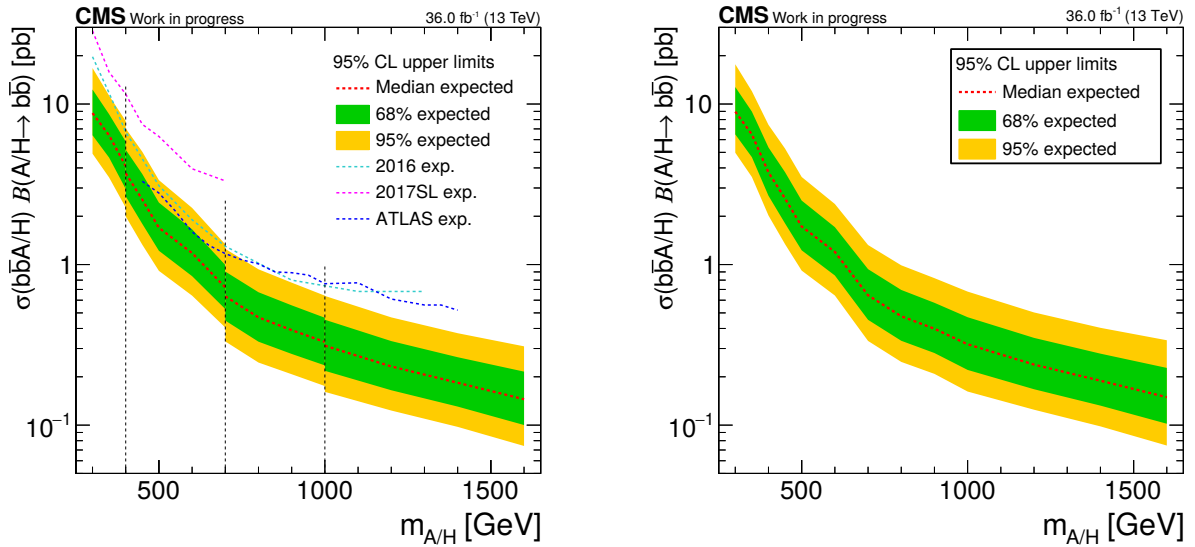


Figure 6.1.: Expected limits on the b-associated Higgs boson production cross-section times branching ratio into a pair of bottom quarks at 95 % confidence level in the range from 300 to 1600 GeV with (left) and without (right) evaluating mass points in multiple fit ranges. Dashed vertical lines in the left plot indicate the FR borders and the respective mass points are evaluated in either range. In the right plot, each mass point is only evaluated in the FR with the higher expected sensitivity. For comparison, also the results of the 2016 (cyan [178]) and the upper mass-range of the 2017 semi-leptonic (pink [34]) CMS analyses as well as the ATLAS analysis (dark blue [174]) are shown. The mass range of this analysis exceeds all of the previous studies towards high masses while providing significantly better sensitivity over a large part of the investigated mass range.

6.2. After Unblinding

The signal extraction process is performed in the way it is described in Sections 5.9 and 6.1 for each mass point in its respective fit range or fit ranges for those mass points at FR borders.

In Figures 6.2 to 6.4, the resulting fits are shown for the 400, 600, 900, 1200, and 1600 GeV mass points, i.e. one representative mass point per FR plus the 1600 GeV sample which represents the largest tested mass hypothesis. It can be seen that in all fit ranges both CR and SR are described very well. The largest overall excess with respect to the expectation is observed for the 1600 GeV mass point with slightly less than 2σ , which is not significant. This excess is also visible in the m_{12} distribution of the SR, where several adjacent bins appear to fluctuate into the upward direction. However, it has to be noted that this structure is significantly narrower than any signal resolution, as can be seen from the comparison with, e.g., Figure 5.13. It can be concluded that all fits are compatible with the background-only hypothesis within the respective uncertainties.

In order to give an additional impression of the overall fit performance, the ratio of m_{12} in the SR and CR is plotted for all four FR. As a comparison, the TF fit result is overlaid, modeled by the shape parameters as determined in the respective fit for each mass point. While there are small differences depending on the investigated signal sample, all fits describe the data remarkably well. Furthermore, the actual ratio of SR and CR in data is found to be predicted relatively well by the MC shapes which are shown in Figure 5.26, despite the discussed limitations in QCD simulation.

For each mass point, the goodness-of-fit result is investigated as well. This is shown in Figure 6.6 for the 400, 600, 900, 1200, and 1600 GeV mass points, based on 1000 toy data sets per mass point and using the saturated goodness-of-fit model (cf. Section 5.10.2). None of the respective shapes shows unexpected behavior and the corresponding p-values show a good agreement with the data.

As done for the Asimov data sets and the VR, pulls and impacts are also determined for each nuisance parameter in the SR fits. The respective results for the 400, 600, 900, and 1200 GeV mass points are shown in Figure 6.7. As before, it has to be noted that the shape parameters are significantly constrained by construction due to their large priors from the CR. No nuisance parameter which is related to a systematic uncertainty is found to be significantly constrained. Similar to the previously observed behavior using the VR, main impacts originate from the SR normalization and the TF shape parameters and it has to be kept in mind that some parameters are correlated and their respective impacts may cancel partially.

To illustrate the background description in the SR further, a background-only fit is shown in

6. Results

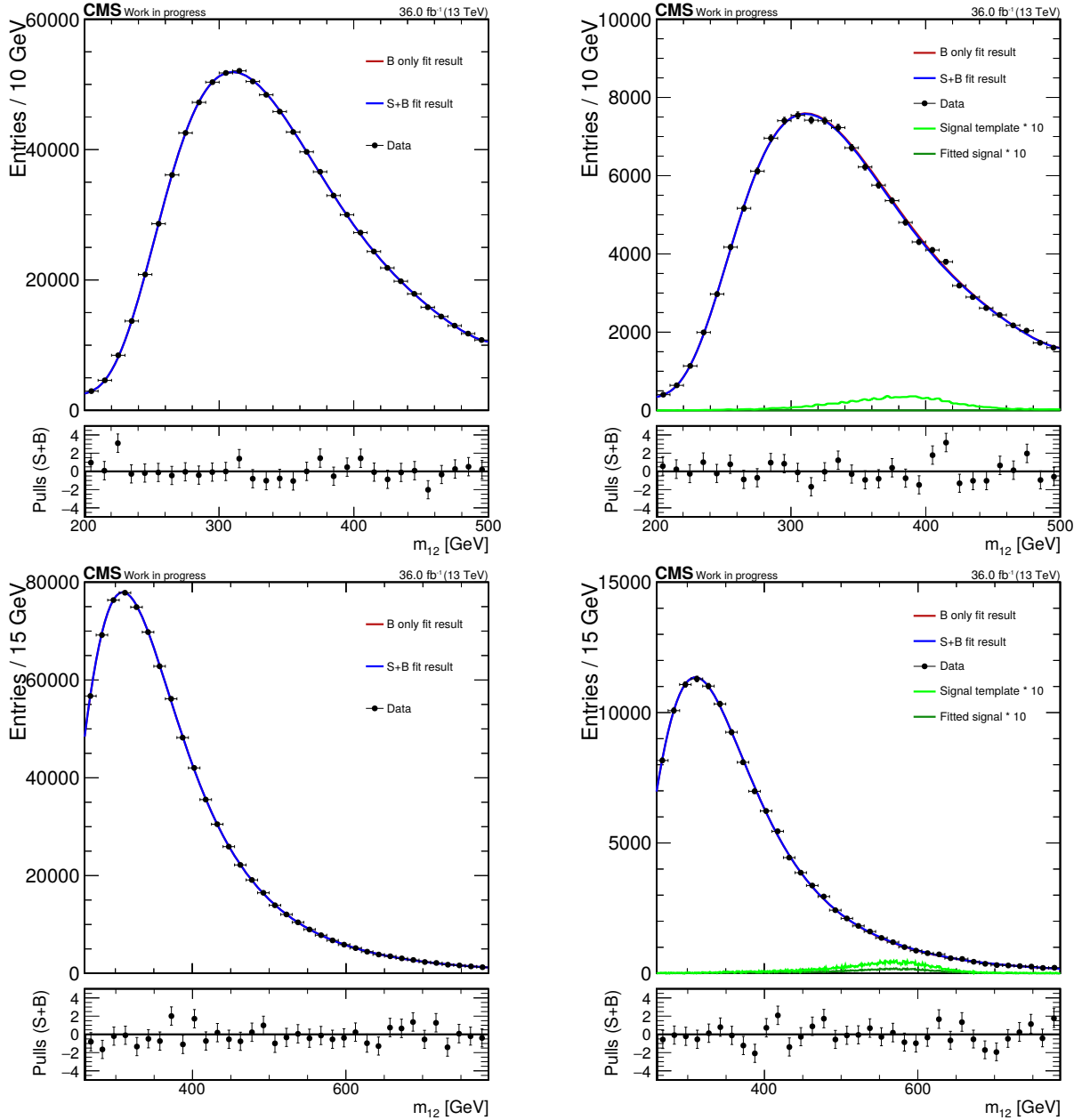


Figure 6.2.: Combined fit of CR (left) and SR (right) in fit ranges 1 (top) and 2 (bottom) with the 400 and 600 GeV mass points investigated, respectively. The red and blue curves show the background-only and signal-plus-background fit results, respectively, while the light and dark green curves represent the signal template and the fitted signal. Note that the signal curves have been multiplied by a factor of 10 for presentational purposes. For each plot, the pulls are shown in the bottom panel, defined as the difference between the signal-plus-background fit result and the data, divided by the statistical uncertainty. With a very good overall description of the data in both CR and SR in either FR, no significant signal is observed.

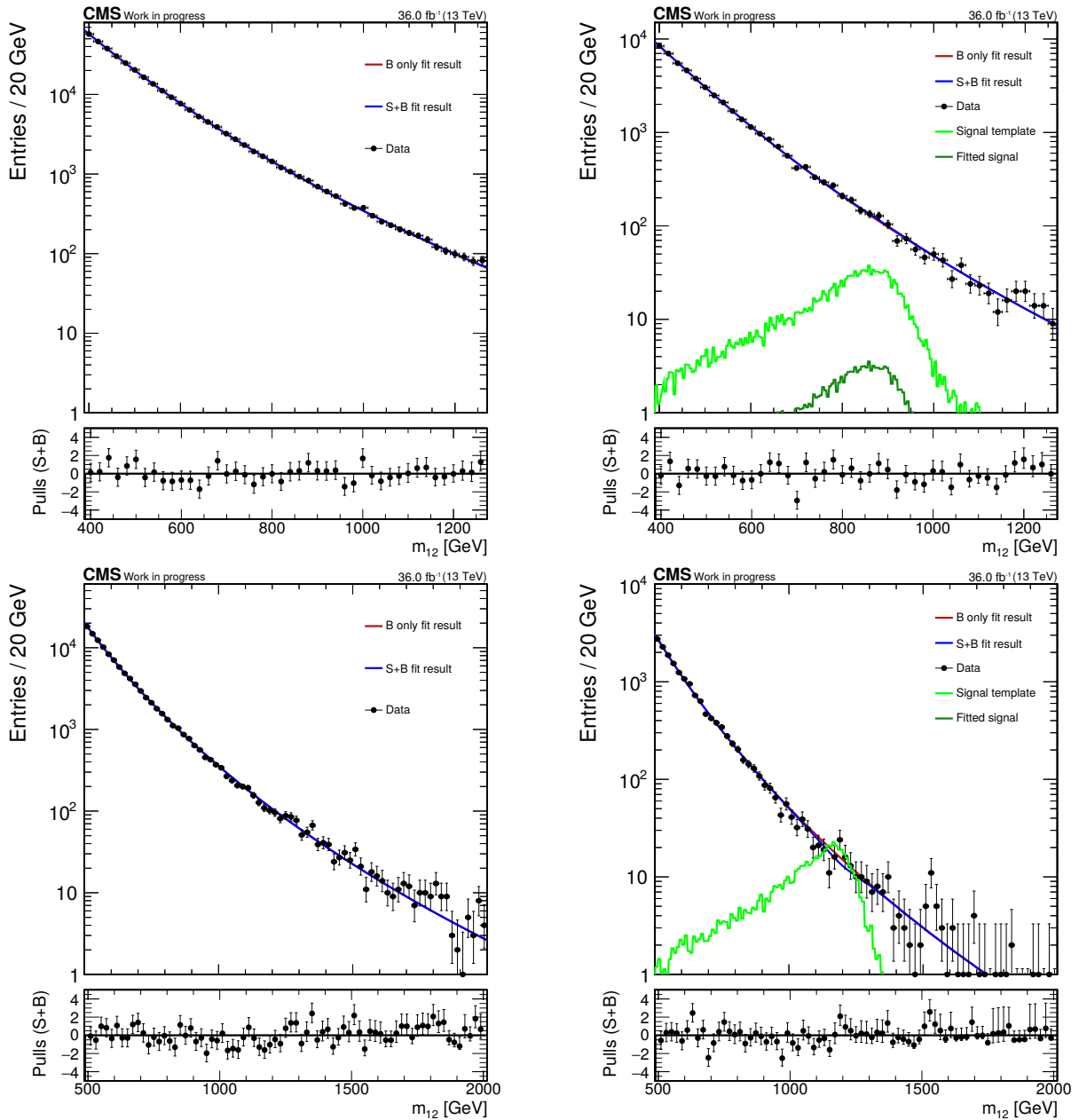


Figure 6.3.: Combined fit of CR (left) and SR (right) in fit ranges 3 (top) and 4 (bottom) with the 900 and 1200 GeV mass points investigated, respectively. The red and blue curves show the background-only and signal-plus-background fit results, respectively, while the light and dark green curves represent the signal template and the fitted signal. For each plot, the pulls are shown in the bottom panel, defined as the difference between the signal-plus-background fit result and the data, divided by the statistical uncertainty. With a very good overall description of the data in both CR and SR in either FR, no significant signal is observed. The fitted signal strength for the 1200 GeV mass point is negative, as reflected by the absence of a dark green curve and the downward deviation of the blue curve from the background-only fit result.

6. Results

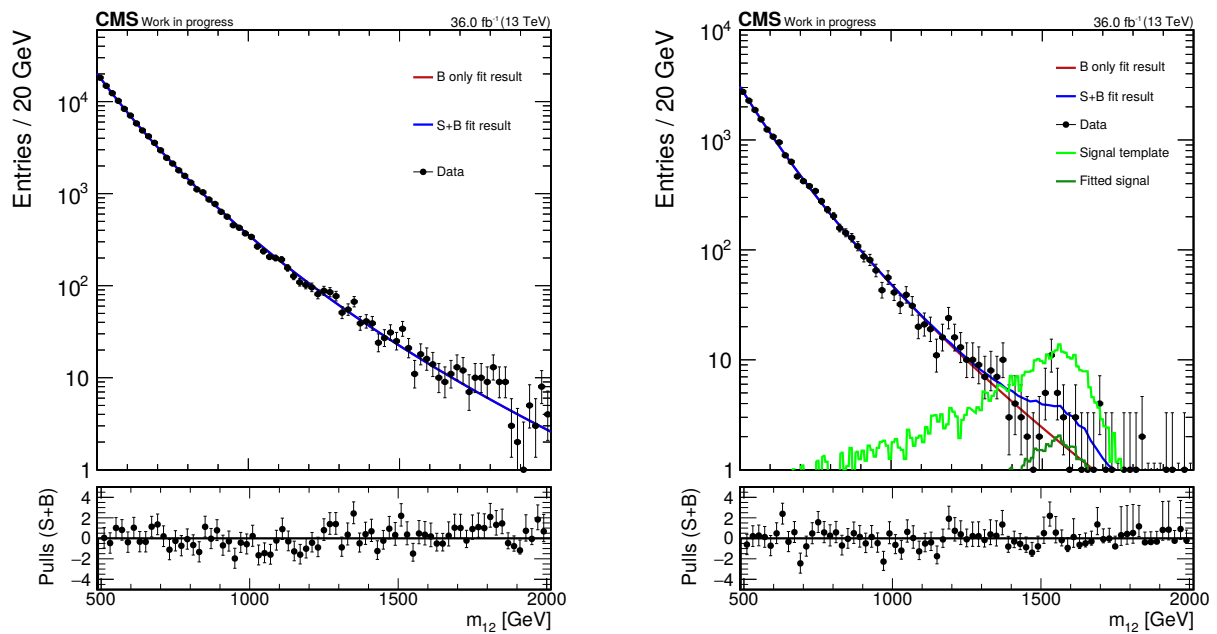


Figure 6.4.: Combined fit of CR (left) and SR (right) in FR 4 with the 1600 GeV mass point investigated. The red and blue curves show the background-only and signal-plus-background fit results, respectively, while the light and dark green curves represent the signal template and the fitted signal. For each plot, the pulls are shown in the bottom panel, defined as the difference between the signal-plus-background fit result and the data, divided by the statistical uncertainty. With a very good overall description of the data in both CR and SR in either FR, no significant signal, but an insignificant excess, slightly below two standard deviations from the expectation, is observed.

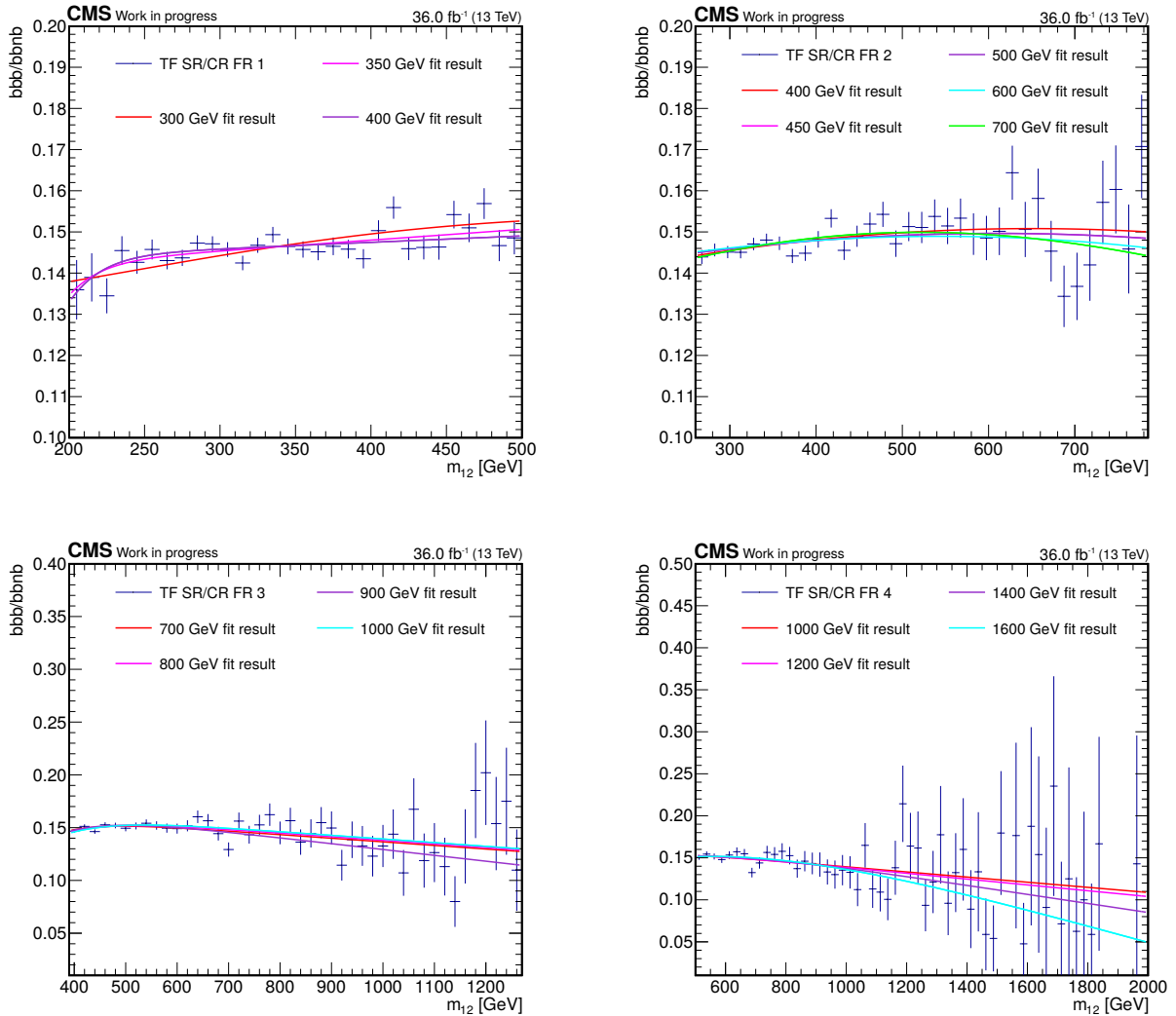


Figure 6.5.: Comparison of the ratio of m_{12} distributions in SR and CR for all four fit ranges and the fit results obtained based on the signal-plus-background fit for each mass point. The blue points represent the ratio of SR and CR in data, while the colored lines show the TF shape based on the respective fit result with this mass hypothesis. Note that the signal contribution is not shown here. All curves are found to describe the data relatively well and the MC prediction of the ratio of m_{12} distributions in SR and CR resembles the data remarkably closely.

6. Results

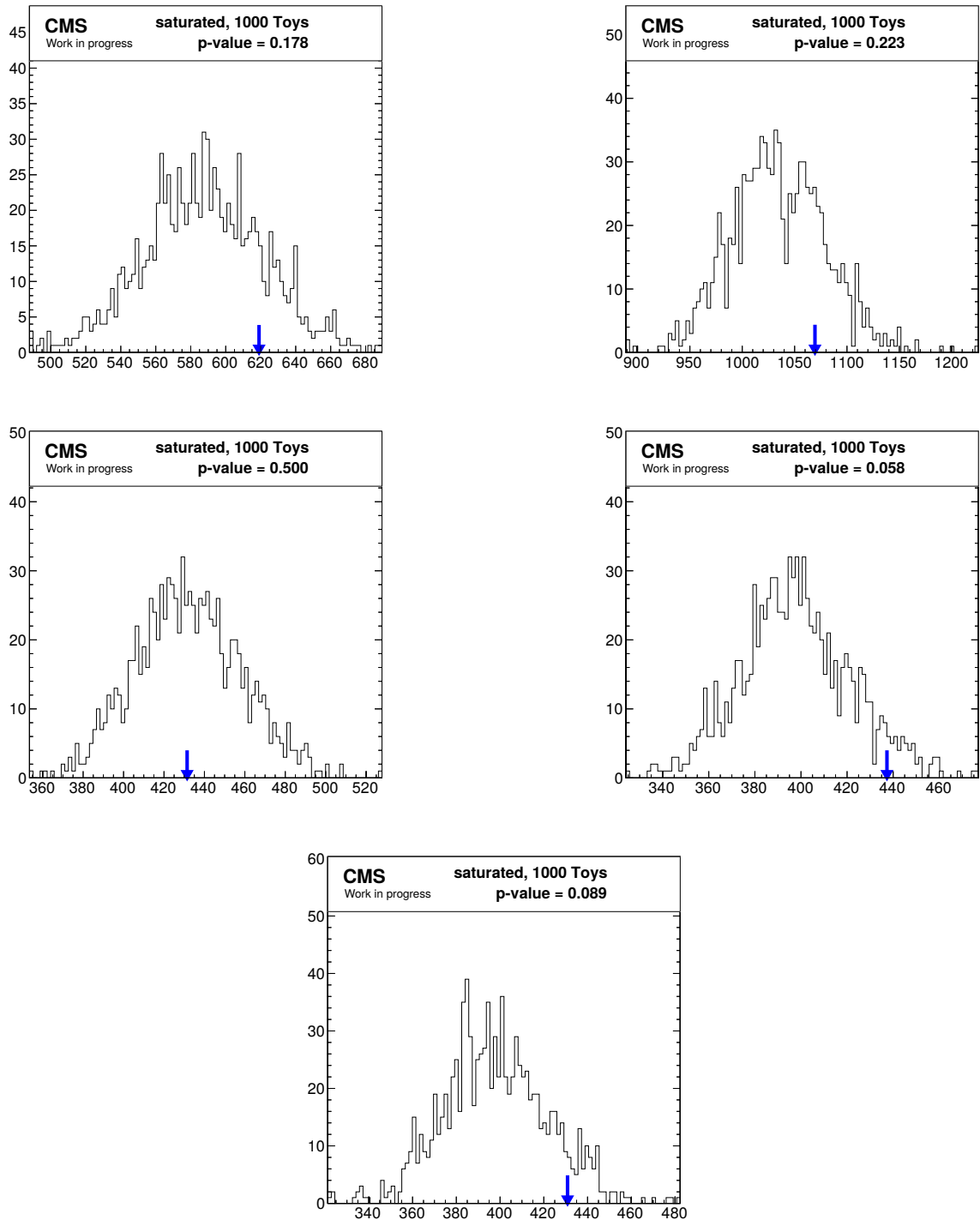


Figure 6.6.: Goodness-of-fit (gof) results based on the saturated model for the 400 (top left), 600 (top right), 900 (center left), 1200 (center right), and 1600 (bottom) GeV mass points evaluating the fit result of the unblinded SR data. 1000 toy data sets are generated and fitted for each mass point and the respective gof results are shown in the histograms. A p-value of 0.5 corresponds to obtaining the expected gof value. No significant deviations from the expectation are observed for either the structure of the distributions or the gof results observed in data.

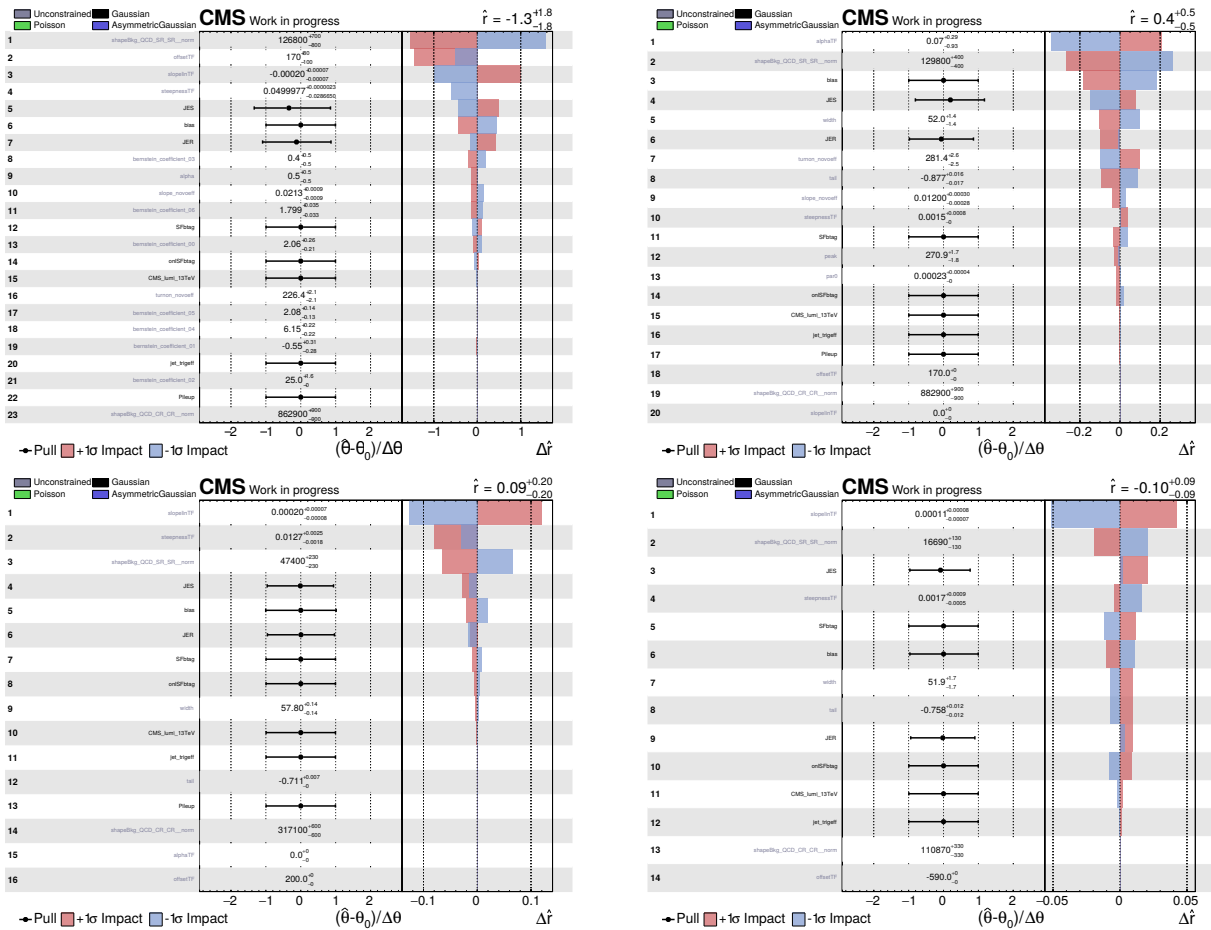


Figure 6.7.: Pulls and impacts for the 400 (FR 1, top left), 600 (FR 2, top right), 900 (FR 3, bottom left), and 1200 (FR 4, bottom right) GeV mass points, based on unblinded SR data without injected signal. No nuisance parameter related to a systematic uncertainty is found to be significantly constrained and the most significant impacts are observed due to the TF parameters and the SR normalization.

Figure 6.8 for the four fit ranges. A very good modeling of the signal region is observed in this fit as well. Unlike Figures 6.2 to 6.4, no signal hypothesis is included in these fits. Moreover, the fit uncertainty is shown in both the upper panels for the background curve and the bottom panel for the pulls. As expected, the largest uncertainties are observed around the background peak and, for FR 3 and 4, at the lower edge of the respective FR. Node-like structures can be observed in the fit uncertainties of each FR. They are attributed to the functional form of the TF, which contains a linear term in all fit ranges. This structure implies that the background model is rather independent of the slope parameter at certain m_{12} values, leading to small uncertainties at these points.

Since no significant excess is observed, upper limits are calculated on the production cross-section of a heavy, neutral Higgs boson in the b-associated production mode times branching ratio into a pair of bottom quarks. The observed limits do not deviate from the expectation significantly, as shown in Figure 6.9. They reach from slightly below 16 pb (about 9 pb expected) at 300 GeV down to just above 0.1 pb at 1000 GeV (about 0.3 pb expected). For the highest mass studied in this analysis, 1600 GeV, an upper limit of 0.23 pb is observed (just above 0.1 pb expected). This constitutes a significant improvement over previous analyses for the entire investigated mass range. Results from the analyses using the 2016 inclusive [177, 178] and 2017 semi-leptonic [34] selection based on CMS data, respectively, are shown as well as the ATLAS result [174]. Furthermore, larger Higgs boson masses can be included than before. Fit range borders are shown as vertical dashed lines, at which the limits for both adjacent fit ranges are shown. Whenever a mass point is assigned to two fit ranges, the observed measurement is only indicated by a black dot for the range providing the lower expected limit, i.e. better sensitivity. The largest tensions between observed and expected limits are found at 1000 and 1600 GeV in FR 4 with a deficit of slightly more than two standard deviations and an excess just below 2σ , respectively. These statistically insignificant disagreements correspond to fluctuations which are also visible in the m_{12} distribution in the SR. Exact values for observed and expected limits as well as $\pm 1\sigma$ and $\pm 2\sigma$ uncertainties are shown in Table 6.1.

6.3. Model Interpretation

The limits on cross-section times branching fraction presented in Section 6.2 are interpreted in terms of specific benchmark scenarios. First, interpretations based on MSSM scenarios will be discussed in this section, before 2HDM scenarios are analyzed.

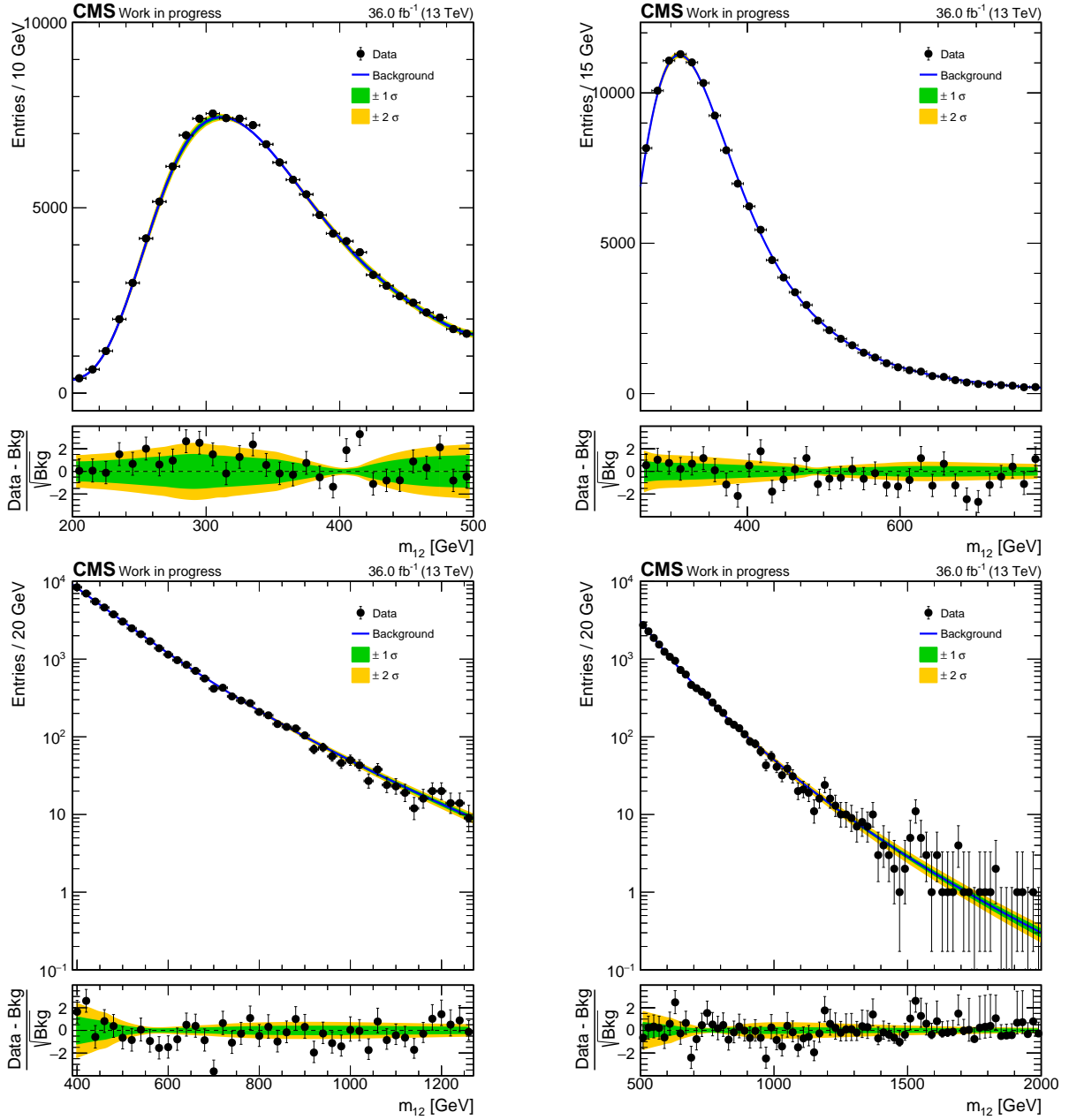


Figure 6.8.: Background-only fit results from the combined fit of CR and SR, showing the agreement of the fit with the SR data in FR 1 (top left), 2 (top right), 3 (bottom left) and 4 (bottom right). Pulls are shown in the bottom panel of each plot together with the one- and two-standard-deviation error bands of the fit. In all plots, SR data is shown as black dots and the Background-only fit result is represented by the blue curve, with the corresponding fit uncertainties indicated by the green and yellow bands. The node-like structures in the error bands are attributed to the linear part of the TF which exists in all FR. They imply that the background model is relatively independent of the slope parameter at certain m_{12} values, which results in small uncertainties.

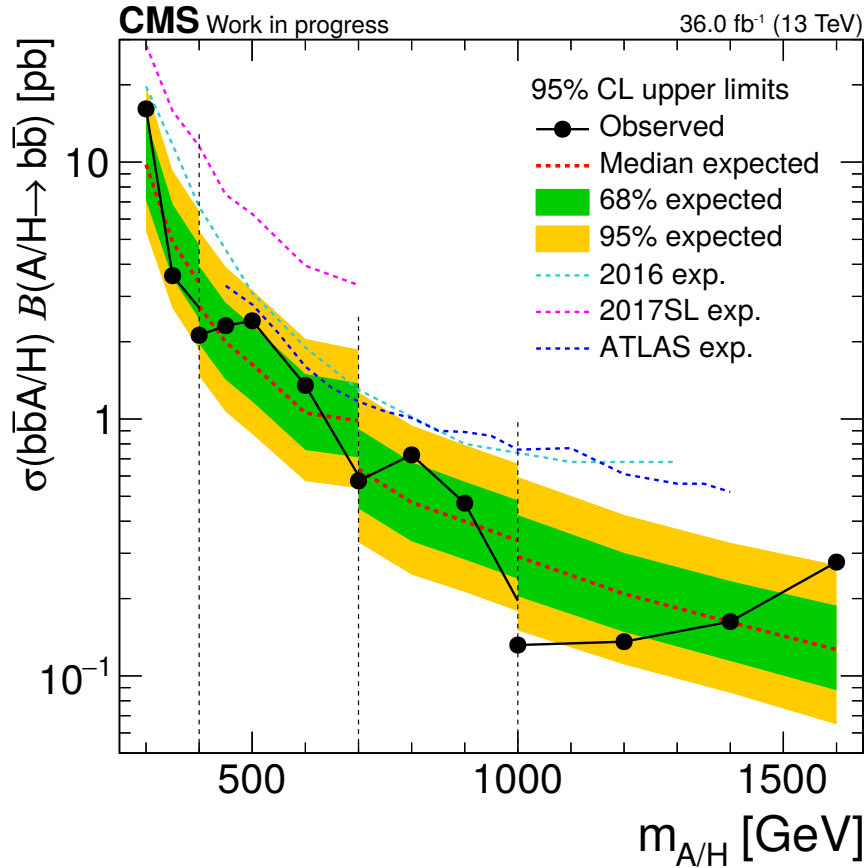


Figure 6.9.: Expected and observed limits on the production cross-section times branching ratio of the process $b\bar{b}A/H(A/H \rightarrow b\bar{b})$ at 95 % C.L. in the range of 300 to 1600 GeV. Previous results are shown for the inclusive 2016 (cyan [178]) and semi-leptonic 2017 (pink [34]) CMS analyses as well as the ATLAS result (dark blue [174]). Note that only the upper part of the mass range of the semi-leptonic analysis is shown here. The vertical dashed lines represent the edges of the four fit ranges. No significant excess or deficit is observed with the largest deviations being slightly larger (smaller) than 2σ for the 1000 (1600) GeV mass points in FR 4, respectively. All observed limits are found to be below the previous results for the respective mass hypotheses and the reach of this analysis towards higher masses exceeds the previous results.

Mass [GeV]	-2σ	-1σ	exp.	$+1\sigma$	$+2\sigma$	obs.
300	4.63	6.15	8.59	12.16	16.63	15.96
350	2.59	3.40	4.67	6.52	8.83	4.19
400	1.90	2.51	3.45	4.84	6.54	2.73
400	1.50	1.99	2.78	3.96	5.45	2.16
450	1.07	1.43	1.99	2.83	3.89	2.36
500	0.88	1.17	1.62	2.31	3.16	2.43
600	0.57	0.75	1.04	1.48	2.03	1.34
700	0.54	0.72	1.00	1.41	1.90	0.61
700	0.32	0.44	0.62	0.89	1.24	0.57
800	0.25	0.34	0.48	0.69	0.95	0.76
900	0.22	0.29	0.40	0.58	0.80	0.47
1000	0.18	0.23	0.33	0.48	0.90	0.19
1000	0.15	0.20	0.29	0.42	0.58	0.13
1200	0.11	0.14	0.20	0.28	0.39	0.14
1400	0.08	0.11	0.15	0.21	0.29	0.15
1600	0.06	0.08	0.11	0.16	0.23	0.23

Table 6.1.: Observed and expected upper limits at 95 % C.L. and $\pm 1\sigma$ and $\pm 2\sigma$ uncertainties depending on the Higgs boson mass. The observed limit at 1600 GeV is slightly smaller than the $+2\sigma$ expected value which is hidden by the rounding.

In order to compare the analysis presented here with the previous results, some of the same benchmark scenarios that were used then are also investigated here. For MSSM scenarios, this means analyzing the hMSSM and m_h^{mod+} scenarios. As discussed in Section 5.2, the corresponding production cross-sections are calculated based on the Santander matching scheme [179], which incorporates both 4FS and 5FS predictions. While the 4FS calculations are done up to NLO [199, 200], 5FS computations are available up to NNLO [201]. Branching ratios are determined using FeynHiggs [202, 203] and HDECAY [204, 205]. The cross-sections and branching fractions are provided centrally by the LHC Higgs Cross Section Working Group [94].

For the MSSM benchmark scenarios, limits are expressed in terms of the parameters $\tan\beta$ and m_A . The respective results, based on the limits on cross-section times branching ratio shown in Figure 6.9, are presented in Figure 6.10 for the hMSSM and m_h^{mod+} scenarios. For both of these scenarios, a higgsino mass parameter $\mu = 200$ GeV is selected. A comparison with the 2016 [178] and 2017 semi-leptonic [34] CMS analyses is included as well. Similar to the results for the cross-section times branching ratio, significant improvements can be observed. For the hMSSM scenario, exclusion limits down to $\tan\beta \approx 14$ can be observed between 350

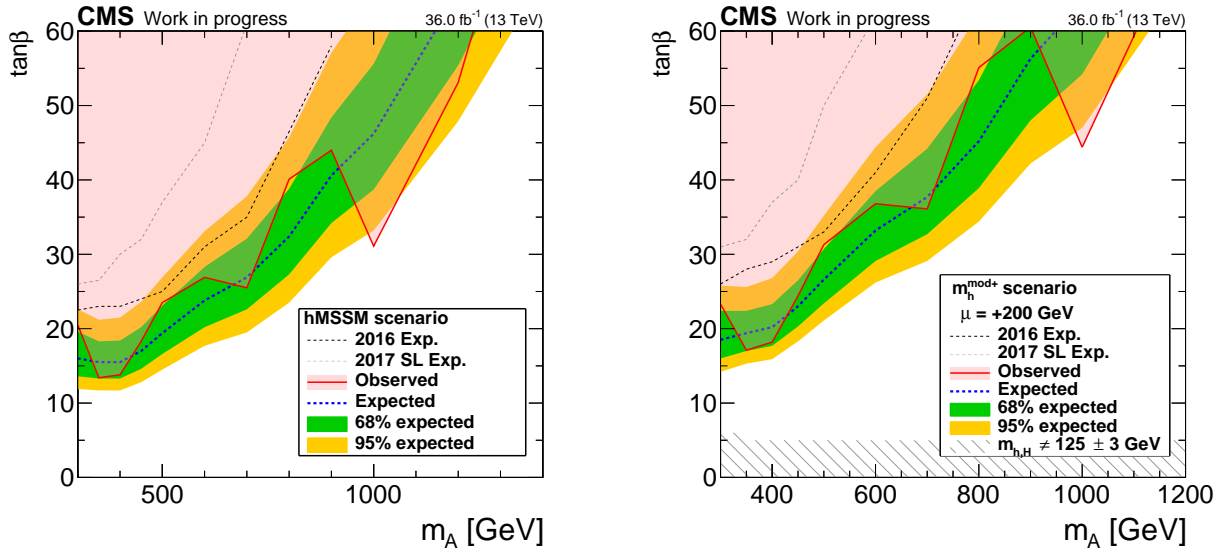


Figure 6.10.: Expected and observed limits of the parameter $\tan\beta$ vs. m_A in the context of the hMSSM (left) and m_h^{mod+} (right, using a higgsino mass parameter of $\mu = 200$ GeV) scenarios. Expected limits from the inclusive 2016 [178] and semi-leptonic 2017 [34] CMS analyses are shown as dashed black and gray lines, respectively. The hatched area indicates the parameter space which does not agree with the light scalar Higgs boson h having a mass of 125 GeV.

and 400 GeV. The upper end of the sensitivity range is marked by $\tan\beta \sim 60$ (cf. Section 2.2.2), which is reached at slightly above 1200 GeV. This model takes experimental SUSY constraints into account, for example all SUSY particles are assumed to be relatively heavy. Therefore, the Higgs boson can not decay into these particles, leading to a larger sensitivity in the $b\bar{b}$ decay channel compared to the m_h^{mod+} scenario. In terms of the m_h^{mod+} scenario, limits from $\tan\beta \approx 16$ at 350 GeV up to $\tan\beta = 60$ around 1100 GeV are observed. In this scenario, the Higgs boson decay into light SUSY particles is possible for moderate $\tan\beta$ and larger m_A . At large $\tan\beta$ and large values of μ , also the Yukawa-coupling correction Δ_b becomes important, increasing the Higgs boson coupling to b quarks proportional to $\mu \tan\beta$.

A more recent, widely utilized MSSM scenario is the m_h^{125} benchmark scenario. It features rather heavy SUSY particles and, hence, Higgs bosons exclusively decay into SM particles up to a mass of $m_\phi \approx 2$ TeV. Four distinct variants of the m_h^{125} benchmark scenario are evaluated here. All of them feature the same parameter settings, apart from the higgsino mass parameter μ , which is set to 1 (standard), -1 , -2 , and -3 TeV, respectively. A new matching scheme is used compared to the hMSSM and m_h^{mod+} scenarios, namely the FONLL scheme [181, 182]. As discussed in Section 5.2, it was tested against the alternative NLO+NNLLpart+ybytb [183, 184] scheme and both models were found to yield exactly the same results. Overall, the limits in

terms of the standard m_h^{125} scenario with $\mu = 1$ TeV are relatively similar to the results from the m_h^{mod+} scenario. However, the $b\bar{b}$ decay channel is particularly sensitive to the value of μ , i.e. lower limits are observed for larger μ , due to changes in the Yukawa couplings at larger $\tan\beta$. Also the sensitivity towards negative μ values is unique in the $b\bar{b}$ decay channel. For $\mu = -3$ TeV, upper limits below $\tan\beta = 10$ are observed for the 350 and 400 GeV mass points. At the upper end of the mass range, upper limits of $\tan\beta \approx 55$ (50), 55 (45), and 50 (35) are observed (expected) for $\mu = -1, -2$, and -3 TeV, respectively. Note that also the regions of the parameter space, which do not agree with either of the CP-even Higgs bosons having a mass of 125 GeV, increase with larger negative values of μ . These regions only reflect theoretical considerations and do not include experimental observation of other properties as used in Figure 2.6. The individual results for the four utilized scenarios are shown in Figure 6.11 and they are compared to each other directly in Figure 6.12. The visible direct impact of the higgsino mass parameter is much larger than for the $\tau\tau$ decay channel.

The second group of studied scenarios included here belongs to the 2HDM. Since these general models feature a large number of free parameters, several assumptions are put into the calculations of production cross-sections and branching fractions. These assumptions follow the scenario G defined in [106], fixing the mass of the lighter CP-even Higgs boson to $m_h = 125$ GeV, assuming mass degeneracy between A and H , and, thereby, providing an MSSM-like Higgs sector. Hence, only three parameters are left free at tree-level, namely $\tan\beta$, $m_A = m_H$, and $\cos(\beta - \alpha)$. Respective parameter scans for both the production cross-sections and the branching fractions are performed as described in Section 2.2.2 and more detailed results are shown in Appendix B. The computations are done using the software packages 2HDMC [107], SusHi [108], LHAPDF6 [109], and FeynHiggs [202, 203].

Out of the four 2HDM scenarios, the type-II model features properties similar to the MSSM. However, for $|\cos(\beta - \alpha)|$ significantly different from zero, additional processes become possible, namely $A \rightarrow Zh$ and $H \rightarrow hh$. This is mainly visible at larger masses of the heavy Higgs bosons, since the coupling strength is proportional to the Higgs boson mass. Note that SM-like Higgs boson couplings are only realized at $\cos(\beta - \alpha) \simeq 0$. Therefore, the $A \rightarrow Zh$ analysis can not be sensitive in this area. Limits in the $(\cos(\beta - \alpha), \tan\beta)$ plane of the parameter space are shown for mass values of 300, 600, 900, and 1200 GeV for the type-II and flipped scenarios in Figures 6.13 and 6.14, respectively. It can be seen that the observed exclusion power at 300 GeV reaches down to $\tan\beta$ slightly above 20, while roughly a value of 20 is expected. Comparisons with the $A \rightarrow Zh$ analysis [206] are shown in both cases for the 300 GeV mass point. The lobe features for positive values of $\cos(\beta - \alpha)$ and small $\tan\beta$ values in the $A \rightarrow Zh$ limits

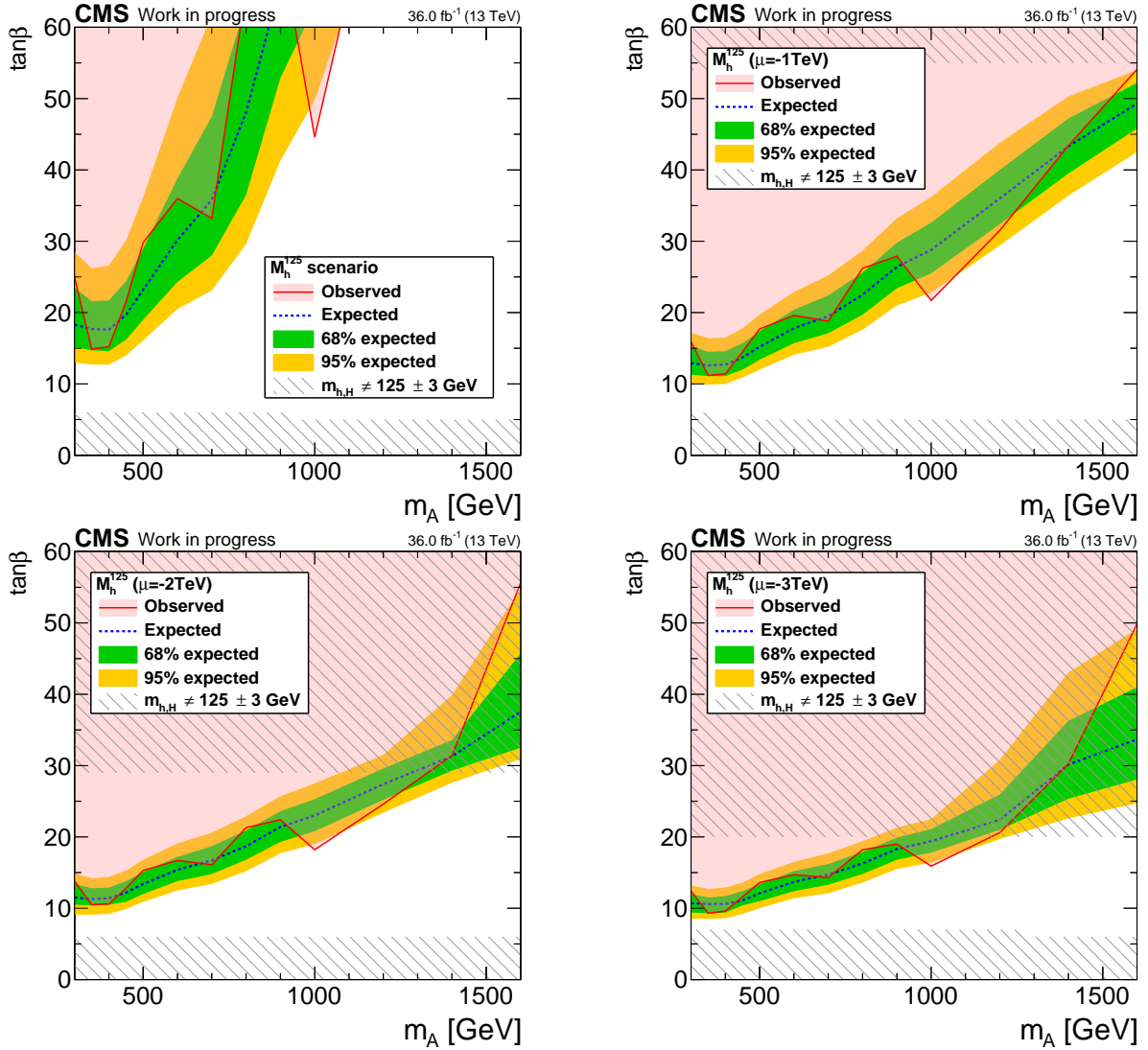


Figure 6.11.: Expected and observed limits of the parameter $\tan\beta$ vs. m_A in the context of the m_h^{125} scenarios, featuring a higgsino mass parameter of $\mu = 1$ TeV (top left), $\mu = -1$ TeV (top right), $\mu = -2$ TeV (bottom left), and $\mu = -3$ TeV (bottom right). The hatched area indicates the parameter space which does not agree with the light scalar Higgs boson h having a mass of 125 GeV.

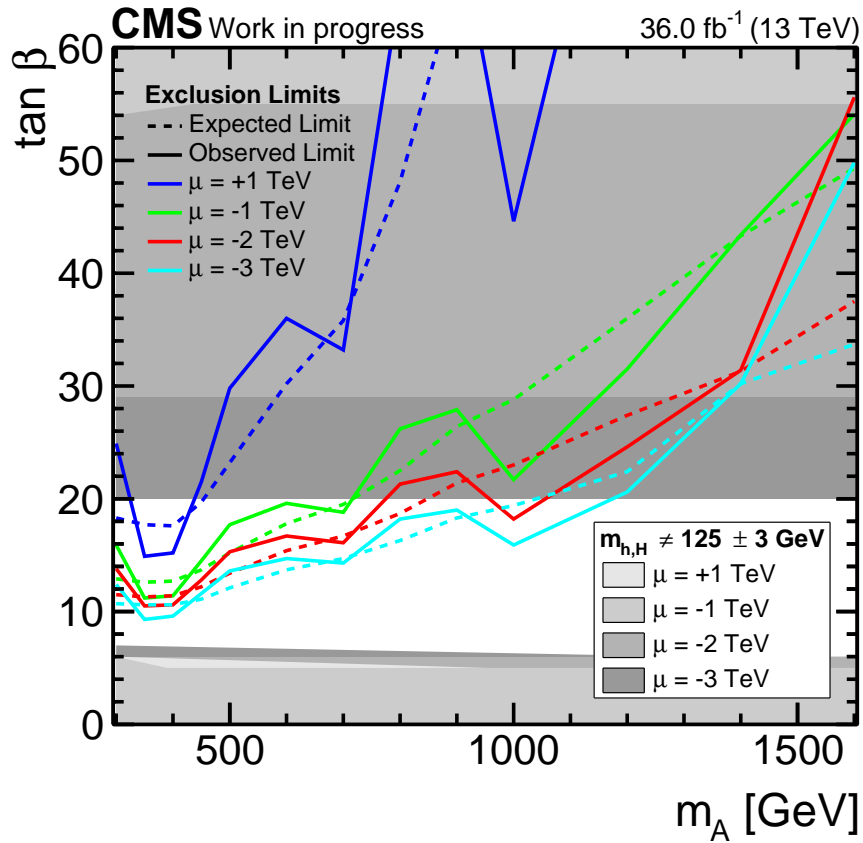


Figure 6.12.: Direct comparison of expected and observed limits of the parameter $\tan \beta$ vs. m_A in the context of the m_h^{125} scenarios, featuring a higgsino mass parameter of $\mu = 1$ TeV (top left), $\mu = -1$ TeV (top right), $\mu = -2$ TeV (bottom left), and $\mu = -3$ TeV (bottom right). The shaded areas indicate the parameter space which does not agree with the light scalar Higgs boson h having a mass of 125 GeV.

are due to negative coupling modifiers which can not be excluded with the current sensitivity [207]. In the flipped scenario for $\tan \beta \gg 1$, the Higgs boson coupling to leptons and up-type quarks is suppressed, i.e. only down-type quarks provide significant sensitivity in these models and, consequently, the coupling to b quarks is enhanced. As in the type-II models, the $A \rightarrow Zh$ channel is not sensitive around the alignment limit $\cos(\beta - \alpha) = 0$. Overall, exclusion limits in terms of the type-II and flipped scenarios are found to be very similar. The slight asymmetry with respect to $\cos(\beta - \alpha) = 0$ which can be observed in all of these limits originates in the fermiophobic point (cf. Section 2.2.2) of the CP-even mixing angle α .

In Figure 6.15, exclusion limits in terms of $\tan \beta$ and $m_{A/H}$ are shown for a fixed value of $\cos(\beta - \alpha) = 0.1$. Because of the suppression of Higgs boson couplings to leptons, these limits are slightly more stringent in the flipped scenario. Exclusion power down to $\tan \beta$ slightly above 10 is observed for Higgs boson masses of 350 GeV, and at roughly 1350 GeV, the limits exceed $\tan \beta = 100$. Note that in these more general models, $\tan \beta = 100$ is conventionally taken as the upper edge of theoretical predictions, while $\tan \beta = 60$ is selected in MSSM scenarios.

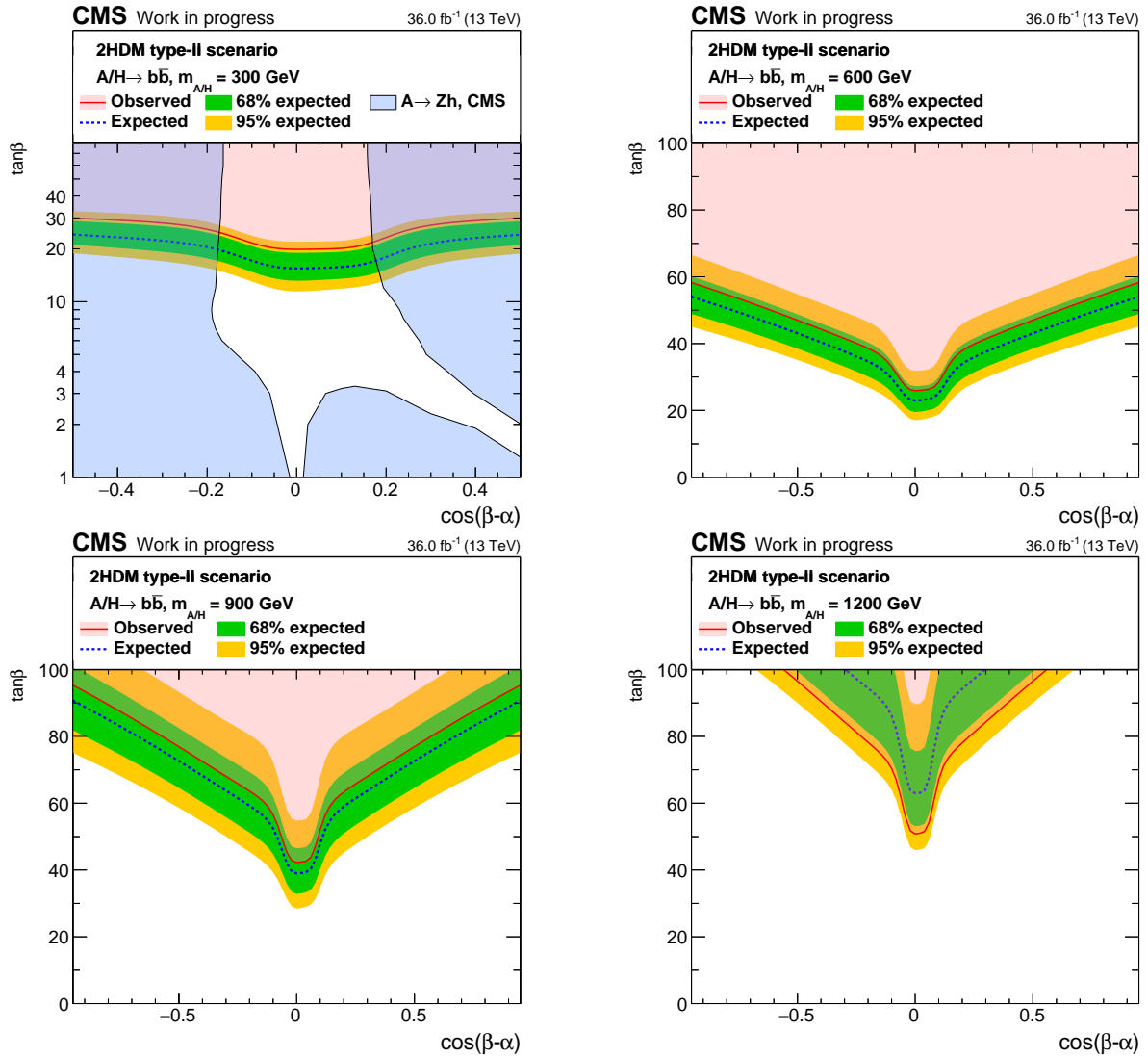


Figure 6.13.: Expected and observed limits of the parameter $\tan \beta$ vs. $\cos(\beta - \alpha)$ in the 2HDM type-II scenario for the 300, 600, 900, and 1200 GeV mass points (top left to bottom right). For the 300 GeV mass point, a comparison to the CMS $A \rightarrow Zh$ [206] analysis is shown, represented by the shaded blue areas.

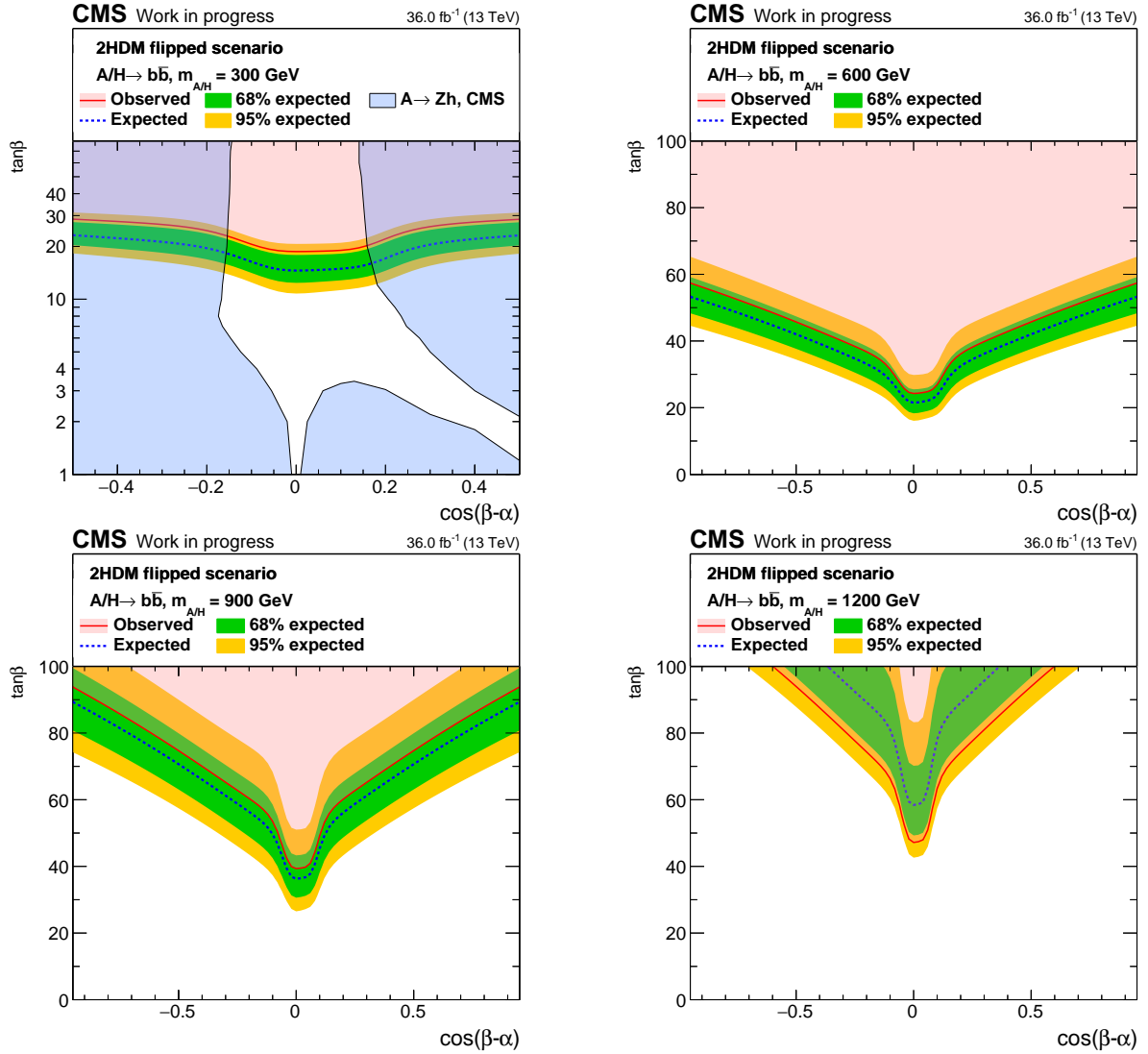


Figure 6.14.: Expected and observed limits of the parameter $\tan\beta$ vs. $\cos(\beta - \alpha)$ in the 2HDM flipped scenario for the 300, 600, 900, and 1200 GeV mass points (top left to bottom right). For the 300 GeV mass point, a comparison to the CMS $A \rightarrow Zh$ [206] analysis is shown, represented by the shaded blue areas.

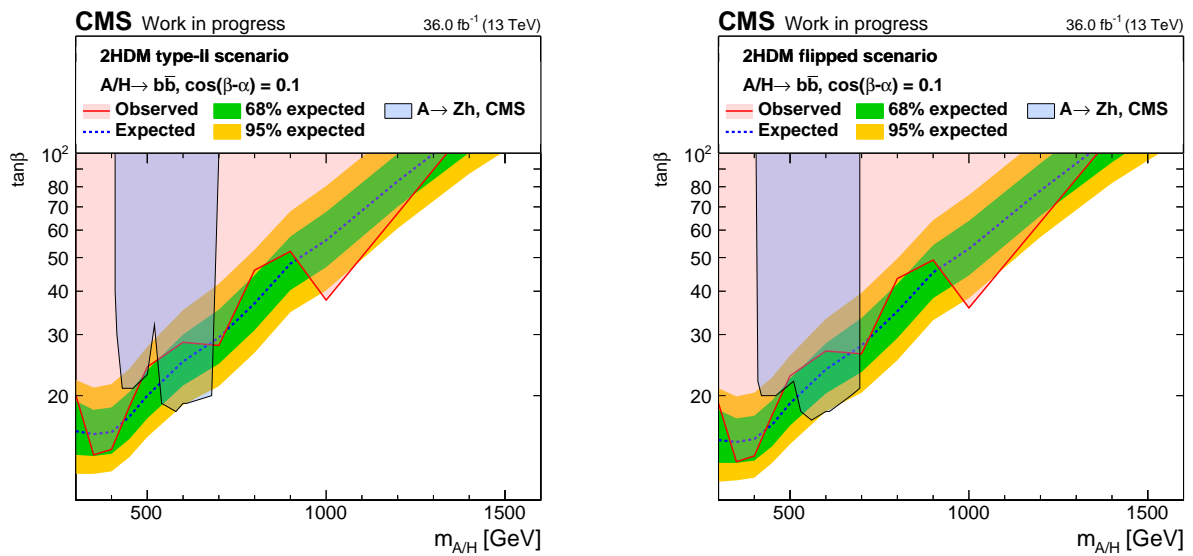


Figure 6.15.: Expected and observed limits of the parameter $\tan\beta$ vs. $m_{A/H}$ in the 2HDM type-II (left) and flipped (right) scenarios for $\cos(\beta - \alpha) = 0.1$ together with a comparison to the CMS $A \rightarrow Zh$ [206] analysis, which is represented by the shaded blue area.

7. Summary and Outlook

A search for heavy, neutral Higgs bosons which are produced in association with b quarks and decay into a pair of b quarks, is presented, targeting the all-hadronic final state of this process. Data collected by the CMS experiment at the LHC during proton-proton collisions in 2017 at a center-of-mass energy of 13 TeV is used, corresponding to an integrated luminosity of 36.02 fb^{-1} .

An extended Higgs sector is predicted by various theories beyond the Standard Model, like the MSSM or the general 2HDM. These theories are discussed and investigated thoroughly in this thesis. In many scenarios of theories featuring an extended Higgs sector, the Yukawa coupling to b quarks is significantly enhanced. Therefore, this specific combination of production and decay mode is particularly promising for those scenarios. Furthermore, the requirement of additional b quarks in the final state significantly helps to reduce the background contribution from QCD-multi-jet events which are present in hadron collisions and form the dominant background contribution in searches of Higgs boson decays into a pair of quarks. High-mass Higgs bosons can potentially be produced at the LHC and the general-purpose detectors ATLAS and CMS are well-suited to detect respective decay products.

In order to select the events for this analysis, a dedicated trigger was developed, which requires two b-tags and two high-energy jets. In the final state of this search, at least three well-separated b-tagged jets with large transverse momentum are required in the signal region (SR), of which two are the candidates for the Higgs boson decay and the third is assigned to a b quark originating from the associated production mode. Signal samples are generated for thirteen Higgs boson masses ranging from 300 to 1600 GeV with next-to-leading order (NLO) precision. Simulated background data sets with and without enhanced b-quark content are used for additional studies. The background in the signal region is estimated based entirely on data as the complex QCD processes are not modeled accurately enough in simulation. Two signal-depleted regions of data are defined based on the b-tag discriminant of the third-leading jet in transverse momentum. The control region (CR) is based on the jet being explicitly not b-tagged, while the validation region (VR) is situated between CR and SR. Since the two leading jets are selected based on identical requirements in all regions, the analysis observable m_{12} is distributed simi-

7. Summary and Outlook

larly in each region. A signal would manifest as an excess of events in the distribution of this observable. The signal extraction is performed in a combined fit of CR and SR, modeling small shape differences in the di-jet mass spectrum by using a transfer factor (TF). This function is slowly varying and depends on m_{12} . A mass range from 200 to 2000 GeV is investigated with the lower bound roughly defined by the kinematic requirements of the trigger and the upper end of the range being set by the availability of a sufficient number of events.

As no significant deviation from the Standard-Model background-only prediction is observed, upper limits are calculated for the production cross-section of a heavy, neutral Higgs boson in the b-quark-associated production mode times the branching fraction into a pair of bottom quarks. The observed upper limits at 95 % confidence level reach from about 16 pb at 300 GeV down to 0.13 pb at 1000 GeV with the expected limits covering a range from slightly below 9 pb at 300 GeV to 0.11 pb at 1600 GeV. The overall reach of this analysis extends previous searches and the sensitivity is found to be better than for earlier studies over the entire investigated mass range. These limits are further interpreted in terms of MSSM and 2HDM benchmark scenarios.

A set of MSSM scenarios is considered and limits are computed in terms of the corresponding free phase-space parameters at tree-level, $\tan \beta$ and m_A . The first group which is investigated consists of recent models, based on the m_h^{125} benchmark scenario. In addition to other updates with respect to more traditional models, the higgsino mass parameter of $\mu = 200$ GeV in the m_h^{mod+} scenario is increased to $\mu = 1000$ GeV in this updated scenario. Three variants with $\mu = \{-1, -2, -3\}$ TeV are analyzed as well, where all other parameters remain unchanged with respect to the m_h^{125} scenario. The $b\bar{b}$ decay mode is particularly sensitive to the value of μ . Limits of $\tan \beta < 10$ are observed for 350 and 400 GeV in the $m_h^{125}(\mu = -3 \text{ TeV})$ scenario and for the full mass range, i.e. up to 1600 GeV, and for all considered values of μ , limits are found to be below $\tan \beta = 60$. Also two more traditional models are analyzed, mainly to allow for comparisons with previous analyses. First, the relatively model independent hMSSM scenario is investigated. It incorporates rather recent SUSY search results and, thus, assumes relatively heavy SUSY particles which restricts the Higgs boson decays into these particles, enhancing the sensitivity of the $b\bar{b}$ decay channel. Limits down to $\tan \beta \approx 14$ are observed at $m_A = 350$ GeV, while limits of $\tan \beta \approx 60$ are observed slightly above 1200 GeV. Second, the limits are interpreted in terms of the m_h^{mod+} model. Limits range from $\tan \beta$ slightly above 15 at a Higgs boson mass of 350 GeV to $\tan \beta \approx 60$ at about 1200 GeV. In both scenarios, significant improvements with respect to the 2016 inclusive and the upper mass-range of the 2017 semi-leptonic analyses are achieved.

The second family of investigated models is based on the 2HDM. Specifically the type-II and flipped scenarios are particularly interesting for this analysis since they feature enhanced

Higgs boson couplings to b quarks. Exclusion limits are given in terms of the free parameters at tree-level, $\tan \beta$, m_A and $\cos(\beta - \alpha)$. In both scenarios, a large part of the allowed phase space can be accessed and excluded. Around the alignment limit $\cos(\beta - \alpha) = 0$, a region which can not be assessed by SM Higgs boson coupling analyses, the $b\bar{b}$ decay channel is particularly sensitive and in the case of the flipped scenario, this sensitivity is unique. All results presented in this thesis have been reviewed and endorsed by the CMS collaboration.

In conclusion, the large center-of-mass energy of 13 TeV enables searches for heavy Higgs bosons up to a mass of 1600 GeV as presented in this analysis. The inclusion of a transfer factor to the background model allowed to improve the sensitivity of this search significantly, making it an extremely promising technique for the combination of the full LHC Run 2 data. This inclusion of the semi-leptonic channel in 2017 as well as the entire 2016 and 2018 data sets is expected to increase the statistical power of this analysis. Currently, the limits presented here are the most powerful constraints so far in the $b\bar{b}$ decay channel, which is uniquely sensitive in case of the 2HDM flipped scenario around the alignment limit. A further improvement of sensitivity is assumed to arise from the LHC Run 3, which is scheduled to start in 2022, and the increase of the center-of-mass energy to 14 TeV as well as the high-luminosity upgrade of the LHC.

Appendices

A. Tracker Alignment

For the b-tagging procedure used in this analysis, which requires an excellent hit resolution (cf. Section 4.2), a precise knowledge of the positions and orientations of the sensors of the CMS tracking system as well as their surface shape is particularly important. This is also true for various other applications of the tracking system, since variations in these parameters might impact the measurements of a sensor. Furthermore, the design resolution of about 10 % p_T uncertainty for a charged particle with a transverse momentum of 1 TeV as well as the targeted hit resolution of about 10 to 30 μm [208] can only be achieved with a correctly aligned detector. Impacts on the individual sensors as well as larger mechanical structures like an entire half barrel of the strip tracking detector can, for example, originate from magnet cycles and temperature changes in the detector cavern. In this chapter, a brief overview is provided on the efforts to align the tracking detector, using the MILLEPEDEII algorithm [209], as well as major challenges of this process.

A.1. Global Position of High-Level Structures

As described in Section 3.2.1, the CMS tracking system consists of several parts which each comprise a number of smaller structures containing the modules on which the actual sensors are located. In Figure A.1, the hierarchical structure of the tracking system is shown. The modules are the smallest part which can be aligned and they are arranged in various high-level structures (HLS). The largest sub-detector, the Tracker Outer Barrel (TOB), is used as a global reference frame for the other parts of the tracking system [208]. Shift and rotation of the TOB are determined with respect to the beam axis. Together with other large mechanical structures like the Tracker End-Caps (TEC) or the entire tracking system, the position of the TOB is surveyed by use of an infrared laser system. This array of lasers provides positional information for substructures like the TOB on the order of 100 μm , which can be used as additional input to the alignment process. It is critical to know not only any possible shift of the detector but also its position with respect to the magnetic field, which is represented by rotations around the x and y axes of the CMS coordinate system. Since a wrong assumption would lead to a worse

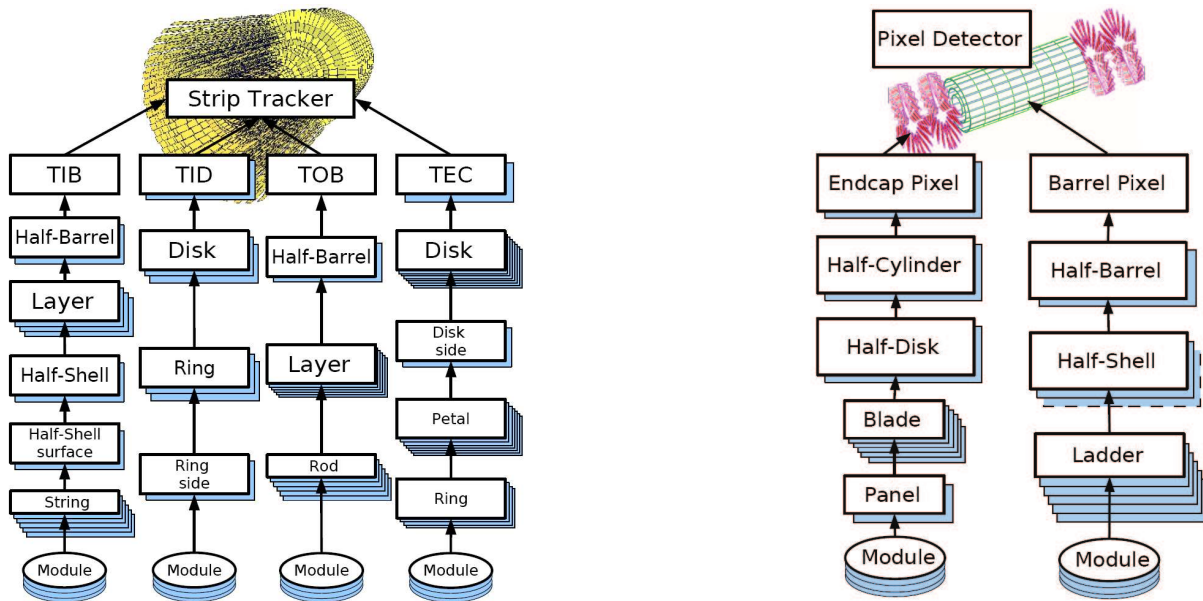


Figure A.1.: Hierarchical structure of the strip (left) and pixel (right) tracking detectors as used for the alignment and determined by the mechanical location of modules [210, 211].

track fitting result, this global tilt has to be determined before the alignment of the other detector parts can be performed.

A.2. Track-Based Alignment

For the alignment procedure, it is necessary to parametrize the tracks particles leave in the detector as well as the detector modules themselves. This is done using three parameters for the shift, rotation, and surface deformation of a sensor, i.e. nine parameters overall. In case of larger structures, only shift and rotation are considered. A track in a homogeneous magnetic field can be described by five parameters n_{par} for negligible material effects. If the interactions with the detector are non-negligible, however, as it is the case in the CMS tracking system, $n_{\text{par}} = 5 + 2n_{\text{scat}}$. Here, n_{scat} describes the number of scattering events and the factor of two reflects the two angles of the trajectory this scattering can affect.

Track-based alignment algorithms use the distribution of residuals of individual hits in a track. If the assumed positions of detector modules are different from their actual locations, these residuals will increase, as can be seen in Figure A.2. A least-square method is used to evaluate this behavior and the target of the alignment process is to minimize the sum of squares of normalized residuals from a large number of tracks [208],

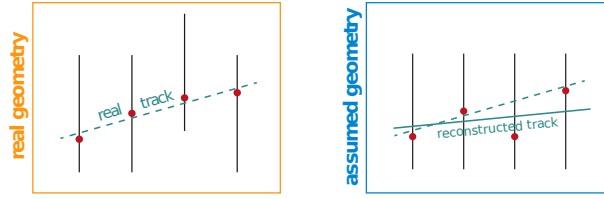


Figure A.2.: Correction of reconstructed hits based on alignment: If the actual state of the tracking detector (left) is not reflected by the assumed geometry (right), hits are reconstructed wrongly and, hence, the same real track (dashed green line) is reconstructed badly in an unaligned detector (solid green line in the right frame). In this simplified case, only one of four depicted modules is not modeled correctly by the assumed geometry. Taken from [212].

$$\chi^2(\vec{p}, \vec{q}) = \sum_j^{\text{tracks}} \sum_i^{\text{hits}} \left(\frac{m_{ij} - f_{ij}(\vec{p}, \vec{q}_j)}{\sigma_{ij}} \right)^2. \quad (\text{A.1})$$

Here, m_{ij} are the reconstructed positions of hits with the corresponding uncertainty σ_{ij} , and f_{ij} is the predicted trajectory from the track fit. The parameters which are taken into account describe the geometry of the detector (\vec{p}), i.e. the alignment parameters, and the track (\vec{q}_j), respectively. This χ^2 function can depend on millions of parameters in case of the CMS tracking system. For small alignment corrections, f_{ij} can be linearized around the initial values \vec{p}_0 and \vec{q}_{j0} . After the linearization, determining the alignment corrections corresponds to solving a linear equation system which is treated like a matrix inversion problem. For larger corrections, the procedure is repeated iteratively. For the CMS tracking system, a global fit approach is used, executed by the MILLEPEDEII algorithm. It exploits the properties of the linear equation system to reduce the number of parameters significantly. For 10^7 tracks with approximately 20 track parameters and 10^5 alignment parameters, this reduction can be as large as 4×10^6 parameters without loss of precision [208].

The MILLEPEDEII algorithm significantly reduces the required computing time to solve the linear equation system. Usually, this effort scales with the number of parameters cubed but exploiting the general broken lines algorithm [213] breaks that dependence by defining a custom track parametrization. Thus, increases in computing efficiency of up to a factor of 8.4 for cosmic tracks, which traverse the full detector leading to up to 50 track parameters, are observed [208].

A.3. Weak Modes

Certain combinations of the alignment parameters which do not significantly change the overall χ^2 are called weak modes. They occur if a change in the alignment parameters $\Delta\vec{p}$ can be counteracted by a respective alteration of the track parameters $\Delta\vec{q}$. In this specific case, one valid set of tracks is transformed into another one and therefore, the track fit result is not affected. However, this can cause issues if, e.g., the track topology or angular correlations between tracks are measured. Weak modes can not be solved by the approach described in Section A.2 but require additional information to be taken into account. At CMS, because of its cylindrical structure around the beam pipe and due to the use of tracks traversing the beam line, some weak modes occur predominantly. By using additional sets of tracks for the alignment, this symmetry can be broken and the weak modes can be assessed. For example, one of the most important weak modes at CMS is the twist, i.e. an azimuthal distortion $\Delta\phi \sim z$. It can be resolved by using $Z \rightarrow \mu^+\mu^-$ events as muons are reconstructed accurately and the Z mass is precisely known. The effects because of other weak modes can also be addressed using different approaches like cosmic tracks passing the entire detector on trajectories which break the symmetry, therefore providing a good handle on the Sagitta weak mode, a radial distortion $\Delta\phi \sim \phi$. Further details on specific validation methods of the extracted alignment parameters are given in Section A.5.

A.4. Alignment Strategies

In order to separate parameters which do and do not depend on the time, a differential approach is exploited [208], dividing the data into smaller periods called intervals of validity (IOV). In these periods, all alignment parameters are considered time-independent. Combining the differential approach and the hierarchical structure of the CMS tracking system, high-level structures are evaluated in each IOV and the modules are aligned with respect to the corresponding HLS. This relative position is assumed to be constant over time. Therefore, time-dependent and time-independent parameters can be determined simultaneously. Moreover, in case the number of tracks in a data set is insufficient for a full module-level alignment procedure, exploiting the hierarchical properties of the detector allows to obtain an alignment of the much smaller set of high-level structures.

As mentioned in Section A.3, tracks with different properties are used in order to obtain information required for the alignment procedure. Specifically, four types of tracks are utilized which are reconstructed as described in Section 4.1.2. Basic quality criteria are applied to all of

these tracks.

The first type of samples contains tracks originating from isolated muons, which mainly come from leptonic decays of W bosons. The muons are required to provide certain kinematic properties and to be detected in both the tracking detector and the muon system.

Di-muon topologies are used as well and, similar to the single-muon selection, the muons have to be detected in the tracking system and the muon chambers. Furthermore, their invariant mass is restricted in order to provide relatively pure samples of Z boson or Υ meson decays.

Tracks from cosmic rays are recorded in two different modes [208]. The peak mode makes use of the full signal and it is used in periods without a beam in the LHC. Since this full readout of the signal is relatively slow, the deconvolution mode is utilized during collisions, based on a dedicated cosmic-ray trigger. This mode measures the signal only at some points and extrapolates in between them.

The largest set of tracks which is used for the alignment originates from minimum-bias samples. They are recorded based on different basic triggers which require, e.g., a minimal number of tracks or energy in the calorimeters for an event to be triggered.

Overall more than 200000 alignment parameters [214] are determined at the same time, exploiting the differential and hierarchical alignment, and more than 100 constraints are taken into account in this procedure.

A.5. Validation Techniques

Several validation techniques are used in order to obtain information on the detector alignment. These methods exploit the different properties provided by the track samples discussed in Section A.4. By using different validation approaches, also several weak modes can be addressed.

One of the most important validations is the distance of median residuals (DMR) in a track. In this method, the hit under investigation is removed from the track fit and the distance between the reconstructed hit and the track fitted without this hit is calculated. Results of such a validation are shown in Figure A.3 for the six sub-detectors of the tracking system. It can be seen that the original assumption of the tracker parameters, which was used during data taking in 2016, can be improved significantly in the alignment process. For comparison, also a simulated detector without misalignment is shown.

In the primary vertex (PV) validation, the track under investigation is removed from the vertex fit and the distance between the track and the vertex is measured. This unbiased track-vertex

A. Tracker Alignment

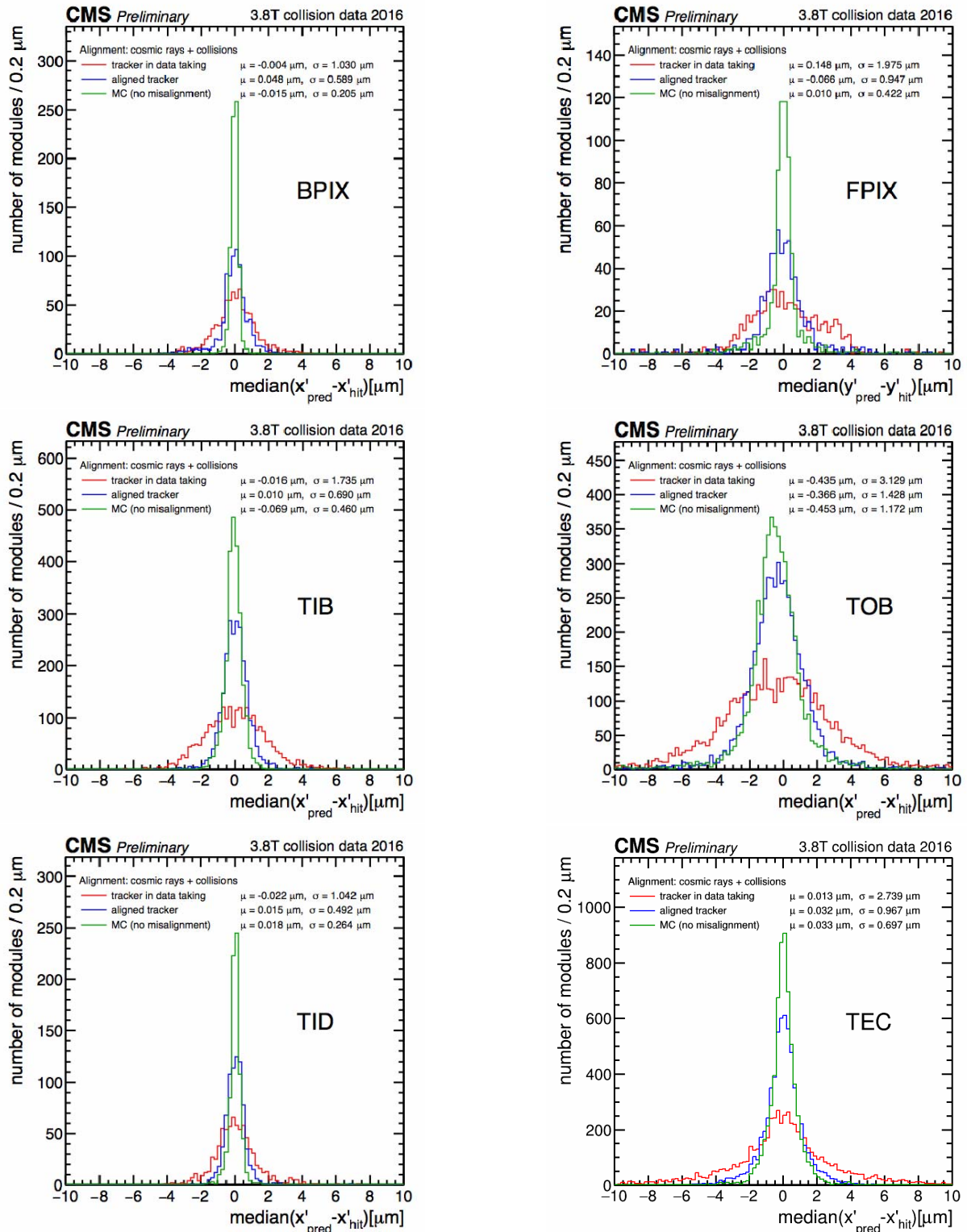


Figure A.3.: Distance of median residuals (DMR) in x and y (top right, FPIX) direction for the six sub-detectors of the CMS tracking system [215]. The results based on the parameters used during the 2016 data-taking period are shown in red, while the improved results for the aligned detector are shown in blue and, for comparison, results based on a simulation of the detector without misalignment are shown in green.

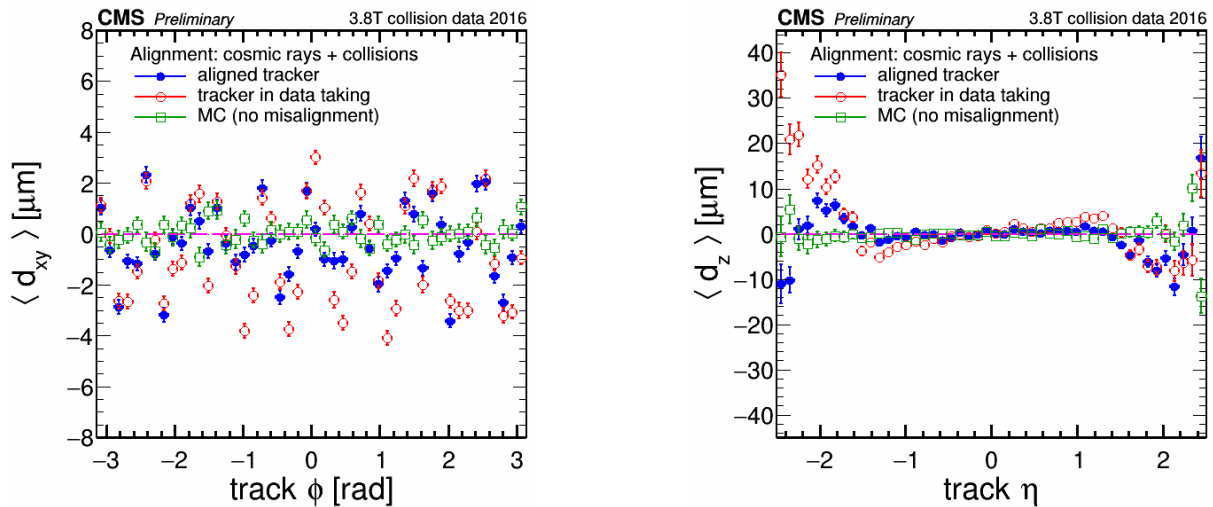


Figure A.4.: Distance of closest approach in the transverse plane (xy , left) and longitudinal direction (z , right) in terms of the azimuthal angle ϕ (left) and the pseudorapidity η (right) of a track to the vertex it is assigned to which is refitted without that track [215].

residual is investigated in the transverse plane (xy) and longitudinal direction (z) in terms of the azimuthal angle ϕ and the pseudorapidity η of the analyzed track. Results are shown in Figure A.4 for the alignment at the end of the 2016 data-taking period. Again, the assumed parameters during data-taking are compared to the aligned detector and simulation.

The geometry comparison (GC) validation is used to compare two detector geometries to each other. This can, for example, be the aligned vs. the not aligned detector. In the ideal case, the differences between these two geometries would be close to zero, indicating that the detector parameters do not have to be corrected. Such a comparison for the detector geometry used during the 2016 data-taking period and the alignment result at the end of that year is shown in Figure A.5.

In the $Z \rightarrow \mu^+ \mu^-$ validation, the mass of the Z boson is reconstructed from two muons. The corresponding events are selected by a di-muon trigger. The invariant mass distribution is fitted with a Voigtian function [216] in which the Breit-Wigner decay width is fixed. The mean of this fit is used to describe the reconstructed Z boson mass. Deviations from the known value indicate imperfect alignment parameters. In Figure A.6, reconstructed Z boson masses are shown for the alignment used during the 2016 data-taking period and the result of the alignment at the end of the year, depending on the azimuthal angle of the muons, their pseudorapidity difference, and the angle θ_{CS} in the Collins-Soper frame of the reconstructed Z boson. Similarly, the decay $\Upsilon \rightarrow \mu^+ \mu^-$ can be exploited to connect different modules to each other than in the $Z \rightarrow \mu^+ \mu^-$

A. Tracker Alignment

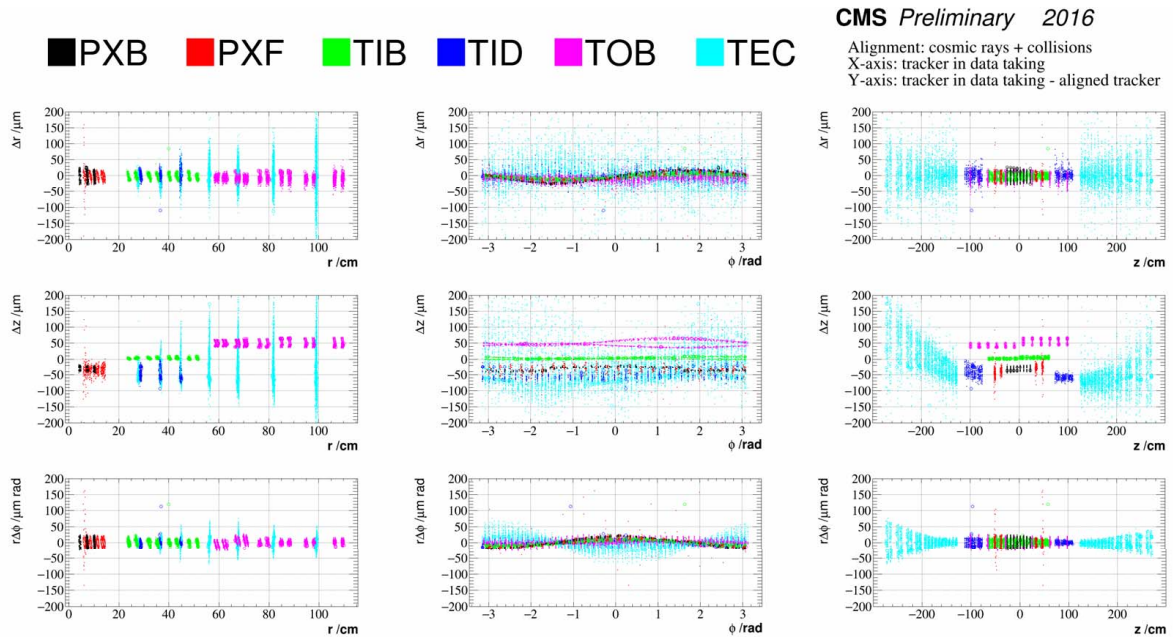


Figure A.5.: Comparison of the detector geometry used during the data-taking period of 2016 and the result of the alignment at the end of that year [215]. Small residuals indicate that the respective parameter was not significantly changed during the alignment process.

validation due to the different opening angles between the two muons. Note that in case of the Υ , the invariant mass distribution is fitted with a Gaussian function.

Cosmic tracks provide a unique insight to the alignment of the detector since they pass the entire detector volume and do not originate from an interaction point in the beam pipe. Two different techniques of validation based on cosmic tracks are shown in Figure A.7. First, track-hit residuals are shown. In order to calculate them, the respective track is fitted with the hit under investigation being removed from the fitting procedure. Second, tracks originating from cosmic radiation are split in half at the point closest to the origin of the CMS coordinate system. The two halves are refitted and compared to each other. Differences in the track parameters may indicate a misalignment in the respective modules. For the plots shown in Figure A.7, tracks are considered if they produce at least two hits inside the tracking system. Results are shown for different alignment parameters, showing the improvement due to additional data being taken into account.

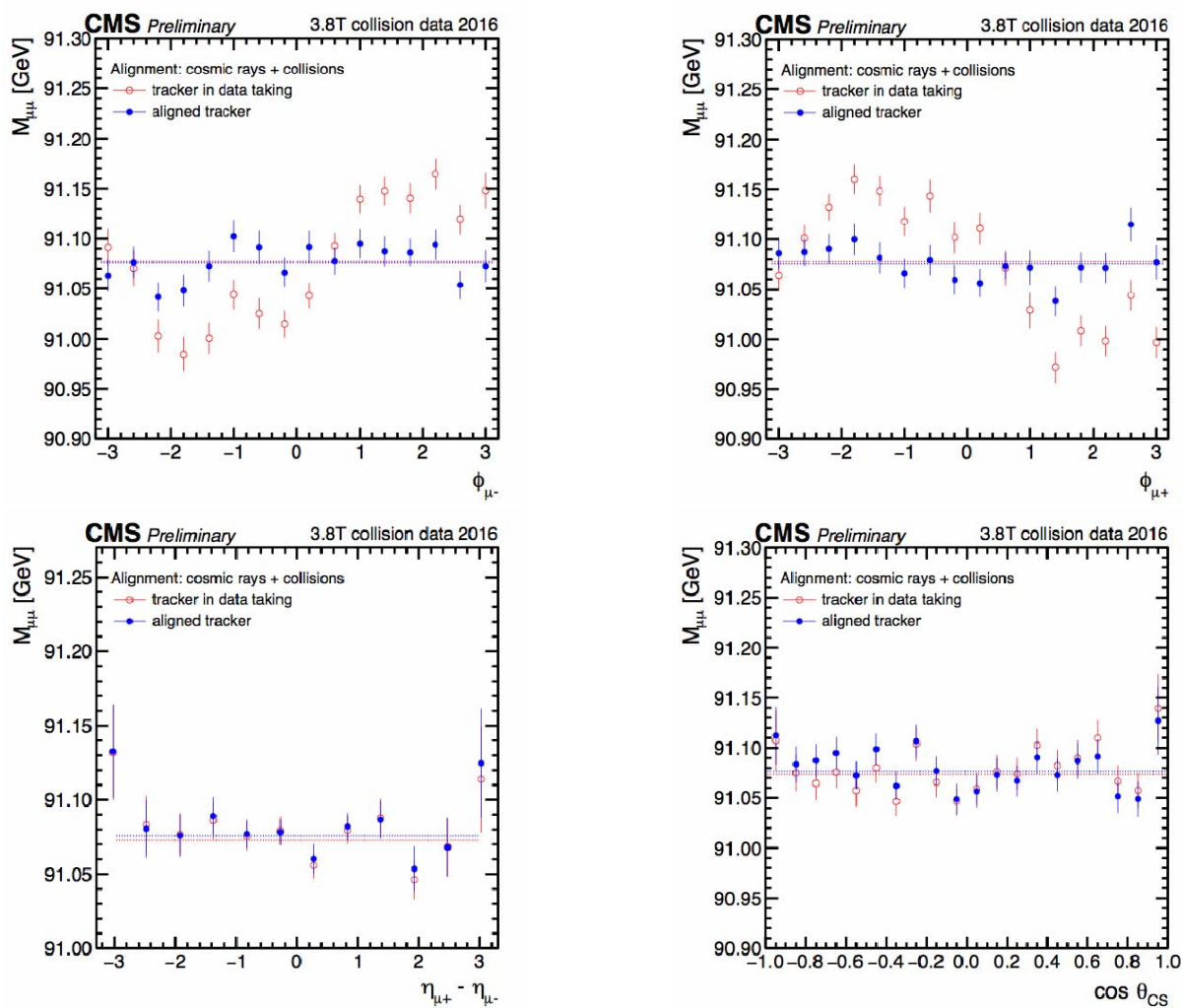


Figure A.6.: Reconstructed mass of the Z boson from two muons, depending on their azimuthal angle (top), pseudorapidity difference (bottom left) and the angle θ_{CS} in the Collins-Soper frame of the reconstructed Z boson [215].

A. Tracker Alignment

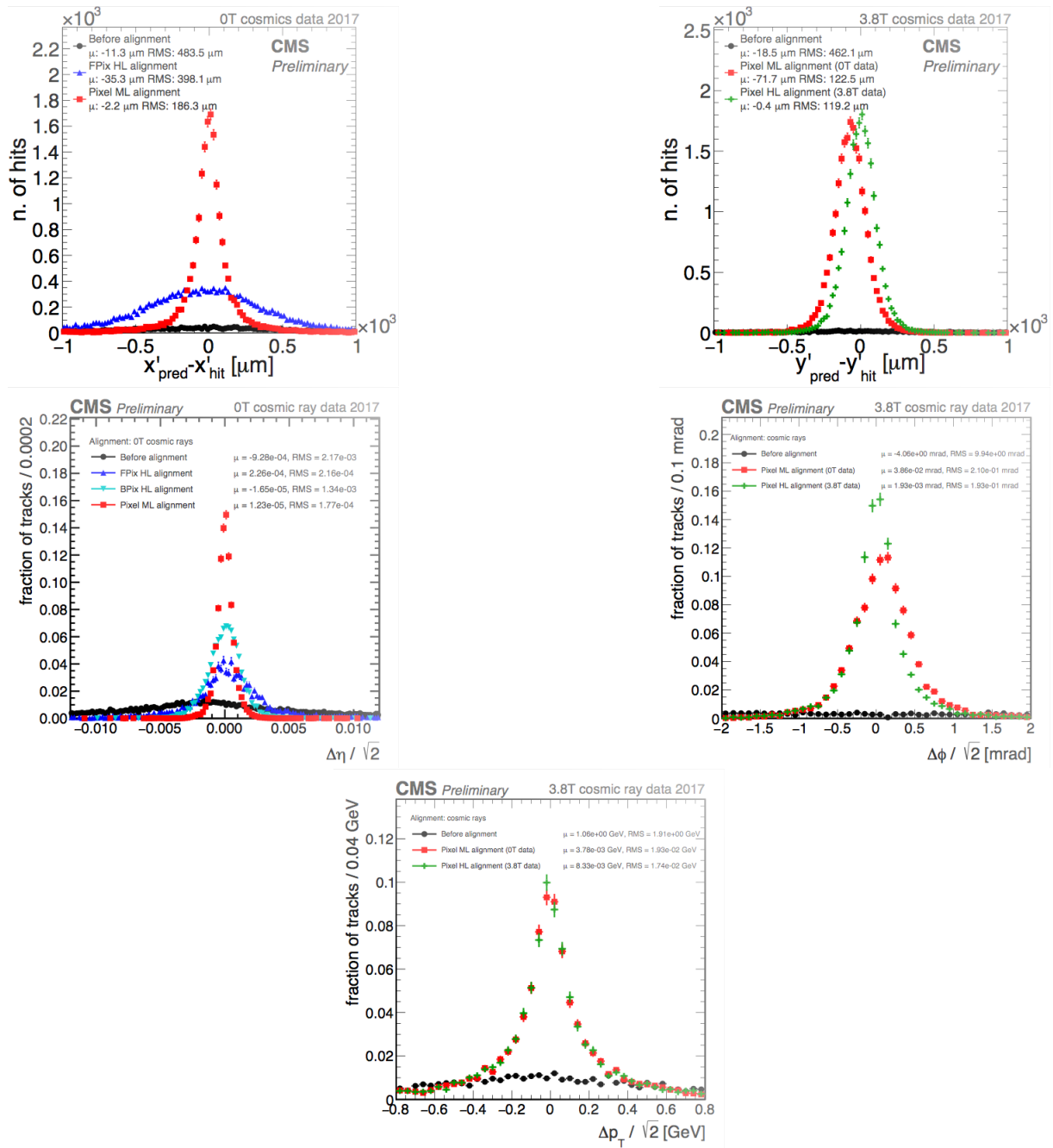


Figure A.7.: Track-hit residuals in x and y direction for the BPIX and FPIX sub-detectors (top, left and right, respectively) and comparisons in η , ϕ , and p_T of the two halves of one track (center left and right and bottom, respectively). The plots on the left were obtained from tracks left by cosmic rays traversing the detector while the magnet was off. There, the module-level (ML) alignment of the full pixel significantly improves the results. The plots on the right and bottom are based on tracks recorded with a magnetic field being present. In these cases, a HLS realignment was necessary after the magnet was ramped up, which is reflected by the mean value of the green points being closer to zero than for the red points reflecting the parameters before that realignment [217].

A.6. Conclusion

The MILLEPEDEII algorithm provides a powerful, memory- and computing-efficient tool to determine alignment parameters for the CMS tracking system. Various validation methods are used to confirm that the thereby calculated parameters describe the real positions of the detector modules well. The determined alignment is used in all analyses in order to provide the best possible resolution of tracks in the detector and, thus, allow a good reconstruction of the objects creating these tracks as well as their properties.

B. Cross-Sections and Branching Fractions in the 2HDM

Branching fractions and total production rates, i.e. cross-section times branching ratio, in the 2HDM of the heavy, neutral Higgs bosons A and H are presented, as calculated at next-to-next-to-leading-order (NNLO) precision, using the SusHi (v. 1.6.1) [108], 2HDMC (v. 1.7.0) [107], and LHAPDF (v. 6.1.6) [109] program packages. In Figures B.1 to B.4 and B.5 to B.8, branching fractions of the A and H boson are given, respectively, vs. $\cos(\beta - \alpha)$ for $\tan \beta$ values of 10, 30, and 60 and Higgs-boson masses of 300, 600, 900, and 1200 GeV, while Figures B.9 to B.12 show the cross-section times branching ratio for the process $b\bar{b}A \rightarrow b\bar{b} + b\bar{b}H \rightarrow b\bar{b}$ vs. $m_{A/H}$ in the type I, type II, lepton specific, and flipped scenarios, respectively, for $\cos(\beta - \alpha)$ values of 0, ± 0.1 , and ± 0.3 .

B. Cross-Sections and Branching Fractions in the 2HDM

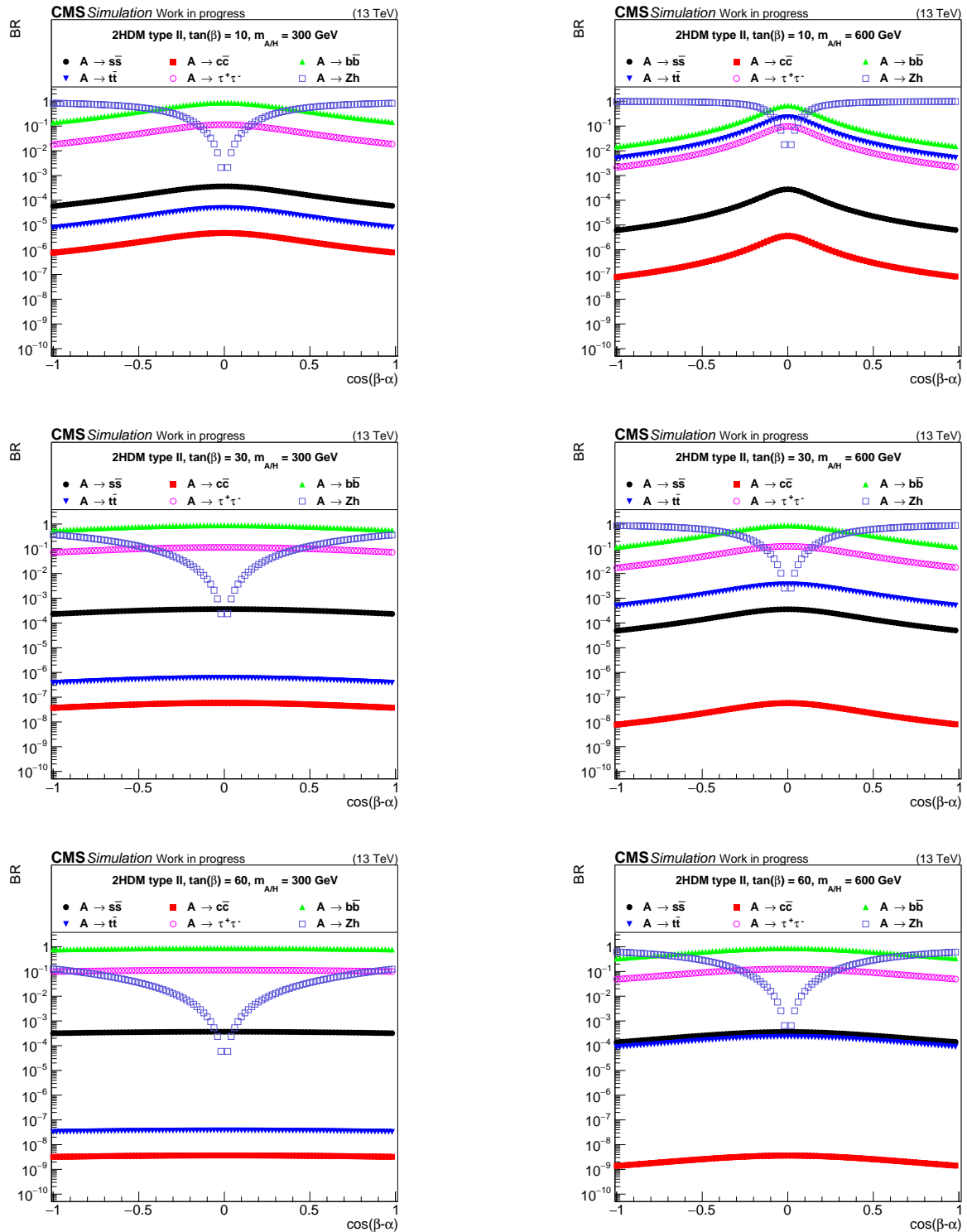


Figure B.1.: Branching ratios of the CP-odd A boson with a mass of 300 (left) and 600 GeV (right) for representative values of $\tan\beta = 10$ (top), $\tan\beta = 30$ (center), and $\tan\beta = 60$ (bottom) in the 2HDM type II scenario as a function of $\cos(\beta - \alpha)$.

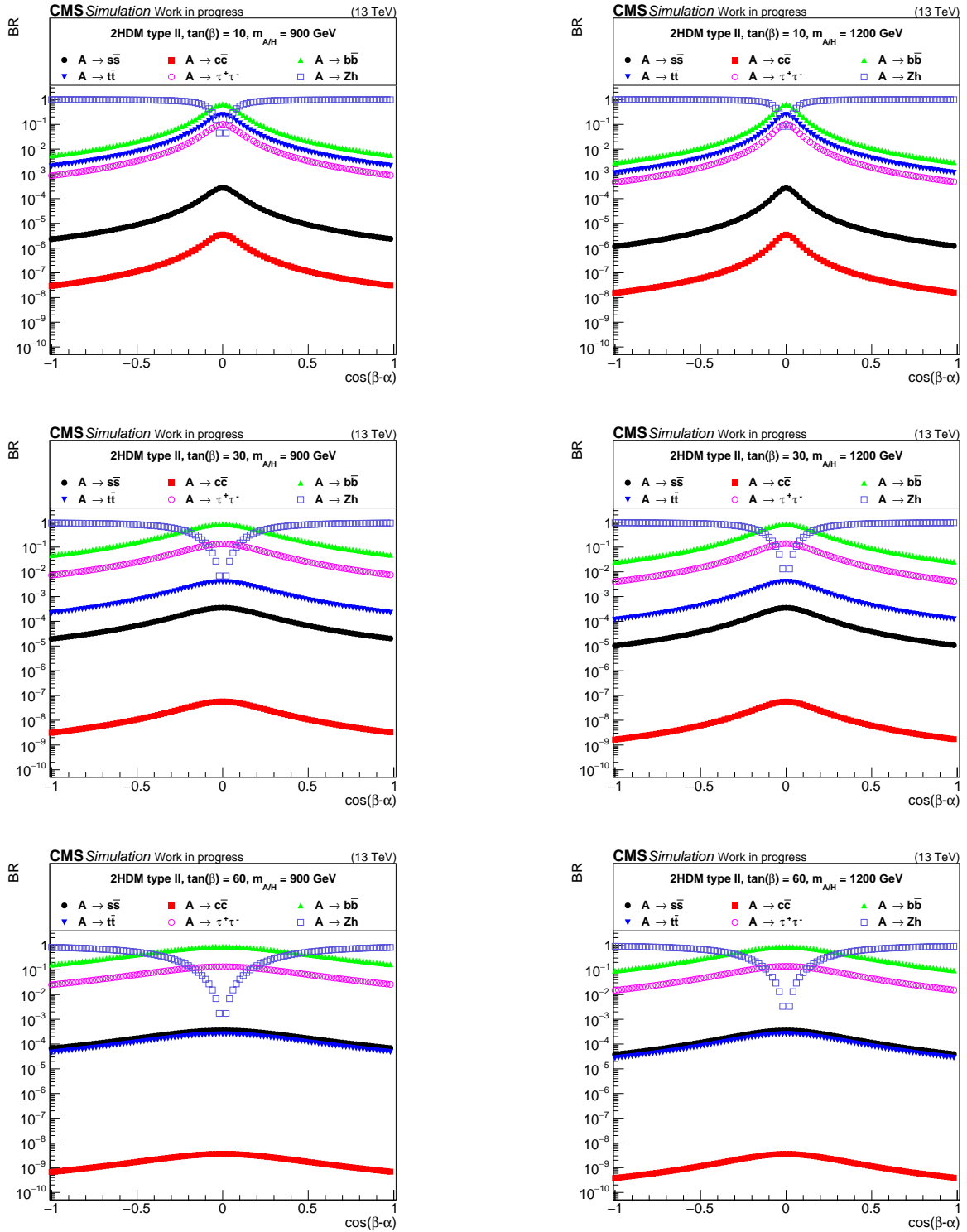


Figure B.2.: Branching ratios of the CP-odd A boson with a mass of 900 (left) and 1200 GeV (right) for representative values of $\tan\beta = 10$ (top), $\tan\beta = 30$ (center), and $\tan\beta = 60$ (bottom) in the 2HDM type II scenario as a function of $\cos(\beta - \alpha)$.

B. Cross-Sections and Branching Fractions in the 2HDM

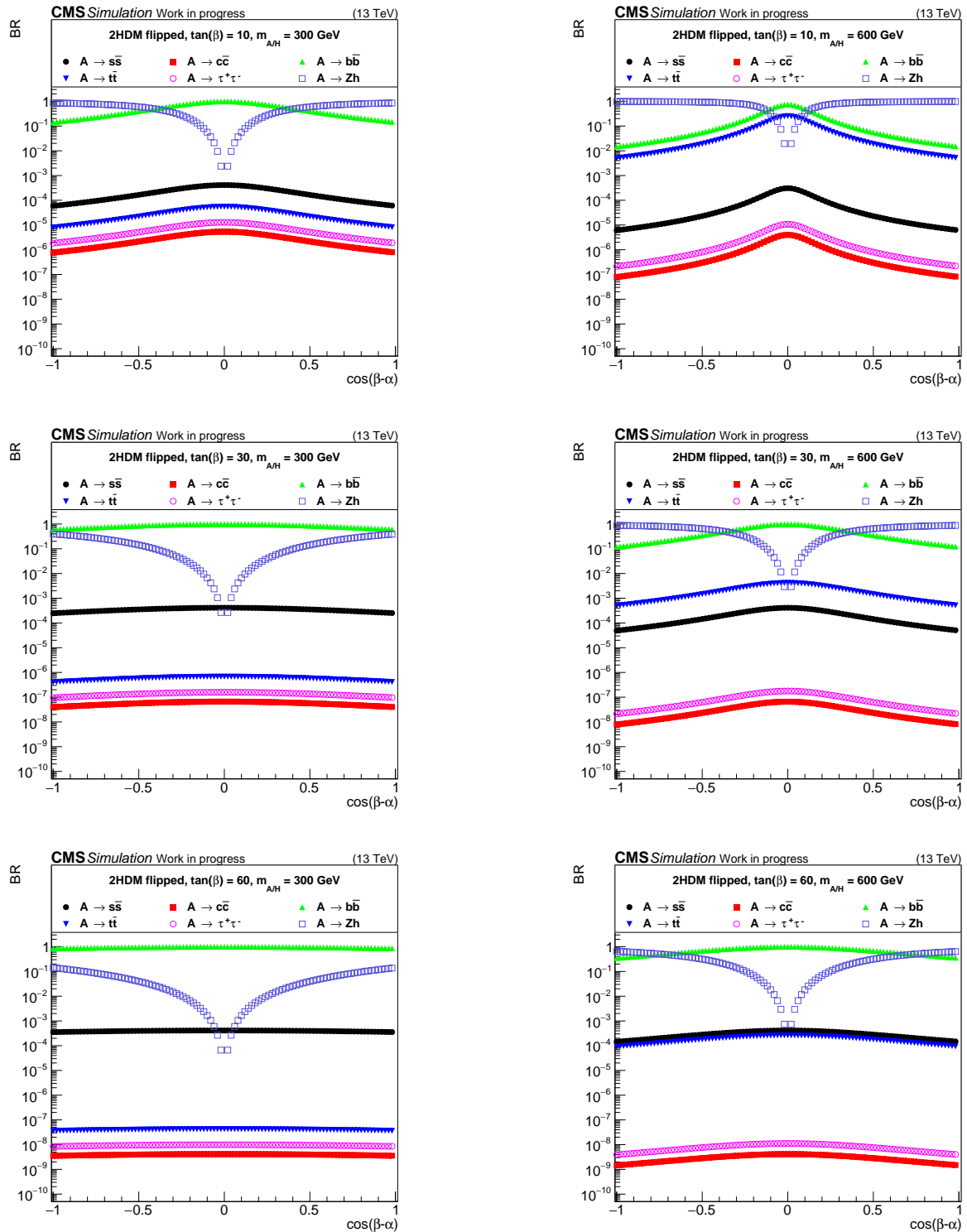


Figure B.3.: Branching ratios of the CP-odd A boson with a mass of 300 (left) and 600 GeV (right) for representative values of $\tan\beta = 10$ (top), $\tan\beta = 30$ (center), and $\tan\beta = 60$ (bottom) in the 2HDM flipped scenario as a function of $\cos(\beta - \alpha)$.

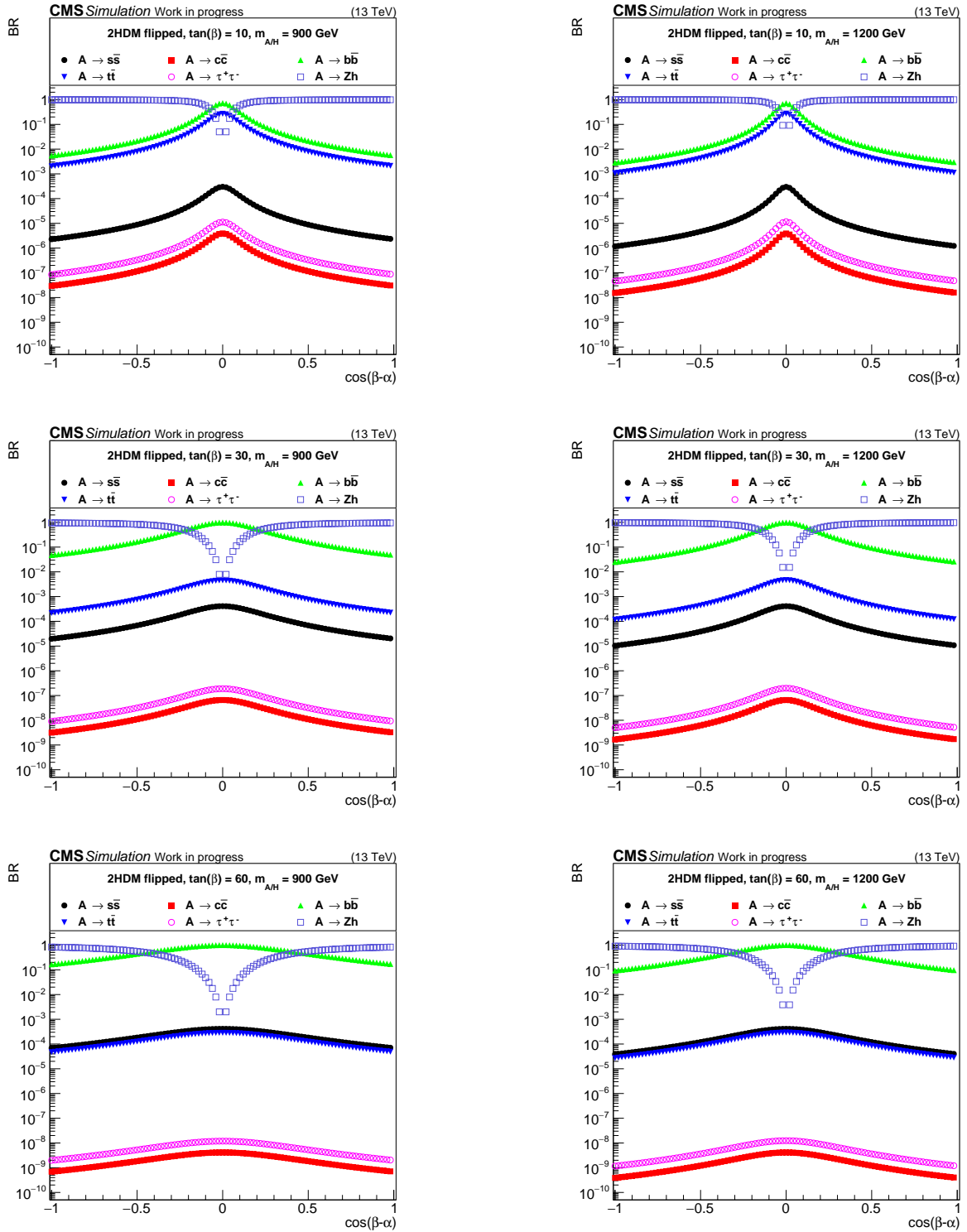


Figure B.4.: Branching ratios of the CP-odd A boson with a mass of 900 (left) and 1200 GeV (right) for representative values of $\tan\beta = 10$ (top), $\tan\beta = 30$ (center), and $\tan\beta = 60$ (bottom) in the 2HDM flipped scenario as a function of $\cos(\beta - \alpha)$.

B. Cross-Sections and Branching Fractions in the 2HDM

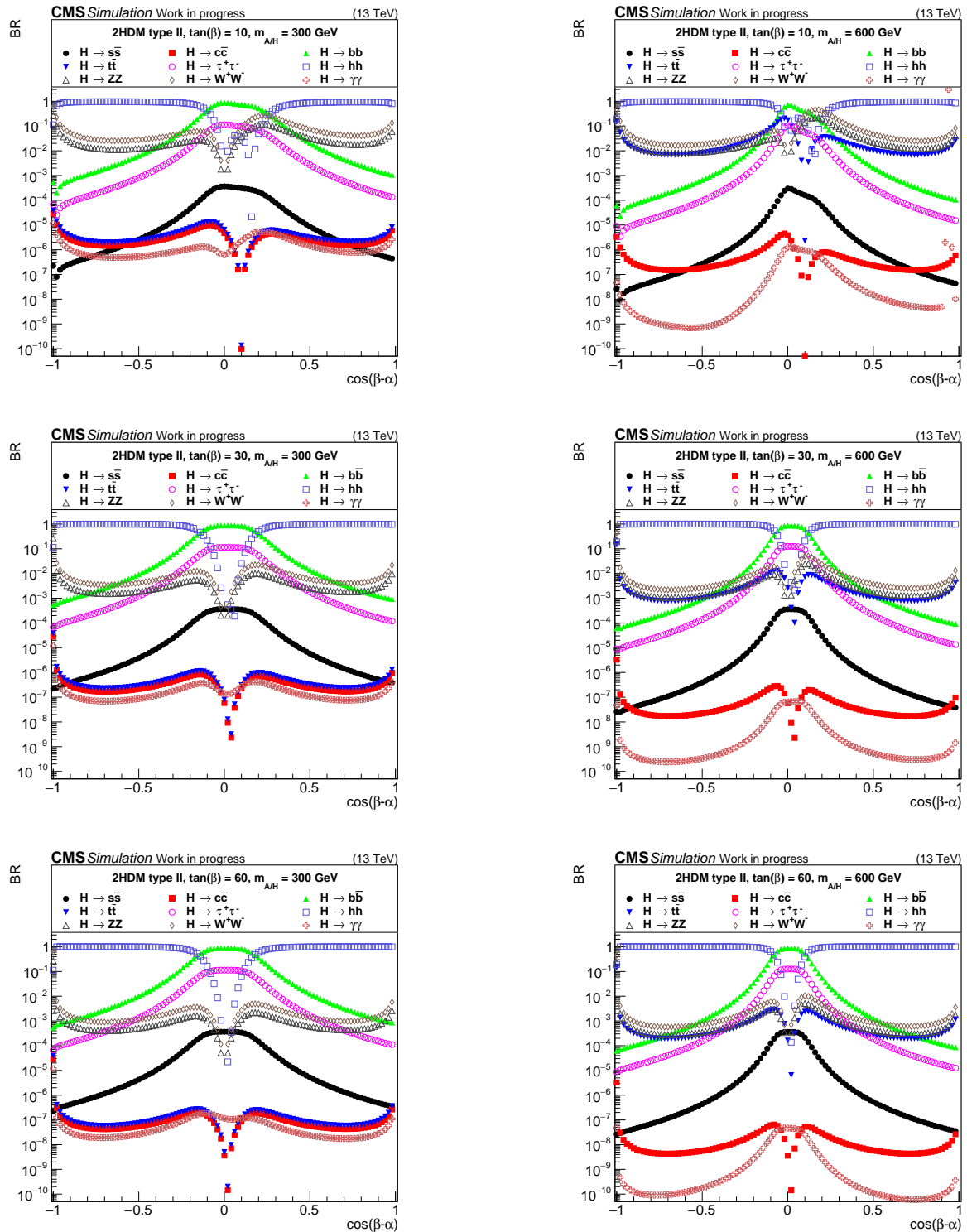


Figure B.5.: Branching ratio of the CP-even H boson with a mass of 300 (left) and 600 GeV (right) for representative values of $\tan\beta = 10$ (top), $\tan\beta = 30$ (center), and $\tan\beta = 60$ (bottom) in the 2HDM type II scenario as a function of $\cos(\beta - \alpha)$.

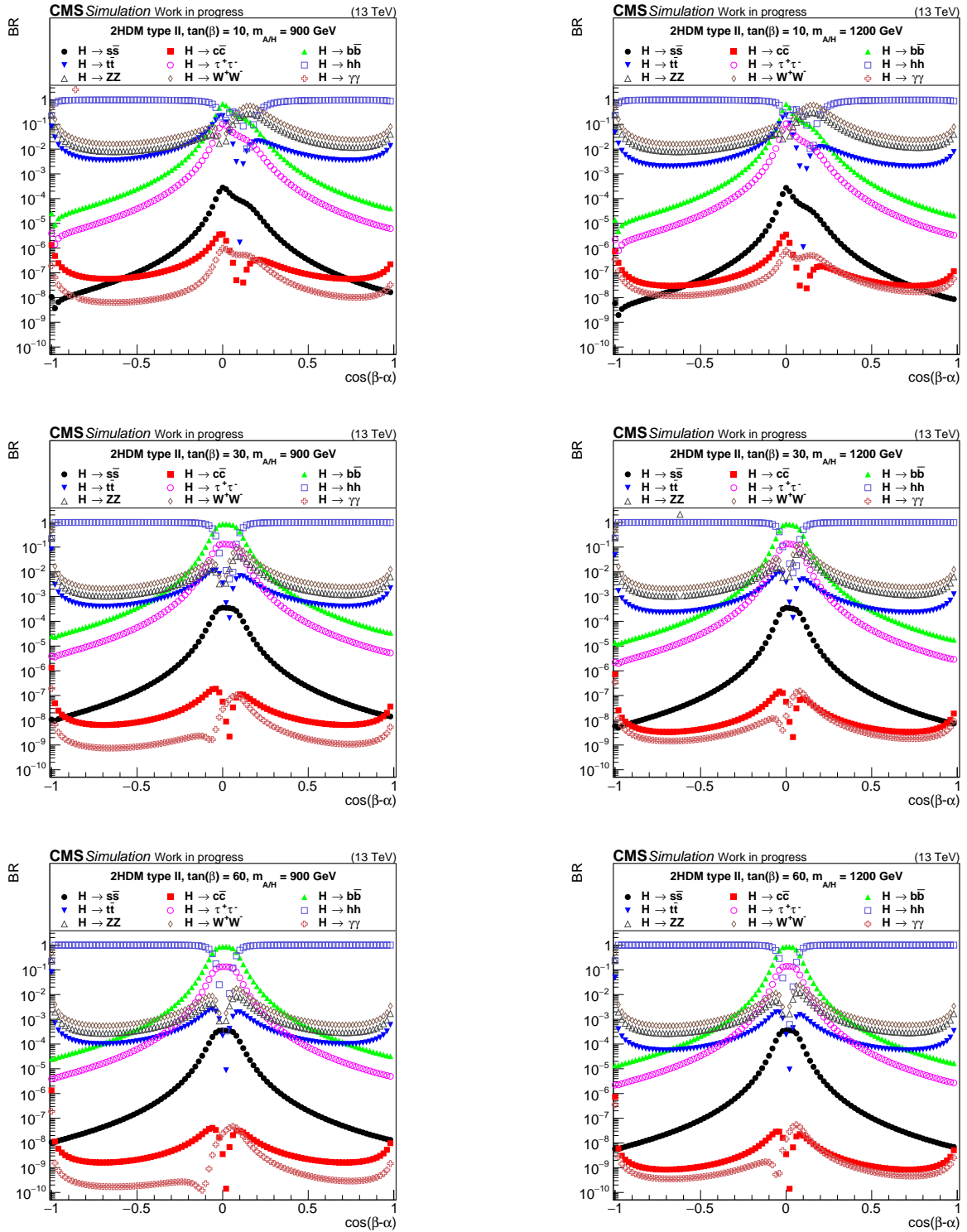


Figure B.6.: Branching ratio of the CP-even H boson with a mass of 900 (left) and 1200 GeV (right) for representative values of $\tan\beta = 10$ (top), $\tan\beta = 30$ (center), and $\tan\beta = 60$ (bottom) in the 2HDM type II scenario as a function of $\cos(\beta - \alpha)$.

B. Cross-Sections and Branching Fractions in the 2HDM

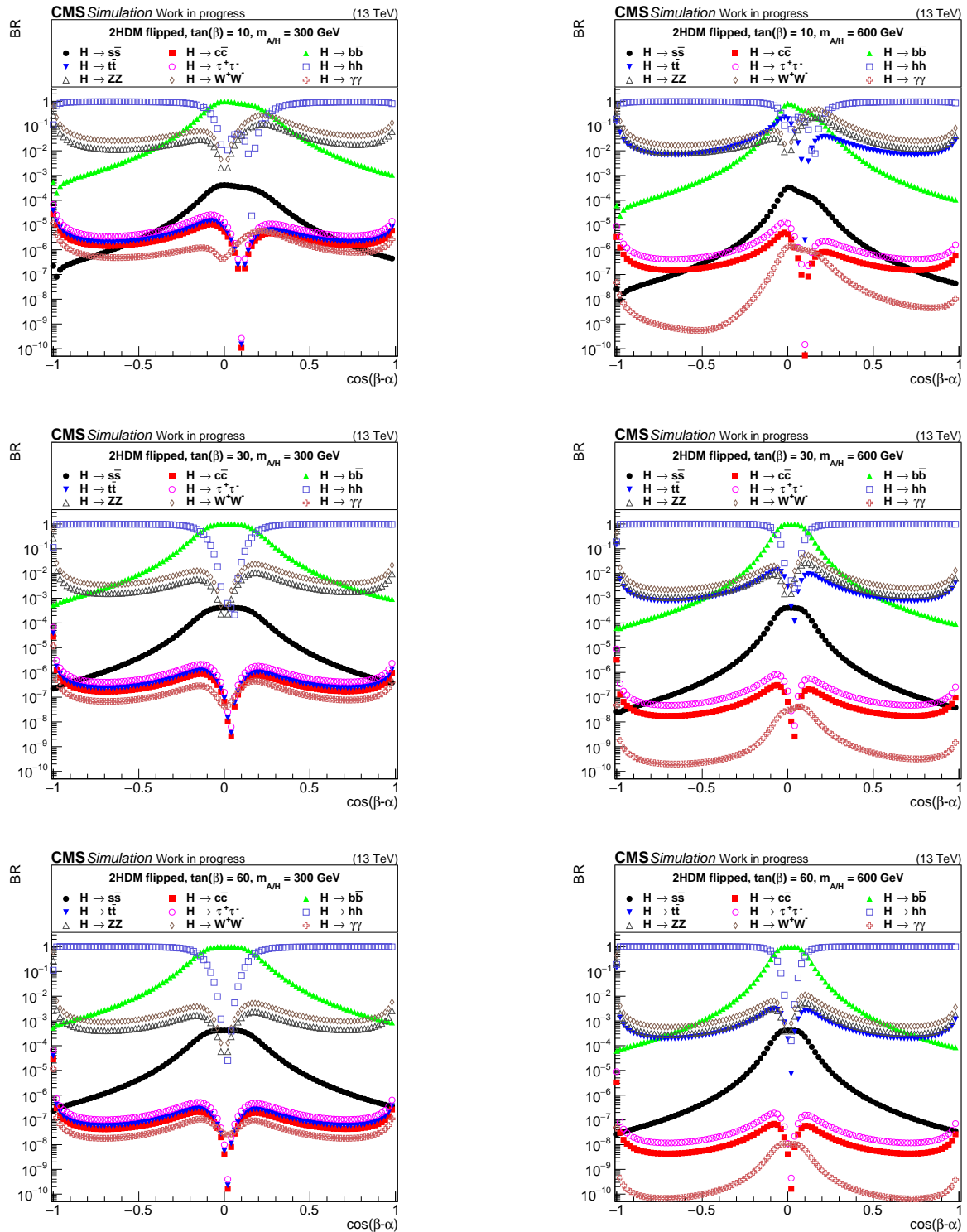


Figure B.7.: Branching ratio of the CP-even H boson with a mass of 300 (left) and 600 GeV (right) for representative values of $\tan\beta = 10$ (top), $\tan\beta = 30$ (center), and $\tan\beta = 60$ (bottom) in the 2HDM flipped scenario as a function of $\cos(\beta - \alpha)$.

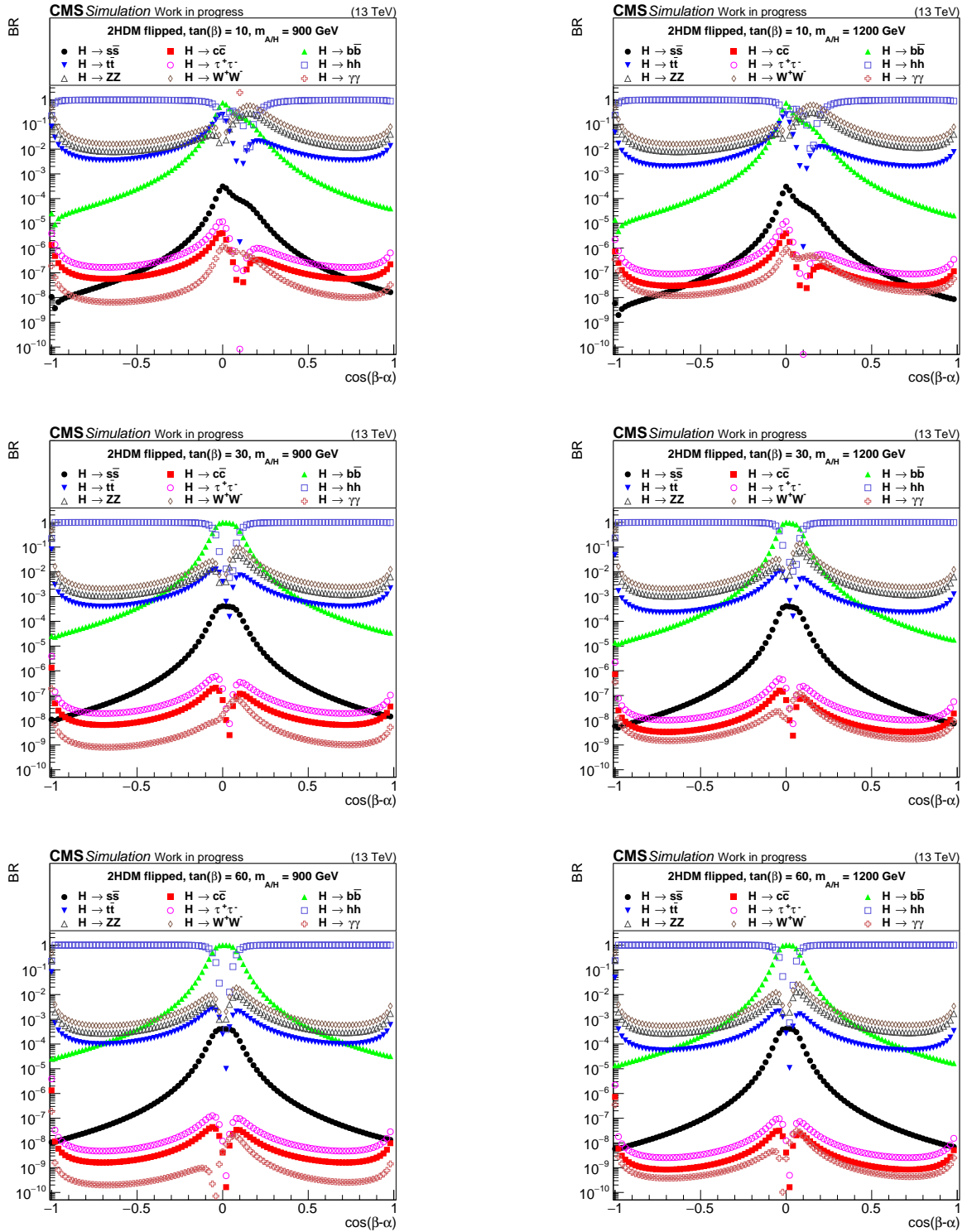


Figure B.8.: Branching ratios of the CP-even H boson with a mass of 900 (left) and 1200 GeV (right) for representative values of $\tan\beta = 10$ (top), $\tan\beta = 30$ (center), and $\tan\beta = 60$ (bottom) in the 2HDM flipped scenario as a function of $\cos(\beta - \alpha)$.

B. Cross-Sections and Branching Fractions in the 2HDM

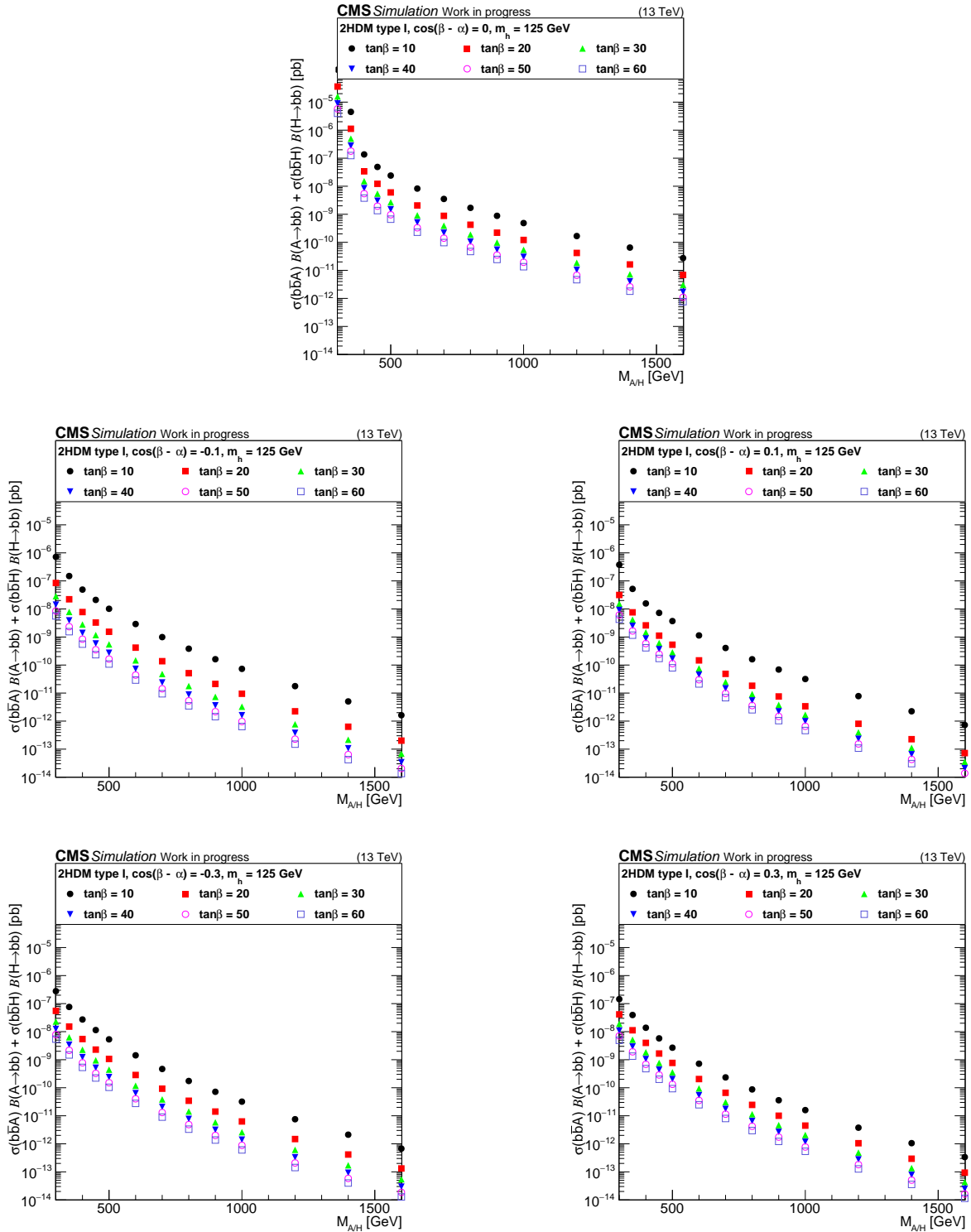


Figure B.9.: Cross-section times branching ratio for a b-associated production and subsequent decay into a pair of b quarks for the A and H boson, $\sigma(b\bar{b}A)\mathcal{B}(A \rightarrow b\bar{b}) + \sigma(b\bar{b}H)\mathcal{B}(H \rightarrow b\bar{b})$ in the 2HDM type I scenario vs. the Higgs-boson mass $m_{A/H}$ for $\cos(\beta - \alpha) = 0$ (top), $\cos(\beta - \alpha) = \pm 0.1$ (center), and $\cos(\beta - \alpha) = \pm 0.3$ (bottom). The differently colored points represent various values of $\tan\beta$.

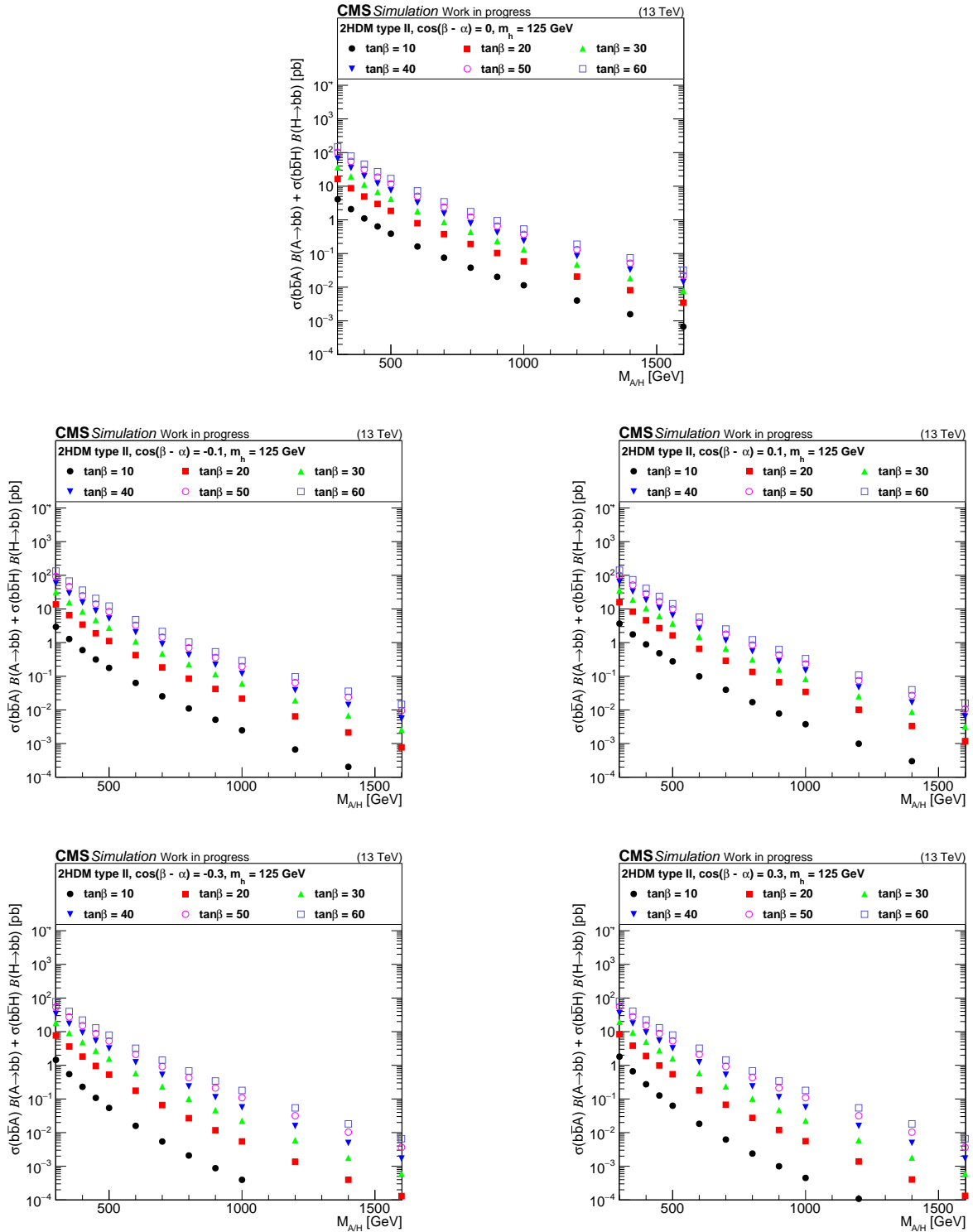


Figure B.10.: Cross-section times branching ratio for a b-associated production and subsequent decay into a pair of b quarks for the A and H boson, $\sigma(b\bar{b}A)\mathcal{B}(A \rightarrow b\bar{b}) + \sigma(b\bar{b}H)\mathcal{B}(H \rightarrow b\bar{b})$ in the 2HDM type II scenario vs. the Higgs-boson mass $m_{A/H}$ for $\cos(\beta - \alpha) = 0$ (top), $\cos(\beta - \alpha) = \pm 0.1$ (center), and $\cos(\beta - \alpha) = \pm 0.3$ (bottom). The differently colored points represent various values of $\tan\beta$.

B. Cross-Sections and Branching Fractions in the 2HDM

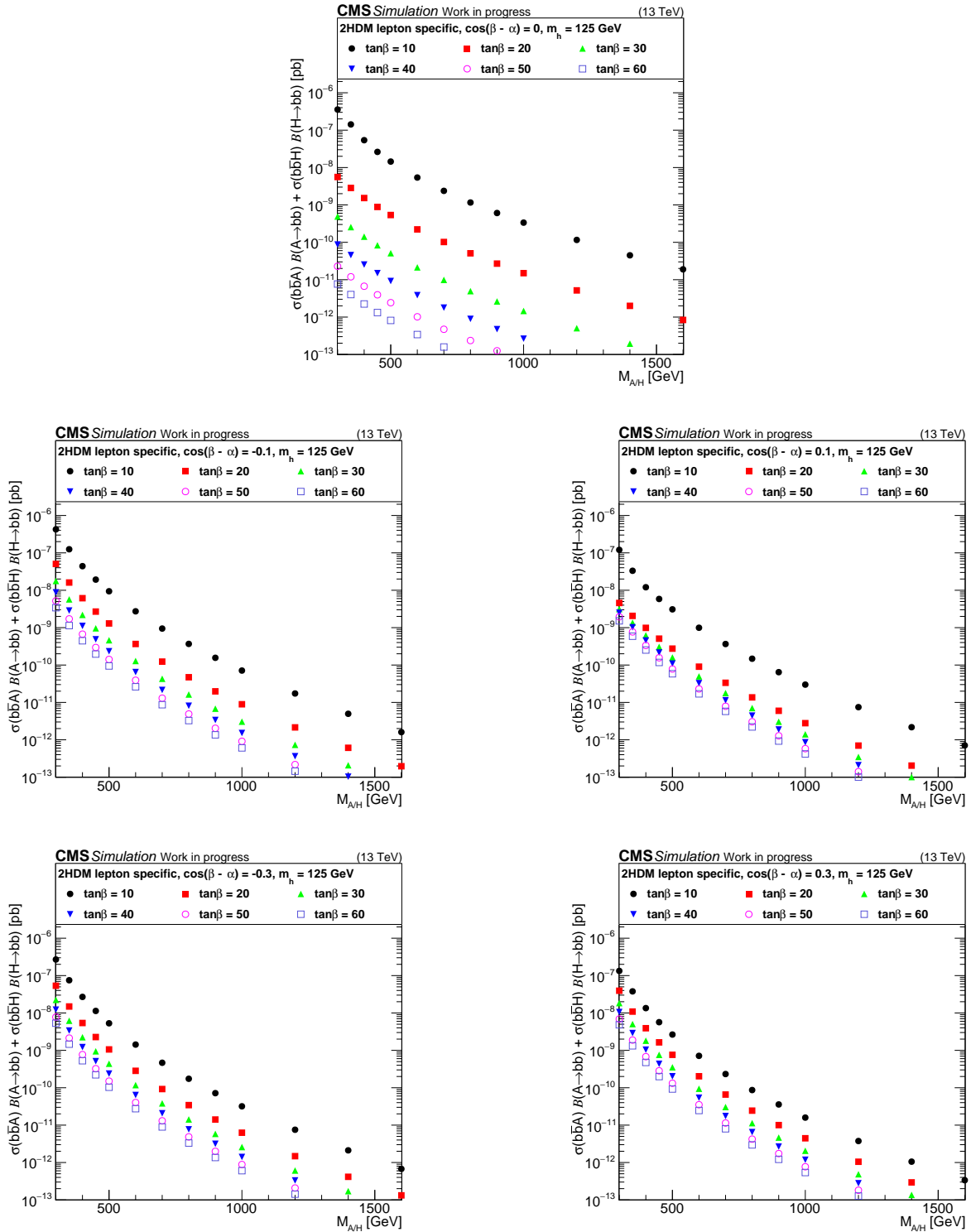


Figure B.11.: Cross-section times branching ratio for a b-associated production and subsequent decay into a pair of b quarks for the A and H boson, $\sigma(b\bar{b}A)\mathcal{B}(A \rightarrow b\bar{b}) + \sigma(b\bar{b}H)\mathcal{B}(H \rightarrow b\bar{b})$ in the 2HDM lepton specific scenario vs. the Higgs-boson mass $m_{A/H}$ for $\cos(\beta - \alpha) = 0$ (top), $\cos(\beta - \alpha) = \pm 0.1$ (center), and $\cos(\beta - \alpha) = \pm 0.3$ (bottom). The differently colored points represent various values of $\tan\beta$.

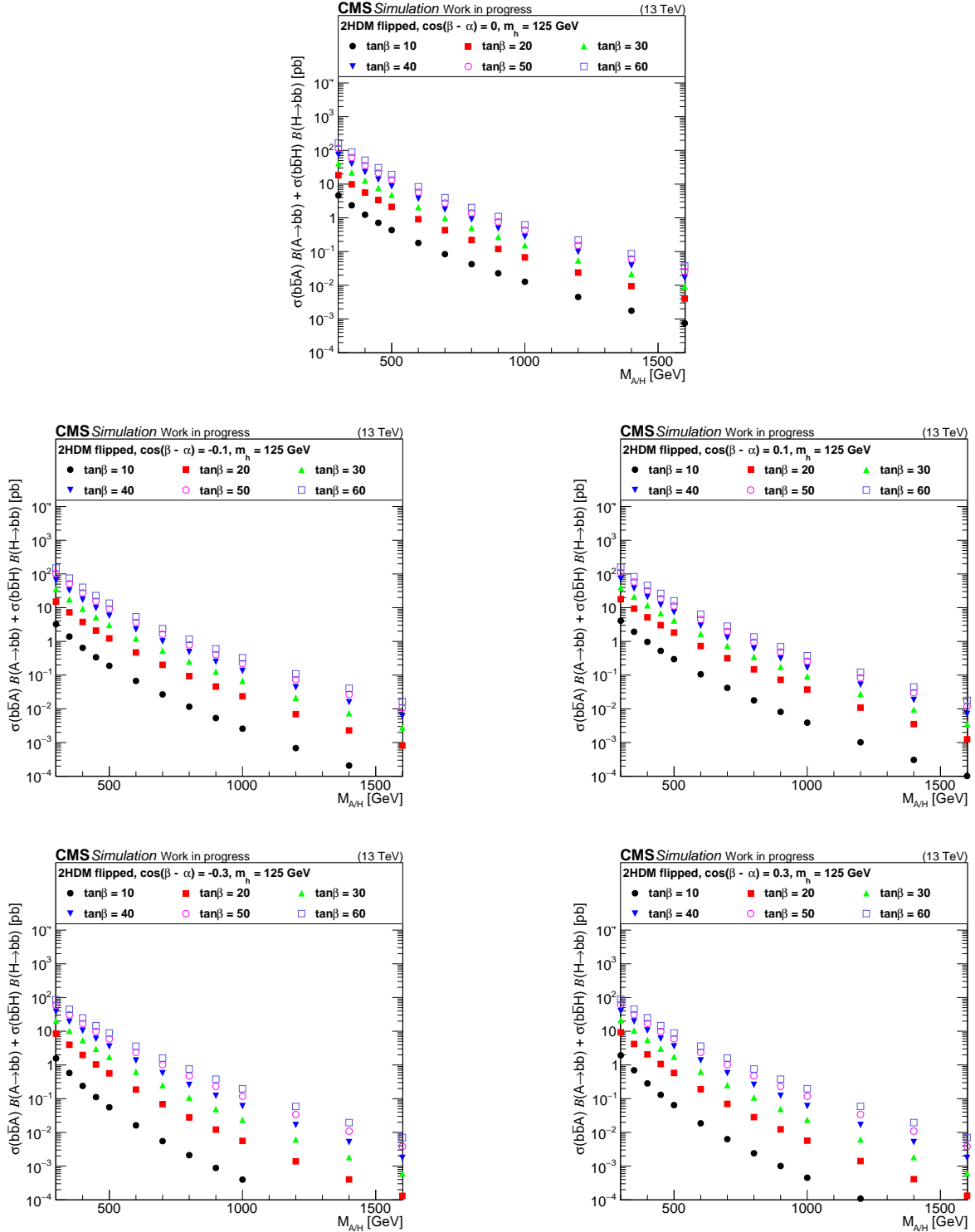


Figure B.12.: Cross-section times branching ratio for a b-associated production and subsequent decay into a pair of b quarks for the A and H boson, $\sigma(b\bar{b}A)\mathcal{B}(A \rightarrow b\bar{b}) + \sigma(b\bar{b}H)\mathcal{B}(H \rightarrow b\bar{b})$ in the 2HDM flipped scenario vs. the Higgs-boson mass $m_{A/H}$ for $\cos(\beta - \alpha) = 0$ (top), $\cos(\beta - \alpha) = \pm 0.1$ (center), and $\cos(\beta - \alpha) = \pm 0.3$ (bottom). The differently colored points represent various values of $\tan\beta$.

C. Model Dependent Limits

Model independent upper limits at 95 % C. L. on the cross-section times branching ratio of the b-associated production of a heavy, neutral Higgs boson which subsequently decays into a pair of b quarks, i.e. $\sigma(pp \rightarrow b\bar{b}A)\mathcal{B}(A \rightarrow b\bar{b}) + \sigma(pp \rightarrow b\bar{b}H)\mathcal{B}(H \rightarrow b\bar{b})$, are given in Table 6.1. They are translated into the parameter space of various MSSM and 2HDM benchmark scenarios, which is shown in detail in Section 6.3. Numerical results for each scenario are given here, where Tables C.1 to C.6 show the limits on the parameter $\tan\beta$ of the MSSM scenarios hMSSM, m_h^{mod+} , $m_h^{125}(\mu = 1 \text{ TeV})$, $m_h^{125}(\mu = -1 \text{ TeV})$, $m_h^{125}(\mu = -2 \text{ TeV})$, and $m_h^{125}(\mu = -3 \text{ TeV})$, respectively, and Tables C.7 and C.8 show contain the results for the 2HDM type II and flipped scenarios, respectively. In case of the MSSM scenarios, the limits on $\tan\beta$ are given in terms of the mass of the CP-odd A boson, while for the 2HDM scenarios, the mass of either boson, $m_{A/H}$, is regarded. For the MSSM scenarios, limits above $\tan\beta = 60$ are indicated by $-$, since theoretical predictions are not considered reliable in this part of the phase space (see Section 2.2). Similarly, limits in terms of the 2HDM scenarios exceeding $\tan\beta = 100$ are also indicated by $-$.

C. Model Dependent Limits

Mass [GeV]	-2σ	-1σ	exp.	$+1\sigma$	$+2\sigma$	obs.
300	11.9	13.6	16.0	19.6	22.6	20.5
350	11.7	13.3	15.5	18.3	21.2	13.4
400	11.7	13.3	15.5	18.4	21.5	13.8
450	12.8	14.6	17.0	20.2	23.6	18.3
500	14.5	16.6	19.4	23.1	26.9	23.5
600	17.7	20.2	23.8	28.3	33.1	26.9
700	19.5	22.6	26.9	32.1	37.8	25.5
800	23.5	27.3	32.4	38.8	45.7	40.1
900	29.6	34.2	40.6	48.4	57.1	44.0
1000	33.2	38.7	46.2	55.6	—	31.1
1200	47.9	55.4	—	—	—	53.1
1400	—	—	—	—	—	—
1600	—	—	—	—	—	—

Table C.1.: Upper limits at 95 % C. L. for the MSSM parameters $\tan \beta$ and m_A in terms of the hMSSM benchmark scenario.

Mass [GeV]	-2σ	-1σ	exp.	$+1\sigma$	$+2\sigma$	obs.
300	14.2	16.0	18.5	22.4	25.8	23.3
350	15.3	17.0	19.4	22.4	25.6	17.1
400	15.9	17.7	20.2	23.3	26.8	18.2
450	18.3	20.3	23.0	26.5	30.4	24.4
500	21.1	23.4	26.6	30.7	35.2	31.3
600	26.2	29.1	33.2	38.5	44.4	36.8
700	29.1	32.7	37.7	44.2	51.5	36.1
800	34.4	38.9	45.2	53.4	—	55.1
900	42.2	48.0	56.3	—	—	—
1000	47.0	54.2	—	—	—	—
1200	—	—	—	—	—	—
1400	—	—	—	—	—	—
1600	—	—	—	—	—	—

Table C.2.: Upper limits at 95 % C. L. for the MSSM parameters $\tan \beta$ and m_A in terms of the m_h^{mod+} benchmark scenario.

Mass [GeV]	-2σ	-1σ	exp.	$+1\sigma$	$+2\sigma$	obs.
300	13.0	15.2	18.3	23.5	28.5	24.9
350	12.7	14.7	17.7	21.6	26.2	14.9
400	12.7	14.6	17.6	21.7	26.6	15.2
450	14.0	16.2	19.7	24.4	30.1	21.5
500	16.1	19.0	23.2	29.0	36.2	29.8
600	20.5	24.3	30.2	38.8	50.1	36.0
700	23.1	28.0	35.8	47.5	—	33.2
800	29.6	36.5	48.1	—	—	—
900	41.3	52.9	—	—	—	—
1000	49.8	—	—	—	—	—
1200	—	—	—	—	—	—
1400	—	—	—	—	—	—
1600	—	—	—	—	—	—

Table C.3.: Upper limits at 95 % C. L. for the MSSM parameters $\tan \beta$ and m_A in terms of the $m_h^{125}(\mu = 1 \text{ TeV})$ benchmark scenario.

Mass [GeV]	-2σ	-1σ	exp.	$+1\sigma$	$+2\sigma$	obs.
300	10.0	11.3	12.9	15.3	17.2	15.9
350	9.9	11.1	12.6	14.5	16.4	11.2
400	10.0	11.1	12.7	14.6	16.5	11.4
450	10.9	12.0	13.7	15.7	17.8	14.5
500	12.0	13.4	15.2	17.4	19.7	17.7
600	14.1	15.7	17.8	20.4	22.9	19.6
700	15.2	17.1	19.5	22.4	25.2	18.8
800	17.6	19.7	22.5	25.6	28.7	26.2
900	21.0	23.4	26.4	29.8	33.2	27.9
1000	22.8	25.5	28.8	32.6	36.2	21.7
1200	29.4	32.4	36.0	40.0	43.8	31.5
1400	36.4	39.5	43.3	47.2	50.3	43.4
1600	42.5	45.8	49.3	52.2	54.0	54.1

Table C.4.: Upper limits at 95 % C. L. for the MSSM parameters $\tan \beta$ and m_A in terms of the $m_h^{125}(\mu = -1 \text{ TeV})$ benchmark scenario.

C. Model Dependent Limits

Mass [GeV]	-2σ	-1σ	exp.	$+1\sigma$	$+2\sigma$	obs.
300	9.1	10.5	11.5	13.4	14.9	13.8
350	9.1	10.4	11.3	12.8	14.2	10.5
400	9.2	10.5	11.4	12.9	14.4	10.6
450	9.9	10.9	12.2	13.8	15.3	12.8
500	10.9	12.0	13.4	15.1	16.8	15.3
600	12.5	13.8	15.4	17.2	19.1	16.7
700	13.4	14.8	16.7	18.7	20.6	16.1
800	15.2	16.8	18.7	20.9	22.9	21.3
900	17.7	19.3	21.4	23.6	25.7	22.4
1000	19.0	20.8	23.0	25.3	27.5	18.2
1200	23.4	25.2	27.4	29.6	31.5	24.6
1400	27.6	29.3	31.3	33.6	39.9	31.4
1600	30.9	32.5	37.5	45.7	54.8	55.6

Table C.5.: Upper limits at 95 % C. L. for the MSSM parameters $\tan\beta$ and m_A in terms of the $m_h^{125}(\mu = -2 \text{ TeV})$ benchmark scenario.

Mass [GeV]	-2σ	-1σ	exp.	$+1\sigma$	$+2\sigma$	obs.
300	8.5	9.4	10.7	12.0	13.2	12.4
350	8.5	9.3	10.6	11.5	12.7	9.3
400	8.6	9.4	10.6	11.7	12.9	9.6
450	9.2	10.4	11.1	12.4	13.6	11.6
500	10.0	11.0	12.1	13.4	14.8	13.6
600	11.4	12.4	13.7	15.2	16.5	14.7
700	12.1	13.3	14.7	16.2	17.7	14.3
800	13.6	14.8	16.3	17.9	19.4	18.2
900	15.5	16.8	18.3	19.9	21.3	19.0
1000	16.4	17.8	19.4	21.1	22.5	15.9
1200	19.7	21.0	22.4	25.9	30.8	20.6
1400	22.6	25.4	30.2	36.3	43.0	30.2
1600	24.7	28.1	33.7	41.0	49.2	49.8

Table C.6.: Upper limits at 95 % C. L. for the MSSM parameters $\tan\beta$ and m_A in terms of the $m_h^{125}(\mu = -3 \text{ TeV})$ benchmark scenario.

Mass [GeV]	-2σ	-1σ	exp.	$+1\sigma$	$+2\sigma$	obs.
300	11.9	13.5	15.8	19.3	22.2	20.1
350	11.9	13.4	15.5	18.2	21.1	13.5
400	12.1	13.6	15.7	18.5	21.6	14.0
450	13.3	15.0	17.4	20.5	23.9	18.6
500	15.2	17.2	20.0	23.7	27.7	24.2
600	18.8	21.4	25.1	30.0	35.3	28.5
700	21.3	24.7	29.4	35.4	42.0	27.9
800	26.6	30.9	36.9	44.5	52.7	46.0
900	34.8	40.3	48.0	57.5	68.0	52.1
1000	40.2	46.9	56.1	67.7	80.4	37.7
1200	60.7	70.1	83.0	99.6	—	67.1
1400	87.2	—	—	—	—	—
1600	—	—	—	—	—	—

Table C.7.: Upper limits at 95 % C. L. for the parameter $\tan \beta$ in terms of $m_{A/H}$ for the 2HDM type II scenario.

Mass [GeV]	-2σ	-1σ	exp.	$+1\sigma$	$+2\sigma$	obs.
300	11.3	12.8	14.9	18.2	21.0	19.0
350	11.4	12.8	14.7	17.2	19.9	12.9
400	11.6	13.0	15.0	17.5	20.4	13.4
450	12.8	14.3	16.5	19.4	22.6	17.6
500	14.5	16.4	19.0	22.4	26.1	22.8
600	18.0	20.3	23.8	28.3	33.3	26.9
700	20.4	23.4	27.9	33.5	39.6	26.4
800	25.3	29.3	35.0	42.0	49.7	43.5
900	33.0	38.2	45.3	54.3	64.1	49.2
1000	38.2	44.4	53.0	63.8	75.7	35.8
1200	57.3	66.0	78.0	93.5	—	63.3
1400	82.0	94.1	—	—	—	—
1600	—	—	—	—	—	—

Table C.8.: Upper limits at 95 % C. L. for the parameter $\tan \beta$ in terms of $m_{A/H}$ for the 2HDM flipped scenario.

D. Higgs Physics Within and Beyond the Standard Model at CMS

In this section, an overview is given on the current status of Higgs physics and respective searches within and beyond the Standard Model, as published in [218]. The first part is dedicated to the discovery of the Higgs boson and precision measurements of its properties as well as ongoing efforts to observe additional decay channels like $H \rightarrow c\bar{c}$ and Higgs boson self-coupling. In the second part, searches for BSM Higgs bosons are presented, for example analyses targeting heavy, neutral Higgs bosons in the decay channels $H/A \rightarrow \tau^+\tau^-$ or $H/A \rightarrow b\bar{b}$ and charged Higgs bosons H^\pm in the decay into $\tau^\pm\nu_\tau$. Also searches for light Higgs bosons a are presented which are predicted by, e.g., next-to-minimal supersymmetric SM (NMSSM) and Two-Higgs-Doublet-Plus-Singlet (2HDM+S) scenarios. Specifically, the process $h \rightarrow aa \rightarrow \mu^+\mu^-\mu^+\mu^-$ is discussed, where h is the observed 125 GeV boson.

Higgs Physics Within and Beyond the Standard Model at CMS

Paul Asmuss¹ on behalf of the CMS Collaboration

¹ DESY Hamburg, Germany, paul.asmuss@desy.de

Abstract:

Ever since a new boson was found at a mass of 125 GeV in 2012, this particle has been studied intensively. So far, all measurements agree with the Standard Model predictions and the particle is assumed to be the Higgs boson. Nevertheless, many tests still have to be performed to either confirm or disprove this assumption. Here, several discoveries and searches related to the Higgs boson and conducted with the CMS experiment are presented.

1 Introduction

In 1964, Brout, Englert and Higgs postulated a new theory to explain the non-zero masses of vector bosons [1, 2]. In that theory, they introduced spontaneous electroweak symmetry breaking which would also yield a new boson. It was searched intensively and finally discovered at a mass of about 125 GeV in 2012 [3–5] by the two general purpose experiments at the LHC [6] at CERN, ATLAS [7] and CMS [8]. Up to now, all measurements of e.g. cross sections and branching ratios show a good agreement with the Standard Model predictions. While for the proton-proton collisions at the LHC, there are four main production channels for the Higgs boson, the range of possible decays is huge and still a subject of many different searches. In recent years, the four main production channels and many of the predicted decays have been observed. For instance in 2018, the production in association with a top quark pair [9, 10] and the decay to bottom quarks [11, 12] were discovered and will also be described in more detail later.

While the ongoing precision measurements are a large field of studies by themselves, there is also a vast variety of models beyond the Standard Model which can be accessed via the Higgs boson. Several of these models include additional Higgs bosons or changes in its properties. So far, the LHC delivered data corresponding an integrated luminosity of over 150/fb at a center-of-mass energy of 13 TeV [13]. In the coming years it is expected to produce up to 3/ab [14] of integrated luminosity, which would enable physicists not only to study the Higgs boson's properties precisely but also search for extremely rare decays and look for tiny deviations from the prediction in order to find new physics.

In Section 2, the CMS detector and the LHC are described in detail, while Sections 3 and 4 are dedicated to Higgs-related searches and studies within and without the Standard Model, respectively. Finally, Section 5 consists of a short summary and an outlook to the prospects of the HL-LHC.

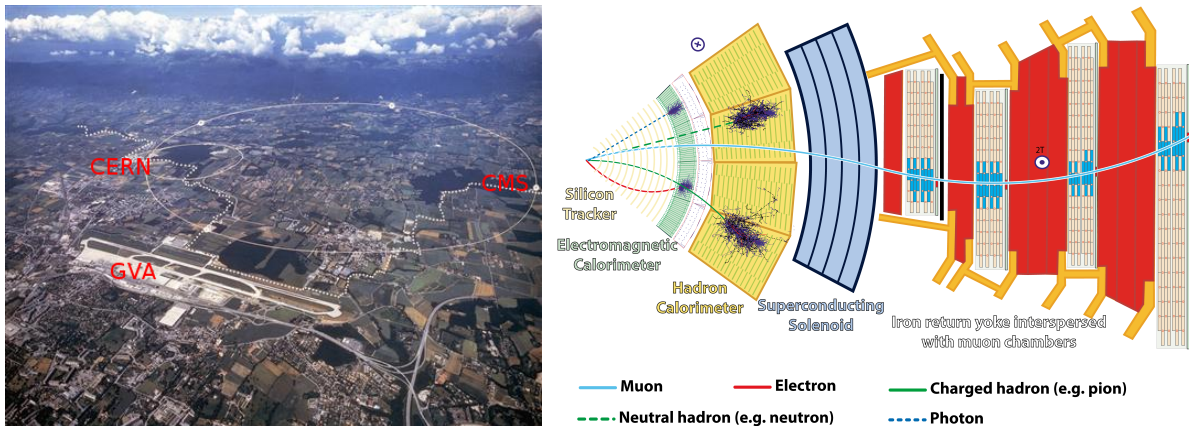


Figure 1: Areal view on the LHC together with the locations of CERN, Meyrin site, and CMS (left, [15]) and slice through the CMS detector with some example particle signatures (right, [16])

2 The CMS Detector at the LHC

Located in Geneva, Switzerland, CERN hosts the most powerful particle accelerator built so far, the Large Hadron Collider (LHC) [6]. It has a circumference of around 27 km and stretches below Switzerland and France. Its location is shown in Figure 1 (left). Until now, the LHC was operating at a center-of-mass energy of up to $\sqrt{s} = 13$ TeV while being designed for up to $\sqrt{s} = 14$ TeV. This design energy is planned to be reached in the future (see Section 5).

The LHC hosts two general purpose experiments, ATLAS (A Toroidal LHC Apparatus) [7] and CMS (Compact Muon Solenoid) [8]. As such, CMS is designed to detect, identify and measure all kinds of high-energy objects, e.g. it provides good tracking quality used for b tagging as well as a high momentum resolution for muons in its outer chambers. The detector is arranged in shells around the beam with one of its main features being the superconducting solenoid magnet which provides a magnetic field of 3.8 T. A slice through CMS is shown in Figure 1 (right) together with the signatures various particles would leave in it if they passed the detector.

3 Higgs Physics Within the Standard Model

Since the 1970s, the Standard Model (SM) of particle physics has been established and intensively tested. Its fundamental particle content is shown in Figure 2 (left). Out of these particles, the fermions constitute matter, while the gauge bosons mediate the interactions. Namely, these are the electromagnetic, weak and strong interactions. So far, all measurements conducted are in good agreement with the SM. When the Higgs boson was found in 2012, it was considered being the last missing piece. Since then, the

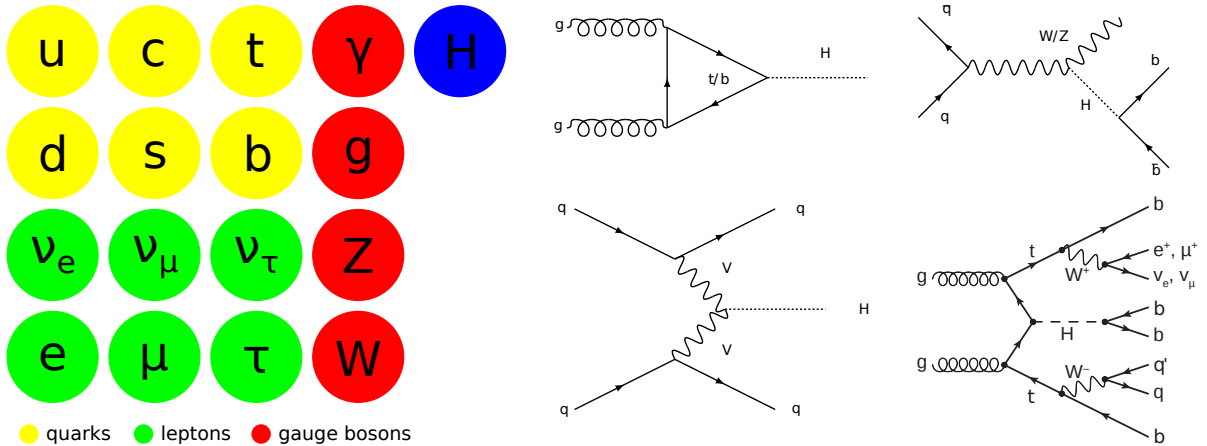


Figure 2: Particle content of the Standard Model, including the Higgs boson in blue (left), and main production modes for the Higgs boson (right)

production and decay modes of the Higgs boson and its interactions with other particles in general have been investigated thoroughly.

3.1 Discovery and Precision Measurements

While there are various decay modes for the Higgs boson, only four main production mechanisms exist, which are shown in Figure 2. Namely, these are gluon-gluon fusion (ggH , production fraction of around 88%), vector-boson fusion (VBF, 7%), higgsstrahlung or vector-boson associated production (VH, 4%) and production in association with top quarks (ttH , 1%).

For the first discovery, two decay channels, $\gamma\gamma$ and $ZZ(4l)$, were of great importance due to their very clean signatures despite their rather low branching fractions (0.2 and 2%, respectively). To announce the discovery of a new boson with a mass of (125.06 ± 0.29) GeV, data corresponding to an integrated luminosity of around 10/fb was used, collected at $\sqrt{s} = 7$ TeV and $\sqrt{s} = 8$ TeV. The corresponding mass distribution for two photons with the well visible peak is shown in Figure 3 (left).

By now, including data from RunII (2016–2018), precision measurements can be performed. Results of such studies are shown in Figure 3 for the two discovery channels. In the center plot, the advantages of the $4l$ can be seen: the Z- and Higgs-peaks are clearly distinguished and there is only little background around m_H . From these new measurements in the two discovery channels, an updated mass value of $m_H = (125.35 \pm 0.15)$ GeV is extracted [17].

The four-lepton channel also allows to draw additional conclusions on production and decay modes [18]. As can be seen from Figure 3 (right), all main production modes agree with the SM within their respective uncertainties. Furthermore, vector-boson and fermion induced production modes also agree with each other. For the inclusive result of

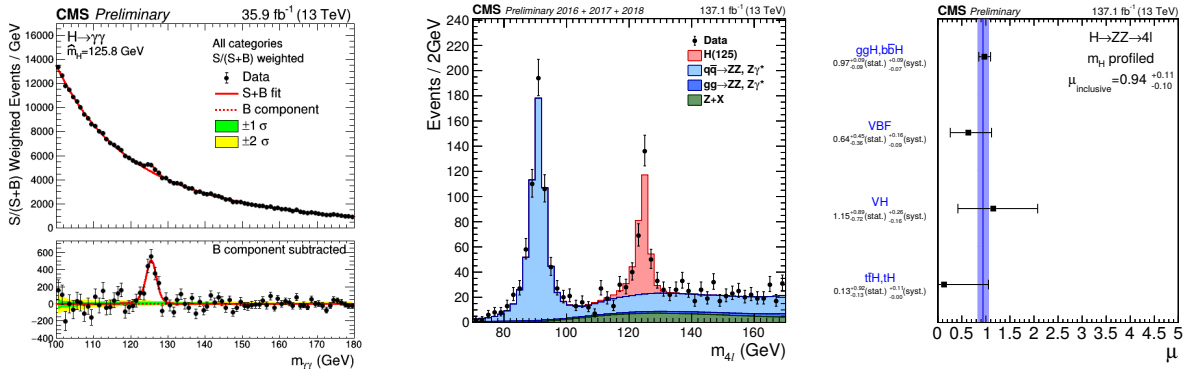


Figure 3: Left: first observation of a new boson at around 125 GeV in the di-photon ($\gamma\gamma$) channel in 2012 [3]; center: mass distribution of second discovery channel (four leptons, using full RunII data); right: fitted signal strength, extracted from the four-lepton channel, also using all of RunII [18]

$\mu = 0.94_{-0.10}^{+0.11}$, the various signal regions have been combined. Here, the signal strength μ , a key quantity for many searches, is the ratio of the measured cross section and the SM prediction. Thus, for the SM, a value of 1 is expected.

3.2 Observations of $t\bar{t}H$ Production and $H \rightarrow b\bar{b}$ Decay

After the Higgs boson was discovered, focus changed to its properties as well as production and decay modes. Since they are predicted precisely by the theory, they can also be used to test the SM. As particles are predicted to couple to the Higgs boson stronger the heavier they are, couplings of top and bottom quarks were searched for in particular. While the Higgs coupling to b quarks can be studied through the $H \rightarrow b\bar{b}$ decay, which is predicted to be the dominant decay mode with a branching fraction of about 58%, the coupling to the top quark can be investigated in the $t\bar{t}H$ production mode. Adding the data from 2016 and 2017 to the RunI dataset, both channels could be observed [9, 11].

For the $t\bar{t}H$ search, background distributions were predicted based on data where possible. To reduce the fraction of background events, multivariate analyses (MVAs) had to be used as well as for most other searches involving multiple jets in the final states. The distribution of events is shown in Figure 4 (left), grouped by their signal-to-background ratio as obtained from the MVA. As can be seen, only in the right bins, with the highest ratio, the excess of signal over background is significant. Signal strengths could be extracted for various decay modes of the Higgs boson. They were then combined for RunI and RunII, respectively, before calculating the overall result. All of these results are shown in Figure 4 (center).

While the $t\bar{t}H$ production mode was observed based on combining several decay modes and using data from RunI and 2016, an even larger amount of data was needed to also announce the observation of $H \rightarrow b\bar{b}$, which was done with the dataset of RunI +

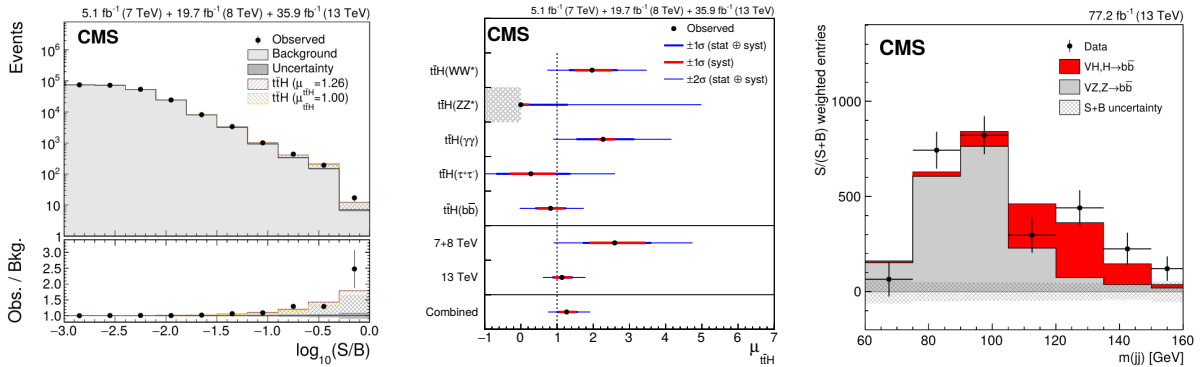


Figure 4: Observation of the ttH production mode and decay into a pair of bottom quarks: Distribution of MVA discriminant, sorted by signal-to-background ratio (left) and fitted signal strength for ttH , separated by decay channel of the Higgs boson (center) [9]. Right, from the $H \rightarrow b\bar{b}$ decay observation: Mass distribution of two b jets, peaking at the Higgs-boson mass with all backgrounds but $VZ(bb)$ subtracted [11]

2016 + 2017. As for the ttH observation, MVAs were used to increase the signal-to-background ratio. This observation is particularly important because it has been the first direct observation of Yukawa couplings to down-type quarks. In this search, the VH production channel was of great use. It features a very clean signature due to the vector boson and, thus, using leptonic decays, additional leptons which are easy to identify. A mass distribution for two b jets is shown in Figure 4 (right), where only the VH production mode is used and all backgrounds but $VZ(bb)$ have been subtracted.

3.3 Search for $H \rightarrow c\bar{c}$ Decay and the Higgs Boson Self-Coupling

While many predictions of the SM could already be verified, several searches are still ongoing. On the one hand, these are decays of the Higgs boson to lighter particles like muons or charm quarks. On the other hand, one key prediction of the SM is that the Higgs boson features a self-coupling which is also searched for.

Testing the Higgs boson for rare decays allows to further investigate how well the SM predictions describe nature. In the case of the Higgs decay into a pair of charm quarks, the charm Yukawa coupling can be measured. As in the search for the decay into bottom quarks, the VH production mode is used to reduce the large QCD background. Additionally, the optimization of selecting c jets is three-dimensional since not only light jets need to be rejected but also those originating from b quarks. Thus, c -jet efficiency is reduced in favor of good b -jet rejection and excellent light-jet cuts. Nevertheless, the signal-to-background ratio is low, as can be seen in Figure 5 (left). Although this is one of the channels where the signal is most prominent, it still has to be enlarged significantly to be visible. Note that the limits on μ (around 70) are still far away from the value

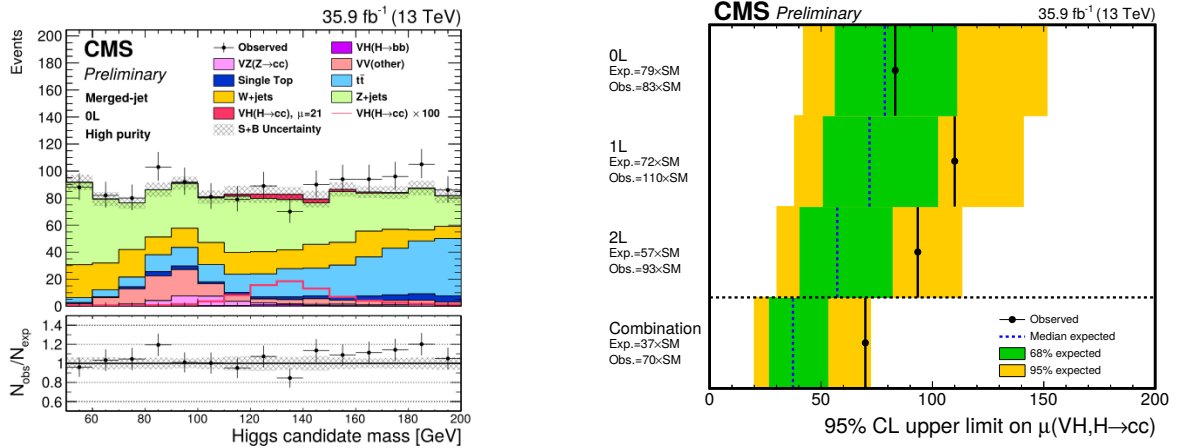


Figure 5: Mass distribution for the Higgs candidate for the $H \rightarrow c\bar{c}$ search (left) and best limits to date in terms of signal strength (right) [19]

of 1 which would be expected for the SM. Nevertheless, these are the most stringent limits to date and they are shown in Figure 5 (right) for different signal regions. The excess visible is well covered within the uncertainties and mainly driven by the large contribution of background events.

Similar to the $H \rightarrow c\bar{c}$ study, also the search for Higgs self-coupling suffers from a low signal-to-background ratio. Here, the main issue is the low cross section of a (virtual) Higgs boson decaying into two Higgs bosons (around 30 fb). This di-Higgs production is also covered in background originating from two Higgs bosons being produced via a rather common box diagram which is shown in Figure 6 (left) together with the signal process. Furthermore, these two processes are expected to have an almost destructive interference, making it even harder to detect the signal. Overall, the search [20] is dedicated to constrain the coupling modifier $k_\lambda = \lambda_{HHH}/\lambda_{SM}$. When the limits on the production cross section are expressed in terms of this modifier, they follow the features of the HH production cross section, allowing to distinguish the signal from background. In Figure 6 (right), this limit is shown. It also shows how close the SM prediction is to completely destructive interference. As for the $H \rightarrow c\bar{c}$ search, the finally extracted result $\mu \lesssim 20$ is an upper limit on the signal strength which is not yet close to SM sensitivity.

4 Searches for Beyond-the-SM Higgs Bosons

While all measurements so far agree with the SM, there are strong indications that the SM is not complete. For instance, the SM does not feature neutrino masses or a candidate for Dark Matter. While we definitely know from experiments that neutrinos are extremely light but have a non-zero mass, there are only indirect measurements of

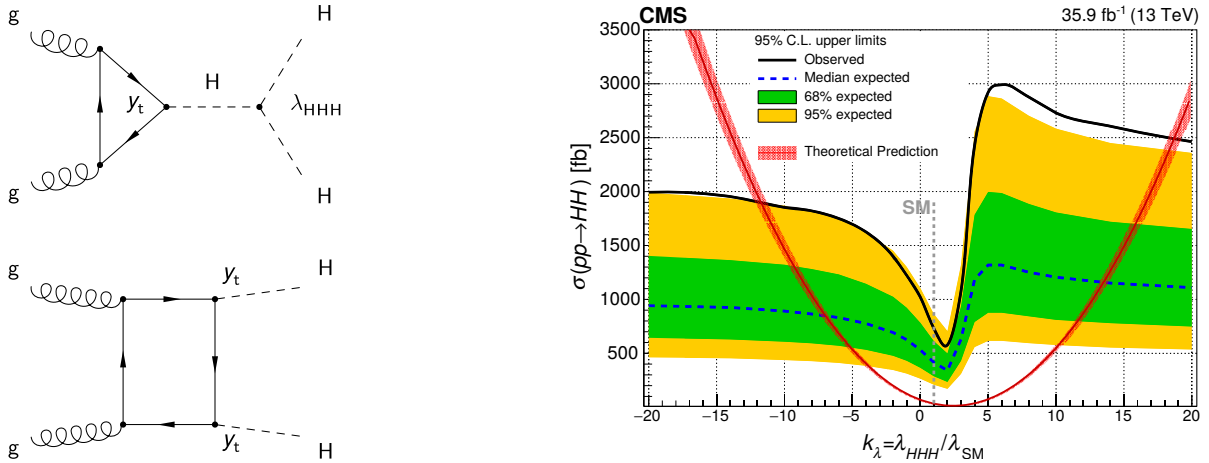


Figure 6: Signal (top left) and main background (bottom left) diagrams for di-Higgs production together with limits in terms of $k_\lambda = \lambda_{HHH} / \lambda_{SM}$ (right) [20]

Dark Matter, e.g. from gravitational lensing or rotational curves of galaxies.

Various theories beyond the SM (BSM) are proposed and out of these, many feature an extended Higgs sector. By introducing a second doublet to the Higgs theory, five physical Higgs bosons arise. Out of these, one would be the 125 GeV boson (h), another (H) would also be neutral and CP-even but heavier. Furthermore, there would be a CP-odd, neutral boson (A) with a similar or the same mass as the heavy CP-even one as well as two charged Higgs bosons (H^\pm). If another singlet is added to the theory, also light Higgs bosons ($a_{1,2}$) are present as well as a second CP-even state close to 125 GeV ($h_{1,2}$).

4.1 Heavy Neutral Higgs Bosons

Searches for the H and A bosons can be conducted by looking for various final states, e.g. $\tau^+\tau^-$ [21] or $b\bar{b}$ [22]. Here, the focus will be on the $b\bar{b}$ final state, while the H/A boson is produced in association with one or two additional b quarks. This specific process is strongly enhanced in some models like the general Two-Higgs-Doublet Model (2HDM [23]) type II and flipped, where the coupling of neutral Higgs bosons to down-type quarks is enhanced by $\tan^2 \beta$. Here, $\tan \beta$ is the ratio of the vacuum expectation values of the two Higgs doublets. Because of this enhancement, the branching fraction for a decay into a pair of b quarks is expected to be particularly large. Another important parameter for this kind of search, $\cos(\beta - \alpha)$, is based on the angle α which affects the mixing between the CP-even states H and h . Note that the minimal supersymmetric extension of the Standard Model, MSSM, is very similar to 2HDM type II.

Depending on the precise process, there are one or two spectator b quarks in the associated production. Together with the two decay products from the H/A boson, there are at least three b jets in the final state. Due to the low selection efficiency of b jets in

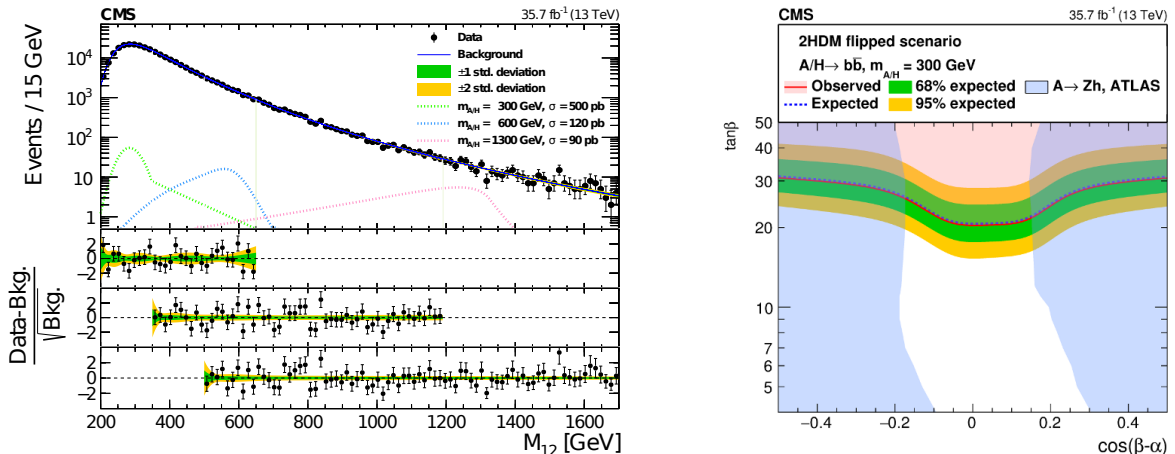


Figure 7: Fit of the m_{12} distribution in three subranges, obtained from a control region and applied to the signal region (left), and model dependent limits in the $\tan\beta$ vs. $\cos(\beta - \alpha)$ plane (right) [22]

case of good light jet rejection, this leads to low overall signal efficiencies. Furthermore, the QCD multijet background is large. In order to obtain a precise parametrization of the background, a control region (CR) is used in which the b tag requirement on the third leading jet in p_T is reversed, i.e. this jet is explicitly required not to be b tagged. By dividing the mass range into three smaller subranges, the fit quality is improved significantly. As shown in Figure 7 (left), this parametrization also fits the signal region very well over a huge mass range reaching from 200 up to 1700 GeV.

After extracting model independent limits, also interpretations in terms of specific models are done. One of these is shown in Figure 7 (right) in the $\tan\beta - \cos(\beta - \alpha)$ plane. As can be seen there, this particular study is uniquely sensitive around the so-called alignment limit $\cos(\beta - \alpha) = 0$, where h would be completely SM-like. By combining various searches and interpretations, increasing areas of the parameter space can be excluded.

4.2 Charged Higgs Bosons

There are various decay modes that can be used to search for charged Higgs bosons. How a H^\pm boson decays is also impacted significantly by its mass. While a light H^\pm would rather decay into $\tau^\pm\nu_\tau$, a heavy H^\pm is more likely to yield a $t\bar{b}$ final state. In this context, light and heavy refer to masses smaller or lighter than $m_t - m_b$. There is also an intermediate region around the top-quark mass. For the special case of 2HDM type II, the decay into $\tau^\pm\nu_\tau$ is still important at large $\tan\beta$, even in the high-mass region. Although also the production is affected by the assumed particle mass, it is generally associated with t and b quarks.

Limits over a large range of masses can be calculated by fitting the main observable,

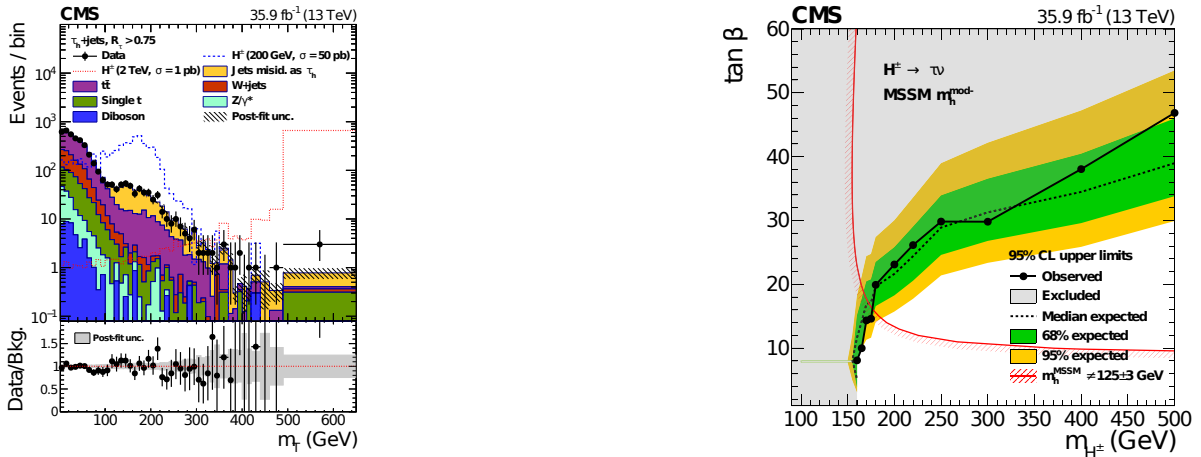


Figure 8: m_T distribution with measurement and expected backgrounds in one signal region (left) as well as model dependent limits in terms of candidate mass and $\tan \beta$ (right) [24]

m_T , in all 36 signal regions. m_T is the transverse mass for which one distribution is shown in Figure 8 (left). There, the dashed lines indicate simulated signals at certain masses of H^\pm . In the same figure (right), a limit interpretation in terms of a specific MSSM model is shown. It is based on model independent limits similar to the aforementioned search for heavy neutral Higgs bosons. The region indicated by the red line is excluded in this model since it would require $m_h \neq 125$ GeV. Thus, H^\pm boson masses up to around 170 GeV can actually be excluded in this model.

4.3 Light Higgs Bosons

The search presented here [25] is based on a general 2HDM + Singlet type II model [26]. There, the dominant decay modes of light Higgs bosons (a) vary depending on their mass. For masses below 4 GeV, the decay into a pair of muons dominates, while from 4 to 10 GeV, mainly tau leptons are produced. In the region of 10 to 63 GeV, the dominant decay is into a pair of b quarks. Since it is assumed that the 125 GeV h boson can decay into a pair of bosons, their mass is restricted to be below around 63 GeV. The search presented here [25] is focused on the lower side of the spectrum, thus targeting events with four muons in the final state.

To define the signal region, it is demanded that the two di-muon candidate masses are close to each other. The effect of that requirement can be seen in Figure 9 (left), indicated by the dashed cone. Events passing the kinematic requirements for the signal but lying outside this cone are shown as white circles while those inside the cone are marked as yellow triangles. In the end, nine events remain in that signal region, being in good agreement with the SM prediction of 8 ± 2 . This is based on the main backgrounds J/Ψ , bb and electroweak production of four muons, all of which can be precisely estimated.

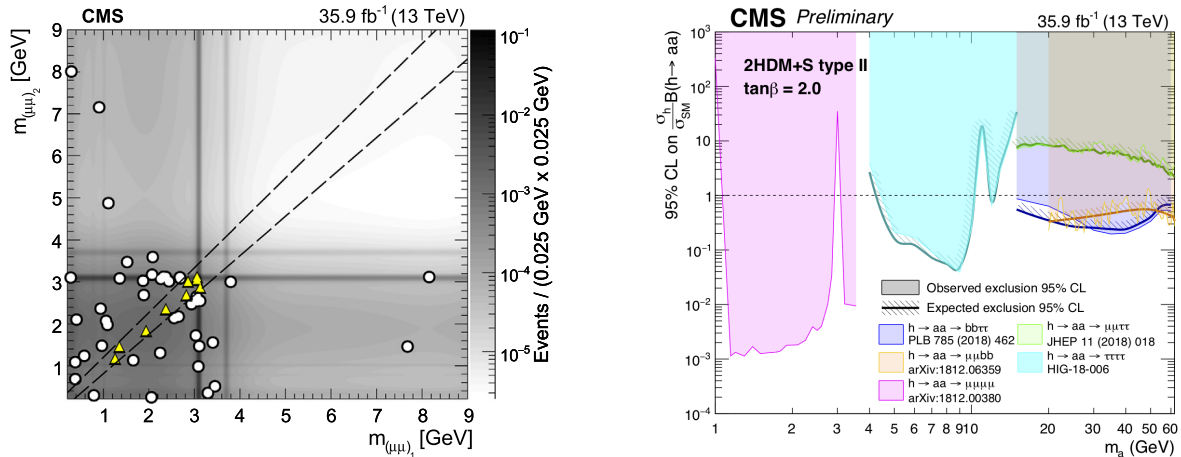


Figure 9: Events in signal and control regions dependent on the two candidate masses (left) and limits over a large mass range (right) [25]

By combining this search with those focusing on other final states of di- a production, limits over a wide range of masses can be calculated as shown in Figure 9 (right). These limits reach from masses as low as 1 GeV up to the mentioned kinematic border of 63 GeV.

5 Conclusions and Outlook

For most SM processes, significant improvements could be made by adding 13 TeV data to existing measurements. While the full RunII dataset is already included in some studies, this inclusion is still ongoing for others. So far, all measurements are in good agreement with the SM predictions. Nevertheless, some rare processes are still searched for, e.g. the decay of a Higgs boson into a pair of charm quarks or muons and the Higgs self-coupling. Also, searches for new physics in the Higgs sector are ongoing, looking for charged, light or heavy Higgs bosons.

With the ongoing work and plans, it is intended to increase the LHC center-of-mass energy to 14 TeV and, later, to install the high-luminosity LHC. It is expected to collect data corresponding to an integrated luminosity of up to $3/\text{ab}$, compared to ca. $150/\text{fb}$ collected until now. With this data, the uncertainties of many searches will decrease and more processes will be in reach for new studies. For example, the search for $H \rightarrow c\bar{c}$ is assumed to profit from significantly decreased uncertainties and for the Higgs boson self-coupling, a sensitivity of around 2.6σ is expected. Projections for the signal strength uncertainties as well as the Higgs boson self-coupling coupling modifier are shown in Figure 10.

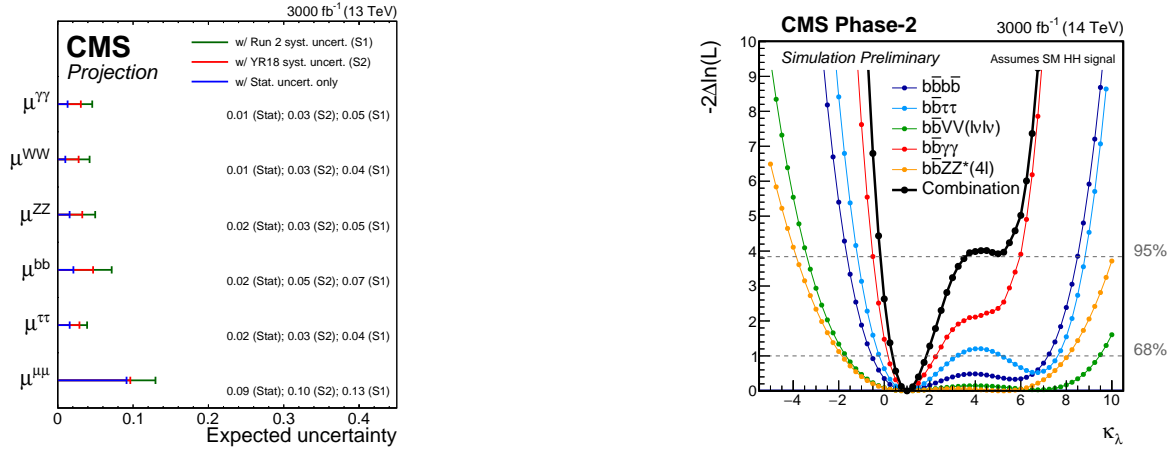


Figure 10: Signal strength uncertainties Higgs boson decays into different bosons and fermions as predicted for the complete HL-LHC dataset (left, [27]) as well as prediction for the Higgs boson self-coupling coupling modifier (right, [28])

References

- [1] F. Englert and R. Brout. Broken Symmetry and the Mass of Gauge Vector Mesons. *Phys. Rev. Lett.*, 13:321, 1964. [,157(1964)].
- [2] P. Higgs. Broken Symmetries and the Masses of Gauge Bosons. *Phys. Rev. Lett.*, 13:508, 1964. [,160(1964)].
- [3] CMS Collaboration. Observation of a new boson at a mass of 125 GeV with the CMS experiment at the LHC. *Physics Letters B*, 716(1):30, 2012.
- [4] CMS Collaboration. Observation of a new boson with mass near 125 GeV in pp collisions at $\sqrt{s} = 7$ and 8 TeV. *Journal of High Energy Physics*, 2013(6):81, Jun 2013.
- [5] ATLAS Collaboration. Observation of a new particle in the search for the Standard Model Higgs boson with the ATLAS detector at the LHC. *Physics Letters B*, 716(1):1 – 29, 2012.
- [6] O. Brüning et al. *LHC Design Report*. CERN Yellow Reports: Monographs. CERN, Geneva, 2004.
- [7] ATLAS Collaboration. The ATLAS Experiment at the CERN Large Hadron Collider. *JINST* 3, S08003 (2008).
- [8] CMS Collaboration. The CMS experiment at the CERN LHC. *JINST* 3, S08004 (2008).
- [9] CMS Collaboration. Observation of $t\bar{t}H$ Production. *Phys. Rev. Lett.*, 120:231801, Jun 2018.
- [10] ATLAS Collaboration. Observation of Higgs boson production in association with a top quark pair at the LHC with the ATLAS detector. *Phys. Lett.*, B784:173, 2018.
- [11] CMS Collaboration. Observation of Higgs Boson Decay to Bottom Quarks. *Phys. Rev. Lett.*, 121:121801, Sep 2018.

- [12] ATLAS Collaboration. Observation of $H \rightarrow b\bar{b}$ decays and VH production with the ATLAS detector. *Phys. Lett.*, B786:59, 2018.
- [13] CMS Collaboration. Public CMS Luminosity Information. <https://twiki.cern.ch/twiki/bin/view/CMSPublic/LumiPublicResults>. Status: November 14, 2019.
- [14] L. Rossi et al. *High-Luminosity Large Hadron Collider (HL-LHC): Technical Design Report V. 0.1*. CERN Yellow Reports: Monographs. CERN, Geneva, 2017.
- [15] J. Caron. CERN Aerial view. AC Collection. Legacy of AC. Pictures from 1992 to 2002, Jun 1986.
- [16] D. Barney. CMS Detector Slice. CMS Collection, Jan 2016.
- [17] CMS Collaboration. A measurement of the Higgs boson mass in the diphoton decay channel. Technical Report CMS-PAS-HIG-19-004, CERN, Geneva, 2019. <https://cds.cern.ch/record/2691211>.
- [18] CMS Collaboration. Measurements of properties of the Higgs boson in the four-lepton final state in proton-proton collisions at $\sqrt{s} = 13$ TeV. Technical Report CMS-PAS-HIG-19-001, CERN, Geneva, 2019. <https://cds.cern.ch/record/2668684>.
- [19] CMS Collaboration. Search for the standard model Higgs boson decaying to charm quarks. Technical Report CMS-PAS-HIG-18-031, CERN, Geneva, 2019. <https://cds.cern.ch/record/2682638>.
- [20] CMS Collaboration. Combination of Searches for Higgs Boson Pair Production in Proton-Proton Collisions at $\sqrt{s} = 13$ TeV. *Phys. Rev. Lett.*, 122:121803, Mar 2019.
- [21] CMS Collaboration. Search for a heavy pseudoscalar Higgs boson decaying into a 125 GeV Higgs boson and a Z boson in final states with two tau and two light leptons at $\sqrt{s} = 13$ TeV. Technical Report CMS-HIG-18-023-003, CERN, Geneva, 2019. <https://cds.cern.ch/record/2696366>.
- [22] CMS Collaboration. Search for beyond the standard model Higgs bosons decaying into a $b\bar{b}$ pair in pp collisions at $\sqrt{s} = 13$ TeV. *Journal of High Energy Physics*, 2018(8):113, Aug 2018.
- [23] G. Branco et al. Theory and phenomenology of two-Higgs-doublet models. *Phys. Rept.*, 516:1, 2012.
- [24] CMS Collaboration. Search for charged Higgs bosons in the $H^\pm \rightarrow \tau^\pm \nu \tau$ decay channel in proton-proton collisions at $\sqrt{s} = 13$ TeV. *Journal of High Energy Physics*, 2019(7):142, Jul 2019.
- [25] CMS Collaboration. A search for pair production of new light bosons decaying into muons in proton-proton collisions at 13 TeV. *Physics Letters B*, 796:131, 2019.
- [26] A. Teixeira U. Ellwanger, C. Hugonie. The Next-to-Minimal Supersymmetric Standard Model. *Physics Reports*, 496(1):1, 2010.
- [27] CMS Collaboration. Sensitivity projections for Higgs boson properties measurements at the HL-LHC. Technical Report CMS-PAS-FTR-18-011, CERN, Geneva, 2018. <https://cds.cern.ch/record/2647699>.
- [28] CMS Collaboration. Prospects for HH measurements at the HL-LHC. Technical Report CMS-PAS-FTR-18-019, CERN, Geneva, 2018. <https://cds.cern.ch/record/2652549>.

List of Figures

2.1.	Main Higgs boson production processes at the LHC	17
2.2.	Production cross-sections and branching ratios for the Higgs boson	18
2.3.	Known Standard Model particle content	19
2.4.	Tree-level masses of the Higgs bosons in the MSSM	25
2.5.	Typical Feynman diagram of a neutral Higgs boson produced in the $b\bar{b}\phi$ channel and decaying into a $b\bar{b}$ pair	27
2.6.	Impact of μ on excluded areas of phase space in m_h^{125} scenarios	32
2.7.	Branching ratios of the A boson vs. $\cos(\beta - \alpha)$ in 2HDM type II and flipped scenarios for different masses at $\tan\beta = 30$	36
2.8.	Branching ratios of the H boson vs. $\cos(\beta - \alpha)$ in 2HDM type II and flipped scenarios for different masses at $\tan\beta = 30$	37
2.9.	Cross-section times branching ratio for the full process $\sigma(b\bar{b}A/H)\mathcal{B}(A/H \rightarrow$ $b\bar{b})$ for all four 2HDM scenarios	38
3.1.	CERN accelerator complex	40
3.2.	Integrated luminosity as recorded by CMS and delivered by the LHC	42
3.3.	Slice through the CMS detector	43
3.4.	Comparison of the pixel phase-1 and phase-0 designs	46
3.5.	Calorimeter E_T resolution as a function of E_T	49
3.6.	Schematic setup of sub-detectors in CMS	51
4.1.	Primary vertex resolution for 2016 and 2017 tracker geometry	57
4.2.	Distribution of mean number of proton-proton interactions per bunch crossing for the 2017 data-taking period	57
4.3.	Shape of jets based on various reconstruction algorithms	59
4.5.	Production of jets originating from a primary vertex and a heavy-flavor jet as well as a charged lepton linked to a secondary vertex	63

LIST OF FIGURES

4.6.	Residuals on the position of primary vertices using either information from the pixel detector alone or the full tracking system and performance of the CSVv2 algorithm in the slimmed online version and the complete offline version	65
4.7.	Comparison of CSVv2 and DeepCSV b tagging algorithms	66
4.8.	Comparison of misidentification rates of the DeepCSV and DeepJet algorithms	67
5.1.	Main BSM Higgs boson production modes at LEP: Higgsstrahlung and pair production	70
5.2.	Production processes for a heavy, neutral Higgs boson in association with b quarks at TeVatron and LHC	70
5.3.	Limits on cross-section times branching ratio of the BSM Higgs boson search in the $b\bar{b}$ decay channel at TeVatron as well as interpretation in terms of the m_h^{max} scenario	71
5.4.	Model independent limits of the LHC Run 1 analyses together with model interpretations in the m_h^{max} and m_h^{mod+} scenarios	73
5.5.	Limits on the production cross-section times branching fraction and interpretations in terms of specific benchmark scenarios for LHC Run 2 searches	75
5.6.	Feynman diagrams of main background processes: SM production of four b jets, QCD multi-jet events, and $t\bar{t}$	77
5.7.	Kinematic trigger efficiency for 2017 data and MC	87
5.8.	Comparison of fit results for kinematic trigger efficiency in data and MC as well as resulting scale factor	88
5.9.	Offline b-tag scale factor for the DeepJet b-tagging algorithm	90
5.10.	Online b-tag efficiency for data and Monte Carlo as well as resulting scale factor	91
5.11.	Comparison of $\Delta\eta_{12}$ distributions in QCD MC and the 300 GeV signal sample .	93
5.12.	Data vs. MC in the bbnb control region with and without MC scale factors	97
5.13.	Invariant mass spectrum of three representative signal mass points	100
5.14.	Invariant-mass distributions of representative signal mass points with and without including FSR recovery, JER correction, b-jet energy regressen and all three combined	102
5.15.	Effect of systematic uncertainties on the signal template of the 350 GeV mass point	103
5.16.	Effect of systematic uncertainties on the signal template of the 600 GeV mass point	104

5.17. Effect of systematic uncertainties on the signal template of the 1200 GeV mass point	105
5.18. Signal selection efficiency in the CR, VR, and SR depending on the analyzed signal sample	108
5.19. Background parametrization in CR and SR for the 2016 inclusive analysis . . .	109
5.20. Overview of mass shapes from signal samples in each fit range	111
5.21. Background parametrization results of CR fit ranges	113
5.22. First attempt of determining a TF shape for the full mass spectrum, based on b-enhanced QCD MC samples and a fit with a Gaussian error function multiplied by a linear term	115
5.23. B-tagging efficiencies for the medium working point of the DeepJet algorithm .	116
5.24. Selected closure tests for the b-tag weighting method	117
5.25. B-tag-cut- and b-tag-weight-based ratios of m_{12} in SR and CR	118
5.26. Ratios of m_{12} in SR and CR with fit results, evaluated in the same fit ranges as the CR	119
5.27. Distribution of individual bias values of about 5000 Asimov data sets for the 400 GeV mass point in FR 1 with a Gaussian fit	123
5.28. Bias results in percent for the four fit ranges	124
5.29. Combined fit of Asimov data sets for the CR and SR for the 400 GeV mass point in FR 1	125
5.30. Pulls and impacts for the 400, 600, 900, and 1200 GeV mass points, based on Asimov data sets	126
5.31. Combined fit result of CR and VR for the 400 and 600 GeV mass points	128
5.32. Combined fit result of CR and VR for the 900 and 1200 GeV mass points . . .	129
5.33. Pulls and impacts for the 400, 600, 900, and 1200 GeV mass points in the simultaneous fit of CR and VR	130
5.34. short text	131
6.1. Expected limits on cross-section times branching ratio with and without fit-range borders	138
6.2. Combined fit of CR and SR for FR 1 and 2	140
6.3. Combined fit of CR and SR for FR 3 and 4	141
6.4. Combined fit of CR and SR for FR 4 (1600 GeV)	142

LIST OF FIGURES

6.5. Comparison of the ratio of m_{12} distributions in SR and CR for all four fit ranges and the fit results obtained based on the signal-plus-background fit for each mass point	143
6.6. Goodness-of-fit results for the 400, 600, 900, 1200, and 1600 GeV mass points using unblinded SR data	144
6.7. Pulls and impacts for the 400, 600, 900, and 1200 GeV mass points, based on unblinded SR data	145
6.8. Background-only fit results from the combined fit of CR and SR, showing the agreement of the fit with the SR data	147
6.9. Expected and observed limits on cross-section times branching ratio	148
6.10. Expected and observed limits of the parameter $\tan \beta$ vs. m_A in the context of the hMSSM and m_h^{mod+} scenarios	150
6.11. Expected and observed limits of the parameter $\tan \beta$ vs. m_A in the context of the m_h^{125} scenarios	152
6.12. Direct comparison of expected and observed limits of the parameter $\tan \beta$ vs. m_A in the context of the m_h^{125} scenarios	153
6.13. Expected and observed limits of the parameter $\tan \beta$ vs. $\cos(\beta - \alpha)$ in the 2HDM type-II scenario for the 300, 600, 900, and 1200 GeV mass points . . .	155
6.14. Expected and observed limits of the parameter $\tan \beta$ vs. $\cos(\beta - \alpha)$ in the 2HDM flipped scenario for the 300, 600, 900, and 1200 GeV mass points . . .	156
6.15. Expected and observed limits of the parameter $\tan \beta$ vs. $m_{A/H}$ in the 2HDM type-II and flipped scenarios	157
A.1. Hierarchical structure of the strip and pixel tracking detectors	166
A.2. Correction of reconstructed hits based on alignment	167
A.3. Distance of median residuals (DMR) for the six sub-detectors of the CMS tracking system	170
A.4. Distance of closest approach of a track to the unbiased vertex	171
A.5. Comparison of the detector geometry used during the data-taking period of 2016 and the result of the alignment at the end of that year	172
A.6. Reconstructed mass of the Z boson from two muons	173
A.7. short text	174
B.1. Branching ratios of the CP-odd A boson (300 and 600 GeV) for $\tan \beta$ values of 10, 30, and 60, vs. $\cos(\beta - \alpha)$ in the 2HDM type II scenario	178

B.2. Branching ratios of the CP-odd A boson (900 and 1200 GeV) for $\tan\beta$ values of 10, 30, and 60, vs. $\cos(\beta - \alpha)$ in the 2HDM type II scenario	179
B.3. Branching ratios of the CP-odd A boson (300 and 600 GeV) for $\tan\beta$ values of 10, 30, and 60, vs. $\cos(\beta - \alpha)$ in the 2HDM flipped scenario	180
B.4. Branching ratios of the CP-odd A boson (900 and 1200 GeV) for $\tan\beta$ values of 10, 30, and 60, vs. $\cos(\beta - \alpha)$ in the 2HDM flipped scenario	181
B.5. Branching ratio of the CP-even H boson (300 and 600 GeV) for $\tan\beta$ values of 10, 30, and 60, vs. $\cos(\beta - \alpha)$ in the 2HDM type II scenario	182
B.6. Branching ratio of the CP-even H boson (900 and 1200 GeV) for $\tan\beta$ values of 10, 30, and 60, vs. $\cos(\beta - \alpha)$ in the 2HDM type II scenario	183
B.7. Branching ratio of the CP-even H boson (300 and 600 GeV) for $\tan\beta$ values of 10, 30, and 60, vs. $\cos(\beta - \alpha)$ in the 2HDM flipped scenario	184
B.8. Branching ratios of the CP-even H boson (900 and 1200 GeV) for $\tan\beta$ values of 10, 30, and 60, vs. $\cos(\beta - \alpha)$ in the 2HDM flipped scenario	185
B.9. Cross-section times branching ratio for a b-associated production and subsequent decay into a pair of b quarks for the A and H boson in the 2HDM type I scenario vs. the Higgs-boson mass $m_{A/H}$ for $\cos(\beta - \alpha) = 0$, $\cos(\beta - \alpha) = \pm 0.1$, and $\cos(\beta - \alpha) = \pm 0.3$	186
B.10. Cross-section times branching ratio for a b-associated production and subsequent decay into a pair of b quarks for the A and H boson in the 2HDM type II scenario vs. the Higgs-boson mass $m_{A/H}$ for $\cos(\beta - \alpha) = 0$, $\cos(\beta - \alpha) = \pm 0.1$, and $\cos(\beta - \alpha) = \pm 0.3$	187
B.11. Cross-section times branching ratio for a b-associated production and subsequent decay into a pair of b quarks for the A and H boson in the 2HDM lepton specific scenario vs. the Higgs-boson mass $m_{A/H}$ for $\cos(\beta - \alpha) = 0$, $\cos(\beta - \alpha) = \pm 0.1$, and $\cos(\beta - \alpha) = \pm 0.3$	188
B.12. Cross-section times branching ratio for a b-associated production and subsequent decay into a pair of b quarks for the A and H boson in the 2HDM flipped scenario vs. the Higgs-boson mass $m_{A/H}$ for $\cos(\beta - \alpha) = 0$, $\cos(\beta - \alpha) = \pm 0.1$, and $\cos(\beta - \alpha) = \pm 0.3$	189

List of Tables

2.1.	Fermion content of the Standard Model	6
2.2.	Forces and mediators in the Standard Model	12
2.3.	Particle content of the MSSM	23
2.4.	Coupling modifiers of neutral Higgs bosons in the MSSM	26
2.5.	Coupling of right-handed fermions to Higgs doublets in the four 2HDM types	33
2.6.	Yukawa coupling modifiers in the four types of 2HDMs	34
4.1.	Efficiencies of the CSVv2, DeepCSV, and DeepJet algorithms for b, c, and light jets	68
5.1.	Recorded integrated luminosity for the analysis main and control triggers in the 2017 data-taking period	79
5.2.	Signal samples and event content	80
5.3.	Background samples: general QCD as well as b-enhanced data sets	81
5.4.	Triggers used in the analysis. Based on the main trigger, events are selected for the search for a BSM Higgs boson. The control triggers are used to assess efficiencies of the main trigger.	82
5.5.	Fit results of the jet kinematic trigger efficiency for data and MC	86
5.6.	Cutflow in data for CR, VR, and SR	95
5.7.	Cutflow for MC signal samples depending on the generated Higgs boson mass	98
5.8.	Effect in percent on the normalization of the signal template due to systematic uncertainties	106
5.9.	Fit ranges with parametrization function, mass range and assigned mass points	114
5.10.	TF fit results in the four fit ranges, together with the number of free shape parameters as well as the resulting χ^2/ndf and probability values	120
5.11.	Nominal and alternative TF descriptions in each fit range	121
6.1.	Observed and expected upper limits at 95 % C.L. and $\pm 1\sigma$ and $\pm 2\sigma$ uncertainties depending on the Higgs boson mass	149

LIST OF TABLES

C.1.	Upper limits at 95 % C. L. for the MSSM parameters $\tan \beta$ and m_A in terms of the hMSSM benchmark scenario.	192
C.2.	Upper limits at 95 % C. L. for the MSSM parameters $\tan \beta$ and m_A in terms of the m_h^{mod+} benchmark scenario.	192
C.3.	Upper limits at 95 % C. L. for the MSSM parameters $\tan \beta$ and m_A in terms of the $m_h^{125}(\mu = 1 \text{ TeV})$ benchmark scenario.	193
C.4.	Upper limits at 95 % C. L. for the MSSM parameters $\tan \beta$ and m_A in terms of the $m_h^{125}(\mu = -1 \text{ TeV})$ benchmark scenario.	193
C.5.	Upper limits at 95 % C. L. for the MSSM parameters $\tan \beta$ and m_A in terms of the $m_h^{125}(\mu = -2 \text{ TeV})$ benchmark scenario.	194
C.6.	Upper limits at 95 % C. L. for the MSSM parameters $\tan \beta$ and m_A in terms of the $m_h^{125}(\mu = -3 \text{ TeV})$ benchmark scenario.	194
C.7.	Upper limits at 95 % C. L. for the parameter $\tan \beta$ in terms of $m_{A/H}$ for the 2HDM type II scenario.	195
C.8.	Upper limits at 95 % C. L. for the parameter $\tan \beta$ in terms of $m_{A/H}$ for the 2HDM flipped scenario.	195

Bibliography

- [1] H. Thurston, *Early Astronomy*. Springer-Verlag New York, 1994.
- [2] S. M. Nikolaou, *Die Atomlehre Demokrits und Platons Timaios*. De Gruyter, 1998.
- [3] J. J. Thomson, “Cathode Rays,” *The London, Edinburgh, and Dublin Philosophical Magazine and Journal of Science*, vol. 44, no. 269, pp. 293–316, 1897.
- [4] CMS Collaboration, “Measurement and QCD analysis of double-differential inclusive jet cross sections in pp collisions at $\sqrt{s} = 8$ TeV and cross sections ratios to 2.76 and 7 TeV,” *JHEP*, vol. 156 (2017), 2017.
- [5] G. Arnison et al., “Experimental observation of isolated large transverse energy electrons with associated missing energy at $s=540$ GeV,” *Physics Letters B*, vol. 122, no. 1, pp. 103–116, 1983.
- [6] G. Arnison et al., “Experimental observation of lepton pairs of invariant mass around 95 GeV/c² at the CERN SPS collider,” *Physics Letters B*, vol. 126, no. 5, pp. 398–410, 1983.
- [7] CDF Collaboration, “Observation of top quark production in $p\bar{p}$ collisions with the collider detector at fermilab,” *Physical Review Letters*, vol. 74, no. 14, p. 2626–2631, 1995.
- [8] D0 Collaboration, “Observation of the top quark,” *Il Nuovo Cimento A Series 11*, vol. 109, pp. 755–769, 1996.
- [9] CMS Collaboration, “Observation of a new boson with mass near 125 GeV in pp collisions at $\sqrt{s} = 7$ and 8 TeV,” *Journal of High Energy Physics*, vol. 2013, p. 81, Jun 2013.
- [10] CMS Collaboration, “Observation of a new boson at a mass of 125 GeV with the CMS experiment at the LHC,” *Physics Letters B*, vol. 716, no. 1, p. 30, 2012.

BIBLIOGRAPHY

- [11] ATLAS Collaboration, “Observation of a new particle in the search for the Standard Model Higgs boson with the ATLAS detector at the LHC,” *Physics Letters B*, vol. 716, no. 1, pp. 1 – 29, 2012.
- [12] ATLAS Collaboration, “Evidence for the spin-0 nature of the Higgs boson using ATLAS data,” *Physics Letters B*, vol. 726, no. 1-3, p. 120–144, 2013.
- [13] CMS Collaboration, “Constraints on the spin-parity and anomalous HVV couplings of the Higgs boson in proton collisions at 7 and 8 TeV,” *Physical Review D*, vol. 92, no. 1, 2015.
- [14] ATLAS Collaboration, “Measurements of the Higgs boson production and decay rates and coupling strengths using pp collision data at $\sqrt{s} = 7$ and 8 TeV in the ATLAS experiment,” *The European Physical Journal C*, vol. 76, no. 1.
- [15] D. de Florian, C. Grojean et al., *Handbook of LHC Higgs Cross Sections: 4. Deciphering the Nature of the Higgs Sector*. CERN Yellow Reports: Monographs, Oct 2016. 869 pages, 295 figures, 248 tables and 1645 citations. Working Group web page: <https://twiki.cern.ch/twiki/bin/view/LHCPhysics/LHCHXSWG>.
- [16] B. T. Cleveland et al., “Measurement of the Solar Electron Neutrino Flux with the Homestake Chlorine Detector,” *The Astrophysical Journal*, vol. 496, no. 1, pp. 505–526, 1998.
- [17] Y. F. et al., “Evidence for Oscillation of Atmospheric Neutrinos,” *Physical Review Letters*, vol. 81, no. 8, p. 1562–1567, 1998.
- [18] F. P. A. et al., “Observation of electron-antineutrino disappearance at daya bay,” *Phys. Rev. Lett.*, vol. 108, p. 171803, Apr 2012.
- [19] Planck Collaboration, “Planck2015 results,” *Astronomy & Astrophysics*, vol. 594, p. A13, 2016.
- [20] E. Corbelli, P. Salucci, “The extended rotation curve and the dark matter halo of M33,” *Monthly Notices of the Royal Astronomical Society*, vol. 311, pp. 441–447, 2000.
- [21] S. W. Allen, A. E. Evrard, A. B. Mantz, “Cosmological Parameters from Observations of Galaxy Clusters,” *Annual Review of Astronomy and Astrophysics*, vol. 49, no. 1, p. 409–470, 2011.
- [22]

- [23] G. Bertone, D. Merritt, “Dark Matter Dynamics And Indirect Detection,” *Modern Physics Letters A*, vol. 20, no. 14, p. 1021–1036, 2005.
- [24] G. ’t Hooft, “Naturalness, chiral symmetry, and spontaneous chiral symmetry breaking,” *NATO Sci. Ser. B*, vol. 59, pp. 135–157, 1980.
- [25] G. C. Branco et al., “Theory and phenomenology of two-Higgs-doublet models,” *Physics Reports*, vol. 516, no. 1-2, p. 1–102, 2012.
- [26] L. Honorez, E. Nezri, J. Oliver, M. Tytgat, “The inert doublet model: an archetype for dark matter,” *Journal of Cosmology and Astroparticle Physics*, vol. 2007, no. 02, p. 028–028, 2007.
- [27] H. Nilles, “Supersymmetry, supergravity and particle physics,” *Physics Reports*, vol. 110, no. 1, pp. 1–162, 1984.
- [28] S. L. G. H. Georgi, “Unity of All Elementary-Particle Forces,” *Phys. Rev. Lett.*, vol. 32, pp. 438–441, 1974.
- [29] CERN, “LHC Design Report,” *CERN Yellow Reports: Monographs*, vol. 1: the LHC Main Ring, 2004.
- [30] CERN, “LHC Machine,” *Jinst*, vol. 3, no. 08, p. S08001, 2008.
- [31] ATLAS Collaboration, “The ATLAS experiment at the CERN large hadron collider,” *Journal of Instrumentation*, vol. 3, no. 08, p. S08003, 2008.
- [32] CMS Collaboration, “The CMS experiment at the CERN LHC,” *Journal of Instrumentation*, vol. 3, no. 08, p. S08004, 2008.
- [33] LHC Higgs Cross Section Working Group, *Handbook of LHC Higgs Cross Sections: 1. Inclusive Observables*. CERN Yellow Reports: Monographs, Geneva: CERN, 2011.
- [34] A. Vagnerini, *Search for Higgs bosons in the final state with b -quarks in the semi-leptonic channel with the CMS 2017 data*. Dissertation, Universität Hamburg, Hamburg, 2020. Dissertation, Universität Hamburg, 2020.
- [35] D. Griffiths, *Introduction to Elementary Particles*. WILEY-VCH, Second, Revised Edition ed., 2014.

BIBLIOGRAPHY

- [36] A. Zannoni, “On the Quantization of the Monoatomic Ideal Gas,” 1999. Translation of Enrico Fermi’s original work, arXiv: cond-mat/9912229.
- [37] P. Dirac, “On the theory of quantum mechanics,” *Proc. R. Soc. Lond. A*, vol. 112, pp. 661–677, 1926.
- [38] S. Bose, “Planck’s Law and Light Quantum Hypothesis,” *Zeits. Physik*, vol. 26, p. 178, 1924.
- [39] R. Bhalerao, “Relativistic Heavy-Ion Collisions,” in *1st Asia-Europe-Pacific School of High-Energy Physics* (M. Mulders, K. Kawagoe, ed.), pp. 219 – 239, 2012. arXiv:1407.1694 .
- [40] P. Zyla *et al.*, “Review of Particle Physics,” *PTEP*, vol. 2020, no. 8, p. 083C01, 2020.
- [41] P. Söding, “On the discovery of the gluon,” *The European Physical Journal H*, vol. 35, pp. 3 – 28, 2010.
- [42] M. Thomson, *Modern Particle Physics*. Cambridge University Press, 2013.
- [43] E. Noether, “Invariante Variationsprobleme,” *Nachrichten von der Gesellschaft der Wissenschaften zu Göttingen, Mathematisch-Physikalische Klasse*, vol. 1918, pp. 235–257, 1918.
- [44] A. Einstein, *Relativity: The Special and the General Theory (Popular Exposition)*. Methuen & Co. Ltd. London, third edition ed., 1920. Original German version from 1917, authorized translation by R. Lawson.
- [45] L3 Collaboration, “Measurement of the running of the electromagnetic coupling at large momentum-transfer at LEP,” *Physics Letters B*, vol. 623, no. 1-2, p. 26–36, 2005.
- [46] OPAL Collaboration, “Measurement of the running of the QED coupling in small-angle Bhabha scattering at LEP,” *The European Physical Journal C*, vol. 45, no. 1, p. 1–21, 2006.
- [47] M. Gell-Mann, Y. Ne’eman, *The Eightfold Way*. Benjamin, New York, 1964.
- [48] O. W. Greenberg, “Resource Letter Q1: Quarks,” *American Journal of Physics*, vol. 50, no. 12, pp. 1074–1089, 1982.

-
- [49] M. L. Perl et al., “Evidence for Anomalous Lepton Production in $e^+ - e^-$ Annihilation,” *Phys. Rev. Lett.*, vol. 35, pp. 1489–1492, 1975.
- [50] E. Fermi, “An attempt of a theory of beta radiation,” *Z. Phys.*, vol. 88, pp. 161–177, 1934.
- [51] C. S. W. et al., “Experimental Test of Parity Conservation in Beta Decay,” *Phys. Rev.*, vol. 105, pp. 1413–1415, 1957.
- [52] N. Cabibbo, “Unitary Symmetry and Leptonic Decays,” *Phys. Rev. Lett.*, vol. 10, pp. 531–533, 1963.
- [53] S. L. Glashow, J. Iliopoulos, L. Maiani, “Weak Interactions with Lepton-Hadron Symmetry,” *Phys. Rev. D*, vol. 2, pp. 1285–1292, 1970.
- [54] M. Kobayashi, T. Maskawa, “CP-Violation in the Renormalizable Theory of Weak Interaction,” *Progress of Theoretical Physics*, vol. 49, no. 2, pp. 652–657, 1973.
- [55] S. Bludman, “On the universal fermi interaction,” *Nuovo Cim*, vol. 9, pp. 433–445, 1958.
- [56] S. L. Glashow, “Partial-symmetries of weak interactions,” *Nuclear Physics*, vol. 22, no. 4, pp. 579–588, 1961.
- [57] S. Weinberg, “A Model of Leptons,” *Phys. Rev. Lett.*, vol. 19, pp. 1264–1266, 1967.
- [58] A. Salam and J. C. Ward, “Electromagnetic and weak interactions,” *Physics Letters*, vol. 13, no. 2, pp. 168–171, 1964.
- [59] G.’t Hooft, “Renormalizable Lagrangians for massive Yang-Mills fields,” *Nuclear Physics B*, vol. 35, no. 1, pp. 167–188, 1971.
- [60] G. ’tHooft, “Renormalization of massless Yang-Mills fields,” *Nuclear Physics B*, vol. 33, no. 1, pp. 173–199, 1971.
- [61] F.J. Hasert et al., “Observation of neutrino-like interactions without muon or electron in the gargamelle neutrino experiment,” *Physics Letters B*, vol. 46, no. 1, pp. 138–140, 1973.
- [62] P. Higgs, “Broken Symmetries and the Masses of Gauge Bosons,” *Phys. Rev. Lett.*, vol. 13, pp. 508–509, 1964.
- [63] F. Englert and R. Brout, “Broken Symmetry and the Mass of Gauge Vector Mesons,” *Phys. Rev. Lett.*, vol. 13, pp. 321–323, 1964.

BIBLIOGRAPHY

- [64] CMS Collaboration, “Measurements of Higgs boson properties in the diphoton decay channel in proton-proton collisions at $\sqrt{s} = 13$ TeV,” *Journal of High Energy Physics*, vol. 2018, no. 11, 2018.
- [65] CMS Collaboration, “Measurements of properties of the Higgs boson decaying into the four-lepton final state in pp collisions at $\sqrt{s} = 13$ TeV,” *Journal of High Energy Physics*, vol. 2017, no. 11, 2017.
- [66] A. Aivazis, “A javascript application for creating feynman diagrams.” Website: <https://feynman.aivazis.com/>.
- [67] CMS Collaboration, “Observation of $t\bar{t}H$ Production,” *Phys. Rev. Lett.*, vol. 120, p. 231801, Jun 2018.
- [68] ATLAS Collaboration, “Observation of Higgs boson production in association with a top quark pair at the LHC with the ATLAS detector,” *Phys. Lett.*, vol. B784, p. 173, 2018.
- [69] C. Collaboration, “Observation of Higgs Boson Decay to Bottom Quarks,” *Phys. Rev. Lett.*, vol. 121, p. 121801, Sep 2018.
- [70] ATLAS Collaboration, “Observation of $H \rightarrow b\bar{b}$ decays and VH production with the ATLAS detector,” *Phys. Lett.*, vol. B786, p. 59, 2018.
- [71] ATLAS Collaboration, “Measurement of inclusive and differential cross sections in the $H \rightarrow ZZ^* \rightarrow 4l$ decay channel in pp collisions at $\sqrt{s} = 13$ TeV with the ATLAS detector,” *Journal of High Energy Physics*, vol. 2017, no. 10, 2017.
- [72] CMS Collaboration, “Observation of the Higgs boson decay to a pair of τ leptons with the CMS detector,” *Physics Letters B*, vol. 779, p. 283–316, 2018.
- [73] ATLAS Collaboration, “Cross-section measurements of the Higgs boson decaying into a pair of τ -leptons in proton-proton collisions at $\sqrt{s} = 13$ TeV with the ATLAS detector,” *Phys. Rev. D*, vol. 99, p. 072001, 2019.
- [74] ATLAS Collaboration, “Measurements of higgs boson properties in the diphoton decay channel with $36 fb^{-1}$ of pp collision data at $\sqrt{s} = 13$ TeV with the atlas detector,” *Physical Review D*, vol. 98, no. 5, 2018.
- [75] CMS Collaboration, “Search for the standard model Higgs boson decaying to charm quarks,” Tech. Rep. CMS-PAS-HIG-18-031, CERN, Geneva, 2019. <https://cds.cern.ch/record/2682638>.

-
- [76] CMS Collaboration, “Evidence for Higgs boson decay to a pair of muons,” *Journal of High Energy Physics*, vol. 2021, no. 1, 2021.
- [77] C. Collaboration, “Combination of Searches for Higgs Boson Pair Production in Proton-Proton Collisions at $\sqrt{s} = 13$ TeV,” *Phys. Rev. Lett.*, vol. 122, p. 121803, 2019.
- [78] A. Purcell, “Go on a particle quest at the first CERN webfest,” no. BUL-NA-2012-269. 35/2012, p. 10, 2012.
- [79] KATRIN Collaboration, “Improved Upper Limit on the Neutrino Mass from a Direct Kinematic Method by KATRIN,” *Physical Review Letters*, vol. 123, no. 22, 2019.
- [80] G. Giudice, “Naturally Speaking: The Naturalness Criterion and Physics at the LHC,” *Perspectives on LHC Physics*, p. 155–178, 2008.
- [81] S. Martin, “A Supersymmetry Primer,” *Advanced Series on Directions in High Energy Physics*, p. 1–98, 1998.
- [82] K. Intriligator and N. Seiberg, “Lectures on supersymmetry breaking,” *Classical and Quantum Gravity*, vol. 24, no. 21, p. S741–S772, 2007.
- [83] S. Coleman and J. Mandula, “All Possible Symmetries of the S Matrix,” *Phys. Rev.*, vol. 159, pp. 1251–1256, 1967.
- [84] A. Lahanas, “LSP as a Candidate for Dark Matter,” *The Invisible Universe: Dark Matter and Dark Energy*, p. 35–68.
- [85] J. H. R. Cotta, J. Gainer and T. Rizzo, “Dark matter in the MSSM,” *New Journal of Physics*, vol. 11, no. 10, p. 105026, 2009.
- [86] E. Bagnaschi et al., “Benchmark scenarios for low $\tan\beta$ in the MSSM,” Tech. Rep. LHCHXSWG-2015-002, CERN, Geneva, 2015.
- [87] ATLAS Collaboration, “Combined measurements of Higgs boson production and decay using up to 80fb^{-1} of proton-proton collision data at $\sqrt{s} = 13\text{TeV}$ collected with the ATLAS experiment,” *Physical Review D*, vol. 101, no. 1, 2020.
- [88] CMS Collaboration, “Combined measurements of Higgs boson couplings in proton-proton collisions at $\sqrt{s} = 13\text{TeV}$,” *The European Physical Journal C*, vol. 79, no. 5, 2019.

- [89] CMS Collaboration, “Precise determination of the mass of the Higgs boson and tests of compatibility of its couplings with the standard model predictions using proton collisions at 7 and 8 TeV,” *The European Physical Journal C*, vol. 75, no. 5, 2015.
- [90] CMS Collaboration, “Search for mssm higgs bosons decaying to $\mu^+\mu^-$ in proton-proton collisions at $\sqrt{s} = 13\text{tev}$,” *Physics Letters B*, vol. 798, p. 134992, 2019.
- [91] M. Carena, D. Garcia, U. Nierste, E. Carlos, “Effective Lagrangian for the interaction in the MSSM and charged Higgs phenomenology,” *Nuclear Physics B*, vol. 577, no. 1-2, p. 88–120, 2000.
- [92] M. Carena, S. Heinemeyer, C. Wagner, G. Weiglein, “MSSM Higgs boson searches at the Tevatron and the LHC: Impact of different benchmark scenarios,” *The European Physical Journal C*, vol. 45, no. 3, p. 797–814, 2006.
- [93] A. Bednyakov, B. Kniehl, A. Pikelner, O. Veretin, “On the b-quark running mass in QCD and the SM,” *Nuclear Physics B*, vol. 916, p. 463–483, 2017.
- [94] LHC Higgs Working Group, “MSSM Neutral Higgs.” <https://twiki.cern.ch/twiki/bin/view/LHCPhysics/LHCHWGMSSMNeutral>. Website, accessed April 08, 2021.
- [95] A. Celis, V. Ilisie, A. Pich, “LHC constraints on two-Higgs doublet models,” *Journal of High Energy Physics*, vol. 2013, no. 7, 2013.
- [96] M. Carena, G. Weiglein et al., “MSSM Higgs boson searches at the LHC: benchmark scenarios after the discovery of a Higgs-like particle,” *The European Physical Journal C*, vol. 73, no. 9, 2013.
- [97] H. Bahl, T. Stefaniak, G. Weiglein et al., “HL-LHC and ILC sensitivities in the hunt for heavy Higgs bosons,” *The European Physical Journal C*, vol. 80, no. 10, 2020.
- [98] E. Bagnaschi, T. Stefaniak et al., “MSSM Higgs boson searches at the LHC: benchmark scenarios for Run 2 and beyond,” *The European Physical Journal C*, vol. 79, no. 7, 2019.
- [99] H. Bahl, S. Liebler, T. Stefaniak, “MSSM Higgs benchmark scenarios for Run 2 and beyond: the low $\tan\beta$ region,” *The European Physical Journal C*, vol. 79, no. 3, 2019.
- [100] P. Ferreira, R. Santos, M. Sher, J. Silva, “Could the LHC two-photon signal correspond to the heavier scalar in two-Higgs-doublet models?,” *Physical Review D*, vol. 85, no. 3, 2012.

- [101] The LEP Working Group for Higgs Boson Searches, “Search for neutral MSSM Higgs bosons at LEP,” *The European Physical Journal C*, vol. 47, no. 3, 2006.
- [102] ATLAS Collaboration, “Search for heavy neutral higgs bosons produced in association with b-quarks and decaying into b-quarks at $\sqrt{s} = 13\text{TeV}$ with the atlas detector,” *Physical Review D*, vol. 102, no. 3, 2020.
- [103] CMS Collaboration, “Search for additional neutral mssm higgs bosons in the $\tau\tau$ final state in proton-proton collisions at $\sqrt{s} = 13\text{TeV}$,” *Journal of High Energy Physics*, vol. 2018, no. 9, 2018.
- [104] S. L. Glashow and S. Weinberg, “Natural Conservation Laws for Neutral Currents,” *Phys. Rev. D*, vol. 15, p. 1958, 1977.
- [105] E. A. Paschos, “Diagonal neutral currents,” *Phys. Rev. D*, vol. 15, pp. 1966–1972, Apr 1977.
- [106] H. Haber, and O. Stål, “New LHC benchmarks for the \mathcal{CP} -conserving two-Higgs-doublet model,” *The European Physical Journal C*, vol. 75, no. 10, 2015.
- [107] D. Eriksson, J. Rathsman, Johan, O. Stål, “2HDMC – two-Higgs-doublet model calculator,” *Computer Physics Communications*, vol. 181, no. 1, p. 189–205, 2010.
- [108] R. Harlander, S. Liebler, H. Mantler, “SusHi: A program for the calculation of Higgs production in gluon fusion and bottom-quark annihilation in the Standard Model and the MSSM,” *Computer Physics Communications*, vol. 184, no. 6, p. 1605–1617, 2013.
- [109] A. Buckley et al., “LHAPDF6: parton density access in the LHC precision era,” *The European Physical Journal C*, vol. 75, no. 3, 2015.
- [110] CMS Collaboration, “Combined measurements of Higgs boson couplings in proton–proton collisions at $\sqrt{s} = 13\text{TeV}$,” *The European Physical Journal C*, vol. 79, no. 5, 2019.
- [111] F. Guthrie, “On a new relation between heat and electricity,” *Proceedings of the Royal Society of London*, vol. 21, pp. 168 – 169, 1873.
- [112] S. L. Wu, “e+e- physics at petra—the first five years,” *Physics Reports*, vol. 107, no. 2, pp. 59 – 324, 1984.

BIBLIOGRAPHY

- [113] “Design Report Tevatron 1 project,” Tech. Rep. FERMILAB-DESIGN-1984-01, 1984.
- [114] *LEP design report*. CERN, 1984.
- [115] M.-J. Collaboration, “Discovery of Three-Jet Events and a Test of Quantum Chromodynamics at PETRA,” *Phys. Rev. Lett.*, vol. 43, pp. 830–833, 1979.
- [116] The ALEPH Collaboration, the DELPHI Collaboration, the L3 Collaboration, the OPAL Collaboration, the SLD Collaboration, the LEP Electroweak Working Group, the SLD electroweak, heavy flavour groups, “Precision Electroweak Measurements on the Z Resonance,” *Physics Reports*, vol. 427, no. 5-6, p. 257–454, 2006.
- [117] “The Tevatron legacy: a luminosity story,” *CERN Courier*, vol. 56, pp. 25–30, May 2016.
- [118] C. Lefèvre, “The CERN accelerator complex.” 2008.
- [119] ALICE Collaboration, “The ALICE experiment at the CERN LHC,” *Journal of Instrumentation*, vol. 3, no. 08, p. S08002, 2008.
- [120] LHCb Collaboration, “The LHCb detector at the LHC,” *Journal of Instrumentation*, vol. 3, no. 08, p. S08005, 2008.
- [121] TOTEM Collaboration, “The TOTEM experiment at the CERN large hadron collider,” *Journal of Instrumentation*, vol. 3, no. 08, p. S08007, 2008.
- [122] LHCf Collaboration, “The LHCf detector at the CERN large hadron collider,” *Journal of Instrumentation*, vol. 3, no. 08, p. S08006, 2008.
- [123] MoEDAL Collaboration, “Technical Design Report of the MoEDAL Experiment,” tech. rep., Jun 2009.
- [124] FASER Collaboration, “Technical Proposal: FASER, the Forward Search Experiment at the LHC,” tech. rep., CERN, Geneva, 2018.
- [125] CMS Collaboration, “Lumi Public Results.” https://twiki.cern.ch/twiki/bin/view/CMSPublic/LumiPublicResults#2017_proton_proton_collisions. Website, accessed October 15, 2020.
- [126] S. R. Davis, “Interactive Slice of the CMS detector,” 2016.
- [127] A. Saha, “Phase 1 upgrade of the CMS pixel detector,” *Journal of Instrumentation*, vol. 12, no. 02, p. C02033, 2017.

- [128] CMS Collaboration, *The CMS hadron calorimeter project: Technical Design Report*. CERN, 1997.
- [129] CMS Collaboration, *The CMS muon project: Technical Design Report*. Technical Design Report CMS, CERN, 1997.
- [130] CMS Collaboration, “Observation of a new boson at a mass of 125 GeV with the CMS experiment at the LHC,” *Physics Letters B*, vol. 716, no. 1, pp. 30 – 61, 2012.
- [131] C. Collaboration”, “The CMS trigger system,” *Journal of Instrumentation*, vol. 12, no. 01, p. P01020, 2017.
- [132] W. Hastings, “Monte Carlo Sampling Methods Using Markov Chains and Their Applications,” *Biometrika*, vol. 57, pp. 97–109, 1970.
- [133] T. Sjöstrand, S. Mrenna, P. Skands, “A brief introduction to PYTHIA 8.1,” *Computer Physics Communications*, vol. 178, no. 11, p. 852–867, 2008.
- [134] J. Alwall, M. Herquet et al., “MadGraph 5: going beyond,” *Journal of High Energy Physics*, vol. 2011, no. 6, 2011.
- [135] R. Frederix, S. Frixione, S. Prestel et al., “On the reduction of negative weights in MC@NLO-type matching procedures,” *Journal of High Energy Physics*, vol. 238, 2020.
- [136] “Geant4—a simulation toolkit,” *Nuclear Instruments and Methods in Physics Research Section A: Accelerators, Spectrometers, Detectors and Associated Equipment*, vol. 506, no. 3, pp. 250 – 303, 2003.
- [137] “Recent developments in Geant4,” *Nuclear Instruments and Methods in Physics Research Section A: Accelerators, Spectrometers, Detectors and Associated Equipment*, vol. 835, pp. 186 – 225, 2016.
- [138] ALEPH Collaboration, “Performance of the aleph detector at lep,” *Nuclear Instruments and Methods in Physics Research Section A: Accelerators, Spectrometers, Detectors and Associated Equipment*, vol. 360, no. 3, pp. 481 – 506, 1995.
- [139] CMS Collaboration, “Particle-flow reconstruction and global event description with the CMS detector,” *Journal of Instrumentation*, vol. 12, no. 10, p. P10003, 2017.
- [140] R. Kalman, “A new approach to linear filtering and prediction problems,” *Journal of Basic Engineering*, vol. Series D, no. 82, 1960.

BIBLIOGRAPHY

- [141] W. Adam et al., “Track Reconstruction in the CMS tracker,” Tech. Rep. CMS-NOTE-2006-041, CERN, 2006.
- [142] K. Rose, “Deterministic annealing for clustering, compression, classification, regression, and related optimization problems,” *Proceedings of the IEEE*, vol. 86, no. 11, pp. 2210–2239, 1998.
- [143] W. Waltenberger, R. Frühwirth, P. Vanlaer, “Adaptive vertex fitting,” *Journal of Physics G: Nuclear and Particle Physics*, vol. 34, no. 12, pp. N343–N356, 2007.
- [144] W. Waltenberger, “Adaptive Vertex Reconstruction,” Tech. Rep. CMS-NOTE-2008-033, 2008.
- [145] CMS Collaboration, “CMS Tracking POG Performance Plots For 2017 with Phase I pixel detector.” https://twiki.cern.ch/twiki/bin/view/CMSPublic/TrackingPOGPerformance2017MC#Vertex_Resolutions. Website, accessed October 15, 2020.
- [146] CMS Collaboration, “Description and performance of track and primary-vertex reconstruction with the CMS tracker,” *JINST*, vol. 9, no. 10, p. P10009, 2014.
- [147] R. Atkin, “Review of jet reconstruction algorithms,” *Journal of Physics: Conference Series*, vol. 645, p. 012008, 2015.
- [148] *Run II Jet Physics*, Proceedings of the Run II QCD and Weak Boson Physics Workshop, G. C. Blazey et al., 2000. arXiv:hep-ex/0005012v2.
- [149] S. D. Ellis, D. E. Soper, “Successive combination jet algorithm for hadron collisions,” *Phys. Rev. D*, vol. 48, pp. 3160–3166, 1993.
- [150] Y. L. Dokshitzer et al., “Better jet clustering algorithms,” *Journal of High Energy Physics*, vol. 1997, no. 08, p. 001, 1997.
- [151] M. Cacciari, G. P. Salam, G. Soyez, “The anti-kt jet clustering algorithm,” *Journal of High Energy Physics*, vol. 2008, no. 04, p. 063, 2008.
- [152] S. D. Ellis, D. E. Soper, “Successive combination jet algorithm for hadron collisions,” *Phys. Rev. D*, vol. 48, pp. 3160–3166, 1993.
- [153] CMS Collaboration, “Jet algorithms performance in 13 TeV data,” Tech. Rep. CMS-PAS-JME-16-003, 2017.

- [154] CMS Collaboration, “Jet Identification for the 13 TeV data Run2017.” Website, accessed April 15th, 2021.
- [155] CMS Collaboration, “Jet energy scale and resolution in the CMS experiment in pp collisions at 8 TeV,” *Journal of Instrumentation*, vol. 12, no. 02, p. P02014, 2017.
- [156] CMS Collaboration, “CMS Jet and Missing Energy Results.” <https://twiki.cern.ch/twiki/bin/view/CMSPublic/PhysicsResultsJME>. Website, accessed February 23, 2021.
- [157] CMS Collaboration, “Jet Energy Resolution.” <https://twiki.cern.ch/twiki/bin/viewauth/CMS/JetResolution>. Website, accessed February 23, 2021.
- [158] L3 Collaboration, “Measurement of the branching ratios $b \rightarrow e\nu X$, $\mu\nu X$, $\tau\nu X$ and νX ,” *Z. Phys. C – Particles and Fields* 71, pp. 379 – 389 (1996).
- [159] CMS Collaboration, “Identification of heavy-flavour jets with the CMS detector in pp collisions at 13 TeV,” *Journal of Instrumentation*, vol. 13, no. 05, p. P05011, 2018.
- [160] “Identification of b quark jets at the CMS Experiment in the LHC Run 2,” Tech. Rep. CMS-PAS-BTV-15-001, CERN, 2016.
- [161] CMS Collaboration, “Identification of b-quark jets with the CMS experiment,” *Journal of Instrumentation*, vol. 8, no. 04, p. P04013, 2013.
- [162] C. Collaboration, “Deep learning in jet reconstruction at CMS,” *Journal of Physics: Conference Series*, vol. 1085, p. 042029, 2018.
- [163] E. Bols et al., “Jet flavour classification using DeepJet,” *Journal of Instrumentation*, vol. 15, no. 12, p. P12012, 2020.
- [164] CMS Collaboration, “B-tagging reference plots.” <https://twiki.cern.ch/twiki/bin/view/CMSPublic/SWGuideBTagPerformance>. Website, accessed February 25, 2021.
- [165] V. Khachatryan et al., “Measurement of $b\bar{b}$ angular correlations based on secondary vertex reconstruction at $\sqrt{s} = 7\text{ teV}$,” *Journal of High Energy Physics*, vol. 2011, no. 3, 2011.

BIBLIOGRAPHY

- [166] CMS Collaboration, “CMS B-Tagging and Vertexing Results.” <https://twiki.cern.ch/twiki/bin/view/CMSPublic/PhysicsResultsBTV>. Website, accessed March 02, 2021.
- [167] CMS Collaboration, “Performance of the DeepJet b tagging algorithm using 41.9/fb of data from proton-proton collisions at 13TeV with Phase 1 CMS detector,” 2018.
- [168] R. Assmann, M. Lamont, S. Myers, “A brief history of the LEP collider,” *Nucl. Phys. B Proc. Suppl.*, vol. 109, pp. 17–31, 2002.
- [169] ALEPH, DELPHI, L3, OPAL Collaborations. The LEP Working Group "for Higgs Boson Searches", “Search for Neutral MSSM Higgs Bosons at LEP,” *The European Physical Journal C*, vol. 47, pp. 547–587, 2006.
- [170] S. Holmes, R. Moore, V. Shiltsev, “Overview of the Tevatron Collider Complex: Goals, Operations and Performance,” 2011.
- [171] CDF Collaboration, “Search for Higgs bosons produced in association with b quarks,” *Phys. Rev. D*, vol. 85, p. 032005, 2012.
- [172] D0 Collaboration, “Search for neutral Higgs bosons in the multi- b -jet topology in $5.2 fb^{-1}$ of pp^{-} collisions at $\sqrt{s}=1.96$ TeV,” *Physics Letters B*, vol. 698, no. 2, pp. 97–104, 2011.
- [173] “Search for neutral Higgs bosons in events with multiple bottom quarks at the Tevatron,” *Phys. Rev. D*, vol. 86, p. 091101, 2012.
- [174] ATLAS Collaboration, “Search for heavy neutral Higgs bosons produced in association with b -quarks and decaying into b -quarks at $\sqrt{s} = 13$ TeV with the ATLAS detector,” *Phys. Rev. D*, vol. 102, p. 032004, 2020.
- [175] CMS Collaboration, “Search for a higgs boson decaying into a b -quark pair and produced in association with b quarks in proton–proton collisions at 7 tev,” *Physics Letters B*, vol. 722, no. 4, pp. 207–232, 2013.
- [176] CMS Collaboration, “Search for neutral mssm higgs bosons decaying into a pair of bottom quarks,” *Journal of High Energy Physics*, no. 11, 2015.
- [177] R. Shevchenko, *Search for high mass higgs bosons in the final state with b -quarks with the CMS 2016 data*. Dissertation, Universität Hamburg, Hamburg, 2019. Dissertation, Universität Hamburg, 2019.

- [178] CMS Collaboration, “Search for beyond the standard model Higgs bosons decaying into a $b\bar{b}$ pair in pp collisions at $\sqrt{s}=13$ TeV,” *Journal of High Energy Physics*, no. 08, p. 113, 2018.
- [179] R. Harlander, M. Krämer, M. Schumacher, “Bottom-quark associated Higgs-boson production: reconciling the four- and five-flavour scheme approach,” 2011.
- [180] F. Maltoni, G. Ridolfi, M. Ubiali, “b-initiated processes at the LHC: a reappraisal,” *Journal of High Energy Physics*, vol. 2012, no. 7, 2012.
- [181] S. Forte, D. Napoletano, M. Ubiali, “Higgs production in bottom-quark fusion in a matched scheme,” *Physics Letters B*, vol. 751, pp. 331–337, 2015.
- [182] S. Forte, D. Napoletano, M. Ubiali, “Higgs production in bottom-quark fusion: Matching beyond leading order,” *Physics Letters B*, vol. 763, pp. 190–196, 2016.
- [183] M. Bonvini, A. Papanastasiou, F. Tackmann, “Resummation and matching of b-quark mass effects in $b\bar{b}H$ $b\bar{b}H$ production,” *Journal of High Energy Physics*, vol. 2015, no. 11, 2015.
- [184] M. Bonvini, A. Papanastasiou, F. Tackmann, “Matched predictions for the $b\bar{b}H$ $b\bar{b}H$ cross section at the 13 TeV LHC,” *Journal of High Energy Physics*, vol. 2016, no. 10, 2016.
- [185] CMS Collaboration, “Search for neutral Higgs Bosons Production in Final States with b-quarks in the semi-leptonic channel with the CMS 2017 data,” 2019.
- [186] “A Deep Neural Network for Simultaneous Estimation of b Jet Energy and Resolution,” no. 10.
- [187] CMS Collaboration, “b-jet energy regression at 13 TeV.” Website, accessed April 15th, 2021.
- [188] S. Bernstein, “Démonstration du théorème de Weierstrass fondée sur le calcul des probabilités,” *Communications of the Kharkov Mathematical Society*, vol. XIII, pp. 1–2, 1912.
- [189] H. Ikeda et al., “A detailed test of the CsI(Tl) calorimeter for BELLE with photon beams of energy between 20 MeV and 5.4 GeV,” *Nuclear Instruments and Methods in Physics Research Section A: Accelerators, Spectrometers, Detectors and Associated Equipment*, vol. 441, no. 3, pp. 401–426, 2000.

BIBLIOGRAPHY

- [190] R. Walsh". Private conversation.
- [191] G. Cowan et al., "Asymptotic formulae for likelihood-based tests of new physics," *Eur. Phys. J. C* 71, no. 1554, 2011.
- [192] A. L. Read, "Presentation of search results: theCLstechnique," *J. Phys. G: Nucl. Part. Phys.*, vol. 28, no. 10, pp. 2693–2704, 2002.
- [193] "Procedure for the LHC Higgs boson search combination in Summer 2011," Tech. Rep. CMS-NOTE-2011-005. ATL-PHYS-PUB-2011-11, CERN, Geneva, 2011.
- [194] F. James, "MINUIT Function Minimization and Error Analysis: Reference Manual Version 94.1," 1994.
- [195] S. S. Wilks, "The Large-Sample Distribution of the Likelihood Ratio for Testing Composite Hypotheses," *The Annals of Mathematical Statistics*, vol. 9, no. 1, pp. 60–62, 1938.
- [196] J. S. Conway, "Incorporating Nuisance Parameters in Likelihoods for Multisource Spectra," 2011. arXiv: 1103.0354.
- [197] J. K. Lindsey, *Parametric statistical inference*. Oxford: Clarendon Press, 1996.
- [198] Higgs Combination Group, "Combine – Running Combine – Common Statistical Methods." <http://cms-analysis.github.io/HiggsAnalysis-CombinedLimit/part3/commonstatmethods/#goodness-of-fit-tests>. Website, accessed May 25th, 2021.
- [199] S. Dittmaier, M. Krämer, M. Spira, "Higgs radiation off bottom quarks at the Fermilab Tevatron and the CERN LHC," *Phys. Rev. D*, vol. 70, p. 074010, 2004.
- [200] S. Dawson, C. Jackson, L. Reina, D. Wackerroth, "Exclusive Higgs boson production with bottom quarks at hadron colliders," *Phys. Rev. D*, vol. 69, p. 074027, 2004.
- [201] R. Harlander, W. Kilgore, "Higgs boson production in bottom quark fusion at next-to-next-to-leading order," *Phys. Rev. D*, vol. 68, p. 013001, Jul 2003.
- [202] S. Heinemeyer, W. Hollik, G. Weiglein, "FeynHiggs: A Program for the calculation of the masses of the neutral CP even Higgs bosons in the MSSM," *Comput. Phys. Commun.*, vol. 124, pp. 76–89, 2000.

- [203] H. Bahl, G. Weiglein et al., “Precision calculations in the MSSM Higgs-boson sector with FeynHiggs 2.14,” *Comput. Phys. Commun.*, vol. 249, pp. 99–107, 2020.
- [204] A. Djouadi, J. Kalinowski, M. Spira, “HDECAY: A Program for Higgs boson decays in the standard model and its supersymmetric extension,” *Comput. Phys. Commun.*, vol. 108, pp. 56–74, 1998.
- [205] A. Djouadi, J. Kalinowski, M. Muehlleitner, M. Spira, “HDECAY: Twenty₊₊ years after,” *Comput. Phys. Commun.*, vol. 238, pp. 214–231, 2019.
- [206] CMS Collaboration, “Search for a heavy pseudoscalar boson decaying to a z and a higgs boson at $\sqrt{s} = 13$ TeV,” *The European Physical Journal C*, vol. 79, no. 7, 2019.
- [207] CMS Collaboration, “Combined measurements of Higgs boson couplings in proton–proton collisions at $\sqrt{s} = 13$ TeV,” *The European Physical Journal C*, vol. 79, no. 5, 2019.
- [208] CMS Collaboration, “Alignment of the CMS tracker with LHC and cosmic ray data,” *Journal of Instrumentation*, vol. 9, no. 06, p. P06009, 2014.
- [209] V. Blobel, “Software alignment for tracking detectors,” *Nuclear Instruments and Methods in Physics Research Section A: Accelerators, Spectrometers, Detectors and Associated Equipment*, vol. 566, no. 1, pp. 5–13, 2006. TIME 2005.
- [210] CMS Collaboration, “Alignment of the CMS silicon strip tracker during stand-alone commissioning,” *Journal of Instrumentation*, vol. 4, no. 07, p. T07001, 2009.
- [211] J. Draeger, “Track Based Alignment of the CMS Silicon Tracker and its Implication on Physics Performance”. Dissertation, Universität Hamburg, Hamburg, 2011. Dissertation, Universität Hamburg, 2011.
- [212] M. Schröder for the CMS Collaboration, “Alignment of the Upgraded CMS Pixel Detector,” 2017. Poster presented at the 11th International Hiroshima Symposium on the Development and Application of Semiconductor Tracking Detectors.
- [213] C. Kleinwort, “General Broken Lines as advanced track fitting method,” *Nucl. Instrum. Meth. A*, vol. 673, pp. 107–110, 2012.
- [214] CMS Collaboration, “Alignment of the CMS silicon tracker during commissioning with cosmic rays,” *Journal of Instrumentation*, vol. 5, no. 03, p. T03009, 2010.

- [215] C. Collaboration", "CMS Tracker Alignment Performance Results 2016," 2017.
- [216] F. W. J. Oliver, ed., *NIST Handbook of Mathematical Functions*. Cambridge University Press, 2010.
- [217] C. Collaboration", "CMS Tracker Alignment Performance Results Start-Up 2017," 2017.
- [218] *Higgs Physics Within and Beyond the Standard Model at CMS*, 2020. Presented at the 11th International Conference in High-Energy Physics, Antananarivo, Madagascar, 2019.

Acknowledgements

Throughout my time in academia but especially during my PhD project, I was blessed with the opportunity to work with a set of extraordinary people. They helped me complete this thesis and the research going into it. With this note, I would like to express my appreciation and gratitude towards them. Especially considering the very particular circumstances we all experienced during the second half of my doctoral studies, including a switch to working entirely remotely more or less from one day to another, their help can not be valued highly enough.

First of all, I would like to thank my supervisor, Dr. Rainer Mankel. Nobody has been more involved with this project and helped me advance with it. Even during busy times, he always made it possible to discuss recent developments and issues, and he always found the right questions to ask in order to overcome obstacles as well as develop and improve the line of reasoning. His experience, organized way of thinking, planning, and communicating, as well as his talent to spot the right point to address the next step of the project were indispensable for the completion of this work. Moreover, his careful proof-reading contributed greatly to this thesis.

Also without my second supervisor, Prof. Dr. Elisabetta Gallo, this thesis could never have been written. She enabled me to start in the DESY CMS group which she lead for almost the whole time I was working on this project. Her kind nature and knowledge made it a pleasure to work under her supervision and in the CMS group. She always took care of the PhD students in the group, and encouraged them to participate in (also external) events. For me, this meant attending the Latin-American summer school as well as the HEPMAD conference on Madagascar, which both helped me advance a lot and enabled me to gain experience and create memories I will never forget.

The rest of our amazing Higgs group should of course not be forgotten. It was a gift to work in this group and I will always treasure this remarkable experience. I would like to thank Dr. Roberval Walsh, who took the time to discuss technical questions extensively during the first part of this project. The wide range of knowledge he brought to discussions during meetings and private conversations were vital to progress with the research for this thesis, whether it was related to rather technical topics like the trigger, scale factors and general programming, or considering physics. Also the help from Dr. Alexei Raspereza and Dr. Adinda de Wit with the

BIBLIOGRAPHY

combine tool studies can not be overstated. Without them, it would never have been possible for me to finish this work within any reasonable time frame. The discussions during meetings helped a lot but they also always took time out of their busy schedules for in-depth investigations of results and helped me to get the approach to work.

I would also like to thank my friends and fellow PhD students Dr. Rostyslav Shevchenko, Dr. Antonio Vagnerini, Sam Kaveh, and Aliya Nigamova. Sharing an office with them and chatting during lunch or coffee was a great pleasure and they were always there to help with programming and the analysis framework including the model interpretation, physics, presentations or any other topics that might have occurred. Especially the contributions to the analysis framework by Rostyslav and Antonio were invaluable for the timely completion of this work. Furthermore, I would like to mention Dr. Chayanit Asawatangtrakuldee and Dr. Sandra Consuegra Rodriguez here. Their help with the Monte Carlo samples, organizing the working meetings, rehearsals and more was extremely valuable. In addition, I would like to acknowledge the help of Birgit Breetzke and Gabriele Kalhöfer, our group secretaries, who ensure that organizational things in the group run smoothly and who always very kindly helped in case of questions and issues.

My service work in the tracker alignment group could not have been done without the help, guidance, knowledge, and endurance of Dr. Marco Musich, Dr. Patrick Connor, Dr. Valeria Botta, Dr. Alexander Grohsjean, and Kirill Skovpen. Whether it was assistance with actual alignment tasks, issues with the Monte Carlo generators or taking some workload away from me in extremely busy times (either when we were swamped with Monte Carlo generation requests or when I had to focus on my research project), their help is greatly appreciated.

Finally, without encouragement and support from my family, nothing I did during this period would have been possible for me. Thank you for listening when things got stressful or when I was struggling to progress as quickly as I would have liked to. Of course, this is especially true for the wonderful person who had to endure me and was there for me throughout this entire time, including months of various forms of lock-downs. She also always managed to free up time in her packed schedule for proof-reading, rehearsals, and providing an outside look on my reasoning. Thank you, Theresa, for helping me to stay focused and positive throughout the entire time.